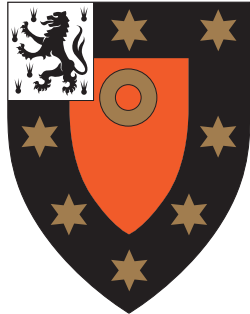


Studies of $D^0 \rightarrow K_s^0 h^+ h^-$ decays at the LHCb experiment

Oliver Lupton
St John's College, University of Oxford



Thesis submitted in partial fulfilment of the requirements for
the degree of Doctor of Philosophy at the University of Oxford

Trinity Term, 2016

Studies of $D^0 \rightarrow K_s^0 h^+ h'^-$ decays at the LHCb experiment

Oliver Lupton
St John's College, University of Oxford

Thesis submitted in partial fulfilment of the requirements for
the degree of Doctor of Philosophy at the University of Oxford.

Trinity Term, 2016

Abstract

This thesis documents two studies of the neutral charm meson system using the LHCb detector, and gives an overview of the numerous changes made to the LHCb software trigger in advance of Run 2 of the LHC.

In the first analysis, amplitude models are applied to studies of the resonance structure in $D^0 \rightarrow K_s^0 K^- \pi^+$ and $D^0 \rightarrow K_s^0 K^+ \pi^-$ decays using proton-proton collision data, corresponding to an integrated luminosity of 3.0 fb^{-1} , collected during Run 1 of the LHC. Relative magnitude and phase information is determined, and coherence factors and related observables are computed for both the whole phase space and a restricted region of $100 \text{ MeV}/c^2$ around the $K^*(892)^\pm$ resonance. Two formulations for the $K\pi S$ -wave are used, both of which give a good description of the data. The ratio of branching fractions $\mathcal{B}(D^0 \rightarrow K_s^0 K^+ \pi^-) / \mathcal{B}(D^0 \rightarrow K_s^0 K^- \pi^+)$ is measured to be $0.655 \pm 0.004 \text{ (stat)} \pm 0.006 \text{ (syst)}$ over the full phase space and $0.370 \pm 0.003 \text{ (stat)} \pm 0.012 \text{ (syst)}$ in the restricted region. A search for CP violation is performed using the amplitude models and no significant effect is found. Predictions from SU(3) flavour symmetry for $K^*(892)K$ amplitudes of different charges are compared with the amplitude model results, and marginal agreement is found.

The second study estimates the sensitivity to $D^0 - \bar{D}^0$ mixing and indirect CP violation parameters that can be achieved using a model-independent technique and the samples of $D^0 \rightarrow K_s^0 K^+ K^-$ decays recorded by LHCb in Run 1 and Run 2 of the LHC. These studies show that constraints on these parameters could be significantly improved by an analysis of the anticipated Run 2 dataset.

In the beginning the Universe was created.
This has made a lot of people very angry and
been widely regarded as a bad move.

— *Douglas Adams*

ACKNOWLEDGEMENTS

I would like to thank my supervisor, Guy Wilkinson, for his advice and support in the last few years, along with Brian Meadows and Vava Gligorov for their help along the way.

There are many more people I would like to thank for their friendship, help and support over the last few years. Thanks to my Oxford LHCb colleagues, in particular Faye Cheung, Tim Evans, Scott Stevenson and Donal Hill, for putting up with my many complaints, and my Oxford ATLAS contemporaries Will Kalderon and Mark Pickering for some memorable adventures in various countries. Thanks also to Neville Harnew, for letting me try my hand at undergraduate teaching, and to the Oxford support staff, particularly Sue Geddes, Sean Brisbane and Kim Proudfoot.

I thoroughly enjoyed my two years at CERN, where I met far too many interesting and diverse friends and colleagues to list. In particular, I spent many enjoyable hours both in the LHCb control room and/or exploring France and Switzerland on two wheels with Tim Head, Hamish Gordon, Conor Fitzpatrick and Mika Vesterinen. Thanks also go to Irene, Rhona and other non-physicist friends in Geneva for keeping me rooted in the wider world.

I am also grateful for the support of my friends, who have remained just that despite my long absences and fleeting visits. Being able to visit see you all in various places has been a highlight of the last few years, particularly those of you sharing the “PhD experience”: Valentijn, Shamim, Katherine, Mireia and Craig among others.

My parents and family also deserve a great deal of credit for their efforts preparing me for, and supporting me in, my academic endeavours. Finally, last but by no means least, thank you to Ruth, for her unwavering love and support, her indefatigable optimism, and for sharing a great many adventures with me over the last few years.

CONTENTS

1.	<i>Introduction</i>	1
2.	<i>Theoretical background</i>	5
2.1	Introduction to the Standard Model of Particle Physics	5
2.2	Physics beyond the Standard Model	9
2.3	Mesons, baryons and beyond	10
2.4	Amplitude analysis	11
2.4.1	The isobar model	13
2.5	<i>CP</i> violation and neutral meson mixing	17
2.5.1	Neutral meson mixing formalism	20
3.	<i>The LHC and the LHCb experiment</i>	27
3.1	The Large Hadron Collider	27
3.2	The LHCb experiment	29
3.2.1	Vertex Locator	32
3.2.2	Downstream Tracking	34
3.2.3	Silicon Tracker	34
3.2.4	Outer Tracker	36
3.2.5	RICH Detectors	37
3.2.6	Calorimeter System	40
3.2.7	Muon System	42
3.2.8	Hardware Trigger (L0)	44
3.2.9	Software Trigger (HLT)	46
3.3	LHCb analysis software	46
4.	<i>The LHCb software trigger</i>	49
4.1	Overview of the LHCb software trigger in Run 1	51
4.2	Overview of the LHCb software trigger in Run 2	54
4.2.1	Incremental improvements	54
4.2.2	Real-time alignment and calibration	56
4.2.3	Additional reconstruction and information in HLT2	56
4.2.4	New data streams	57
4.2.5	Improvements to trigger selections	59
4.3	The swimming technique	61
4.4	Particle identification in HLT2	62
4.4.1	PID calibration datasets	63
4.4.2	Trigger decorrelation	64

4.5	Summary	68
5.	<i>Selection of $D^0 \rightarrow K_s^0 h^+ h^-$ decays</i>	69
5.1	Strategy outline	69
5.2	Trigger strategy and preselection	70
5.3	$D^0 \rightarrow K_s^0 K^\pm \pi^\mp$ amplitude analysis yield extraction	73
5.4	$D^0 \rightarrow K_s^0 K^\pm \pi^\mp$ reconstruction efficiency	76
5.5	$D^0 \rightarrow K_s^0 K^+ K^-$ mixing study yield extraction	78
5.5.1	Run 2 $D^0 \rightarrow K_s^0 K^+ K^-$ yield estimates	82
6.	<i>Amplitude analysis of $D^0 \rightarrow K_s^0 K^\pm \pi^\mp$ decays</i>	87
6.1	Amplitude model probability density functions	89
6.1.1	Fit components	91
6.2	Coherence factor and CP -even fraction	92
6.3	Model-finding procedure	93
6.4	Application of model-finding procedure	95
6.5	Model adjustments	99
6.6	Systematic uncertainties	101
6.7	Model results	105
6.8	CP violation tests	115
6.9	Ratio of branching fractions measurement	115
6.10	Coherence factor and CP -even fraction results	117
6.11	SU(3) flavour symmetry tests	118
6.12	Conclusions	119
7.	<i>Mixing studies using $D^0 \rightarrow K_s^0 K^+ K^-$ decays</i>	121
7.1	Idealised sensitivity studies	123
7.2	Additional corrections and validation	133
7.3	Prospects for $D^0 \rightarrow K_s^0 K^+ K^-$ mixing measurements	138
8.	<i>Conclusions</i>	143
	<i>Appendix</i>	145
A.	<i>Additional isobar formalism information</i>	147
B.	$D^0 \rightarrow K_s^0 K^\pm \pi^\mp$ isobar model evolution	149
C.	$D^0 \rightarrow K_s^0 K^\pm \pi^\mp$ isobar model information	155
D.	$D^0 \rightarrow K_s^0 K^\pm \pi^\mp$ isobar model systematic uncertainties	163
E.	$D^0 \rightarrow K_s^0 K^+ K^-$ information	171
E.1	Pseudoexperiment results	178
E.2	Tracking efficiency parameterisations	183

GLOSSARY

BEH	Brout-Englert-Higgs [boson].
CERN	The European Organisation for Nuclear Research.
CF	Cabibbo-favoured.
CKM	Cabibbo-Kobayashi-Maskawa [matrix].
<i>CP</i>	Charge-parity [symmetry].
<i>CPT</i>	Charge-parity-time reversal [symmetry].
DCS	Doubly Cabibbo-suppressed.
DOCAz	Impact parameter to the LHC beam line.
ECAL	Electromagnetic calorimeter.
EFF	Event Filter Farm.
FOI	Field of interest.
FSI	Final state interactions.
GEM	Gas electron multiplier [detector].
GIM	Glashow-Illiopoulos-Maiani [mechanism].
HCAL	Hadronic calorimeter.
HFAG	Heavy Flavour Averaging Group.
HLT	High Level Trigger, the LHCb software trigger.
HLT1	The first, real-time, stage of the HLT.
HLT2	The second, deferred, stage of the HLT.
HPD	Hybrid Photon Detector.
IP	Impact parameter, distance of closest approach to a point or curve.
IT	Inner Tracker.
L0	Level 0 trigger, the LHCb hardware trigger.
LEP	Large Electron-Positron [accelerator].
LHC	Large Hadron Collider.
LHCb	The Large Hadron Collider beauty experiment.
LS1	Long shutdown 1, the period separating Run 1 and Run 2 of the LHC.

MAPMT	Multianode photomultiplier tube.
MWPC	Multi-wire proportional chamber.
NLL	Negative log-likelihood.
NP	New Physics.
OT	Outer Tracker.
OZI	Okubo-Zweig-Iizuka [rule].
PDF	Probability density function.
PID	Particle identification.
PMNS	Pontecorvo-Maki-Nakagawa-Sakata [matrix].
PMT	Photomultiplier tube.
PS	Preshower detector.
PV	Primary proton-proton interaction vertex.
QCD	Quantum Chromodynamics, the theory of the strong force.
RICH	Ring Imaging Cherenkov [detector].
RICH1	RICH detector upstream of the LHCb magnet.
RICH2	RICH detector downstream of the LHCb magnet.
Run 1	The first run of the LHC, between March 2010 and February 2013.
Run 2	The second run of the LHC, which began in March 2015.
Run 3	The third run of the LHC, which is expected to begin in 2020.
SCS	Singly Cabibbo-suppressed.
SM	Standard Model.
SPD	Scintillator pad detector.
ST	Silicon Tracker.
TIS	Trigger Independent of Signal.
TOS	Trigger on Signal.
TT	Tracker Turicensis.
VELO	Vertex Locator.
WLCG	Worldwide LHC Computing Grid.
WLS	Wavelength-shifting [fibre].

PREFACE

I performed the work presented in this thesis as part of the LHCb collaboration. I produced all diagrams, histograms and other figures in this thesis, unless clearly stated in the caption. During my DPhil studies I have worked on several projects, which are listed below with a short description of my contributions:

$D^0 \rightarrow K_s^0 K^\pm \pi^\mp$	This analysis was a central part of my DPhil studies, and I performed all hands-on aspects of it.
Trigger	I contributed to the software trigger group's preparations for Run 2 of the LHC, including – for example – shifts as the trigger expert on call during data-taking. The content that relates to the use of particle identification information in the trigger, and the selection of relevant calibration samples, is substantially my own work.
<i>Swimming</i>	The “swimming” technique for calculating selection efficiencies as a function of decay time will be discussed in some detail in this thesis. I was responsible for applying the swimming algorithm to the dataset of $D^0 \rightarrow K_s^0 h^+ h^-$ and $D^0 \rightarrow h^+ h'^-$ decays recorded by LHCb during 2012, which required some development of the LHCb implementation of the algorithm.
$D^0 \rightarrow K_s^0 K^+ K^-$	The sensitivity studies, and preparatory work specific to this decay mode, that are presented in this thesis are entirely my own work.

1. INTRODUCTION

From the charm quark in 1974 to the Brout-Englert-Higgs (BEH) boson in 2012, four out of the six modern discoveries of Standard Model (SM) particles were expected because of their indirect contributions to known and precisely measured processes. A wide variety of results have turned out to show the first hints of these particles, from the observation of neutral kaon mixing and the non-observation of the decay¹ $K^0 \rightarrow \mu^+ \mu^-$ that motivated the Glashow-Illiopoulos-Maiani (GIM) [1] mechanism and prediction of the charm quark, to the top quark and electroweak boson measurements that provided strong constraints on the BEH boson mass prior to its eventual discovery in 2012 [2,3]. The various particle discoveries have taken rather different forms, from the very prominent J/ψ [4,5] and Υ [6] mass peaks that signalled the discovery of the charm and beauty quarks to the much less pronounced BEH boson mass peaks, and the complex top quark discovery measurements [7,8] that relied heavily on a good understanding of signal-like backgrounds. At the other extreme, the discovery of the τ^- lepton [9] hinged on the observation of a process completely forbidden in the contemporary mainstream theory of particle physics. Finally, the tau neutrino, ν_τ , is also an excellent example of the discovery power of precision and indirect measurements. This neutrino was widely believed to exist by the time it was detected directly at the turn of the millennium [10] as a result of indirect measurements, such as the precise determination of the Z^0 boson invisible decay width [11] and the single photon cross-section in $e^+ e^-$ collisions [12–15].

Indirect methods therefore have an excellent track record of seeing the first hints of new particles, and are effectively sensitive to much higher energy scales than searches for on-shell production of new particles. Flavour physics, being the study of processes involving quark

¹ The inclusion of charge-conjugate processes is implied, except in the definition of CP asymmetries.

decays and transitions, provides a plethora of opportunities to search for physics beyond the SM in this way. In previous decades there have been several results from within particle physics that constrained the properties of new particles prior to their discovery. For example the observation of charge-parity symmetry (*CP*) violation in neutral kaon mixing [16] hinted at a third generation of quarks [17]; requiring unitarity be respected in longitudinal W^+W^- scattering placed limits on the BEH boson [18]; and indirect constraints from unitarity and electroweak boson measurements provided significant information about the top quark prior to its eventual discovery [19]. While modern particle physics has fewer robust constraints like these, observations in cosmology make it clear that the SM is not complete, and interesting new physics must be there to be found. For example, the Sakharov conditions for baryogenesis [20] require larger *CP* violation than has been discovered in the SM, and observations suggest there is a large fraction of dark matter in the universe that is inconsistent with any known SM particles.

Three years after the end of Run 1 of the Large Hadron Collider (LHC), no incontrovertible departures from SM predictions have been seen, although there have been some interesting anomalies in the angular distribution of $B^0 \rightarrow K^{*0} \mu^+ \mu^-$ decays [21,22], and in the ratios $R(D)$ and $R(D^*)^2$ [23–28]. In both cases the anomalies are around 4σ in significance when the LHCb results are combined with those from the BaBar and Belle collaborations. While it is possible that the step up to $\sqrt{s} = 13$ TeV collision energy in Run 2 will be sufficient to produce new, heavy, particles on-shell – and some preliminary results from the ATLAS [29] and CMS [30] experiments have shown some weak, but tantalising, hints of such a particle in the $\gamma\gamma$ spectrum around $750\text{ GeV}/c^2$ – measuring processes to which new particles can contribute indirectly has a much greater reach in terms of probing the energy scale at which nature deviates from the SM.

Studies of the charm system, such as those presented in this thesis, are motivated by the fact that several theories of physics beyond the SM predict enhancements above the very small levels of *CP* violation expected in the SM [31–33]. Singly Cabibbo-suppressed (SCS)

² $R(D^{(*)}) \equiv \frac{\mathcal{B}(\bar{B} \rightarrow D^{(*)} \tau^- \bar{\nu}_\tau)}{\mathcal{B}(\bar{B} \rightarrow D^{(*)} \ell^- \bar{\nu}_\ell)}$ where $\ell = (\mu, e)$.

decays provide a promising laboratory in which to search for direct CP violation because of the significant role that loop diagrams play in these processes [34]. Multi-body SCS decays, such as $D^0 \rightarrow K_s^0 K^- \pi^+$ and $D^0 \rightarrow K_s^0 K^+ \pi^-$, have in addition the attractive feature that interference between the various resonances that contribute to these decays may lead to CP violation in local regions of phase space, motivating a good understanding of the resonant substructure. This thesis includes a time-integrated study of the resonant substructure of the decays $D^0 \rightarrow K_s^0 K^\pm \pi^\mp$, and a model-dependent search for direct CP violation.

The charm sector can also probe new physics via measurements of D^0 - \bar{D}^0 mixing parameters and indirect CP violation in the mixing process. These mixing and CP violation parameters are not precisely constrained in the latest world averages [35], as the effects of charm mixing are small and the full set of parameters can only be probed by complex analyses of multi-body decays using large data samples. Such analyses may consist of full time-dependent studies of the evolution of the phase space of the decays [36, 37], or instead use input from quantum-correlated D^0 decays [38] to pursue model-independent methods using bins of the phase space [39, 40]. This thesis includes a feasibility study of $D^0 \rightarrow K_s^0 K^+ K^-$ mixing measurements at LHCb using the present dataset, alongside projections of the precision attainable with the full dataset recorded during Run 2 of the LHC and with the upgraded LHCb detector.

The LHC, with its unique combination of high-energy, high-luminosity and high-multiplicity inelastic collisions, provides an environment in which the triggering and selection strategy used to perform the measurements outlined above is more important and challenging than ever. This is a particular challenge for the LHCb experiment, where many important signals are produced prolifically but do not possess clean signatures. The LHC centre-of-mass energy has increased to $\sqrt{s} = 13$ TeV in its present operating period, leading to increased production cross-sections for charm and beauty hadrons [41, 42] and exacerbating the challenge faced by the trigger system.

2. THEORETICAL BACKGROUND

The Standard Model (SM) has been the basis of particle physics for more than 50 years, and despite gradual development and several discoveries of new particles during this time its basic structure has held firm. The main tenet of the SM is that, in addition to the everyday symmetries under translation and rotation that result in conservation of momentum and angular momentum, there are additional, more abstract, symmetries obeyed by a set of fundamental fields in the theory. That such a simple and abstract concept can produce a model that describes nature with such astonishing precision is truly remarkable.

This chapter begins with an overview of the SM, its particle content and free parameters in Sect. 2.1, and outlines its limitations in Sect. 2.2. In Sect. 2.3 the various bound states that can be formed from quarks are described, and Sect. 2.4 introduces amplitude analysis techniques that can be used to study them. These techniques are applied to the rich resonance structure of $D^0 \rightarrow K_s^0 K^\pm \pi^\mp$ decays in Chapter 6. Finally, Sect. 2.5 gives the theoretical background to neutral meson mixing in the charm system and outlines a model-independent technique that can be used to measure the mixing parameters using $D^0 \rightarrow K_s^0 h^+ h^-$ decays ($h = K, \pi$). The application of this technique to the LHCb dataset is studied in Chapter 7.

2.1 *Introduction to the Standard Model of Particle Physics*

The SM consists of 17 particles¹ that are assumed to be point-like and fundamental. There are three generations of fermions, particles with half-odd-integer spin², each of which contains

¹ This figure is sometimes quoted as 61, which is correct if anti-particles and particles with different values of the strong force quantum numbers are counted separately.

² Natural units, where $\hbar = c = |e| = 1$, will be used throughout this chapter.

Table 2.1: Listing of the 17 particles in the SM. The three columns on the left side of the matrix show the three families of fermions, with the two quarks in the upper half and the charged and neutral leptons below. The lower right quadrant shows the four types of force-carrying boson, while the BEH boson is shown in the upper right quadrant.

$$\left(\begin{array}{ccc|c} u & c & t & H^0 \\ d & s & b & \\ \hline e^- & \mu^- & \tau^- & \gamma \quad Z^0 \\ \nu_e & \nu_\mu & \nu_\tau & g \quad W^\pm \end{array} \right)$$

one up-type and one down-type quark, one charged lepton and a neutrino. In addition there are several bosons, particles with integer spin, that mediate the various forces in the SM and, in the case of the BEH boson, generate masses for the other fundamental particles. The various particles are summarised in Table 2.1. Up-type quarks (u, c, t) have charge $+2/3$ in units where the electron has charge -1 , while down-type quarks (d, s, b) have charge $-1/3$. The charged leptons (e^-, μ^-, τ^-) all have charge -1 , while the neutrinos (ν_e, ν_μ, ν_τ) are electrically neutral. Each fermion has an anti-particle ($\bar{u}, \bar{d}, e^+, \bar{\nu}_e, etc.$), which has the same mass but opposite electric charge. The W^\pm bosons carry electrical charge ± 1 , while all the other bosons are neutral.

In technical terms, the SM is a $U(1) \times SU(2) \times SU(3)$ gauge field theory. The $U(1) \times SU(2)$ part of this generates the electroweak theory, while the $SU(3)$ symmetry is the basis of the strong force described by quantum chromodynamics (QCD). In the electroweak theory this means the various fermion fields are assigned to $SU(2)$ weak isospin multiplets. The left-handed fields are assigned to doublets

$$\begin{pmatrix} u \\ d' \end{pmatrix}_L \quad \begin{pmatrix} c \\ s' \end{pmatrix}_L \quad \begin{pmatrix} t \\ b' \end{pmatrix}_L \quad \begin{pmatrix} \nu_e \\ e^- \end{pmatrix}_L \quad \begin{pmatrix} \nu_\mu \\ \mu^- \end{pmatrix}_L \quad \begin{pmatrix} \nu_\tau \\ \tau^- \end{pmatrix}_L , \quad (2.1)$$

with each right-handed component assigned to its own weak isospin singlet. This construction leads to a theory with the properties demanded by experimental results: a set of vector-minus-axial-vector charged-current weak interactions, mediated by the W^\pm , that act only on left-handed fermions, a parity-conserving purely electromagnetic interaction, mediated by

the photon γ , and a neutral, weak interaction mediated by the Z^0 boson.

The $SU(3)$ gauge symmetry of QCD acts on triplets of quark fields

$$\begin{pmatrix} u_{\text{red}} \\ u_{\text{green}} \\ u_{\text{blue}} \end{pmatrix} \quad \begin{pmatrix} d_{\text{red}} \\ d_{\text{green}} \\ d_{\text{blue}} \end{pmatrix} \quad \begin{pmatrix} c_{\text{red}} \\ c_{\text{green}} \\ c_{\text{blue}} \end{pmatrix} \quad \begin{pmatrix} s_{\text{red}} \\ s_{\text{green}} \\ s_{\text{blue}} \end{pmatrix} \quad \begin{pmatrix} t_{\text{red}} \\ t_{\text{green}} \\ t_{\text{blue}} \end{pmatrix} \quad \begin{pmatrix} b_{\text{red}} \\ b_{\text{green}} \\ b_{\text{blue}} \end{pmatrix}, \quad (2.2)$$

where the three components have different values of QCD’s “colour” charge. There are eight massless gauge bosons, the gluons (g), which mediate the strong force and interact only with the quark fields and by self-interaction. The final fundamental SM particle is the BEH scalar boson, H^0 . The masses of the other SM particles are generated by coupling to the BEH field and spontaneous symmetry breaking [43, 44].

The SM has a total of 26 independent parameters that must be measured: masses of the twelve fermions, eight parameters defining quark and neutrino mixing matrices, coupling constants for the $SU(3)$, $SU(2)$ and $U(1)$ parts of the theory, two parameters relating to the BEH field and one angle, θ_{QCD} , that sets the strength of CP violation in the strong force. The so-called “strong CP problem” is that measurements of θ_{QCD} indicate it is very small or zero, but the SM offers no explanation of why this should be the case [45]. The mixing matrices arise because the quark and neutrino mass eigenstates are not identical to the eigenstates that interact by the weak interaction. There are, therefore, 3×3 unitary matrices relating the two sets of eigenstates. The Cabibbo-Kobayashi-Maskawa (CKM) [17, 46] matrix, V_{CKM} , relates the sets of quark eigenstates

$$\begin{pmatrix} d' \\ s' \\ b' \end{pmatrix} = \begin{pmatrix} V_{ud} & V_{us} & V_{ub} \\ V_{cd} & V_{cs} & V_{cb} \\ V_{td} & V_{ts} & V_{tb} \end{pmatrix} \begin{pmatrix} d \\ s \\ b \end{pmatrix}. \quad (2.3)$$

Here the primed states (d' , s' , b') are those present in the $SU(2)$ isospin multiplets of the electroweak interaction, while the states (d , s , b) on the right hand side are the mass eigenstates.

The CKM matrix is conventionally parameterised [47] as

$$V_{\text{CKM}} = \begin{pmatrix} c_{12}c_{13} & s_{12}c_{13} & s_{13}e^{-i\delta} \\ -s_{12}c_{23} - c_{12}s_{23}s_{13}e^{i\delta} & c_{12}c_{23} - s_{12}s_{23}s_{13}e^{i\delta} & s_{23}c_{13} \\ s_{12}s_{23} - c_{12}c_{23}s_{13}e^{i\delta} & -c_{12}s_{23} - s_{12}c_{23}s_{13}e^{i\delta} & c_{23}c_{13} \end{pmatrix}, \quad (2.4)$$

where $s_{ij} = \sin(\theta_{ij})$ and $c_{ij} = \cos(\theta_{ij})$, *i.e.* there are three mixing angles and the CP -violating KM phase [17] δ . Within the SM, this phase is responsible for all CP -violating effects so far observed. Measurements of the CKM parameters often quote the related quantity³ $\gamma \equiv \arg(-V_{\text{ud}}V_{\text{ub}}^*/V_{\text{cd}}V_{\text{cb}}^*)$, because it can be directly measured via tree-level processes that are not expected to be sensitive to physics beyond the SM.

The Pontecorvo-Maki-Nakagawa-Sakata (PMNS) [48, 49] matrix, U_{PMNS} , fills the equivalent role for the neutrino sector, relating the flavour eigenstates $\nu_{e,\mu,\tau}$ that interact via the weak interaction to the mass eigenstates $\nu_{1,2,3}$. This is of limited relevance to the material presented in this thesis, but it is worth noting that the CKM and PMNS matrices are seen to have a rather different structure. The CKM matrix is approximately diagonal [50], while all elements of the PMNS matrix appear to be of comparable size [51], indicating that flavour mixing in the neutrino sector is much greater:

$$|U_{\text{PMNS}}| \approx \begin{pmatrix} 0.82 & 0.55 & 0.15 \\ 0.37 & 0.57 & 0.70 \\ 0.39 & 0.59 & 0.68 \end{pmatrix} \quad |V_{\text{CKM}}| \approx \begin{pmatrix} 0.974 & 0.225 & 0.004 \\ 0.225 & 0.973 & 0.042 \\ 0.009 & 0.041 & 0.999 \end{pmatrix}. \quad (2.5)$$

There is as yet no experimental evidence for CP violation in the lepton sector, although the current best-fit value for the CP -violating phase of the PMNS matrix corresponds to large violation [51].

³ Another notation, $\phi_3 \equiv \gamma$, exists in the literature.

2.2 Physics beyond the Standard Model

In spite of its continuing successes describing a wide variety of processes, there are strong reasons to believe that the SM is not complete, and the modern SM is part of some, as yet unknown, larger theory. Such extensions to the SM are referred to as New Physics (NP).

One of the strongest reasons to believe that NP exists is the large observed matter-antimatter asymmetry in the universe, which must have been generated by some baryogenesis process. The three Sakharov conditions for baryogenesis [20] are C and CP violation, baryon number violation and a departure from thermal equilibrium. While CP violation is present in the SM, no baryon number violation has been observed, and limits on baryon-number-violating processes such as proton decay are very stringent. Some kind of NP is, therefore, required to explain the large matter-antimatter asymmetry in the universe. This is not the only powerful evidence for NP in cosmological data, which also indicate large contributions to the mass-energy of the universe from both dark matter and dark energy. No SM particles are viable dark matter candidates, and there have been no successful attempts to reconcile the measured dark energy with the SM. Many proposed extensions to the SM include weakly interacting massive particles (WIMPs), which could make up the dark matter required by cosmological observations.

Aside from these experimental observations, it is also clear that the SM is not a complete theory of nature because it does not include the final known force, gravity. There is also no explanation of the so-called hierarchy problem that the electroweak scale of ~ 100 GeV is enormously lower than the Planck scale associated with gravity of around 10^{19} GeV. It is, therefore, clear that some kind of NP must become significant at energy scales approaching the Planck energy and reconcile the four known forces.

There are also several more aesthetic reasons to believe that the SM is incomplete, and that NP physics exists at energies much smaller than the Planck scale. The SM contains a large number of free parameters, spanning a wide range of values (*e.g.* neutrino masses \ll top quark mass), and offers no explanation of where they come from, or if there is any

relationship between them. There is also no explanation of the “strong CP problem”, noted above, of why CP -violating effects in the strong force are tiny or zero. The hierarchy problem noted above manifests itself in other ways in the SM, for example requiring highly fine-tuned cancellation between the bare BEH boson mass and its quantum loop corrections, which are each close to the Planck scale, but cancel to produce the observed mass of around $125\text{ GeV}/c^2$.

In addition to the long-standing cosmological and theoretical indications that NP must exist, there have also been several recent experimental results within particle physics that hint at contributions from NP processes. Several such results were described in Chapter 1. In addition, there have recently been hints in nuclear physics of possible NP effects [52] in nuclear transitions [53].

There are, therefore, several reasons to expect that physics beyond the SM exists, which motivates the continuing investment in particle physics research, and the huge variety of analyses that are actively being pursued.

2.3 Mesons, baryons and beyond

The coupling constant of QCD, the theory of the strong force, is large, and runs to still larger values at small energy scales, as shown in Fig. 2.1. At very low energies the coupling reaches unity, and the theory enters a nonperturbative regime. The strength of the strong force at low energies is such that coloured objects – quarks and gluons – rapidly form states with no overall colour charge, and are never observed as free particles. These colourless states are known as hadrons, most known examples of which are $q\bar{q}$ (meson) and qqq (baryon) states. It is not thought possible for there to be any hadronic states containing top quarks, as top quarks decay before they have had time to form hadrons. Hadronic states containing different numbers of quarks have recently been observed, for example the $Z(4430)^-$ [55–57] has been determined to be a $c\bar{c}d\bar{u}$ state, and in 2015 LHCb reported [58] the first discovery of pentaquark states with the observation of the $u\bar{c}cud$ resonances $P_c(4380)^+$ and $P_c(4450)^+$ in Λ_b^0 baryon decays.

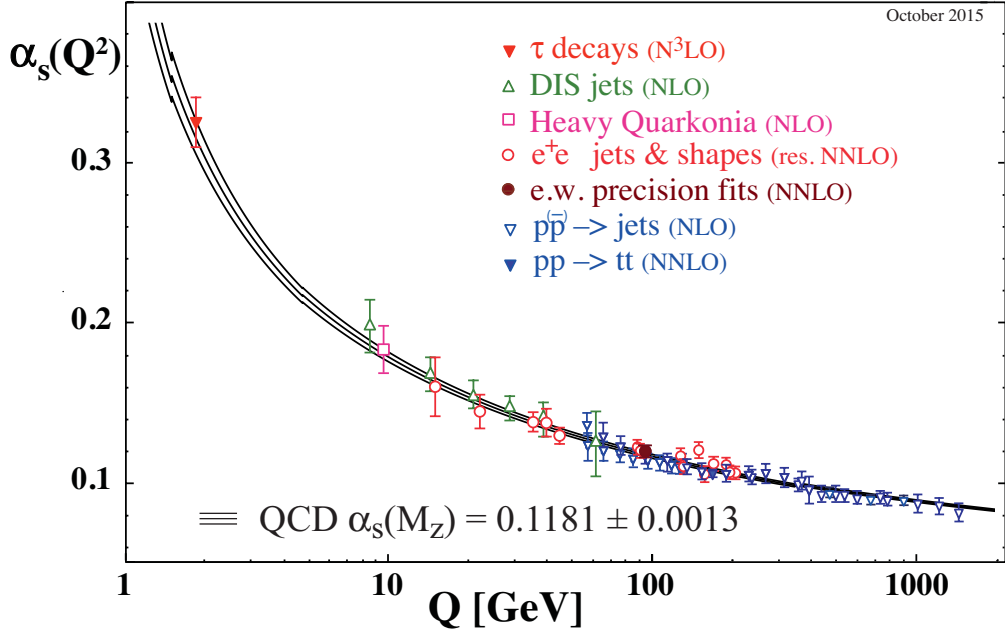


Figure 2.1: Running of the QCD coupling constant, $\alpha_s(Q^2)$, at various energy scales, Q^2 . Figure taken from Ref. [54].

In addition to these exotic four- and five-quark states, there is a huge range of mesons and baryons formed from various combinations of the five lightest quarks. In the broadest sense, flavour physics is the study of these myriad particles and their decay processes.

2.4 Amplitude analysis

Despite the many successes of the SM, precise calculations involving the strong interaction in the low energy, nonperturbative, regime are extremely challenging, and amplitudes involving light mesons cannot typically be calculated precisely from first principles. Amplitude analysis is an umbrella term that includes the study of a variety of scattering and decay processes, but this thesis will focus only on the study of multi-body decays of particles that decay via the weak interaction to short-lived resonances that in turn decay via the strong force. An example is $D^0 \rightarrow K_s^0 K^\pm \pi^\mp$, where the K_s^0 , K^\pm and π^\mp are the final state particles and there are many possible intermediate states such as $K^{*\pm}$, K^{*0} and ρ^\pm . Such analyses rely on a variety of approximations and ad-hoc parameterisations to describe the data, as well as the use of data-driven techniques to relate analyses of different processes.

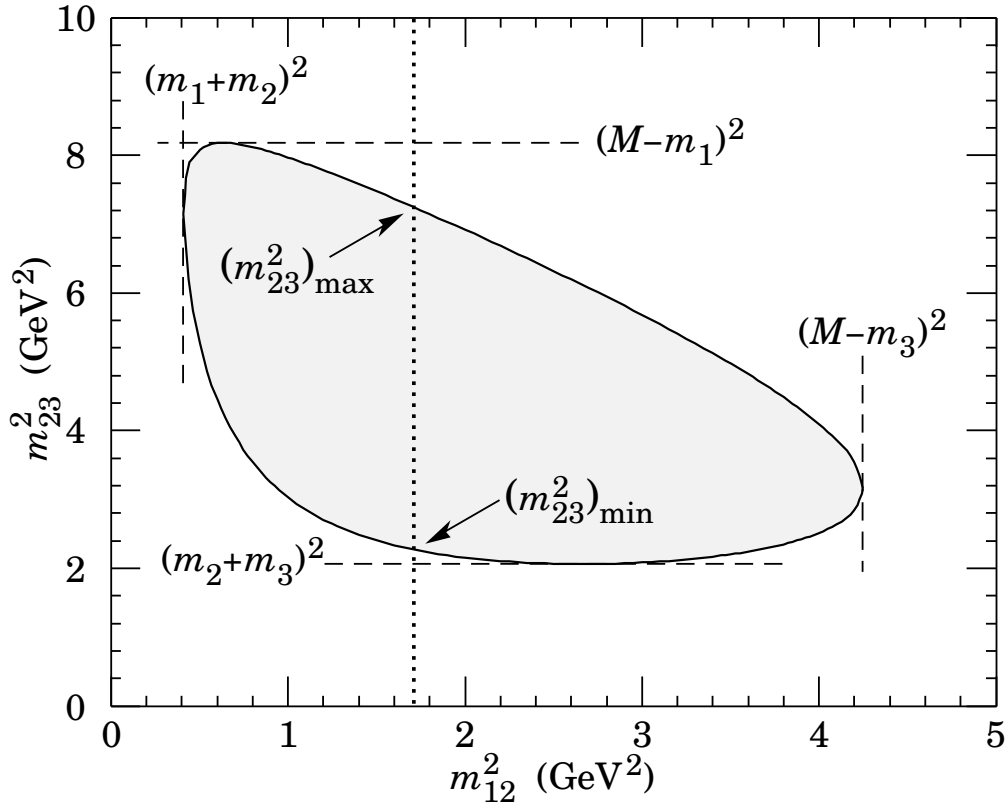


Figure 2.2: Illustration of a Dalitz plot for a three-body final state. Conservation of four-momentum restricts events to the shaded region. M is the invariant mass of the decaying particle and m_1, m_2, m_3 are the final state particle masses, and m_{ij} denote the invariant masses of pairs of final state particles. Figure taken from Ref. [54].

The dynamics of a decay $D^0 \rightarrow ABC$, where D^0 , A, B and C are all pseudoscalar mesons, can be completely described by just two variables, where the conventional choice is to use a pair of squared invariant masses. A scatter plot in these variables is referred to as a Dalitz plot [59], and in the absence of contributions from intermediate resonances the Dalitz plot distribution is flat. Fig. 2.2 illustrates the various kinematic limits in the Dalitz plot of a three-body final state. Decay processes with higher-multiplicity final states, or final state particles with nonzero spin, have substantially more Lorentz-invariant degrees of freedom. A description of the complex amplitude variation across the phase space defined by these degrees of freedom is known as an amplitude model.

In addition to providing this information about the variation of the complex amplitude, such models allow the contributions of various intermediate resonances to a given decay process to be disentangled. This allows tests of important phenomenological tools such as SU(3) flavour symmetry to be carried out, and provides a full description of the decay

process, which can be used in, for example, CP violation and mixing studies.

Important goals in flavour physics include the precise determination of the CKM unitarity-triangle angle γ , which was introduced in Sect. 2.1, and D^0 - \bar{D}^0 mixing parameters, which will be discussed in Sect. 2.5. In both cases, optimal statistical power is achieved by studying the dependence of the CP asymmetry and D-meson decay time distribution on where in three-body phase-space the D-meson decay occurs, provided that the decay amplitude from the intermediate resonances is sufficiently well described.

A substantial part of this thesis is dedicated to the construction of such models for the $D^0 \rightarrow K_s^0 K^\pm \pi^\mp$ decays. Further theoretical background is given in the following sub-section, while the construction of models using LHCb data will be described in Chapters 5 and 6.

2.4.1 The isobar model

The isobar model is a widely used formalism for the construction of amplitude models. It is based on the approximation that the amplitude for a signal decay $D^0 \rightarrow ABC$ can be decomposed into contributions of the form $D^0 \rightarrow (R \rightarrow (AB)_J)C$, where R is a resonance with spin J . The corresponding 4-momenta are denoted p_{D^0} , p_A , p_B and p_C , the reconstructed invariant mass of the resonance is denoted m_{AB} , and the nominal mass m_R . Using the $D^0 \rightarrow K_s^0 K^\pm \pi^\mp$ decays as an example, the matrix element is given by

$$\mathcal{M}_{K_s^0 K^\pm \pi^\mp}(m_{K_s^0 \pi}^2, m_{K\pi}^2) = \sum_R a_R e^{i\phi_R} \mathcal{M}_R(m_{AB}^2, m_{AC}^2), \quad (2.6)$$

where $a_R e^{i\phi_R}$ is the complex amplitude for R and the contributions \mathcal{M}_R from each intermediate state are given by

$$\mathcal{M}_R(m_{AB}^2, m_{AC}^2) = B_J^{D^0}(p, |p_0|, d_{D^0}) \Omega_J(m_{AB}^2, m_{AC}^2) T_R(m_{AB}^2) B_J^R(q, q_0, d_R), \quad (2.7)$$

where $B_J^{D^0}(p, |p_0|, d_{D^0})$ and $B_J^R(q, q_0, d_R)$ are the Blatt-Weisskopf centrifugal barrier factors for the production and decay, respectively, of the resonance R [60]. The parameter p (q) is the

Table 2.2: Blatt-Weisskopf centrifugal barrier penetration factors, $B_J(q, q_0, d)$ [60].

J	$B_J(q, q_0, d)$
0	1
1	$\sqrt{\frac{1+(q_0d)^2}{1+(qd)^2}}$
2	$\sqrt{\frac{9+3(q_0d)^2+(q_0d)^4}{9+3(qd)^2+(qd)^4}}$

Table 2.3: Angular distribution factors, $\Omega_J(p_{D^0} + p_C, p_B - p_A)$. These are expressed in terms of the tensors $T^{\mu\nu} = -g^{\mu\nu} + \frac{p_{AB}^\mu p_{AB}^\nu}{m_R^2}$ and $T^{\mu\nu\alpha\beta} = \frac{1}{2}(T^{\mu\alpha}T^{\nu\beta} + T^{\mu\beta}T^{\nu\alpha}) - \frac{1}{3}T^{\mu\nu}T^{\alpha\beta}$.

J	$\Omega_J(p_{D^0} + p_C, p_B - p_A)$
0	1
1	$(p_{D^0}^\mu + p_C^\mu)T_{\mu\nu}(p_B^\nu - p_A^\nu)/(GeV/c)^2$
2	$(p_{D^0}^\mu + p_C^\mu)(p_{D^0}^\nu + p_C^\nu)T_{\mu\nu\alpha\beta}(p_A^\alpha - p_B^\alpha)(p_A^\beta - p_B^\beta)/(GeV/c)^4$

momentum of C (A or B) in the R rest frame, and p_0 (q_0) is the same quantity calculated using the nominal resonance mass, m_R , in place of the reconstructed mass, m_{AB} . The meson radius parameters are typically set to values around $d_{D^0} = 5.0\text{ }c/\text{GeV}$ and $d_R = 1.5\text{ }c/\text{GeV}$ [61, 62]. Finally, $\Omega_J(m_{AB}^2, m_{AC}^2)$ is the spin factor for a resonance with spin J and T_R is the dynamical function describing the resonance R. The functional forms for $B_J(q, q_0, d)$ are given in Table 2.2 and those for $\Omega_J(m_{AB}^2, m_{AC}^2)$ in Table 2.3 for $J \in \{0, 1, 2\}$. As the form for Ω_1 is antisymmetric in the indices A and B, it is necessary to define the particle ordering convention used in any given analysis.

Resonances with spin J produce characteristic Dalitz plot distributions with J nodes. This is illustrated in Fig. 2.3, where $|\mathcal{M}_R(m_{AB}^2, m_{AC}^2)|^2$ is shown for $J = 0$ (S-wave/scalar, Fig. 2.3a), $J = 1$ (P-wave/vector, Fig. 2.3b) and $J = 2$ (D-wave/tensor, Fig. 2.3c) amplitudes. Because the sum in Eqn. 2.6 is coherent, the intermediate resonances can interfere with one another. Fig. 2.3d illustrates the interference term $\Re[\mathcal{M}_{R_1}(m_{AB}^2, m_{AC}^2)\mathcal{M}_{R_2}^*(m_{AB}^2, m_{AC}^2)]$ between two resonances R_1 and R_2 , which is variously constructive and destructive in different regions of the Dalitz plot.

The dynamical function T_R chosen depends on the resonance R in question. A relativistic Breit-Wigner form

$$T_R(m_{AB}) = \frac{1}{(m_R^2 - m_{AB}^2) - im_R\Gamma_R(m_{AB})}, \quad (2.8)$$

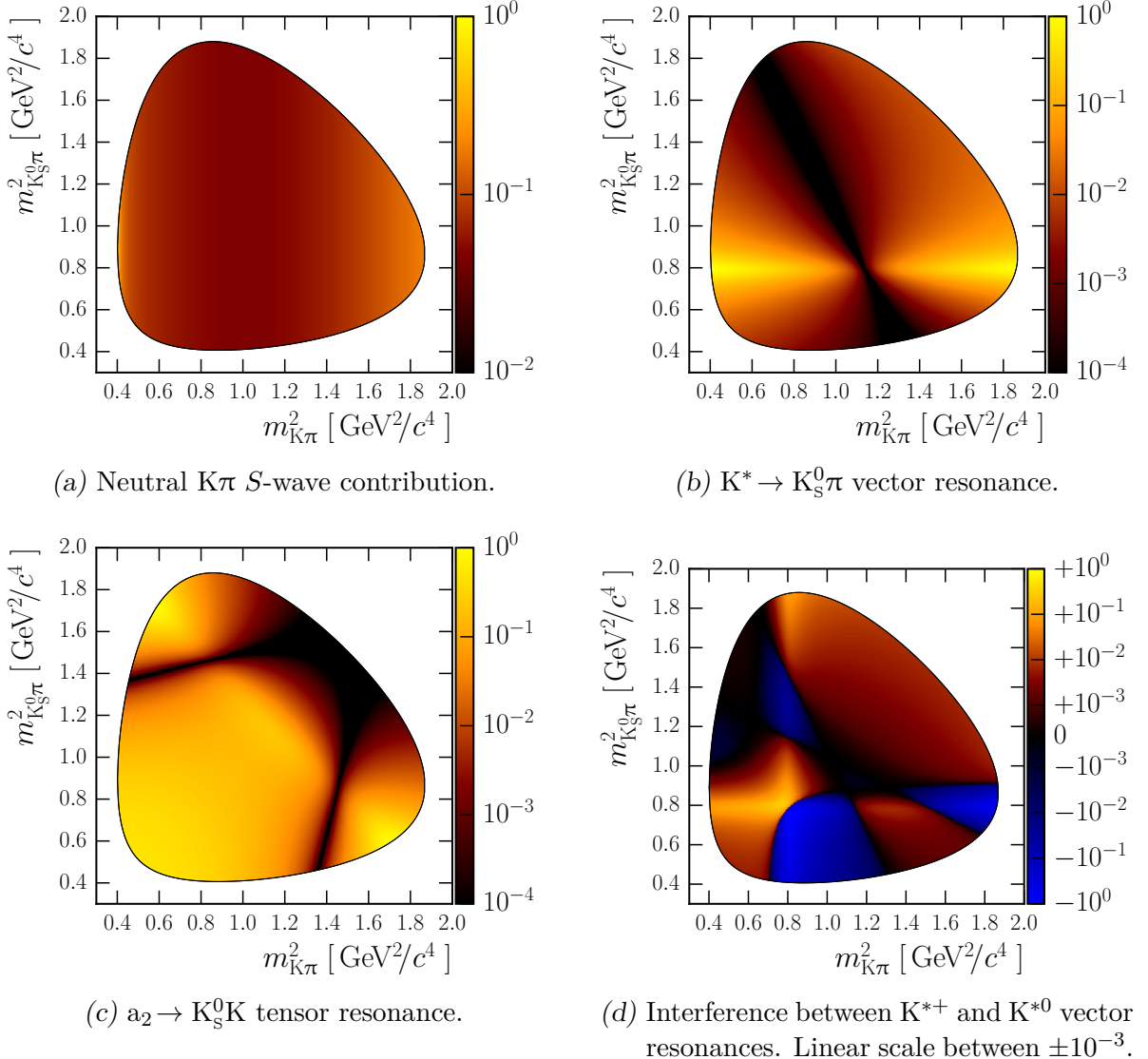


Figure 2.3: Illustrations of the Dalitz plot distributions produced by resonances with different spins. Spin $J = 0, 1, 2$ contributions are shown, along with an example of interference between two vector resonances. The decay process illustrated is $D^0 \rightarrow K_s^0 K^- \pi^+$, although this is of no particular relevance. In all cases the z -units are arbitrary.

is typical, where the mass-dependent width is

$$\Gamma_R(m_{AB}) = \Gamma_R \left[B_J^R(q, q_0, d_R) \right]^2 \frac{m_R}{m_{AB}} \left(\frac{q}{q_0} \right)^{2J+1}, \quad (2.9)$$

but alternative forms are often used to describe resonances that are very broad or close to a kinematic threshold. The Flatté [63, 64] form is a coupled-channel function often used to

describe the $a_0(980)$ resonance that lies close to the $K\bar{K}$ threshold [36, 61, 65–67]

$$T_R = \frac{1}{\left(m_{a_0(980)^\pm}^2 - m_{K\bar{K}}^2\right) - i \left[\rho_{K\bar{K}} g_{K\bar{K}}^2 + \rho_{\eta\pi} g_{\eta\pi}^2\right]}, \quad (2.10)$$

where the phase-space factor is given by

$$\rho_{AB} = \frac{1}{m_{K\bar{K}}^2} \sqrt{\left(m_{K\bar{K}}^2 - (m_A + m_B)^2\right) \left(m_{K\bar{K}}^2 - (m_A - m_B)^2\right)}. \quad (2.11)$$

With trivial modifications this functional form is also used to describe the $f_0(980)^0$ resonance. The coupling constants $g_{K\bar{K}}$ and $g_{\eta\pi}$ have been measured by the Crystal Barrel collaboration and published in Ref. [65].

The Gounaris-Sakurai [68] parameterisation is used to describe ρ resonances [67, 69–72]

$$T_R = \frac{1 + d(m_\rho) \frac{\Gamma_\rho}{m_\rho}}{\left(m_\rho^2 - m_{K\bar{K}}^2\right) + f\left(m_{K\bar{K}}^2, m_\rho^2, \Gamma_\rho\right) - im_\rho \Gamma_\rho(m_{K\bar{K}})}, \quad (2.12)$$

where

$$d(m_\rho) = \frac{3m_K^2}{\pi q_0^2} \log\left(\frac{m_\rho + 2q_0}{2m_K}\right) + \frac{m_\rho}{2\pi q_0} - \frac{m_K^2 m_\rho}{\pi q_0^3}, \quad (2.13)$$

and

$$f\left(m_{K\bar{K}}^2, m_\rho^2, \Gamma_\rho\right) = \Gamma_\rho \frac{m_\rho^2}{q_0^3} \left\{ q_0^2 \left[h\left(m_{K\bar{K}}^2\right) - h\left(m_\rho^2\right) \right] + q_0^2 h'\left(m_\rho^2\right) \left(m_\rho^2 - m_{K\bar{K}}^2\right) \right\}. \quad (2.14)$$

When this lineshape is used to describe a ρ resonance in the $K_s^0 K^\pm$ channel the parameter m_K is taken as the mean of $m_{K_s^0}$ and m_{K^\pm} , and $h'\left(m_\rho^2\right) \equiv \frac{dh(m_\rho^2)}{dm_\rho^2}$ is calculated from

$$h\left(m^2\right) = \frac{2q(m^2)}{\pi m} \log\left(\frac{m + 2q(m^2)}{2m_K}\right), \quad (2.15)$$

in the limit that $m_K = m_{K^\pm} = m_{K_s^0}$. Parameters for the ρ resonances $\rho(1450)^\pm$ and $\rho(1700)^\pm$ have been measured by the OBELIX collaboration and published in Ref. [73]. Additional forms for T_R that are more specialised for use in the amplitude analysis of $D^0 \rightarrow K_s^0 K^\pm \pi^\mp$ will be defined and discussed in Chapter 6.

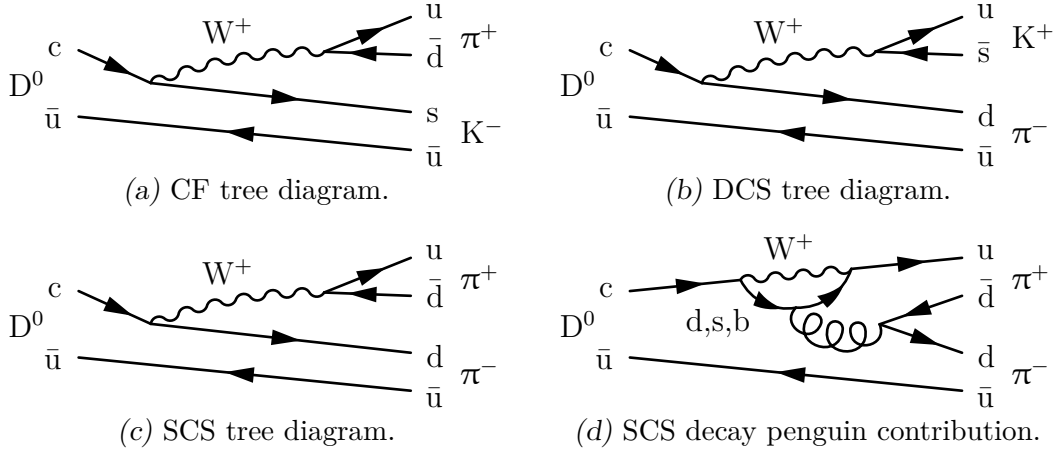


Figure 2.4: Feynman diagrams for the Cabibbo-favoured (CF), singly Cabibbo-suppressed (SCS) and doubly Cabibbo-suppressed (DCS) two-body D^0 decays to $K^\pm\pi^\mp$, and $\pi^+\pi^-$ final states. This illustrates that there are two types of diagram contributing to the the SCS decays, but only one for each of the CF and DCS decays.

2.5 CP violation and neutral meson mixing

There are three types of CP violation, which are divided into two categories: direct and indirect. Direct CP violation occurs in decays when the amplitude for a process and its CP conjugate differ, *e.g.* $\mathcal{A}_{D^0 \rightarrow f} \neq \mathcal{A}_{\bar{D}^0 \rightarrow \bar{f}}$ for some final state f . Indirect CP violation is related to neutral meson mixing: it can either occur directly in mixing, if the rate of $D^0 \rightarrow \bar{D}^0$ mixing differs from that of $\bar{D}^0 \rightarrow D^0$, or in interference between mixing and decay processes. This discussion is phrased in terms of the neutral charm system, but also applies to the neutral kaon and B-meson systems.

CP violation in hadrons can only be generated in processes that involve two or more quark-level amplitudes with different strong and weak phases. Here “strong phase” refers to a CP -even complex phase generated by strong or electromagnetic final state interactions (FSI), and “weak phase” refers to a CP -odd complex phase in the combination of CKM matrix elements relevant to the process [31]. These criteria are satisfied in the SM in $D^0-\bar{D}^0$ mixing and in SCS D-meson decays but, importantly, not in Cabibbo-favoured (CF) or doubly Cabibbo-suppressed (DCS) decays⁴. Figure 2.4 illustrates this using two-body D^0 decays as examples: the CF and DCS processes are driven by a single tree-level diagram, while there

⁴ The small CP impurity in the K_s^0 state means this is not quite true for decays producing K_s^0 mesons [74].

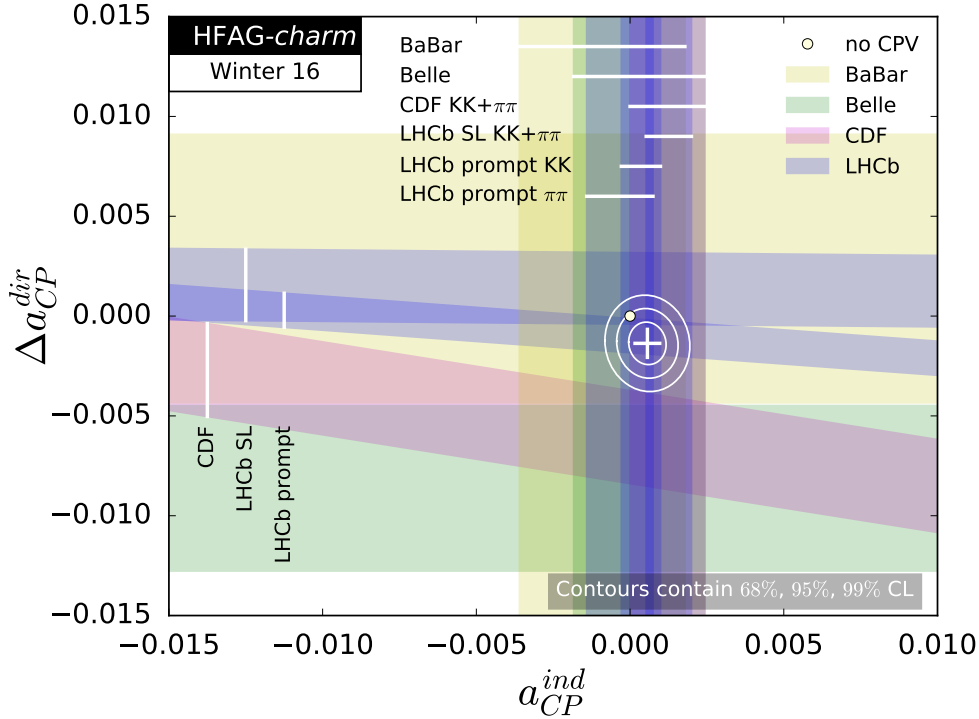


Figure 2.5: Illustration of various searches for direct and indirect CP violation in the charm system (coloured bands) and contours showing the current Heavy Flavour Averaging Group (HFAG) world-average fit results (white cross and rings). a_{CP}^{ind} is a universal indirect CP violation parameter, while Δa_{CP}^{dir} measures direct CP violation in $D^0 \rightarrow \pi^+\pi^-$ and $D^0 \rightarrow K^+K^-$ decays. Figure taken from Ref. [76].

are two different diagrams contributing to the SCS decay. The processes contributing to $D^0 - \bar{D}^0$ mixing will be discussed below.

In the SM, CP violation is expected to be very small in the charm system, of order $\mathcal{O}(10^{-3})$ [31, 34]. The primary reason for this is that both $D^0 - \bar{D}^0$ mixing and SCS D-meson decays involve, to a good approximation, only two generations of quarks, while the third generation is required to generate CP -violating effects. The size of these small direct CP -violating effects in the SM depends on the final state, which motivates the large number of searches. To date no CP violation has been observed in the charm sector, despite some recent measurements reaching sub-permille precision. For example, a recent LHCb study [75] of the time-integrated CP -asymmetry difference $\Delta A_{CP} = A_{CP}(K^+K^-) - A_{CP}(\pi^+\pi^-)$ in D^0 decays measured $[-0.10 \pm 0.08 \text{ (stat)} \pm 0.03 \text{ (syst)}] \%$ – the most precise single measurement of such a quantity. Some of the most precise direct and indirect CP violation results in the charm system are summarised in Fig. 2.5. The small size of SM CP violation means

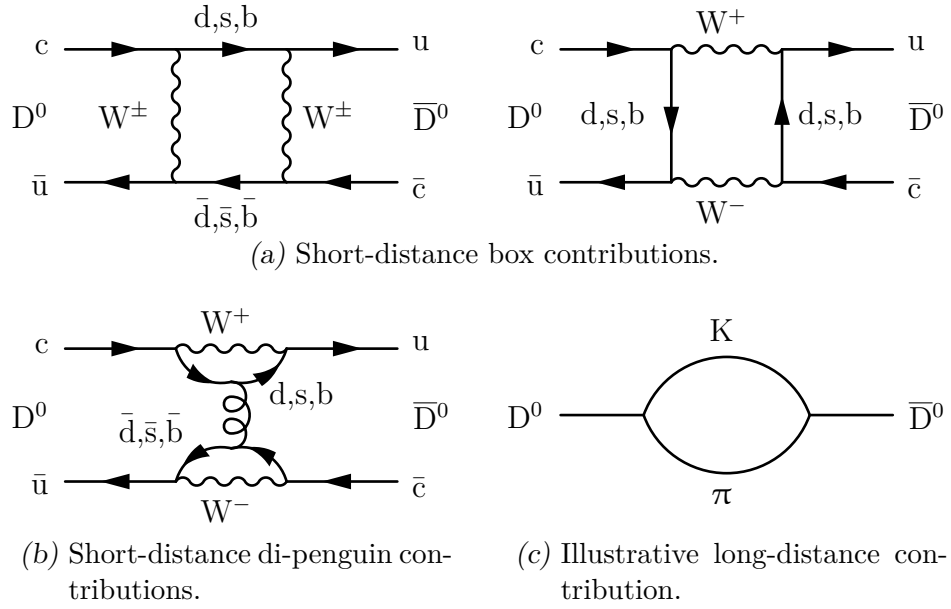


Figure 2.6: Mechanisms for generating $D^0-\bar{D}^0$ mixing. In the long-distance case the intermediate state $K\pi$ has been shown simply to give a concrete example – contributions such as KK and $\pi\pi$ are similarly valid, as are higher-multiplicity intermediate states.

charm measurements can provide powerful constraints on possible contributions from physics beyond the SM, as theories of NP predict larger effects [77–80].

The theoretical treatment of mixing in the charm system is challenging due to the significant effect of long-distance contributions [81, 82]. The short-distance box Feynman diagrams shown in Fig. 2.6a are the analogue of the dominant contributions to B-meson mixing, however they are strongly suppressed in the charm system [83]. There are several reasons for this, chief among which is that, because the D^0 consists of up-type quarks, the virtual quark lines are down-type. This is important because the beauty quark is around 40 times less massive than the top quark, and its contribution is additionally suppressed by the very small value of the CKM matrix element V_{ub} . The contribution from virtual down and strange quarks vanishes in the limit of SU(3) flavour symmetry [84], and is suppressed by a factor $(m_s^2 - m_d^2)/m_c^2$ in the SM. Another way of stating this is that the GIM suppression mechanism is very effective in the charm system. The sensitivity of charm mixing parameters to SU(3) flavour symmetry provides further motivation to test this symmetry whenever possible. Tests using $D^0 \rightarrow K_s^0 K^\pm \pi^\mp$ decays will be explored in Chapter 6. The di-penguin contribution shown in Fig. 2.6b is negligible in B mixing, but in the charm system it is of opposite sign and

comparable size to the box diagrams [85], providing an additional reason that charm mixing is dominated by long-distance contributions such as the $K\pi$ intermediate state illustrated in Fig. 2.6c. Meson resonances may also contribute significantly to the long-distance effects [86].

Several techniques have been used to calculate the mixing parameters in the SM. Inclusive approaches such as heavy quark effective field theory rely on expansions in powers of $1/m_c$, which are of limited validity due to the intermediate value of m_c [87–89], while exclusive methods use measurements of a wide range of D^0 decays to account explicitly for possible long-distance contributions [86, 90–92]. The poor agreement between these methods is evidence that mixing in the charm system is dominated by long-distance effects.

2.5.1 Neutral meson mixing formalism

This sub-section will outline a model-independent method by which mixing and CP violation can be probed in $D^0 \rightarrow K_s^0 h^+ h^-$ decays.

In the $D^0-\bar{D}^0$ system the mass eigenstates are defined, using the Heavy Flavour Averaging Group (HFAG) convention [93], by $|D_{\frac{1}{2}}\rangle \equiv p|D^0\rangle \mp q|\bar{D}^0\rangle$, where the convention is such that $|D_1\rangle$ is CP -even in the absence of CP violation. The decay time (t) evolution of a meson tagged as D^0 at production is described by the Schrödinger equation [94]

$$i\frac{\partial}{\partial t} \begin{pmatrix} |D^0(t)\rangle \\ |\bar{D}^0(t)\rangle \end{pmatrix} = \left(\mathbf{M} - \frac{i}{2}\mathbf{\Gamma}\right) \begin{pmatrix} |D^0(t)\rangle \\ |\bar{D}^0(t)\rangle \end{pmatrix}, \quad (2.16)$$

where \mathbf{M} and $\mathbf{\Gamma}$ are 2×2 Hermitian matrices, and charge-parity-time reversal symmetry (CPT) demands that $M_{11} = M_{22} = m$ and $\Gamma_{11} = \Gamma_{22} = \Gamma$. The off-diagonal entries give the absorptive and dispersive mixing behaviour.

The solutions of Eqn. 2.16 are

$$|D^0(t)\rangle = g_+(t)|D^0\rangle + \frac{q}{p}g_-(t)|\bar{D}^0\rangle, \quad (2.17)$$

with the \bar{D}^0 result obtained by interchanging $p \leftrightarrow q$ and $D^0 \leftrightarrow \bar{D}^0$, and

$$g_{\pm}(t) \equiv e^{-imt - \frac{t\Gamma}{2}} \frac{\cosh\left(\frac{t\Gamma z}{2}\right)}{\sinh\left(\frac{t\Gamma z}{2}\right)}, \quad z \equiv y + ix, \quad (2.18)$$

$$x \equiv \frac{m_1 - m_2}{\Gamma}, \quad y \equiv \frac{\Gamma_1 - \Gamma_2}{2\Gamma}. \quad (2.19)$$

Here m_i and Γ_i are, respectively, the mass and decay width of the state $|D_i\rangle$, and Γ is the mean decay width. The dispersive component, x , is largely generated by off-shell contributions, while the absorptive component, y , is related to on-shell contributions [91]. The short-distance diagrams shown in Fig. 2.6 therefore contribute to x , while long-distance effects contribute to both x and y . The complex parameters z and q/p are related to the matrices \mathbf{M} and $\mathbf{\Gamma}$ defined in Eqn. 2.16 by

$$M_{12} - \frac{i\Gamma_{12}}{2} = \frac{q}{p} \frac{i\Gamma z}{2}, \quad M_{12}^* - \frac{i\Gamma_{12}^*}{2} = \frac{p}{q} \frac{i\Gamma z}{2}. \quad (2.20)$$

In the absence of CP violation in mixing M_{12} and Γ_{12} are real, so $x\Gamma = -2M_{12}$, $y\Gamma = -\Gamma_{12}$ and $q/p = 1$, giving $q = p = 1/\sqrt{2}$. The current HFAG world-average values for z and q/p are shown in Fig. 2.7, where several interesting features can be seen. Firstly, mixing ($z \neq 0$) is well established. Secondly, $|z|$ is better constrained than $\arg(z)$: this is because some techniques, such as those using flavour-tagged $D^0 \rightarrow K^\pm \pi^\mp$ decays, measure $ze^{i\delta}$, where the phase δ must be taken from external measurements with large uncertainties. There is also a small contribution to the world-average results from semileptonic D^0 decays, which are sensitive to $|z|$. Finally, Fig. 2.7 shows that there is no evidence of CP violation in mixing ($q/p \neq 1$), but the constraints are rather weak.

Focusing now on $D^0 \rightarrow K_s^0 h^+ h^-$ decays, the decay amplitude – which varies across the Dalitz plot – is denoted by

$$\mathcal{A}_{D^0}(s_+, s_-) \equiv \langle K_s^0 h^+ h^-; s_+, s_- | D^0 \rangle \quad (2.21)$$

where in D^0 decays $s_+ \equiv m_{K_s^0 h^+}^2$ and $s_- \equiv m_{K_s^0 h^-}^2$, and the definitions are reversed in the \bar{D}^0

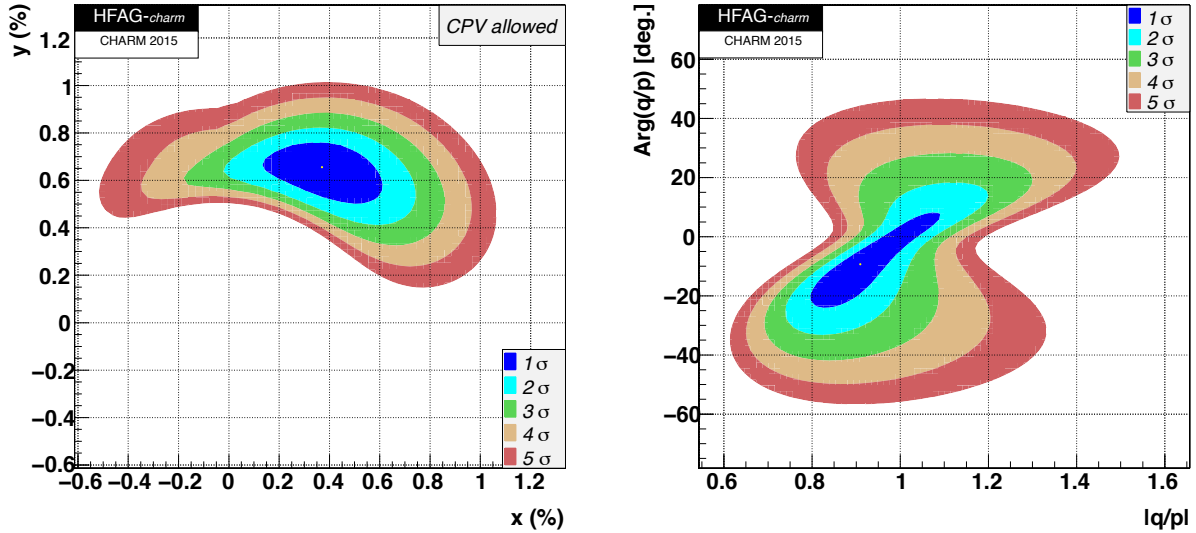


Figure 2.7: Illustrations of the current Heavy Flavour Averaging Group (HFAG) world averages [35] for the D^0 mixing parameters x , y and q/p . The annotation “CPV allowed” on the left figure indicates that the global fit allows indirect CP violation in mixing, *i.e.* $q/p \neq 1$.

amplitude so that, in the absence of direct CP violation

$$\mathcal{A}(s_+, s_-) = \mathcal{A}_{D^0}(s_+, s_-) = \mathcal{A}_{\bar{D}^0}(s_+, s_-). \quad (2.22)$$

The processes $D^0 \rightarrow K_s^0 \pi^+ \pi^-$ and $D^0 \rightarrow K_s^0 K^+ K^-$ are Cabibbo-favoured, so direct CP violation is expected to be small and it will be neglected in the following derivations and discussion. Dividing the Dalitz plot into $2N$ bins, defined symmetrically about the line $s_+ = s_-$, the integrated quantities

$$T_i \equiv \int_i |\mathcal{A}(s_+, s_-)|^2 ds_+ ds_-, \quad (2.23)$$

$$X_i \equiv c_i - is_i \equiv \frac{1}{\sqrt{T_i T_{-i}}} \int_i \mathcal{A}^*(s_+, s_-) \mathcal{A}(s_-, s_+) ds_+ ds_-, \quad (2.24)$$

can be defined, where positive bins $+i$ lie in the $s_- > s_+$ region. Two example binning schemes for $D^0 \rightarrow K_s^0 K^+ K^-$ decays are shown in Fig. 2.8 and will be discussed further below. The normalisation of T_i is set by $\sum_i T_i = 1$ and the sign of s_i is chosen to match the definition adopted [95] in the CLEO measurement of these quantities [38]. The quantity T_i represents the fraction of flavour-specific decays that fall in bin i , while c_i (s_i) represents the weighted average cosine (sine) of the difference in strong phase between the amplitude in bin i and

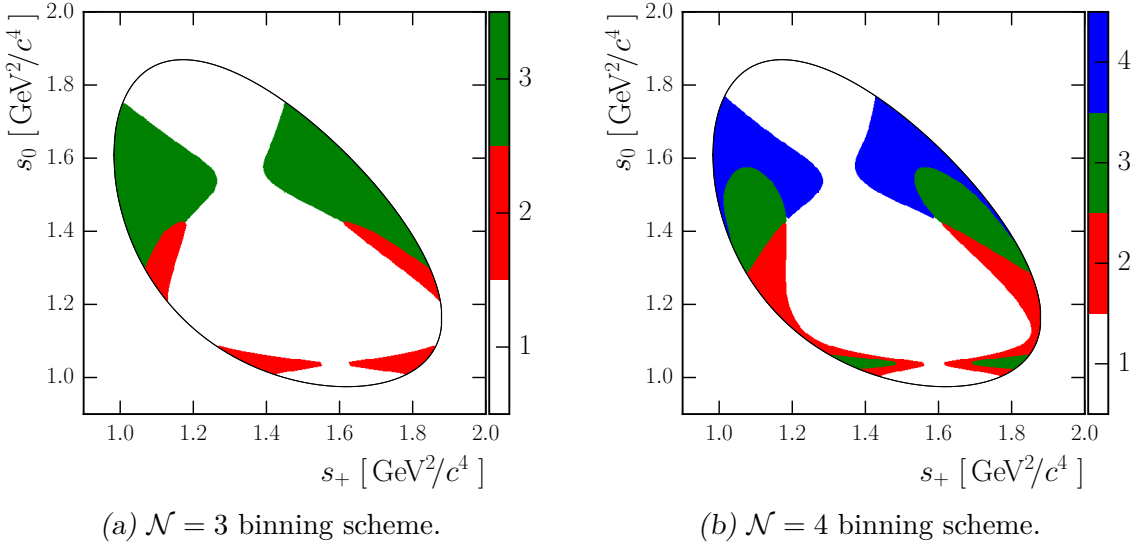


Figure 2.8: Binning schemes [38] for $D^0 \rightarrow K_s^0 K^+ K^-$ decays using three or four bins for each half of the Dalitz plot. The variable $s_0 \equiv m_{K^+ K^-}^2$, and $s_+ + s_- + s_0 = m_{D^0}^2 + m_{K_s^0}^2 + 2m_{K^\pm}^2$.

that in the opposite bin $-i$.

Combining the time evolution expression in Eqn. 2.17 with the definitions in Eqns. 2.21 and 2.22, the probability density function (PDF) describing the decay time evolution of the population in bin i for decays tagged as D^0 at production is

$$|\mathcal{A}_{D^0}(t)|_i^2 = \int_i ds_+ ds_- \left| \mathcal{A}(s_+, s_-) g_+(t) + \mathcal{A}(s_-, s_+) \frac{q}{p} g_-(t) \right|^2 \quad (2.25)$$

$$\approx e^{-\Gamma t} \left[T_i \left(1 + \frac{(\Gamma t)^2}{4} \Re(z^2) \right) + T_{-i} \left| \frac{q}{p} \right|^2 \frac{(\Gamma t)^2}{4} |z|^2 + \Re \left(\frac{q}{p} X_i \Gamma t z \sqrt{T_i T_{-i}} \right) \right]. \quad (2.26)$$

Here terms of order $e^{-\Gamma t} (\Gamma t z)^3$ have been neglected and the \bar{D}^0 expression is obtained by interchanging $p \leftrightarrow q$. Finally, introducing the notation

$$z \left(\frac{q}{p} \right)^{\pm 1} \equiv z_{CP} \pm \Delta z, \quad (2.27)$$

the per-bin PDF is given by

$$\begin{aligned} |\mathcal{A}_\pm(t)|_i^2 &= e^{-\Gamma t} \left[T_i + \frac{(\Gamma t)^2}{4} \left[T_i \Re(z_{CP}^2 - \Delta z^2) + T_{-i} |z_{CP} \pm \Delta z|^2 \right] \right. \\ &\quad \left. + \Gamma t \sqrt{T_i T_{-i}} \Re(X_i (z_{CP} \pm \Delta z)) \right], \end{aligned} \quad (2.28)$$

where the positive (negative) sign corresponds to the D^0 (\bar{D}^0) solution. This parameterisation in terms of z_{CP} and Δz is intended to improve the stability of fits to data with respect to using z and q/p directly by reducing the variation in sensitivity to q/p as a function of z . The important point here is that a decay-time-dependent analysis of $D^0 \rightarrow K_s^0 h^+ h^-$ decays is sensitive to the full set of mixing and CP violation parameters, z_{CP} and Δz .

The key advantage of binning the $D^0 \rightarrow K_s^0 h^+ h^-$ decay phase space in this manner is that the integrated variables T_i and X_i can be measured [96] using quantum-correlated $\psi(3770) \rightarrow D^0 \bar{D}^0$ decays, meaning that there is no need to perform an amplitude analysis of the relevant Dalitz plot, and no model-dependence systematic uncertainty is incurred. It is worth stressing that the flavour-specific fractions T_i can be measured precisely using flavour-tagged data and do not require $\psi(3770)$ decays, but the quantum-correlated decay data are required to measure the averaged strong-phase differences X_i . The original binning scheme proposed in Ref. [96] was rectangular, however this does not provide optimal sensitivity [97, 98], and the measurements [38] by the CLEO collaboration of T_i and X_i used binning schemes optimised using various amplitude models of the decays $D^0 \rightarrow K_s^0 \pi^+ \pi^-$ [67, 99, 100] and $D^0 \rightarrow K_s^0 K^+ K^-$ [99]. One such measurement using the method outlined above has been performed by the LHCb collaboration [101], using the sample of promptly-produced $D^0 \rightarrow K_s^0 \pi^+ \pi^-$ decays recorded in 2011, but there has been no $D^0 \rightarrow K_s^0 K^+ K^-$ measurement using this technique.

The $\mathcal{N} = 3$ and $\mathcal{N} = 4$ binning schemes for the $D^0 \rightarrow K_s^0 K^+ K^-$ mode are shown in Fig. 2.8. These were derived from the amplitude model [99] illustrated in Fig. 2.9, and are chosen to minimise the variation across each bin of the strong-phase difference between opposing points in the Dalitz plot, *i.e.* the integrand in Eqn. 2.24. An optimal binning scheme leads to values $|X_i| \approx 1$, while these values would be smaller in a poor binning scheme. It should be stressed that the use of an amplitude model here does not introduce a model-dependence – a poor amplitude model would simply result in sub-optimal statistical sensitivity. Further studies of mixing in the charm system will be presented in Chapter 7.

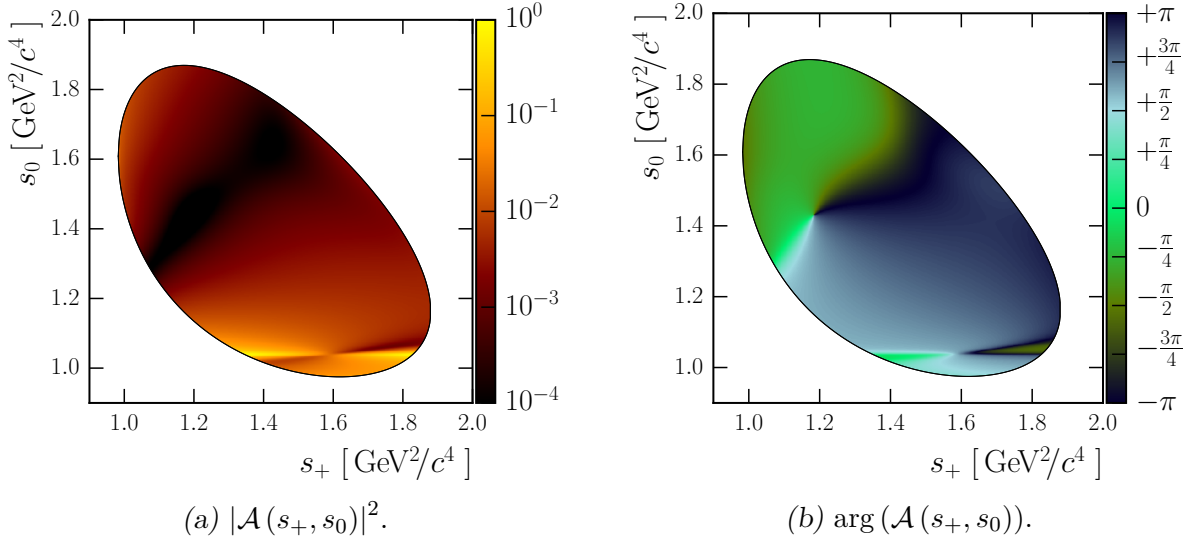


Figure 2.9: Amplitude model [99] used to optimise the binning schemes shown in Fig. 2.8 for the $D^0 \rightarrow K_s^0 K^+ K^-$ decay modes.

It is worth noting that an alternative, unbinned, model-dependent approach to measuring mixing and CP violation in $D^0 \rightarrow K_s^0 h^+ h^-$ decays exists, and has been used by the BaBar and Belle collaborations [36, 37]. Here, instead of integrating over bins in phase space, the integrand in Eqn. 2.25 is used directly, with an amplitude model describing $\mathcal{A}(s_+, s_-)$ inserted. This method can result in a smaller statistical uncertainty, but incurs a model-dependence systematic uncertainty that is particularly challenging to evaluate.

Finally, it is interesting to note that the observables z_{CP} and Δz defined above are trivially related to other observables in charm physics, notably the quantities y_{CP} and A_Γ [93]

$$y_{CP} = \Re(z_{CP}) = \frac{y}{2} \left(\left| \frac{q}{p} \right| + \left| \frac{p}{q} \right| \right) \cos \phi - \frac{x}{2} \left(\left| \frac{q}{p} \right| - \left| \frac{p}{q} \right| \right) \sin \phi, \quad (2.29)$$

$$A_\Gamma = \Re(\Delta z) = \frac{y}{2} \left(\left| \frac{q}{p} \right| - \left| \frac{p}{q} \right| \right) \cos \phi - \frac{x}{2} \left(\left| \frac{q}{p} \right| + \left| \frac{p}{q} \right| \right) \sin \phi, \quad (2.30)$$

where $\phi \equiv \arg(q/p)$. A_Γ can be obtained from the decay-time-dependent CP asymmetry in decays to CP eigenstates such as $D^0 \rightarrow h^+ h^-$, while y_{CP} is obtained from the ratio of effective D^0 lifetimes to CP eigenstate ($h^+ h^-$) and CF ($K^- \pi^+$) final states.

3. THE LHC AND THE LHCb EXPERIMENT

LHCb, the “LHC beauty” experiment, is one of four large experiments that exploit the Large Hadron Collider (LHC) at the European Organisation for Nuclear Research (CERN) near Geneva, Switzerland. The first period of LHC collider and experiment operation, Run 1, began in March 2010 and concluded in February 2013. The second period, Run 2, began in March 2015 and is ongoing. This chapter will describe the LHC and LHCb, their performance and relevant upgrades undertaken during the shutdown separating Run 1 and Run 2, LS1.

3.1 *The Large Hadron Collider*

The LHC [103] is a proton-proton and heavy ion collider installed in the 26.7 km circumference tunnel that once housed the Large Electron-Positron (LEP) accelerator. It consists of 1232 superconducting dipole magnets, one array of accelerating cavities and a variety of higher-order magnets used for focusing and corrections. There are four interaction points where the beams can be collided, each of which hosts one of the large LHC experiments: ALICE, ATLAS, CMS and LHCb. Three additional experiments use LHC collisions without having a dedicated interaction point: LHCf and TOTEM record particles produced at extremely small angles to the proton beams at, respectively, the ATLAS and CMS collision points. Finally, MoEDAL is situated near the LHCb collision point and is primarily designed to search for magnetic monopoles. The LHC normally provides proton-proton (pp) collisions, but is also capable of proton-heavy ion (pA or Ap) and heavy ion-heavy ion (AA) operation. Proton-proton collisions with a centre-of-mass energy $\sqrt{s} = 7 \text{ TeV}$ were provided in 2010 and 2011, $\sqrt{s} = 8 \text{ TeV}$ collisions were achieved in 2012 and, after upgrades carried

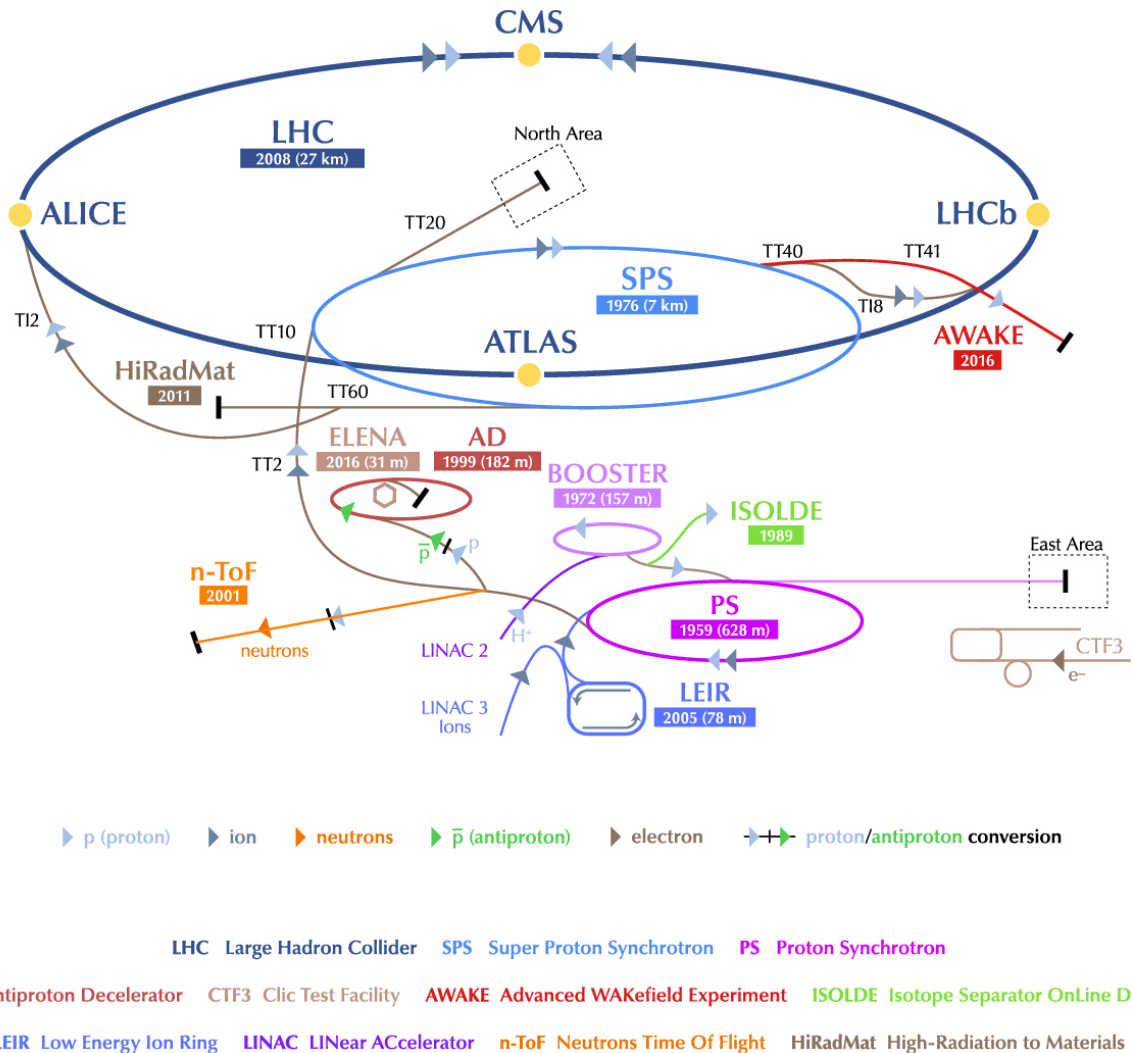


Figure 3.1: The CERN accelerator complex. For pp operation the injection chain is LINAC 2 – BOOSTER – PS – SPS – LHC. Figure taken from Ref. [102].

out during LS1, $\sqrt{s} = 13$ TeV operation began in 2015. The LHC was designed to provide pp collisions at up to $\sqrt{s} = 14$ TeV – a milestone that may be achieved in the next few years.

The CERN accelerator complex is shown in Fig. 3.1, which also illustrates the breadth of non-LHC physics taking place. During proton-proton operation of the LHC, hydrogen ions are accelerated in LINAC 2, a linear accelerator, and pass through the PSB (Proton Synchrotron Booster), PS (Proton Synchrotron) and SPS (Super Proton Synchrotron) before injection into the LHC at a beam energy of 450 GeV.

The LHC can hold up to 2808 bunches of $\mathcal{O}(10^{11})$ protons, with a slightly smaller number colliding at each collision point due to details of the filling scheme. Proton bunches are spaced at 25 ns intervals, although during Run 1 the majority of data were taken with a

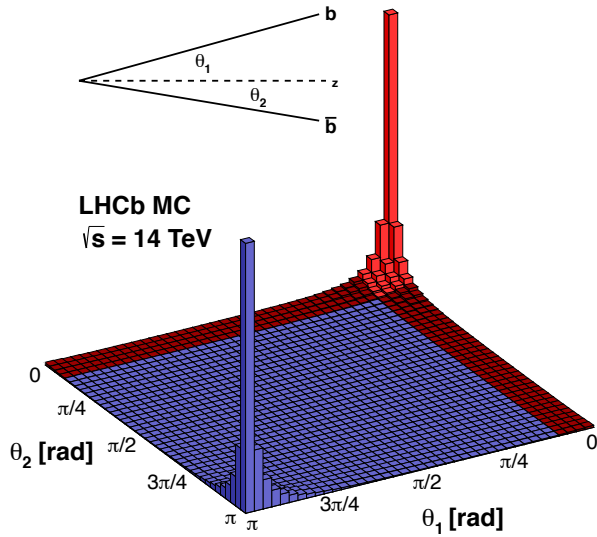


Figure 3.2: Histogram illustrating that the $b\bar{b}$ production cross-section in $\sqrt{s} = 14$ TeV pp collisions is sharply peaked in the forward and backward regions. The z axis in the figure corresponds to the LHC beam line. The dark red regions (small θ_1 or θ_2) indicate where one beauty quark is produced in the LHCb acceptance and the bright red region (small θ_1 and θ_2) corresponds to both beauty quarks flying into the LHCb spectrometer. At least one beauty quark is produced in the LHCb acceptance in around 25 % of events containing a $b\bar{b}$ pair. Figure taken from Ref. [104].

50 ns spacing. This reduction in bunch spacing, together with the increase in centre of mass energy from 8 TeV to 13 TeV, is the most significant change in the accelerator conditions for LHCb in Run 2.

3.2 The LHCb experiment

The LHCb¹ experiment Letter of Intent was submitted in August 1995 [105], eight months after the LHC project was approved [106]. The proposed design was a forward spectrometer equipped with Ring Imaging Cherenkov (RICH) detectors for particle identification (PID) and a silicon vertex detector. The proposed geometry exploits the forward-peaked nature of $b\bar{b}$ production, which is shown in Fig. 3.2. The new experiment would occupy the cavern previously occupied by the DELPHI experiment during LEP operation.

¹ Then LHC-B.

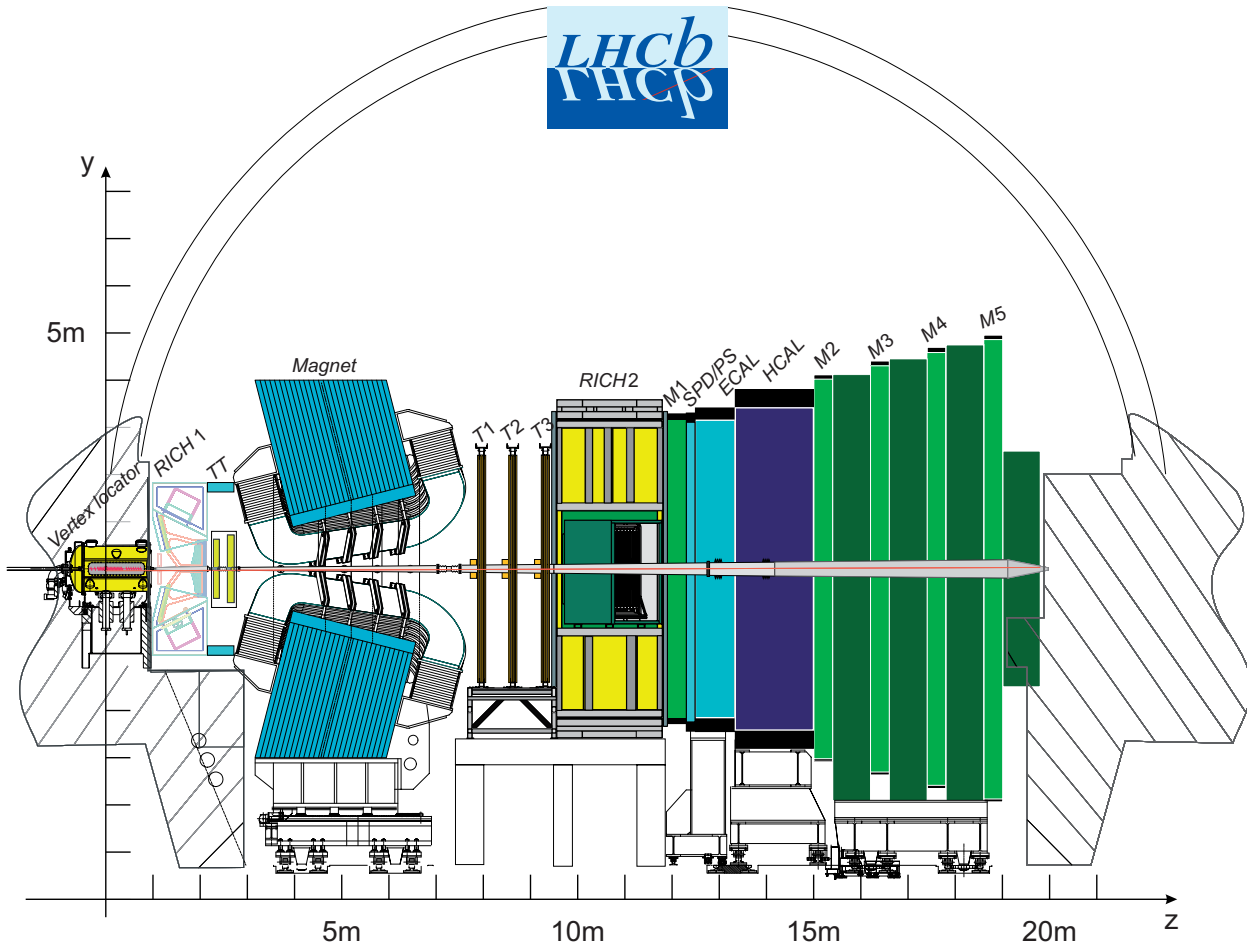


Figure 3.3: The LHCb detector. In the right-handed LHCb coordinate system the z -axis extends along the beam direction from the VELO towards the muon systems. The y -axis is vertical, the origin is near the centre of the VELO and the overall orientation is such that the x -axis points towards the outside of the LHC ring. Figure taken from Ref. [107].

The final design, shown in Fig. 3.3, does not differ significantly from the original proposal. The LHC beams cross near $z = 0$ on the left side of that figure, inside the silicon strip Vertex Locator (VELO). After leaving the VELO, particles produced in the collisions traverse the first RICH detector (RICH1) and the Tracker Turicensis (TT) before entering the magnet. The magnet is a warm, *i.e.* not superconducting, dipole with a bending power of around 4 Tm in the horizontal plane. After the magnet are three tracking stations (T1–3), the second RICH detector (RICH2) and the calorimeter and muon systems. The instrumented region is around 20 m long, from the VELO to the end of the muon system.

The LHCb detector is optimised to operate efficiently at lower luminosities than ATLAS and CMS. This is accommodated using a “luminosity levelling” technique, whereby a transverse offset is introduced between the two LHC beams in order to adjust the instantaneous

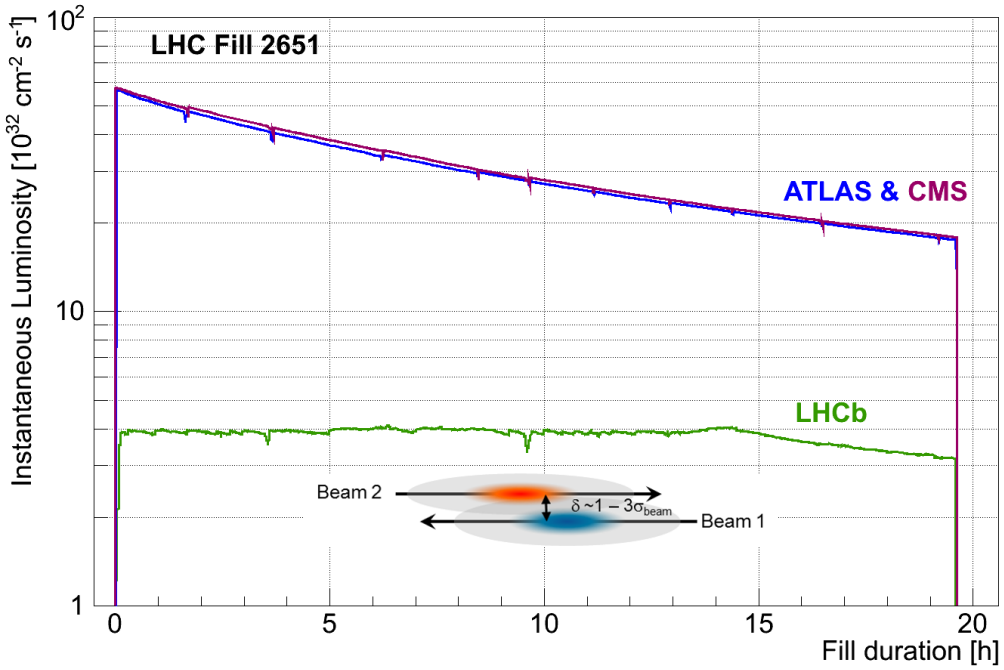


Figure 3.4: Illustration from Ref. [108] of the luminosity levelling employed at LHCb. This shows an unusually long LHC fill where, after around 15 hours, the transverse offset of the beams reaches zero.

luminosity. The offset is tuned during each fill to maintain the desired luminosity. This is illustrated in Fig. 3.4. By reducing the variation in collision conditions throughout each fill the levelling technique also reduces some systematic uncertainties.

By the end of Run 1 the detector operated at an instantaneous luminosity of around $4 \times 10^{32} \text{ cm}^{-2}\text{s}^{-1}$, double the luminosity originally envisaged. This is shown in Fig. 3.5 alongside the average number of visible interactions per bunch crossing, μ . The target luminosity in Run 2 is similar [109], but the value of μ is lower, around 1.1, because the reduction in bunch spacing from 50 ns to 25 ns allows substantially more colliding bunches to circulate in the LHC. The reduction in μ is desirable for much of the LHCb physics programme, as it reduces systematic uncertainties due to mis-association of particles to incorrect primary proton-proton interaction vertices (PVs) and decreases the average event occupancy, improving the efficiency of, in particular, the Outer Tracker (OT) and trigger systems. This preference for low μ values is one of the main reasons that LHCb operates at lower luminosities than ATLAS and CMS. Another motivation is the need to limit the radiation damage suffered by the VELO, which sits extremely close to the interaction point.

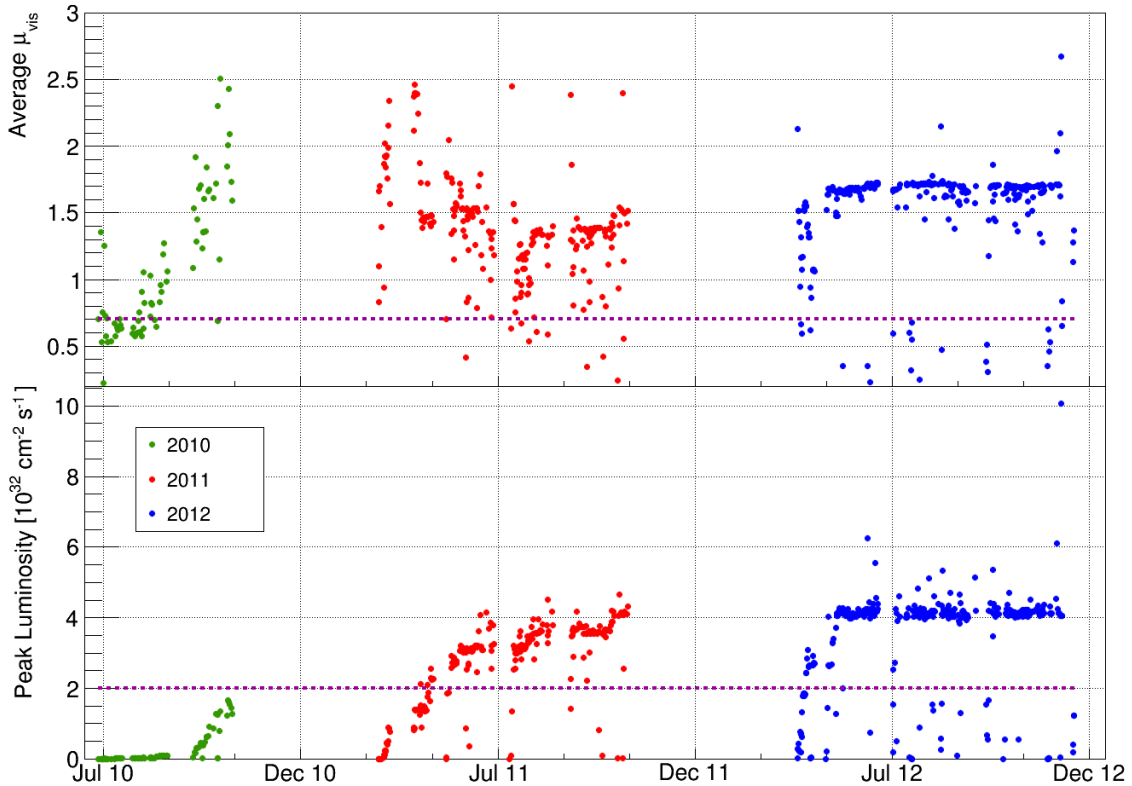


Figure 3.5: Variation in average μ (top), the number of visible interactions per bunch crossing, and peak luminosity (bottom) throughout Run 1, *i.e.* 2010–12. Figure taken from Ref. [108].

3.2.1 Vertex Locator

The LHCb VELO consists of two sets of 21 approximately semicircular silicon detector modules around the collision point. The detector halves are retracted to around 4 cm from the beams when the LHC beams are not stable, and close to around 8 mm from the beams during data-taking. This is illustrated in Fig. 3.6. Each module contains two silicon strip sensors: an R -sensor, which measures the radial distance from the beam, and a ϕ -sensor, which measures the azimuthal angle in the x – y plane. Charged particles must cross 3–5 modules in order to be reconstructed in the VELO, depending on which version of the reconstruction is run, and the irregular layout shown in Fig. 3.6 is designed to ensure this requirement is usually met for charged particles in the LHCb acceptance.

The detector modules are contained in a thin aluminium box, which separates the $\sim 10^{-9}$ mbar beam pipe vacuum from the $\sim 10^{-7}$ mbar detector vacuum and shields the VELO modules against electromagnetic interference from the LHC beams [112].

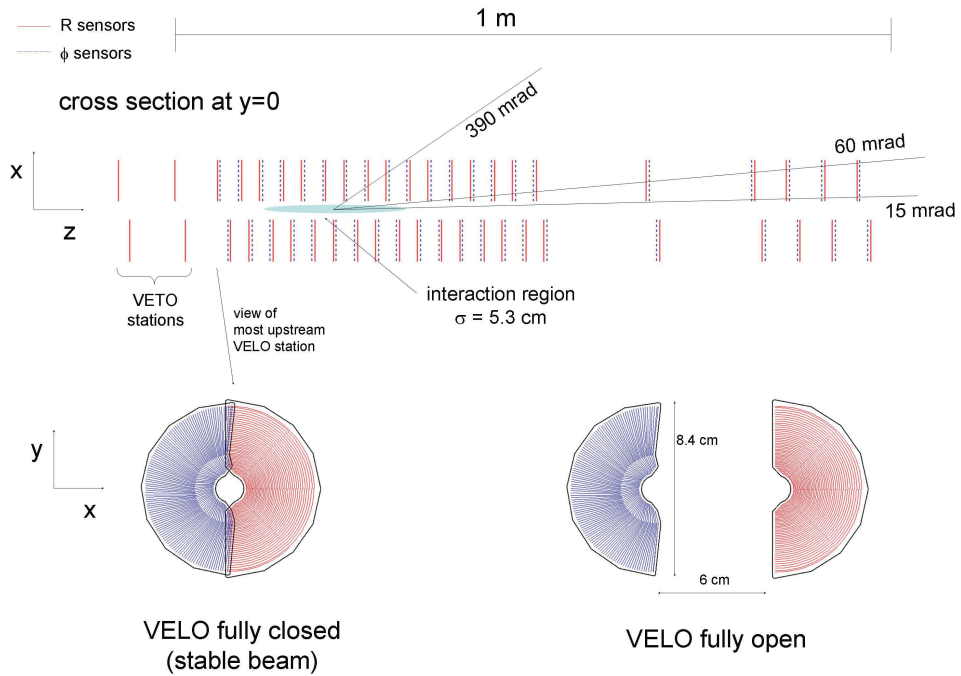


Figure 3.6: Overview of the VELO detector. Figure taken from Ref. [110]. The coordinates used are the same as Fig. 3.3. The “VETO stations” provide input to the hardware trigger, L0, which is described in Sect. 3.2.8.

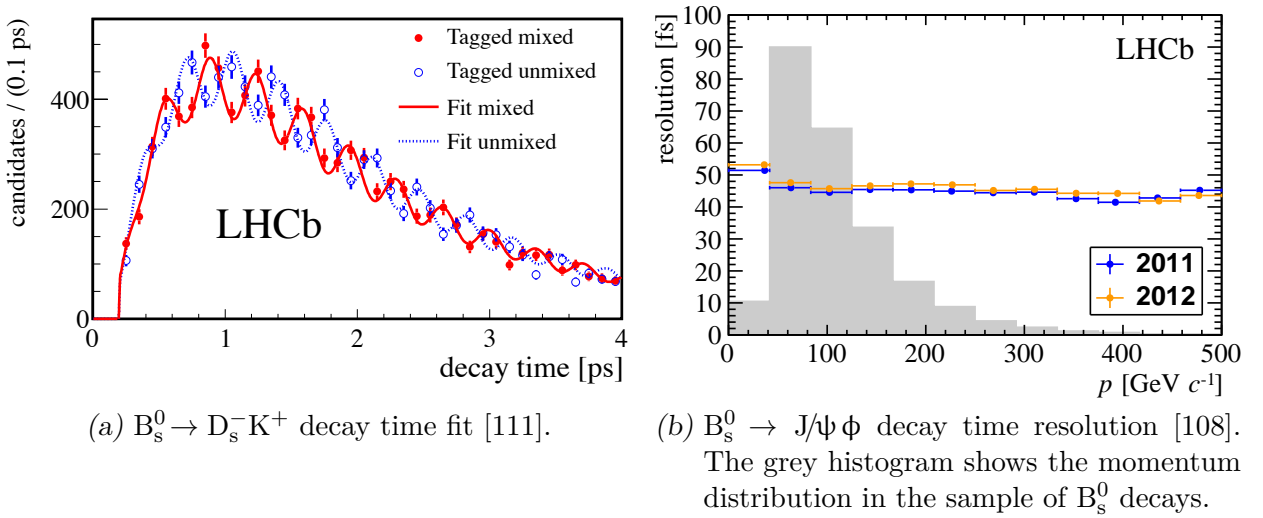


Figure 3.7: Decay time performance illustrations.

The VELO is the main contributor to the excellent vertex reconstruction, impact parameter (IP) resolution and decay time resolution achieved by LHCb. Figure 3.7 shows the decay time fit from an analysis of $B_s^0 \rightarrow D_s^- K^+$ decays, illustrating the excellent decay time resolution and its necessity, and also shows the resolution measured in $B_s^0 \rightarrow J/\psi \phi$ decays.

3.2.2 Downstream Tracking

The tracking system consists of the VELO and TT, which are located upstream of the magnet, and three stations immediately downstream of it. The three stations are each divided into two parts: an inner segment made of silicon (the Inner Tracker, IT) and an outer part consisting of straw-tube drift chambers (the Outer Tracker, OT). The TT is around 150 cm high and 130 cm wide and covers the full LHCb acceptance with silicon sensors. The TT and IT are collectively referred to as the Silicon Tracker (ST). Information from the VELO and TT is used in the first stage software trigger (HLT1) to provide a preliminary momentum estimate for charged particles, while information from the IT and OT is only used in the second stage software trigger (HLT2) and offline reconstruction.

3.2.3 Silicon Tracker

The IT covers a cross-shaped area around 120 cm wide and 40 cm high near the LHC beam pipe, where particle densities are too high for the drift tube technology used in the OT to be effective. This is illustrated on the right side of Fig. 3.8. Each tracking station, T1–3, is around 4.8 m high and 5.8 m wide, so the cost of extending the ST to cover the full area would be prohibitive. The ST detectors were optimised to achieve single-hit resolutions of around 50 μm , operate efficiently at low occupancy in a moderately high radiation environment and minimise the material budget of the detectors. The target resolution is sufficient for the momentum resolution of the spectrometer to be dominated by multiple scattering for most relevant particle momenta [110]. All the ST detector components are contained in light tight boxes that are electrically and thermally insulated, maintained at a temperature below 5°C and continuously flushed with nitrogen to avoid condensation.

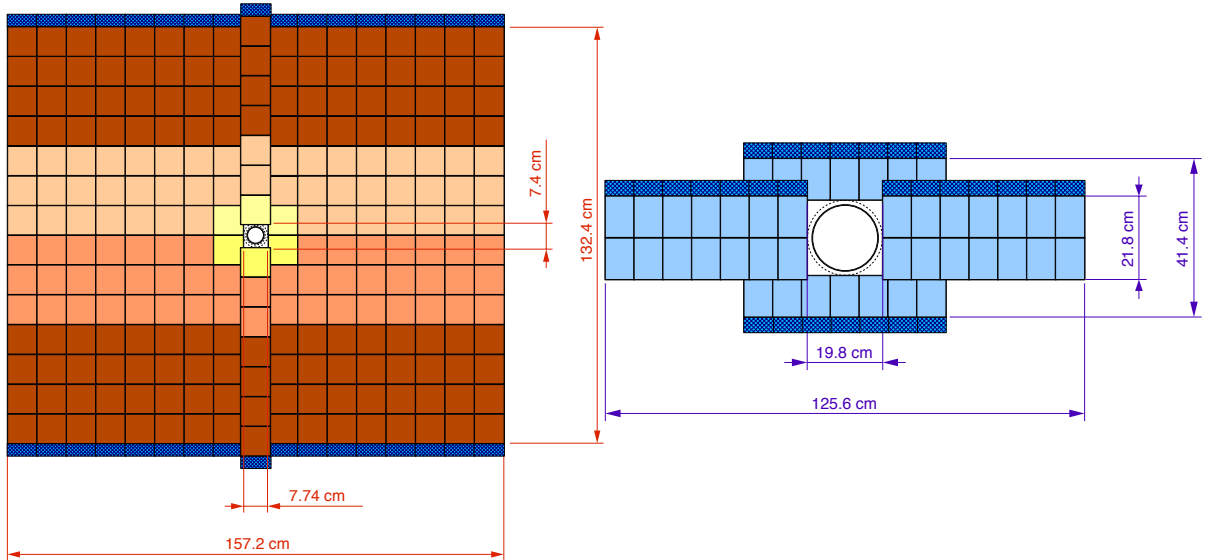


Figure 3.8: TT (left) and IT (right) layers. In the left figure the shading indicates the readout sector. Figures taken from Ref. [113].

The TT consists of four layers similar to that shown on the left side of Fig. 3.8 in a $x-u-v-x$ arrangement where the first and last layers have readout strips oriented vertically and the two intermediate layers are rotated by angles of $\pm 5^\circ$. The layers are arranged in two pairs, which are separated by around 27 cm along the LHC beam axis to aid the track reconstruction algorithms. The detector is logically split into upper and lower halves, with each half further subdivided into rows of seven silicon sensors. The cooling and readout infrastructure is concentrated at the end of each row, outside the LHCb acceptance, to minimise the radiation length traversed by charged particles. Each silicon sensor is around 500 μm thick, 10 cm wide, 9 cm long, and carries 512 readout strips with a pitch of 183 μm . In total the TT has 143 360 readout strips over an active area of around 8.4 m^2 .

The three IT stations each have a similar four-layer design, although the geometry of the T1–3 stations does not allow the cooling and readout infrastructure to be placed outside the spectrometer acceptance. The IT sensors are single-sided, 7.6 cm wide, 11 cm long and have 384 readout strips with a pitch of 190 μm . The sensors to the left and right sides of the beam pipe are 410 μm thick, while those above and below are 320 μm thick. The different thicknesses were chosen to ensure sufficiently high signal-to-noise ratios in each part of the detector while minimising the material budget.

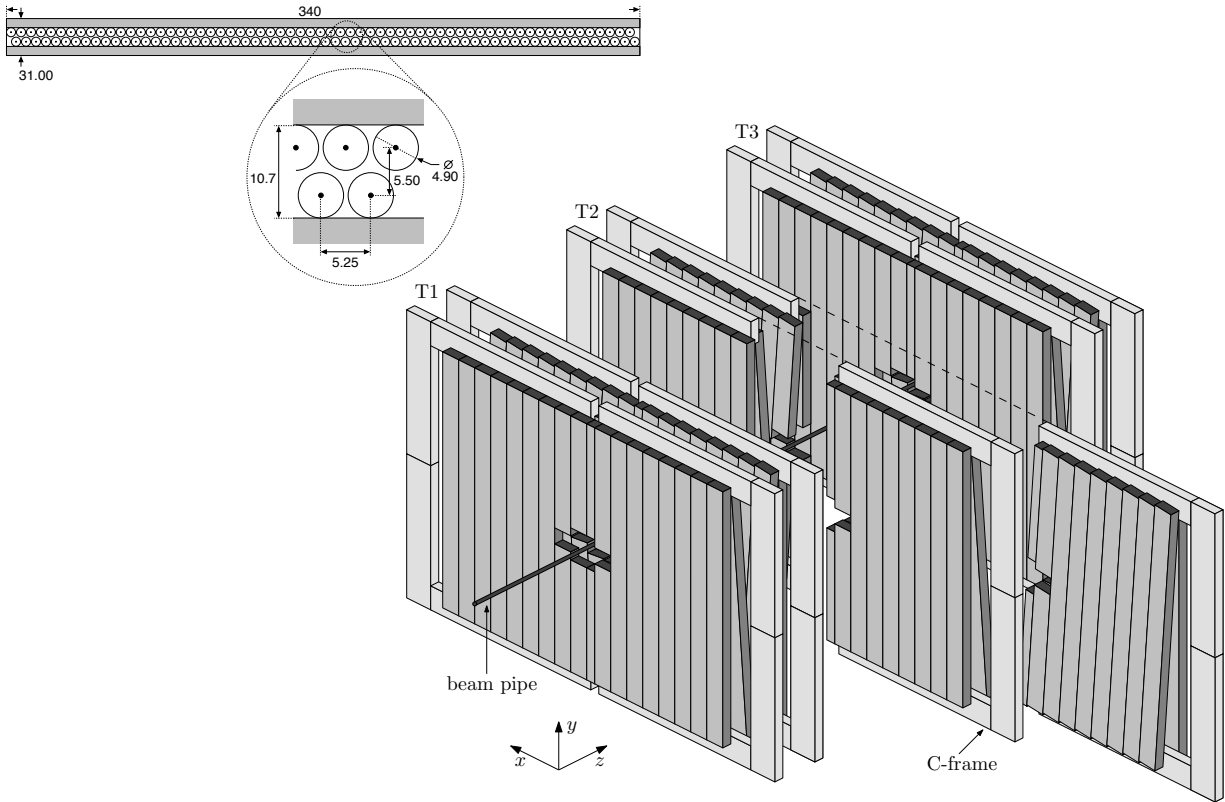


Figure 3.9: Overview of the OT detector. The upper left figure shows the cross-section of one of the four layers that form each OT station. The two staggered sub-layers are known as monolayers. The lower right figure shows the three tracking stations, T1–3, together. Figure taken from Ref. [114].

3.2.4 Outer Tracker

The Outer Tracker is a drift-time detector [114] designed to provide precise tracking of charged particles over a large active detector area. Excellent momentum resolution of around $\Delta p/p = 0.4\%$ is necessary for the detector to achieve an invariant mass resolution of $10 \text{ MeV}/c^2$ in decays such as $B_s^0 \rightarrow D_s^- K^+$, which is important if clean signals are to be isolated in complex, high-multiplicity proton-proton collisions. This target resolution, together with demands of a high tracking efficiency and low fraction of fake tracks, drives the design choices of the OT. The tracker stations, T1–3, each have an active OT area of around $597 \times 485 \text{ cm}^2$ and have the same four-layer $x-u-v-x$ geometry as the ST stations. The OT is illustrated in Fig. 3.9. The relative dimensions of the IT and OT sections of each station are set by the requirement that the OT occupancy should be less than 10% at an instantaneous luminosity of $2 \times 10^{32} \text{ cm}^{-2}\text{s}^{-1}$. Each detector layer consists of two staggered

arrays of straw-tubes with internal diameters of 4.9 mm. Each tube is filled with a mixture of 70 % Ar, 28.5 % CO₂ and 1.5 % O₂ and contains a 25 µm diameter gold-plated tungsten wire. The gas mixture was originally [110] intended to be a 70:30 mix of Ar and CO₂, but a small concentration of O₂ was added to combat ageing effects [115]. The gas mixture was chosen to ensure a drift time of below 50 ns and drift coordinate resolution of around 200 µm. In total the OT has around 55 000 single straw-tube channels, and like the TT is designed such that the readout electronics, detector supports and services are located outside the LHCb acceptance and do not contribute to the material budget.

Because the drift time in the OT is around double the minimum LHC bunch spacing of 25 ns, the spillover effects between bunch crossings have become more significant in Run 2 of the LHC than they were in Run 1 collisions with 50 ns spacing.

3.2.5 RICH Detectors

Two Ring Imaging Cherenkov detectors [116], RICH1 and RICH2, provide discrimination between charged pions, kaons and protons over a wide range of particle momenta. RICH1 is optimised for low and intermediate momentum tracks, providing discrimination over a range of approximately 2–40 GeV/c and covering the full angular acceptance of the spectrometer, 25–300 mrad. RICH2 is optimised for the high momentum range of around 15–100 GeV/c in a restricted angular acceptance near the beam pipe of 15–120 mrad. Because of the strong correlation between polar angle and particle momentum, the restricted acceptance captures a large fraction of tracks in the momentum range where RICH2 has significant discriminatory power. The two detectors are shown in Fig. 3.10.

To minimise its overall volume, RICH1 is placed as close as possible to the interaction region, with its gas enclosure sealed directly to the exit window of the VELO. RICH2 is placed downstream of the tracking stations, T1–3, in order to minimise the material budget within the tracking system.

Both RICH detectors have similar optical systems, with spherical primary focusing mir-

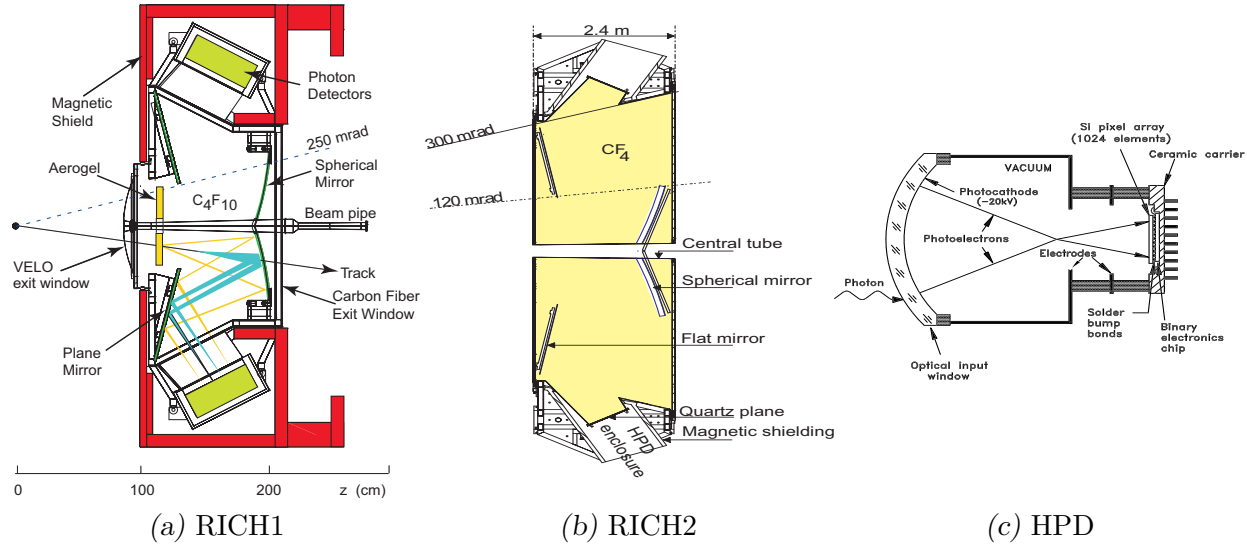


Figure 3.10: Illustrations of the two RICH detectors and the Hybrid Photon Detectors. Figures taken from Ref. [110].

rors and additional, secondary, flat mirrors that allow the photon detectors to be positioned outside the spectrometer acceptance and the length along the beam direction of the RICH detectors to be minimised. The optical system is divided in two halves for each detector, with RICH1 split into upper and lower parts and RICH2 divided into left and right halves.

The detectors use fluorocarbon gases at room temperature and pressure as Cherenkov radiators, with C₄F₁₀ used in RICH1 and CF₄ in RICH2. Around 5 % CO₂ has been added to the RICH2 radiator to quench scintillation. RICH1 also contained blocks of Aerogel [117], a solid consisting of 1–10 nm grains of amorphous SiO₂ linked together in a three-dimensional structure filled by trapped air, which was intended to improve performance at low momentum. While the RICH detectors as a whole performed very well during Run 1 of the LHC, the Aerogel did not contribute as much as had been hoped, and it was removed before Run 2 began. This is expected to improve the performance of RICH1, by increasing the volume of C₄F₁₀, and reduce the processing time required by the reconstruction algorithms by removing a large number of photons produced in the Aerogel that did not provide useful information. These radiators were chosen due to their small dispersion and appropriate refractive indices for the target momentum ranges. The Cherenkov threshold for kaons is 15.6 GeV/c in CF₄, 9.3 GeV/c in C₄F₁₀ and 2.0 GeV/c in Aerogel. Particles below these thresholds can still be

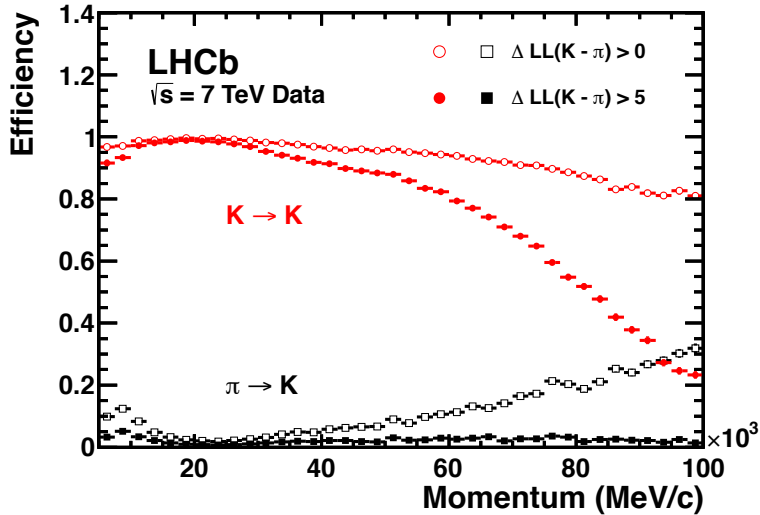


Figure 3.11: Kaon identification efficiency and pion misidentification rate measured in $\sqrt{s} = 7$ TeV data as a function of track momentum. Two different particle identification requirements have been imposed on the samples, resulting in the open and filled marker distributions respectively. Figure taken from Ref. [116].

identified in veto mode by the absence of Cherenkov radiation.

A novel Hybrid Photon Detector (HPD) was developed for the LHCb RICH system. Each HPD consists of a vacuum tube with a 75 mm diameter quartz window and multialkali photocathode. Photoelectrons are accelerated onto a 32×32 silicon pixel array, where each pixel is $2.5 \text{ mm} \times 2.5 \text{ mm}$ in size. The front-end electronics are contained within the HPD vacuum tube and bonded directly to the silicon pixel sensor, resulting in extremely low noise of around 150 e^- for a signal of $5\,000 \text{ e}^-$. The HPDs are sensitive to magnetic fields, which influence photoelectrons and distort the resulting images. While this effect can be corrected, magnetic shielding is positioned around the HPD enclosures to reduce it as much as possible. This is a further motivation for positioning the RICH detectors as far away from the magnet as possible. 196 HPDs are used in RICH1, with a further 288 in RICH2.

The RICH reconstruction algorithms perform a global likelihood fit, which considers all possible mass hypotheses for reconstructed tracks that pass through the RICH detectors. In Run 1 and during data-taking in 2015 six hypotheses were considered for each track: electron, muon, pion, kaon, proton and “below Cherenkov threshold”. An illustration of the kaon-pion separation performance in Run 1 is given in Fig. 3.11. Starting in 2016 the deuteron hypothesis will also be included, allowing several new analyses to be carried out.

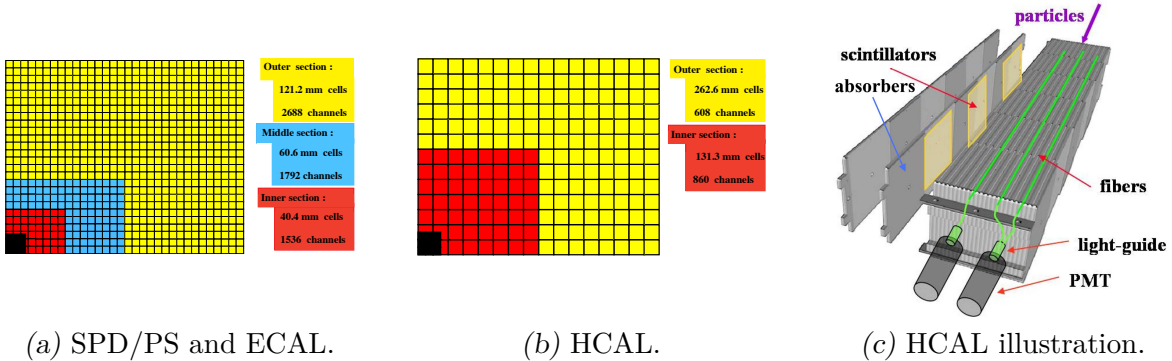


Figure 3.12: Diagrams indicating the lateral segmentation of the SPD/PS and ECAL (left) and HCAL (centre). One quarter of the detector front face is shown. In the left figure the cell dimensions are given for the ECAL. The right-most figure illustrates a module of the HCAL. Figures taken from Ref. [110].

3.2.6 Calorimeter System

The LHCb calorimeter systems have two important roles: firstly, they identify and reconstruct electrons, photons and π^0 mesons. Secondly, they provide transverse energy (E_T) information that allows hadrons, electrons and photons to fire the hardware trigger, L0, which will be discussed further in Sect. 3.2.8.

The calorimeter system has four components: nearest the interaction point is the scintillator pad detector (SPD), this is followed by a preshower (PS) detector, an electromagnetic calorimeter (ECAL) and, finally, a hadronic calorimeter (HCAL). The SPD detector provides discrimination between electron and photon deposits in the ECAL, while the longitudinal (z) separation provided by the PS helps discriminate electron and π^\pm deposits. Due to the much greater hit density in the inner region of the calorimeter, the lateral ($x-y$) segmentation is not uniform; this is shown in Fig. 3.12. The system is located downstream of RICH2 and the first muon station, as illustrated in Figs. 3.3 and 3.13.

The active layers of the SPD and PS detectors are very similar, comprising arrays of scintillator pads. Scintillation light is transmitted to multianode photomultiplier tubes (MAPMTs) by wavelength-shifting (WLS) and clear optical fibres. The MAPMTs are situated above and below the detector acceptance. The SPD and PS detectors are separated by a 1.5 cm lead converter, which corresponds to around 2.5 radiation lengths. The SPD/PS

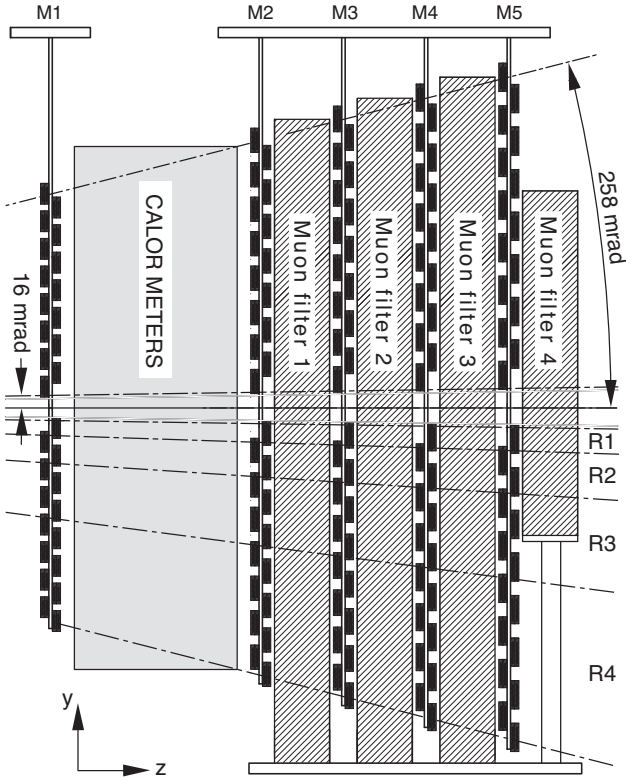


Figure 3.13: Side view of the calorimeter and muon systems. Figure taken from Ref. [110].

detector fits in the 18 cm gap between the first muon station and the ECAL, and has an active area around 6.2 m wide and 7.6 m high. The lateral segmentation of the SPD, PS and ECAL, shown in Fig. 3.12, is such that there is a one-to-one projective correspondence between cells in the three detectors.

The ECAL was designed to achieve an energy resolution of $\sigma_E/E = 10/\sqrt{(E/\text{GeV})} \oplus 1\%$, sufficient to achieve a B-meson mass resolution of $65 \text{ MeV}/c^2$ in the penguin decay $B \rightarrow K^*\gamma$ with a high- E_T photon, and $75 \text{ MeV}/c^2$ for $B \rightarrow (\rho\pi)^0$, where the π^0 mass resolution is around $8 \text{ MeV}/c^2$. It consists of 66 layers, which alternate 2 mm thick lead tiles and 4 mm thick scintillator tiles, separated by 120 μm thick white, reflecting paper. The Molière radius is around 3.5 cm. The active volume of the ECAL is 42 cm deep, corresponding to 25 radiation lengths, enough for almost all of the energy in electromagnetic showers to be captured, which is necessary to attain good energy resolution. The scintillator tiles in each ECAL cell are linked by WLS fibres connected to a photomultiplier tube (PMT) on its back face.

Because the E_T resolution requirements of the L0 trigger (see Sect. 3.2.8) are not very

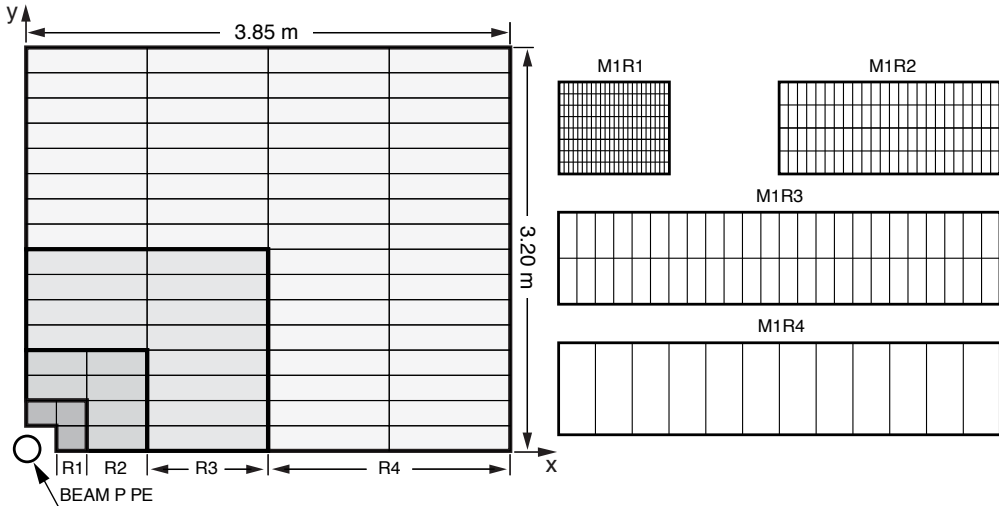


Figure 3.14: One quadrant of the M1 station (left). Each rectangle represents one chamber. Subsequent stations are scaled projectively with their distance from the interaction point. The right side of the figure shows the division into logical pads of chambers from each of the four regions, R1–4. In stations M2–3 (M4–5) the number of pad columns per chamber is double (half) that in the corresponding region of M1, while the number of pad rows is the same. Figure taken from Ref. [118].

stringent, it is not critical to fully contain hadronic showers, and the HCAL is only around 5.6 hadronic interaction lengths thick. Its lateral segmentation is coarser than the rest of the calorimeter system, as illustrated in Fig. 3.12. Also shown is the structure of each HCAL cell, which is a sandwich of iron and scintillator plates. The orientation of the plate is rotated with respect to the ECAL design; the iron plates are 1 cm thick in the lateral direction and one hadronic interaction length long in the longitudinal direction. As in the ECAL, the scintillator plates in each cell are linked by WLS fibres and read out by a PMT on the back face. The HCAL resolution is around $\sigma_E/E = (69 \pm 5)/\sqrt{(E/\text{GeV})} \oplus (9 \pm 2)\%$.

3.2.7 Muon System

The muon system is critical to many important analyses in the LHCb physics programme, such as $B_s^0 \rightarrow \mu^+ \mu^-$ and $B_s^0 \rightarrow (\mu^+ \mu^-)_{J/\psi} (K^+ K^-)_{J/\psi}$, and high- p_T muon tracks are one of the cleanest signatures that can fire the L0 trigger. There are five muon stations, one placed upstream of the calorimeter system (M1) to improve p_T resolution in the L0 trigger, and four downstream of it (M2–5), as shown in Fig. 3.13. The four downstream stations are interleaved with 80 cm thick iron absorber plates to select penetrating muons. Including the calorimeter

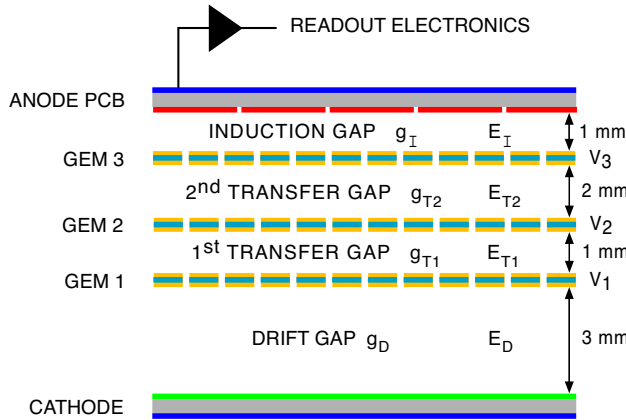


Figure 3.15: Illustration of a gas electron multiplier (GEM) detector as used in the central region of the first muon station, M1. Figure taken from Ref. [110].

system, a muon must penetrate around 20 interaction lengths to reach the final muon station, M5. The first three stations, M1–3, are finely segmented in the bending plane (x) and used to define the track momentum and provide a 20 % estimate of p_T . The final stations, M4 and M5, have limited spatial resolution and are mainly used to identify penetrating particles. The logical segmentation of the M1 station is illustrated in Fig. 3.14, which also shows that information from the inner regions is read out with much finer granularity. In the inner regions the logical channels correspond directly to physical anode strips and cathode pads, while in the outer regions several of these are combined and the logical channels refer to a larger area. A total of 25 920 logical channels are constructed from 122 112 physical channels.

Multi-wire proportional chambers (MWPCs) are used everywhere except the central region of the first station, M1, where the expected particle flux is highest and a detector based on three gas electron multiplier foils (triple-GEM) is used. The MWPC chamber wires are vertical, 20–30 cm long and made from 30 μm gold-plated tungsten. They are centred in a 5 mm gas gap filled with a 40 : 55 : 5 mix of Ar, CO₂ and CF₄. In M2–5 there are four gas layers, whose signals are logically combined into two, while M1 has two layers that are logically combined into one. A triple-GEM detector is shown in Fig. 3.15. Each detector has an active area of $20 \times 24 \text{ cm}^2$, with the readout anode divided into $0.4 \times 0.4 \text{ mm}^2$ pads. The gas mixture used is a 45 : 15 : 40 mix of Ar, CO₂ and CF₄. Ionisation electrons are produced in the drift gap and multiplied as they are accelerated through the three foils towards the anode pads. The multiple foils allow a larger gain to be achieved while avoiding discharges.

Muon identification relies on several different techniques. The simple method used in the L0 trigger is outlined in Sect. 3.2.8, with progressively more sophisticated methods used in the software trigger [119] and offline reconstruction [120]. In the offline reconstruction both binary (“IsMuon”) and likelihood-ratio variables are calculated. These are based on finding hits within a field of interest (FOI) in enough muon stations, where the required number of muon stations and FOI size are dependent on momentum, and considering the distribution of hits around the extrapolated track position.

Information from the RICH, calorimeter and muon systems is combined to produce, for each charged particle track, a likelihood value for each mass hypothesis. Differences in the logarithms of these combined likelihoods (DLLs) are used extensively in event selections to distinguish different types of particle.

3.2.8 Hardware Trigger (L0)

The LHC bunch crossing frequency can, in principle, reach around 40 MHz, with a visible inelastic collision rate of around 30 MHz in LHCb. The hardware trigger, L0, is responsible for reducing this to the 1 MHz rate at which the full detector can be read out. L0 operates fully synchronously, with fixed latencies that depend on neither the detector occupancy nor the bunch crossing history. It is implemented in custom-designed hardware, which produces a decision with a maximum latency of 4 μ s.

Three inputs are provided to the L0, as shown in Fig. 3.16. The first of these, the Pile-Up system, is primarily used to aid determination of the luminosity [121], and does not participate in the L0 decisions that provide the overwhelming majority of data for the LHCb physics programme. It consists of two special VELO stations, labelled as “VETO stations” in Fig. 3.6, which have only *R*-sensors. Information from these stations is used to provide a fast estimate the number of PVs in an event.

The next input, the calorimeter system, allows L0 to trigger on electron, photon and hadronic signals. It also provides, by counting the hit multiplicity in the SPD detector, an

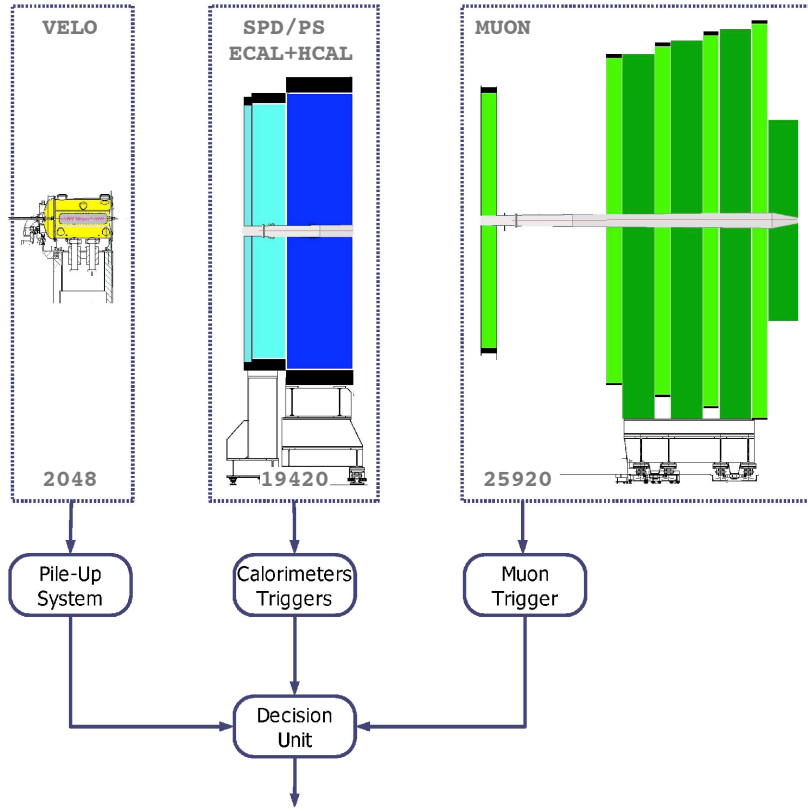


Figure 3.16: Sources of input to the L0 trigger. The numbers given on the figure indicate the number of channels that are read out synchronously at the 40 MHz nominal LHC frequency. Figure taken from Ref. [110].

estimate of the number of charged particles in each event. This is valuable because high-multiplicity events are slow to process in the software trigger and offline reconstruction, so explicitly biasing towards simpler events allows more complex selections to be executed. Electron, photon and hadron candidates are formed from 2×2 cell clusters in the ECAL and HCAL. The hadronic trigger decision is based on the highest E_T HCAL cluster, which also contains the energy of the matching ECAL cluster. The photon trigger decision is based on the highest E_T ECAL cluster with matching hits in the PS detector but none in the SPD. The electron trigger decision is similar, but requires matching hits in the SPD.

The final input to L0 is the muon system. A fast reconstruction is performed that searches for the two muon tracks with the highest p_T in each quadrant of the muon system. The search is restricted to muons with p_T greater than $0.5 \text{ GeV}/c$ and uses a straight line extrapolation to search for hits, starting from those in the third muon station, M3. Hits are required in all five muon stations. The trigger considers the eight muon candidates and

imposes a threshold on either the largest transverse momentum, $p_{\mathrm{T}}^{\mathrm{largest}}$, or the product $p_{\mathrm{T}}^{\mathrm{largest}} \times p_{\mathrm{T}}^{\mathrm{second\ largest}}$.

In typical L0 configurations 450 kHz of output bandwidth is allocated to the hadronic trigger, 400 kHz to the muon triggers and the remaining 150 kHz for electrons and photons.

3.2.9 Software Trigger (HLT)

The final part of the trigger system is the software trigger (High Level Trigger, HLT), which will be described fully in Chapter 4. This is responsible for reducing the 1 MHz output rate of the L0 trigger to a rate that can be sent to permanent offline storage. The HLT output rate has increased substantially as additional computing resources have become available, from around 3.5 kHz in 2011 to 12.5 kHz in 2015.

3.3 *LHCb analysis software*

A wide range of software is necessary to perform physics analysis at LHCb, from the software trigger and subsequent offline selection algorithms, to physics and detector simulation. Most of this software is based on the GAUDI [122] framework, which is also used by ATLAS.

A full Monte Carlo simulation of proton-proton collisions, their interaction with the LHCb detector and the detector response exists, and is widely used to estimate selection efficiencies, test new features in the software and optimise event selections. In the simulation, pp collisions are generated using PYTHIA [123] with a specific LHCb configuration [124]. The leading order production mechanisms for c and b quarks are the $2 \rightarrow 2$ QCD processes given in Ref. [125] and shown in Figs. 3.17a and 3.17b. Several higher order processes, such as those shown in Figs. 3.17c and 3.17d, are non-negligible and included in the simulation [125]. Generated events are normally forced to include a particular signal decay of interest. Selection cuts are normally applied to the generated particles at this stage to save processing time. Typically these require that the decay products of the signal candidate are contained in the detector acceptance, but much harsher requirements can be used in some cases.

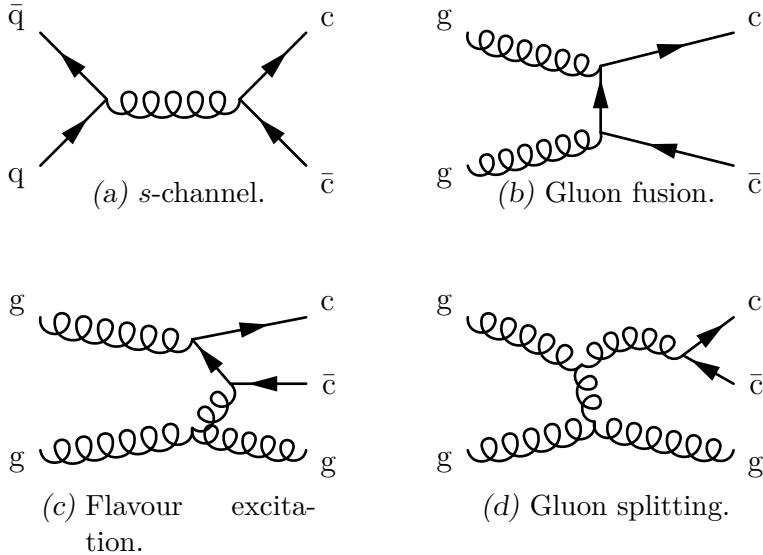


Figure 3.17: $c\bar{c}$ production processes implemented in PYTHIA for LHCb [125].

Decays of hadronic particles, including phenomena such as neutral meson mixing and resonant structure in multi-body final states, are described by EVTGEN [126]. Final-state radiation is generated using PHOTOS [127]. The GEANT4 toolkit [128] is used to describe the interaction of generated particles with the detector and its response, as described in Ref. [129]. Further processing converts the simulated detector response into the same data format produced by the real detector, and emulates the L0 trigger decisions. Finally, simulated collisions are processed using the same trigger software and offline reconstruction algorithms as real data, with additional information about the generated particles retained for use when the data are analysed.

Both real and simulated data are processed using the Worldwide LHC Computing Grid (WLCG) [130] and extensions specific to LHCb [131]. The WLCG is used for the entire simulation process, while real data only reaches the WLCG after the software trigger has been executed. Subsequent processing includes a full offline event reconstruction, where more processing time is available per event than in the software trigger, and a centralised preselection process dubbed “stripping”. The stripping produces signal candidates using particles found in the offline reconstruction and applies additional selection requirements to improve signal purity. These signal candidates are saved to “stripped” files, which are then used for physics analysis. For some signal modes, such as high branching fraction charm

decays, only the signal candidate is saved in order to reduce file sizes, while other modes save the entire reconstructed event. The full dataset is periodically “restripped” to allow new selections to be added and old ones to be improved. There have been several changes in Run 2 that allow physics analyses to proceed without relying on the stripping – this will be described further in the next chapter.

4. THE LHCb SOFTWARE TRIGGER

The LHC provides beams with a unique combination of high energy and luminosity. At these high energies, the cross-section for inelastic proton-proton collisions is large, and collisions typically produce a large number of particles. Coupled with the high luminosity, this results in a high inelastic collision rate and a complex and challenging environment in which to isolate interesting signal decays, which in many cases are very rare.

When running at the limits of its design parameters, the LHC bunch crossing frequency is 40 MHz. The hardware trigger, L0, described in Chapter 3 reduces the rate of crossings that need to be considered further to around 1 MHz, at which rate the full detector is read out into the software trigger, which is also referred to as the High Level Trigger (HLT). The HLT is described at some length in this chapter both because of its importance to the experiment as a whole and the analyses described in this thesis, but also because of the author’s contributions, specifically to the topics described in Sects. 4.3 and 4.4, and the commissioning of the HLT for Run 2.

Each collision event accepted by L0 corresponds to around 60 KiB¹ of raw data, so the HLT must process an input data rate of around 60 GiB/s and reduce it to a rate that is manageable offline. The software trigger is split into two stages: HLT1, the first stage, performs a partial event reconstruction and selects displaced and/or high p_T charged particles, and high E_T photons. The output of HLT1 is fed into HLT2, the second stage, which performs a limited full event reconstruction and contains a wide range of inclusive and exclusive selections, which will not be described in any detail here. Perhaps the most important HLT2 trigger for LHCb physics analysis as a whole is the inclusive b-hadron trigger, which selects

¹ KiB and GiB denote kibibytes (1024 bytes) and gibibytes (1024³ bytes). These binary prefixes are preferred to the decimal kilo- and giga- prefixes when referring to data transmission and processing [134].

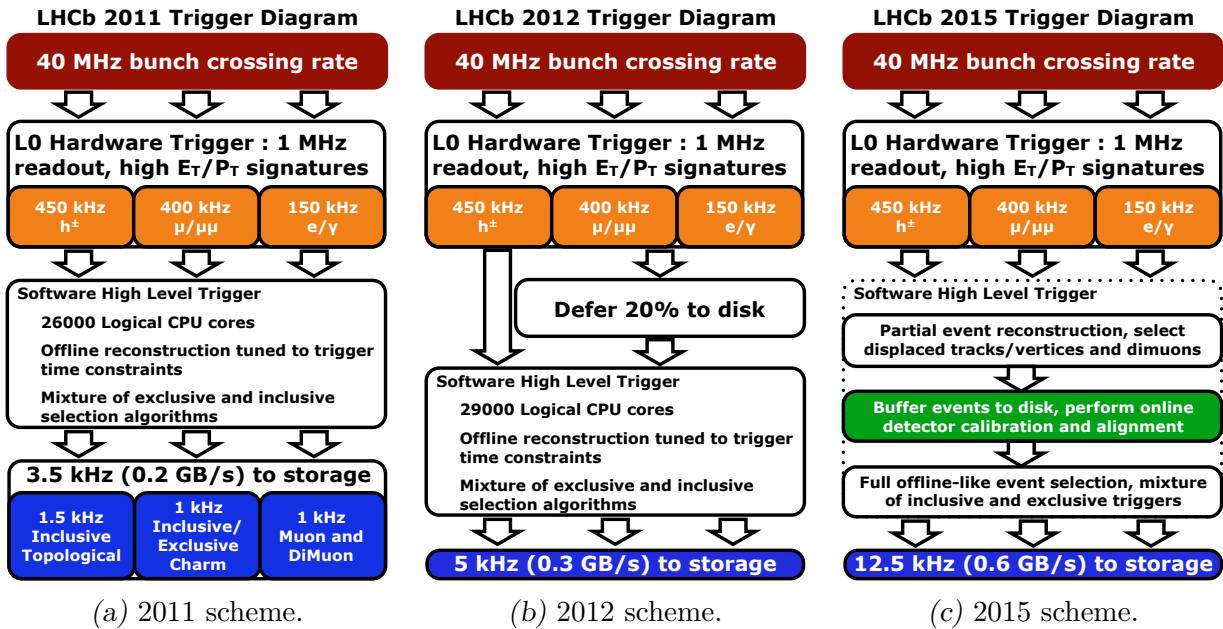


Figure 4.1: Illustrations of the trigger schemes used during various data-taking periods. The right-most figure, while labelled 2015, is expected to be representative of Run 2 in its entirety. Figures taken from Ref. [132].

displaced two-, three- or four-track vertices using a multivariate method. The performance of this trigger in Run 1 is illustrated below in Fig. 4.3. It is not, however, relevant for the physics analysis presented in this thesis. Relevant examples, which are typical of those available for other decay modes, are exclusive selections for the decays $D^0 \rightarrow K_s^0 h^+ h^-$ and, added in 2012, an inclusive selection of $D^{*+} \rightarrow D^0 \pi^+$ decays², where the D^0 meson is partially reconstructed from two charged particles. In all there were around 100 HLT2 selections in the 2011 configuration, 200 in 2012 and around 450 during 2015 data-taking. Illustrations of the trigger schemes used in 2011, 2012 and 2015 are shown in Fig. 4.1.

The HLT runs on the Event Filter Farm (EFF), a large processing farm situated at LHC Point 8, close to the experiment. The EFF for Run 2 consists of around 1800 nodes with a total of 27000 physical processing cores, allowing 50 000 instances of the HLT application to run simultaneously. Roughly half this capacity was available in Run 1.

The HLT has evolved significantly since data-taking began in 2010; this chapter will outline both the configuration used during 2011 and 2012, which is relevant for the physics

² D^{*+} implies the $D^*(2010)^+$ state if not otherwise stated.

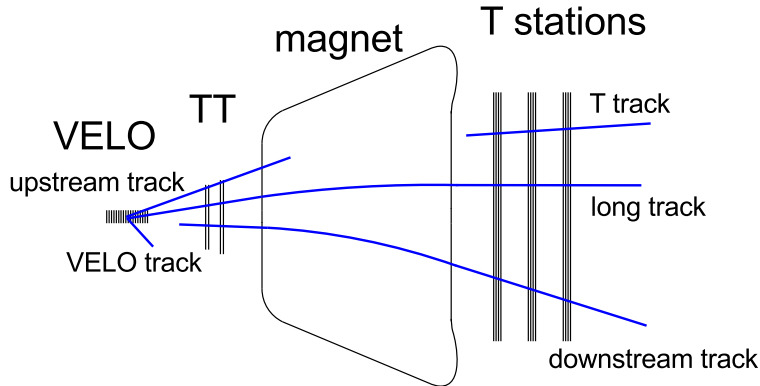


Figure 4.2: Illustration of the various track types that are reconstructed at LHCb. The decay products of b- and c-hadrons are typically reconstructed as *long* tracks. Long-lived s-hadrons such as K_S^0 mesons and Λ^0 baryons, which frequently exit the VELO before decaying, may additionally be reconstructed from pairs of *downstream* tracks. Figure taken from Ref. [133].

analyses presented in later chapters, and describe the substantial changes that have been made for Run 2.

4.1 Overview of the LHCb software trigger in Run 1

In Run 1, there were clear distinctions between the event reconstructions performed in HLT1, HLT2 and offline, with progressively more complex and CPU-intensive algorithms applied at each stage in order to improve efficiency and relax kinematic thresholds. The offline processing time was around 2 seconds per event [135], with the HLT executing around 50 times faster [108].

In all three cases the first step was to reconstruct VELO tracks. The different types of track reconstructed in LHCb are illustrated in Fig. 4.2. The offline algorithm was sufficiently fast to be run in HLT1, although a second iteration that included unused hits to improve the efficiency for tracks with large impact parameters (IPs) to the LHC beams was omitted in the HLT. In HLT1 the resulting tracks were used to reconstruct primary proton-proton interaction vertices (PVs). Due to the stringent timing requirements in HLT1, it was only possible to match a subset of VELO tracks to hits in the tracking stations. This subset consisted of tracks that were matched to muon chamber hits or had a significant IP with respect to all PVs. To further limit the processing time in HLT1, a narrow search window

in the tracking stations was used for each VELO track, which imposed a p threshold of 3–6 GeV/ c . A further p_T threshold of 0.5–1.25 GeV/ c was applied to VELO tracks not matched to hits in the muon system, and tracks that were matched to tracking station hits were fitted using a simplified Kalman filter [136]. In HLT1 a degradation of around 3 % was seen in the invariant mass resolution of $J/\psi \rightarrow \mu^+\mu^-$ with respect to the 15.1 MeV/ c^2 obtained offline.

The largest single contribution to the HLT1 output bandwidth was the inclusive beauty and charm trigger. This trigger is based on the properties of one high quality track, imposing a p_T threshold of around 1.6–1.7 GeV/ c and requiring that the track has a significant IP with respect to any PV. It was the most efficient trigger for physics channels that do not contain leptons in the final state [137], and its performance is illustrated in Fig. 4.3. Several other HLT1 triggers were used in Run 1, which, for example, applied requirements based on additional particle identification information to allow kinematic thresholds to be relaxed, or optimised these thresholds for specific physical processes. The total HLT1 output rate was around 40 kHz in 2011 [135] and 80 kHz in 2012 [108].

In HLT2 there was sufficient processing time to match all VELO tracks with $p > 3$ GeV/ c and $p_T > 300$ MeV/ c to hits in the tracking stations. A further step is included in the offline reconstruction: this searches in the opposite direction, extrapolating [138] track segments in the tracking stations upstream towards the VELO [139], but was not performed in HLT2 due to timing constraints. Muon identification was performed using the offline algorithm, and tracks were associated with ECAL clusters to identify electrons. Photon and π^0 candidates were also constructed, using clusters identified by the L0 calorimeter system. As shown in Fig. 4.1, the total HLT2 output rate was around 3.5 kHz in 2011 and 5 kHz in 2012. The performance of selected HLT2 lines is illustrated in Fig. 4.3.

Several important changes were made to the HLT between 2011 and 2012, as shown in Figs. 4.1a and 4.1b. As well as a modest increase in size of the EFF, a “deferral” scheme was introduced in 2012 [140, 141]. Averaged over a typical period of data collection, the LHC delivers stable beams around 30 % of the time, so, if the HLT were to operate fully synchronously with collisions, the EFF would sit idle for the remaining 70 %. To optimise

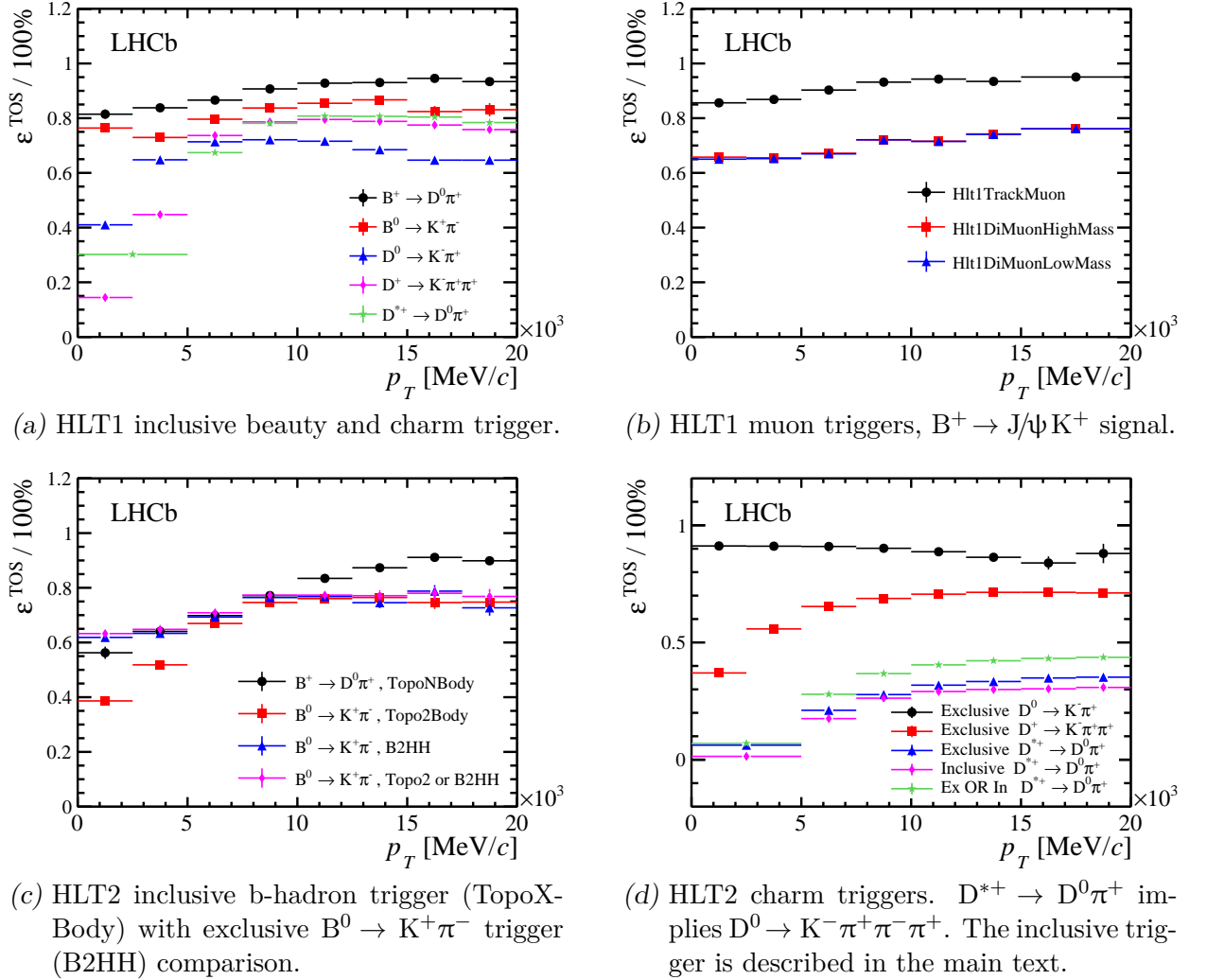


Figure 4.3: Illustrations of the performance of the HLT in Run 1. These show the efficiency of the main inclusive HLT1 (upper left), HLT1 muon (upper right), inclusive HLT2 b-hadron (lower left) and HLT2 charm hadron (lower right) triggers as a function of signal candidate p_T . These show that, for example, the inclusive selections are each $> 90\%$ efficient on high- p_T $B^+ \rightarrow D^0\pi^+$ candidates. Figures taken from Ref. [108].

the use of EFF resources, around 20 % of the events accepted by the L0 trigger were saved to local hard drives of the EFF nodes in 2012. The HLT processed these events later, when the LHC was not providing stable beams.

The deferral scheme effectively increased the CPU power of the EFF and allowed more processing time to be used for each event. Some of this extra time was used in HLT2 to reconstruct downstream tracks [142], which are defined in Fig. 4.2 and allow decay modes that produce K_s^0 and Λ^0 hadrons to be selected substantially more efficiently.

4.2 Overview of the *LHCb* software trigger in Run 2

The HLT underwent significant changes during LS1, the long LHC shutdown separating Run 1 and Run 2. Instead of deferring a fraction of the L0 trigger output, the entire output of HLT1 is saved to the EFF local disks in Run 2, as illustrated in Fig. 4.1c. This new mode of operation allows the detector to be aligned and calibrated [143] before HLT2 is executed, enabling HLT2 selections to make use of offline-quality reconstruction information, and ensuring optimal use is made of EFF resources. Improvements to the computing infrastructure permit more processing time to be allocated to each event in HLT2, and allow around twice as much data to be output by HLT2. The additional processing time is used to perform higher-quality reconstruction than the Run 1 HLT, including full reconstruction of the RICH detectors and calorimeter systems, which were only used sparingly in the Run 1 HLT2 due to timing constraints. The Run 2 HLT1 output rate is around 150 kHz, roughly double that in 2012, while the average processing time per event accepted by L0 has increased by around 25 % to 50 ms.

The reconstruction performed in the Run 2 HLT2 is of sufficiently high quality that no offline reconstruction is necessary for some data (the Turbo stream, Sect. 4.2.4), and this must only be performed once for the remaining data. In contrast, in Run 1 a second offline reprocessing was required after the detector alignment and calibration had been performed.

4.2.1 Incremental improvements

Several changes have been made to the tracking algorithms in Run 2, which allow a more complete reconstruction to be performed in HLT1. VELO tracks are now matched to hits in the TT stations, which lie in the fringes of the spectrometer magnetic field and allow a first estimate of track charge and momentum, with a relative uncertainty of around 20 % on the latter. This matching also reduces the number of fake VELO tracks. The charge estimate allows the search window in the downstream tracking stations to be reduced, which in turn allows the p_T threshold to be reduced to 500 MeV/ c from a typical value of 1.2 GeV/ c during

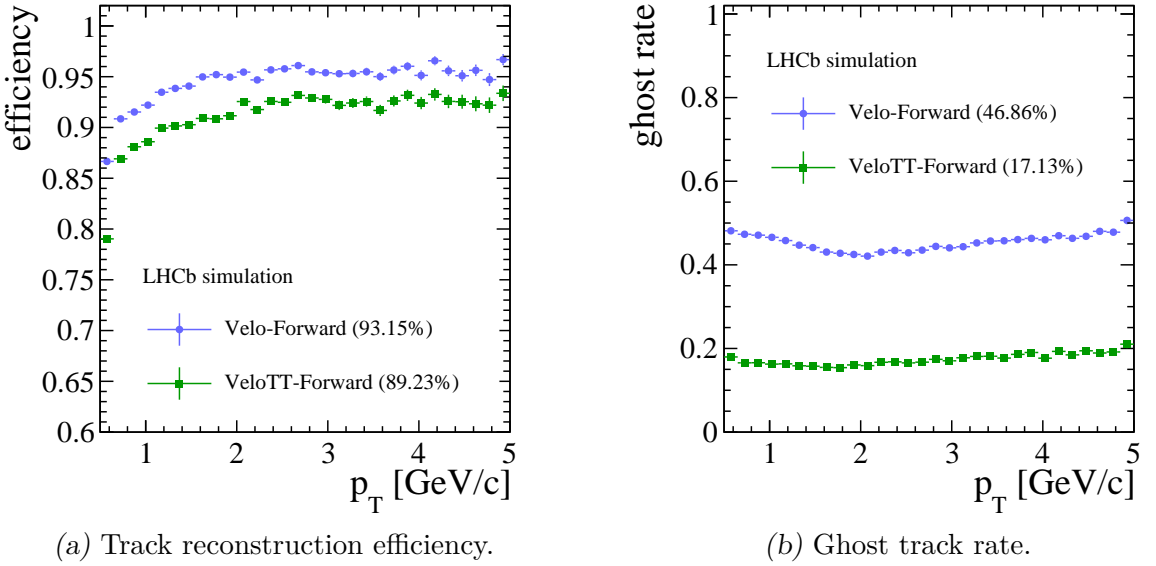


Figure 4.4: Comparison of the “VELO-Forward” tracking algorithm used in Run 1 with the “VELO-TT-Forward” algorithm used in Run 2 to find long tracks. “Forward” refers to the matching of VELO or VELO-TT tracks to hits in the downstream tracking stations. The Run 2 algorithm shows a small loss in efficiency (left) and a substantial reduction in the fraction of reconstructed tracks that are ghosts (right). Figure taken from Ref. [144].

Run 1. The change in long track reconstruction efficiency and ghost rate due to the inclusion of this TT hit matching step is illustrated in Fig. 4.4. The IP requirements present in Run 1 are also removed, which allows so-called “lifetime unbiased” selections to be constructed. These will be discussed later.

The PV reconstruction has also been altered for Run 2, so that it is based only on VELO tracks even in cases – such as the offline reconstruction – where long tracks are available. This means the same set of PVs is available from HLT1 to offline, reducing systematic uncertainties without degrading the vertex resolution. Several other changes have been made to the HLT reconstruction, which will not be listed in detail. The track reconstruction performed in HLT2 is now identical to that performed offline, and of comparable quality to the offline reconstruction used in Run 1.

4.2.2 Real-time alignment and calibration

The new real-time alignment and calibration of the LHCb detector is one of the most ambitious goals for Run 2, and is the first time such a procedure has been attempted at a comparable experiment. Only an overview of the process will be given here. The calibration is performed using candidates selected by HLT1, where special selections ensure that appropriate samples – which typically consist of D^0 and J/ψ mesons – are accumulated rapidly. Alignment and calibration constants are calculated automatically using these samples and, if significant changes are seen with respect to the previous constants, they are updated prior to HLT2 being executed. Systems that are aligned using this scheme include the VELO, tracking stations and RICH mirrors. Calibration of the RICH radiator refractive indices and OT detector time-alignment is also carried out automatically.

4.2.3 Additional reconstruction and information in HLT2

The improvements, discussed above, to the track reconstruction algorithms, and the provision of offline-quality alignment and calibration information, are important steps towards using a full offline-quality reconstruction in HLT2. However, to truly achieve this end, additional reconstruction algorithms are required.

The majority of physics analyses using the LHCb detector rely on PID information to distinguish charged particles of different species. While muon identification information has always been available throughout the trigger system, only limited calorimeter reconstruction has been performed in the trigger, and use of information from the RICH detectors was only used in isolated cases in Run 1 [145]. Starting in Run 2, the full offline-quality reconstruction of the RICH detectors and calorimeter system is included in the event reconstruction performed in HLT2. An example of the discrimination between kaons and pions that can be achieved in HLT2 using the RICH detectors is given in Fig. 4.5. In addition to using additional information from the detector, the additional processing time allocated to HLT2 allows multivariate classifiers to be calculated, which combine information from multiple sub-

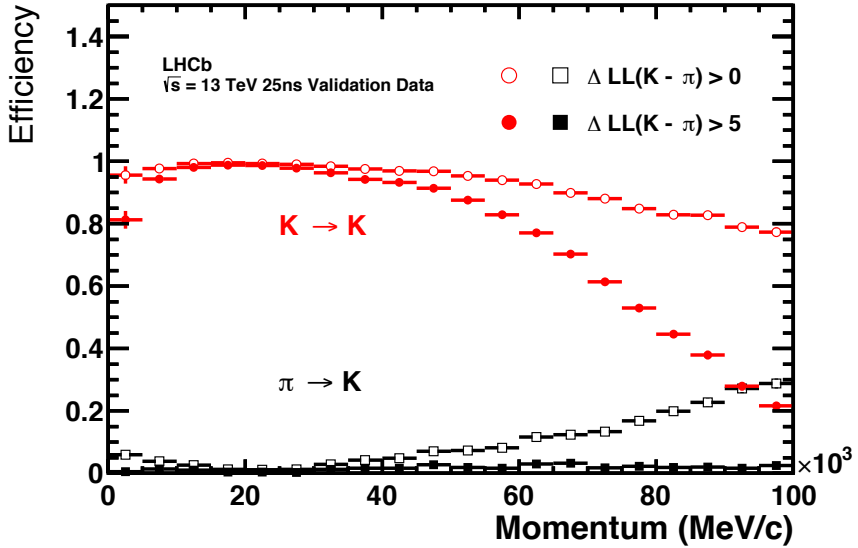


Figure 4.5: Illustration of $K-\pi$ separation performance in Run 2 data. Figure taken from Ref. [146].

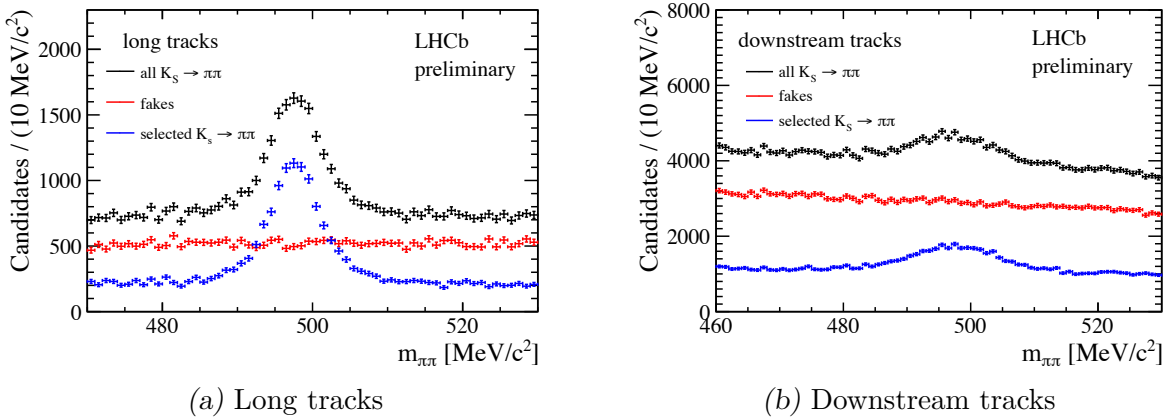


Figure 4.6: Performance of the Run 2 ghost probability multivariate classifier evaluated using $K_S^0 \rightarrow \pi^+\pi^-$ candidates formed using long (left) or downstream (right) tracks. Figures taken from Ref. [147].

detectors to provide improved discriminatory power. Examples include a “ghost probability” multivariate classifier, whose ability to discriminate real and fake charged particle tracks is illustrated in Fig. 4.6, and “ProbNN” artificial neural networks, which combine information from the entire detector and discriminate between different charged particle species.

4.2.4 New data streams

There have also been significant changes to the way data are saved by HLT2 in Run 2. These are a direct consequence of the far-reaching improvements to the event reconstruction

performed in HLT2, as for many analyses there is simply no need to perform a further, resource-intensive, offline reconstruction. To optimise the use of processing and storage capacity, the Run-2 HLT2 saves collision events in several different data streams:

- **Full** This is similar to Run 1, minimal information is saved from HLT2 and physics analysis depends on the offline reconstruction. It is typically used for signals that are not fully reconstructed in HLT2, such as b-hadron decays selected by the inclusive trigger, or for analyses that need to [re]-run dedicated event reconstructions, such as searches for very rare decays and modes with neutral particles.
- **Turbo** Sufficient information is saved from HLT2 that no offline reconstruction is required prior to physics analysis [148]. This stream is suitable for analyses that are fully reconstructed in HLT2 and do need the full reconstructed event information. In principle the raw event information is discarded to save storage space, although in practice this information was retained during 2015 data-taking.
- **TurboCalib** Information is saved from HLT2 as in the Turbo stream, but the raw event information is retained and the offline reconstruction is also performed. This consists exclusively of calibration selections for online monitoring and measurement of PID and tracking efficiencies.

Each HLT2 selection is assigned to one of these three streams, depending on its purpose. The key benefits of the new design are that events stored in the Turbo stream are around an order of magnitude smaller than those in the Full stream, and there is no need for offline reconstruction of events recorded in the Turbo stream. This allows HLT2 to retain a larger fraction of interesting events for a given set of offline computing constraints, allowing increased signal efficiencies, and makes Turbo stream data available for analysis very quickly after they have been processed by HLT2.

The first LHCb publications to use the Turbo stream were measurements of the charm, J/ψ and beauty production cross-sections at $\sqrt{s} = 13$ TeV [41, 42]. Illustrative distributions obtained from the Turbo stream in these measurements are given in Fig. 4.7.

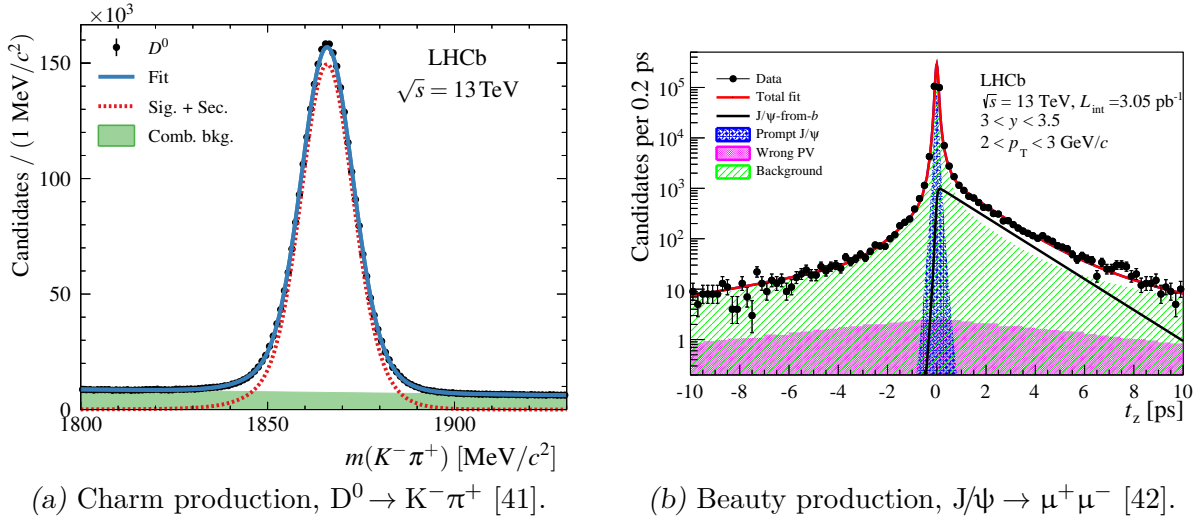


Figure 4.7: Examples of distributions obtained directly from the Turbo stream and HLT reconstruction in the 2015 measurements of charm and beauty production cross-sections.

4.2.5 Improvements to trigger selections

The various improvements to the HLT reconstruction discussed in the previous sections allow event selections to be defined in the HLT that are less biasing in quantities of interest, more efficient, accept fewer background events and require less processing time.

A key point is that the new information available in the HLT introduced in Sect. 4.2.3, particularly that from the RICH detectors, is almost uncorrelated with variables such as hadron decay time and the multi-body invariant masses that are often the key observables in physics analyses. In contrast, kinematic variables such as the smallest IP of a particle to any PV, which was a mainstay of many Run 1 trigger selections, are strongly correlated with these observables and lead to highly biasing selections. A simple example of an IP-requirement biasing a decay time distribution is given below in Fig. 4.9.

The “lifetime unbiased” selections, referred to in Sect. 4.2.1, fully reconstruct two-body decays without imposing IP requirements on the tracks, instead imposing a threshold on the decay time itself and using PID information to enhance signal purity. The result is a dataset where the reconstruction efficiency is, to leading order, a step function in measured decay time, enormously simplifying the subsequent analysis. Figure 4.8 illustrates the output of one of these trigger selections in data recorded by LHCb in 2015.

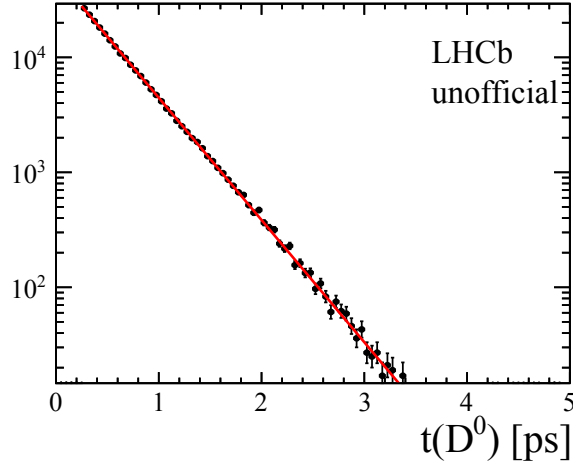


Figure 4.8: Decay time distribution of $D^{*+} \rightarrow D^0\pi^+$, $D^0 \rightarrow K^-\pi^+$ candidates selected by a “lifetime unbiased” trigger selection during 2015 data-taking. The red curve shows a fit to the data using a single exponential function, illustrating that the decay time acceptance is a step function to a good approximation as there are no data below the cut-off. Figure taken from Ref. [149].

Given that a large fraction of the LHCb physics programme concerns the study of multi-body decays of hadrons, it is worth noting that the number of combinations that must be considered when forming signal candidates for an N -body decay from a set of n reconstructed particles roughly scales as $\binom{n}{N}$. Selection requirements that act only on final state particles, for example using PID or ghost probability information can, therefore, lead to substantial savings in processing time. In Run 1, when these quantities were not available, IP requirements were typically used to control this combinatorial time.

Similarly to during Run 1, the HLT1 output rate is dominated by inclusive beauty and charm selections, however the implementation of these has changed substantially in Run 2. A new inclusive selection searches for two-track combinations that form a good quality vertex, and both the one- and two-track inclusive triggers use multivariate classifiers to improve performance [150]. In contrast, the Run 1 inclusive trigger used simple, rectangular, selection requirements. The same multivariate techniques have been applied to the re-optimisation of the inclusive b-hadron trigger in HLT2 for Run 2 [150].

In addition, significant effort has been invested in removing differences between the HLT1, HLT2 and offline reconstructions that were present in Run 1 and described in Sect. 4.1. This removes a class of systematic uncertainties that can be complex and tedious to evaluate.

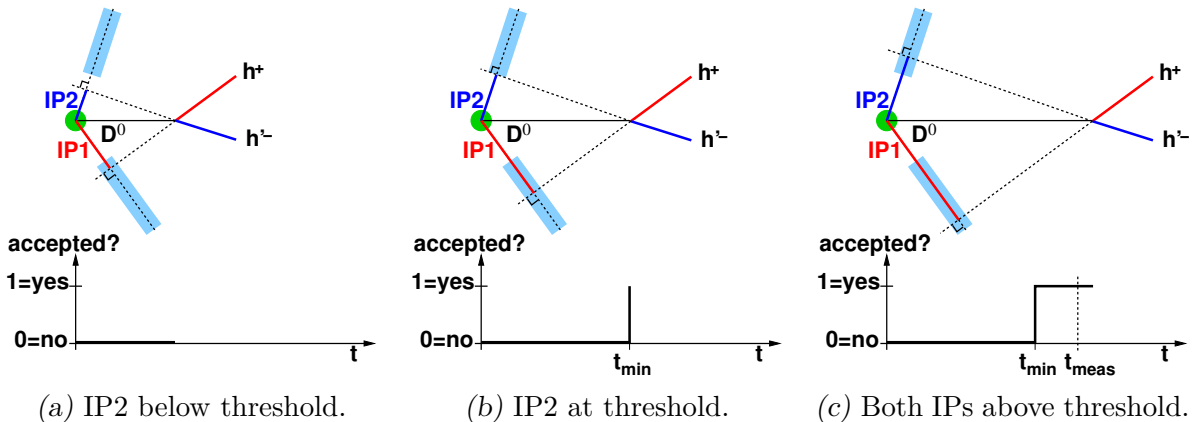


Figure 4.9: Illustration of the swimming technique, and the acceptance functions it produces. In this simplified example a selection that imposes thresholds on the minimum impact parameter (IP) to the D^0 production vertex of both child particles of a $D^0 \rightarrow h^+h^-$ candidate is swum. At small decay times (a), the h^- IP is too low and the candidate would not be accepted. At the intermediate decay time t_{\min} (b), the h^- IP reaches the threshold and the candidate would be accepted. The measured decay time, t_{meas} (c) lies in the accepted region, which extends to higher decay times. At some larger decay time, t_{\max} , the acceptance function will return to zero, creating a top-hat shape. Figure taken from Ref. [159].

4.3 The swimming technique

The so-called swimming technique is a data-driven method for calculating, as a function of decay time, the efficiency of a set of selection requirements that are correlated to decay time, such as the impact parameters (IPs) of final state particles with respect to primary proton-proton interaction vertices (PVs). It was pioneered at the NA11 spectrometer [151], further developed by the DELPHI and CDF collaborations [152–154], adapted for use at LHCb [155–157] and has been used in several LHCb publications [101, 158–160].

The swimming method measures, for each signal candidate, the ranges of decay time where the candidate would have passed the selection in question. By definition, the measured decay time lies inside one of these ranges. This is illustrated in Fig. 4.9. In LHCb this is implemented for signals that are produced promptly, *i.e.* where the production vertex of the long-lived signal coincides with the relevant PV, by coherently moving the entire set of PVs in the direction of the signal candidate momentum, thereby simulating the effect of alternative decay times. For each value of this displacement the selection is re-evaluated,

and a search algorithm identifies those decay time values where the decision changes. These values are known as turning points – an example is t_{\min} in Fig. 4.9b. It is necessary to move the whole set of PVs in each event to account for the possibility that, when alternative decay times are simulated, the signal candidate could be associated with a different PV.

When swimming the software trigger, the entire reconstruction is executed each time the PVs are moved. This is necessary when analysing Run 1 data, because particles reconstructed in HLT1 and HLT2 were not saved, and is possible because the software trigger decisions are reproducible offline with near-perfect precision. The offline reconstruction saves all reconstructed particles and PVs, so selection requirements based on these particles and vertices can be swum without executing the reconstruction each time the PVs are moved.

The result of the swimming process is, therefore, a series of turning points, which can be combined to produce a decay time efficiency function $\varepsilon(t)$ for each candidate. In principle this can be inserted into a fit to the decay time distribution simply by modification of the PDF normalisation range used for each candidate. However, in practice, additional corrections must be included and a more complex scheme is required. These corrections will be outlined in Chapter 7, where the swimming technique is applied to $D^0 \rightarrow K_s^0 K^+ K^-$ decays.

4.4 Particle identification in HLT2

As has already been introduced in Sect. 4.2.3, particle identification (PID) information is an important part of LHCb physics analyses, and as of Run 2 powerful PID is available in HLT2, as well as offline.

This extensive use of PID variables as selection criteria in LHCb analyses – in both LHC runs – has necessitated the development of data-driven methods for measuring the performance of such requirements. The obvious alternative, measuring performance from simulated samples, is undesirable as the PID variables are known to be poorly reproduced in the LHCb Monte Carlo simulation, and for some purposes it is difficult to accumulate a sufficiently large sample of simulated events. The data-driven methods are based on cali-

bration samples; pure samples of charged tracks of different species that have been selected without the use of PID information from the RICH, calorimeter or muon systems. In addition to being used in physics analyses, these samples can be employed to monitor temporal variations in performance, and to study future improvements in reconstruction algorithms.

In Run 2, the requirements for the calibration samples have become more stringent. A more complete discussion is given in Ref. [161], but in brief the widespread use of PID variables in HLT2, which may have small differences with respect to the same variables calculated offline, means that the calibration samples must contain both HLT2-calculated and offline-calculated PID variables on a track-by-track basis. These differences are small, and confined to variables based on calorimeter information, in data recorded in 2015, but future improvements in the offline algorithms could enhance the differences in future re-analysis of these data.

In order to satisfy the various requirements, the strategy for Run 2 is to select the calibration samples directly in HLT2 and send them through a dedicated data processing stream. This stream, dubbed TurboCalib, was introduced in Sect. 4.2.4 and can be used to produce calibration samples containing both HLT2-calculated and offline-calculated PID variables for each charged particle.

4.4.1 PID calibration datasets

The PID calibration datasets consist of large, pure samples of the main five charged, long-lived particles produced in LHCb: kaons, pions, protons, electrons and muons. Generally low-multiplicity decay modes with large branching fractions are chosen; an overview of the utilised modes is given in Table 4.1. Some decays, such as the $D^{*+} \rightarrow D^0\pi^+$, $D^0 \rightarrow K^-\pi^+$ decay chain, which is the primary source of kaon and pion calibration tracks, are selected without the use of PID variables. Other modes, such as the $J/\psi \rightarrow \mu^+\mu^-$ decays used to obtain muon calibration samples, rely on a “tag-and-probe” method where particle identification requirements are made on one of the two muons. In all cases the selections are designed to ensure the L0 and HLT1 triggers do not bias the distributions of PID variables

Table 4.1: Overview of decay modes that are used to select calibration samples. Hard (soft) refers to calibration tracks with high (low) p and p_T .

Species	Soft	Hard
e^\pm	—	$J/\psi \rightarrow e^+e^-$
μ^\pm	$D_s^+ \rightarrow \mu^+\mu^-\pi^+$	$J/\psi \rightarrow \mu^+\mu^-$
π^\pm	$K_s^0 \rightarrow \pi^+\pi^-$	$D^* \rightarrow D^0\pi^+, D^0 \rightarrow K^-\pi^+$
K^\pm	$D_s^+ \rightarrow K^+K^-\pi^+$	$D^* \rightarrow D^0\pi^+, D^0 \rightarrow K^-\pi^+$
p	$\Lambda^0 \rightarrow p\pi^-$	$\Lambda^0 \rightarrow p\pi^-, \Lambda_c^+ \rightarrow pK^-\pi^+$

in the calibration samples.

The calibration samples are selected directly in HLT2 in Run 2, in contrast to Run 1 when the samples were selected offline. One reason for this, discussed in Sect. 4.4, is that the use of PID variables in the Run-2 HLT2 is much more widespread than Run 1. Another reason is that the selection efficiency for some calibration modes can be greatly improved. For example, due to the large production cross section it is essential to discard the majority of $\Lambda^0 \rightarrow p\pi^-$ candidates, but this can be done in a biased manner that enhances the population of high p_T protons, which are most valuable for calibration purposes. This is illustrated in Fig. 4.10, where the Run 2 kinematic coverage is expected to match that required for studies of b- and c-hadron decays more closely than that of Run 1. Figure 4.11 shows some representative examples of invariant mass distributions in the calibration samples, illustrating that dedicated HLT2 selections can isolate these modes with high purity even without PID selection requirements.

4.4.2 Trigger decorrelation

Because information from the calorimeter and muon systems is included in the L0 and HLT1 triggers, care is required to ensure that the calibration samples selected in HLT2 are not biased by the earlier trigger stages. An absence of bias allows the PID and trigger contributions to total efficiencies to be factorised in physics analyses.

In this discussion, and in subsequent chapters of this thesis, it will be useful to introduce the terms TIS (Trigger Independent of Signal) and TOS (Trigger on Signal) [135]. These are used to categorise signal candidates according to what role they played in previous stages of

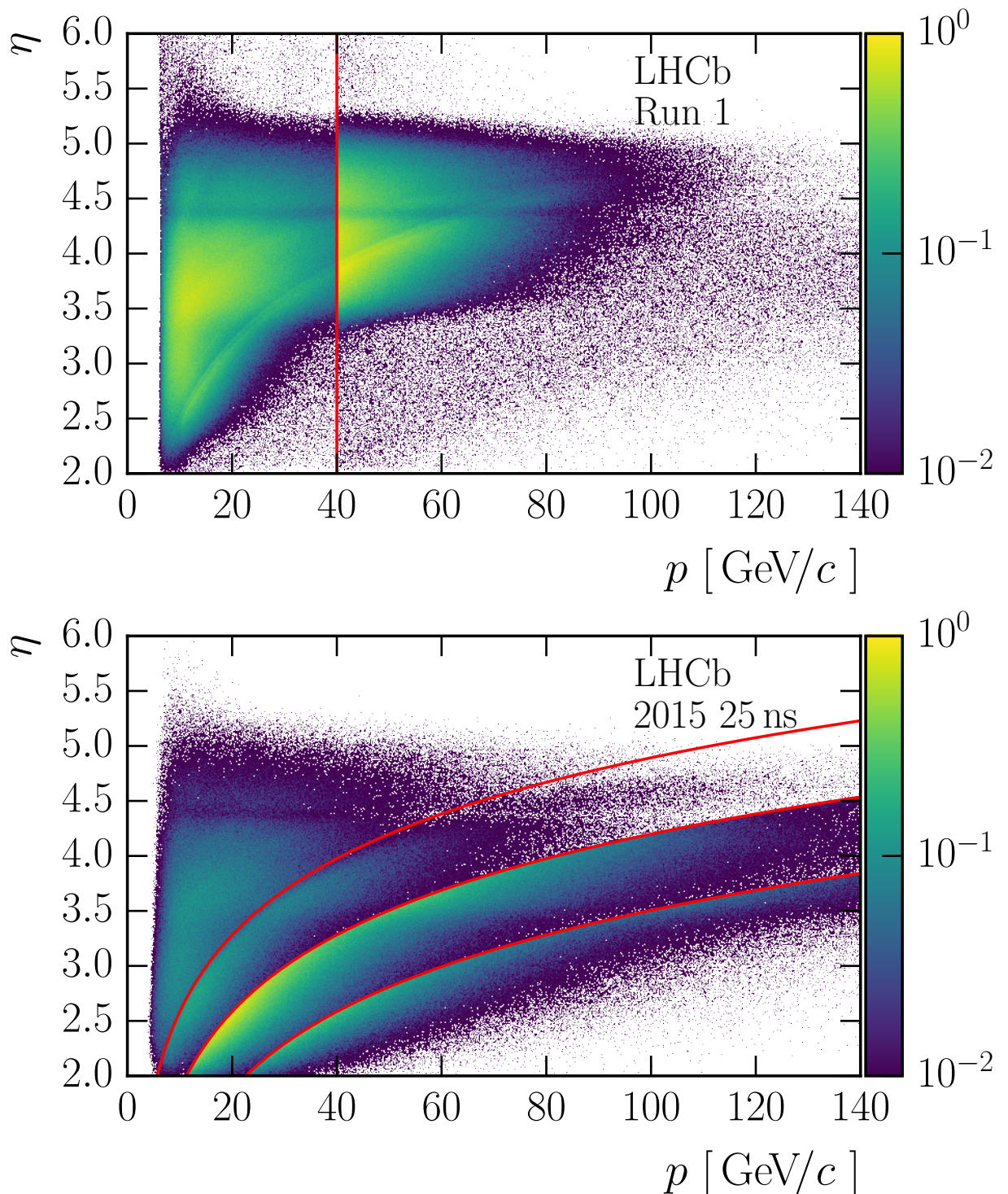


Figure 4.10: Distributions of proton calibration track pseudorapidity, η , and momentum, p . The upper distribution shows the coverage of the Run 1 calibration samples, with the vertical red line highlighting a boundary below which the statistics were artificially suppressed. The lower distribution shows the sample recorded during 2015; the red lines correspond to p_T thresholds of 1.5, 3.0 and 6.0 GeV/ c , where the first threshold comes from HLT1 and the latter two are imposed by the HLT2 selections. The z -units are arbitrary.

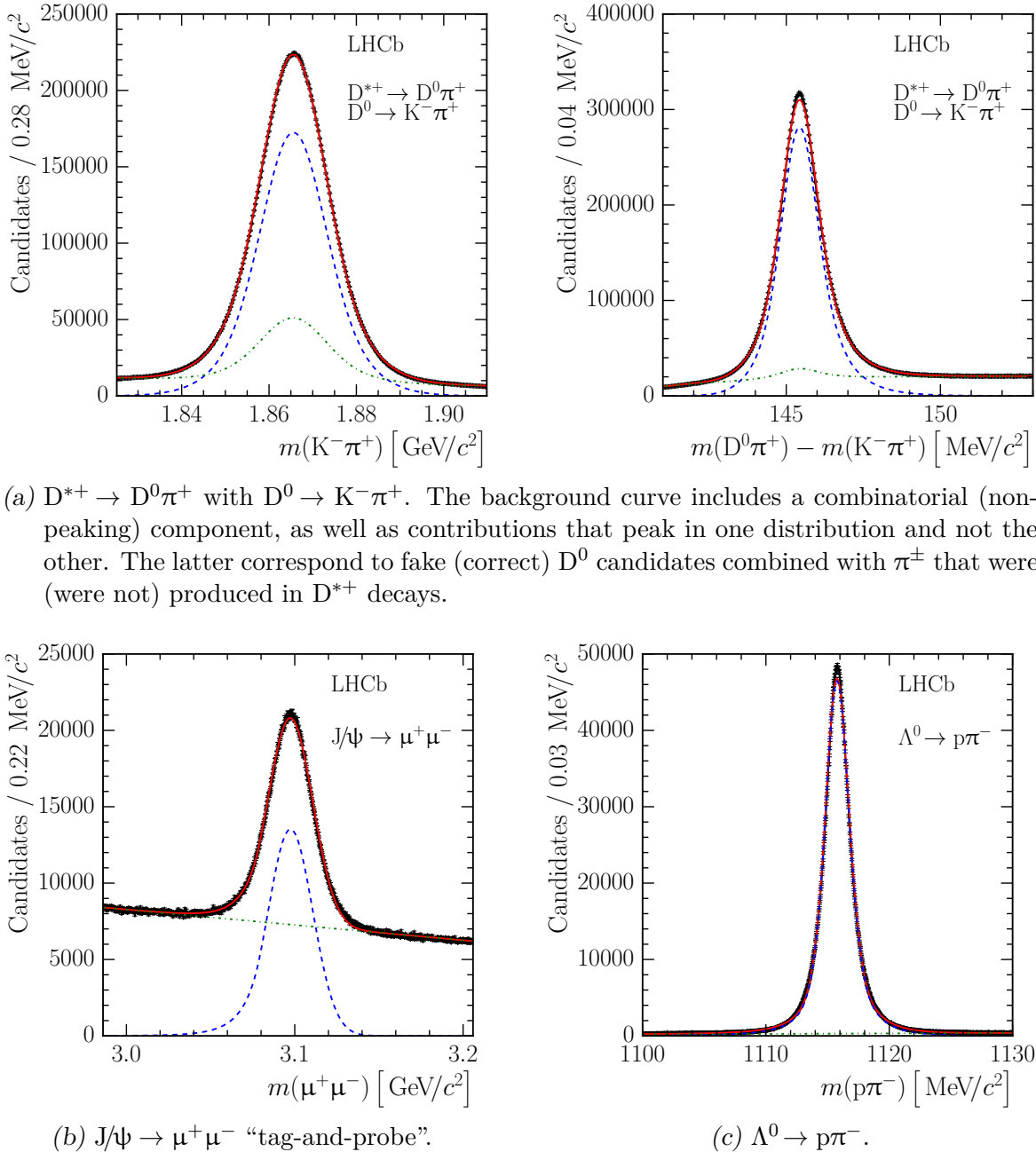


Figure 4.11: Invariant mass distributions in calibration data selected without PID information (a, c) or with a “tag-and-probe” method (b). In all cases the data were recorded during 2015, the dashed (blue) curve shows the signal contribution and the dash-dotted (green) curve shows the background contribution, which is purely combinatorial if not otherwise noted.

the trigger system, *e.g.* in an HLT1 selection a signal candidate may be only TIS and/or TOS with respect to L0, while in an HLT2 selection TIS and TOS can be defined with respect to both L0 and HLT1. A signal candidate is TOS with respect to a particular trigger selection if the candidate alone would be sufficient to produce a positive selection decision. Similarly a signal candidate is TIS with respect to a particular trigger selection if the selection decision is not contingent on any track or deposit in the detector associated with the candidate. This categorisation is possible at LHCb because each trigger stage stores the set of detector hits that contributed to each selection decision. The TIS and TOS status of a signal candidate is evaluated by matching it to these sets of hits.

Precisely what selection requirements are required to avoid problematic correlations in the PID calibration samples depends on the mode in question, and which PID variables are to be studied. This is illustrated in the following examples:

- **Muons** Information from the muon detectors is used in both the L0 and HLT1 triggers, so the charged track used to measure PID performance is required to be TIS with respect to both L0 and HLT1. In line with the definition above, this means that the L0 and HLT1 decisions would still have been positive if the detector hits associated with the muon track in question were removed. The primary source of muons for the calibration samples is the decay $J/\psi \rightarrow \mu^+\mu^-$; in a typical event the two muons will be well-separated in the muon detectors, one will be responsible for triggering L0 and HLT1 and the other will be used for calibration purposes. The selections for electrons are defined similarly.
- **Kaons** Separation of charged hadrons is wholly performed by the RICH detectors. Information from the RICHes is not used in L0 or HLT1, so for some purposes it is acceptable to use kaon tracks for calibration that are not TIS with respect to L0 and HLT1. The primary source of kaons for the calibration samples is the decay chain $D^{*+} \rightarrow D^0\pi^+$, $D^0 \rightarrow K^-\pi^+$; in typical events the hardware trigger, L0, will be triggered either by calorimeter deposits from the charged hadrons (TOS) or by other particles in the event (TIS). HLT1 will typically be triggered by one, or both, of the D^0 decay

products via a selection that makes use of information from the tracking detectors only.

4.5 Summary

The software trigger is a critical part of the LHCb detector, which has performed well for all data-taking to date. Various changes during data-taking in Run 1, such as the deferral scheme introduced in 2012 and described in Sect. 4.1, have demonstrated the value and flexibility of a software-based trigger system. This flexibility is also manifested in the swimming technique that can be used to determine decay time acceptance functions, which is critically dependent on the ability to precisely reproduce trigger decisions during offline analysis.

Significant changes have been made to the software trigger in advance of Run 2, with a full event reconstruction of comparable quality to the Run 1 offline reconstruction now available in HLT2. A key ingredient that has made this possible is a new framework for real-time alignment and calibration, which had not previously been attempted at any comparable experiment. This signals the beginning of a shift in paradigm towards real-time physics analysis and away from the older model of offline alignment, calibration, reconstruction, event selection and analysis.

One substantial addition to HLT2 is the full reconstruction of data from the RICH detectors, which has necessitated several changes to the framework for data-driven measurements of particle identification performance and monitoring of detector performance. The samples used for these measurements are now selected directly in HLT2, which has several benefits with respect to the offline sample selection used in Run 1. New calibration modes and selections have been included in order to improve the statistics and kinematic coverage of the calibration samples.

5. SELECTION OF $D^0 \rightarrow K_s^0 h^+ h'^-$ DECAYS

The two studies of $D^0 \rightarrow K_s^0 h^+ h'^-$ decays ($h, h' = K, \pi$) presented in this thesis use the data sample recorded at LHCb during Run 1 of the LHC, and much of the candidate selection is common to both analyses. The work that relates specifically to the $D^0 \rightarrow K_s^0 K^\pm \pi^\mp$ modes has been published in Ref. [162], while that relevant to the mixing study using $D^0 \rightarrow K_s^0 K^+ K^-$ decays has not been published. It should be noted that the $D^0 \rightarrow K_s^0 K^\pm \pi^\mp$ amplitude analysis is based on the full sample of pp collisions recorded during 2011 and 2012, which corresponds to an integrated luminosity of 3 fb^{-1} , while the mixing study uses only those Run 1 data recorded in 2012. This reduced sample corresponds to an integrated luminosity of around 2 fb^{-1} , but due to improvements in the trigger system it contains a large majority, around 90 %, of the signal candidates recorded during Run 1. These improvements include the addition of downstream track¹ reconstruction to HLT2, an increase in HLT1 retention and the addition of an inclusive $D^{*+} \rightarrow D^0 \pi^+$ trigger. The mixing analysis also includes a preliminary study of data recorded during Run 2, using a sample corresponding to an integrated luminosity of around 280 pb^{-1} recorded in late 2015. The following sections describe the selection strategy used for data recorded in Run 1, with the brief study of Run 2 data confined to Sect. 5.5.1.

5.1 Strategy outline

The offline selection used in these analyses reconstructs the decay chain $D^{*+} \rightarrow D^0 \pi_{\text{slow}}^+$ with $D^0 \rightarrow K_s^0 h^+ h'^-$, where the charged pion π_{slow}^+ from the D^{*+} decay tags the flavour of the neutral D-meson, and the K_s^0 meson is reconstructed from a pair of either long or downstream

¹ The various track types were defined in Chapter 4, Fig. 4.2.

tracks. The charged pion originating in the D^{*+} decay is referred to as ‘slow’ due to the small Q -value of the reaction. One charged particle in the decay chain is required to pass an inclusive single track selection in HLT1, and the signal candidate is required to pass one of two selections in HLT2. The first of these reconstructs the decay chain $D^{*+} \rightarrow D^0 \pi_{\text{slow}}^+$ with $D^0 \rightarrow h^\pm h'^\pm X$, where X refers to any number of additional particles. The second selection fully reconstructs the decay $D^0 \rightarrow K_s^0 h^+ h^-$ without flavour tagging, using either long or downstream tracks to form K_s^0 candidates. During 2011 data-taking the first selection, and the version of the second that uses downstream tracks, were not available.

Signal candidates are formed offline and required to pass a cut-based preselection as part of the centralised processing described in Sect. 3.3. Further cut-based offline selection requirements, which are specific to the analysis in question, are applied before fits to $m(K_s^0 h^+ h^-)$ and $\Delta m \equiv m(K_s^0 h^+ h^- \pi_{\text{slow}}^+) - m(K_s^0 h^+ h^-)$ are carried out to extract signal and other yields of interest.

5.2 Trigger strategy and preselection

The first stage of selection is the hardware trigger, L0, which was described in Sect. 3.2.8. Candidates may pass this in one of two ways: the candidate can fire the hadronic trigger directly (TOS) or, alternatively, other particles in the event may fire L0, so the signal candidate is TIS².

While the hardware trigger does lead to some variation in efficiency across the D^0 decay phase space, which it is important to model correctly, none of the L0 selection criteria are sensitive to the D^0 decay time, and so this trigger does not require special treatment in time-dependent measurements.

Only one route through HLT1 is considered, the inclusive single track beauty and charm trigger described in Sect. 4.1. This requires that at least one charged particle from the signal candidate was reconstructed in HLT1 and passes several track quality and kinematic

² TIS and TOS were defined in Sect. 4.4.2.

thresholds, as well as having a significant IP to any PV [163]. This IP requirement strongly biases the D^0 decay time distribution, reducing efficiency in the low decay time region.

As outlined above, two types of HLT2 selection are considered for $D^0 \rightarrow K_s^0 h^+ h^-$ candidates. Unfortunately, the exclusive $D^0 \rightarrow K_s^0 h^+ h^-$ trigger that forms K_s^0 candidates using downstream tracks suffered several issues during Run 1 operation. This selection was not present during 2011 data taking, and a numerical precision issue prevented it from recording data in the early part of 2012. Additionally, a software issue imposed a more stringent displacement requirement on the positively charged D^0 child particle than its negative counterpart, leading to asymmetric acceptance effects.

Signal candidates are also required to satisfy several offline requirements. These differ between the $D^0 \rightarrow K_s^0 K^\pm \pi^\mp$ amplitude analysis and $D^0 \rightarrow K_s^0 K^+ K^-$ mixing study, and will be described in detail separately. In general terms, the offline selection requirements add information from the RICH detectors, which was not widely used in the software trigger during Run 1, benefit from the improved offline alignment and calibration, and suppress cross-feed background contributions using targeted selection requirements.

In the $D^0 \rightarrow K_s^0 K^\pm \pi^\mp$ analysis, information from the RICH detectors is used to ensure that the charged kaon is well-identified, which reduces the background contribution from the decays $D^0 \rightarrow K_s^0 \pi^+ \pi^- \pi^0$ and $D^0 \rightarrow K_s^0 \pi^- \mu^+ \nu_\mu$. In addition the K_s^0 decay vertex is required to be well-separated from the D^0 decay vertex in order to suppress the $D^0 \rightarrow K^- \pi^+ \pi^+ \pi^-$ background, where a $\pi^+ \pi^-$ combination is close to the K_s^0 mass. D^0 candidates are required to have decay vertices well-separated from any PV, and to be consistent with originating from a PV. This selection suppresses the semileptonic and $D^0 \rightarrow K^- \pi^+ \pi^+ \pi^-$ backgrounds to negligible levels, while a small contribution from $D^0 \rightarrow K_s^0 \pi^+ \pi^- \pi^0$ remains in the Δm distribution. The various selection requirements are summarised in Table 5.1. If multiple signal candidates remain in any event then one is selected at random, resulting in a loss of around 0.7%.

In the mixing study great care must be taken to ensure that the D^0 meson decay time bias induced by any selection requirements is understood. The biasing effects of the software

Table 5.1: Offline selection requirements imposed on $D^0 \rightarrow K_s^0 K\pi^\pm$ signal candidates prior to the $m(K_s^0 K\pi)$ and Δm fits used to extract various yields. The $DLL_{K\pi}$ requirement is not applied to simulated data, where a data-driven weighting is applied instead. In addition, to ensure good overlap with the calibration samples used to calculate these weights, it is required that all five charged particles in the final state are inside the RICH detector acceptance and satisfy $2 < p < 120 \text{ GeV}/c$ and $1.5 < \eta < 5.0$. χ^2_{IP} (χ^2_{VS}) is a variable indicating the change in χ^2 of the given vertex fit if the particle (children of the particle) in question were included in the fit.

1.805	$<$	$m(K_s^0 K\pi)$	$<$	1.925	GeV/ c^2
139	$<$	Δm	$<$	153	MeV/ c^2
$D^0 \chi^2_{IP}$ to PV	$<$	10	(D^0 consistent with originating at PV)		
$D^0 \chi^2_{VS}$ to PV	$>$	100	(D^0 decay vertex well-separated from PV)		
$K_s^0 \chi^2_{VS}$ to D^0	$>$	100	(K_s^0 and D^0 decay vertices well-separated)		
K^\pm $DLL_{K\pi}$	$>$	5	(K^\pm hypothesis favoured over π^\pm hypothesis)		

Table 5.2: Offline selection requirements imposed on $D^0 \rightarrow K_s^0 K^+ K^-$ signal candidates prior to the $m(K_s^0 KK)$ and Δm fits used to extract various yields. In addition the K^\pm and π_{slow}^+ particles are required to satisfy the fiducial requirements $3 < p < 100 \text{ GeV}/c$ and $1.5 < \eta < 5.0$, which ensures good overlap with the PID calibration samples, while the D^0 candidate must satisfy $30 < p < 250 \text{ GeV}/c$ and $2.0 < \eta < 4.4$ to stabilise a re-weighting procedure for simulated events.

1.81	$<$	$m(K_s^0 KK)$	$<$	1.92	GeV/ c^2
140	$<$	Δm	$<$	153	MeV/ c^2
K^\pm “ProbNNk”	$>$	0.1	(K^\pm consistent with kaon mass hypothesis)		
π_{slow}^+ “ProbNNpi”	$>$	0.3	(π_{slow}^+ consistent with pion mass hypothesis)		
K^\pm, π^\pm “GhostProb”	$<$	0.4	(D^0 descendant tracks inconsistent with ghost hypothesis)		

trigger and offline preselection requirements are calculated using the swimming technique described in Sect. 4.3. It is possible to “swim” additional offline requirements, provided these are consistent with the assumptions of the swimming technique, but in order to reduce complexity it is preferable to avoid this and only introduce requirements that do not bias the decay time distribution. For the mixing study only two additional requirements that require swimming are introduced. One of these mitigates two software issues in one of the HLT2 selections, and the other suppresses the contribution from secondary D decays by requiring that the signal candidate is consistent with originating at a PV. These will be discussed further in Sect. 7.2. A further loose selection is applied before the $m(K_s^0 KK)$ and Δm fits are carried out, which consists only of requirements that do not bias the decay time distribution. This is summarised in Table 5.2.

A kinematic fit [164] is applied to the reconstructed D^{*+} decay chain to enhance the resolution in $m(K_s^0 h^+ h'^-)$, Δm , $m(K_s^0 h^+)$, $m(K_s^0 h'^-)$ and $m(h^+ h'^-)$. The two-body invariant masses are used to probe the resonant structure of these decays in the $D^0 \rightarrow K_s^0 K^\pm \pi^\mp$ amplitude analysis, while the mixing study is binned in these variables. This fit is configured differently for the two analyses. In the $D^0 \rightarrow K_s^0 K^\pm \pi^\mp$ analysis the D^{*+} decay vertex is constrained to coincide with the closest PV. This significantly improves the resolution in Δm for prompt decays, but distorts the distribution for secondary D decays in a decay-time-dependent manner. This distortion cannot be accounted for by the swimming algorithm implementation used at LHCb, and therefore the D^{*+} vertex is not constrained in the mixing study. In all cases the K_s^0 candidate mass is constrained to its known value [54] and a data-driven momentum scale correction [165] is applied.

Signal yields and estimates of the various background contributions in the signal window are determined using unbinned maximum likelihood fits to the $m(K_s^0 h^+ h'^-)$ and Δm distributions. The three categories of interest that can be distinguished by these fits are D^{*+} signal decays, mistagged background where a correctly reconstructed D^0 meson is combined with a charged pion that incorrectly tags the D^0 flavour, and a combinatorial background category. The fit details differ between the amplitude analysis and mixing study, and these are discussed separately in Sects. 5.3 and 5.5.

5.3 $D^0 \rightarrow K_s^0 K^\pm \pi^\mp$ amplitude analysis yield extraction

In the amplitude analysis of $D^0 \rightarrow K_s^0 K^\pm \pi^\mp$ decays the various contributions in the signal window are extracted using a series of maximum likelihood fits. The signal window is defined as the region less than $18 \text{ MeV}/c^2$ ($0.8 \text{ MeV}/c^2$) from the peak value of $m(K_s^0 K\pi)$ (Δm), corresponding to approximately three standard deviations of each signal distribution. The sidebands of the $m(K_s^0 K\pi)$ distribution are defined as those parts of the fit range where $m(K_s^0 K\pi)$ is more than $30 \text{ MeV}/c^2$ from the peak value. The distribution of signal candidates in $m(K_s^0 K\pi)$ and Δm is shown in Fig. 5.1, where the contribution from D^0 mesons associated with a random slow pion to form a fake D^{*+} candidate is clearly visible as a horizontal

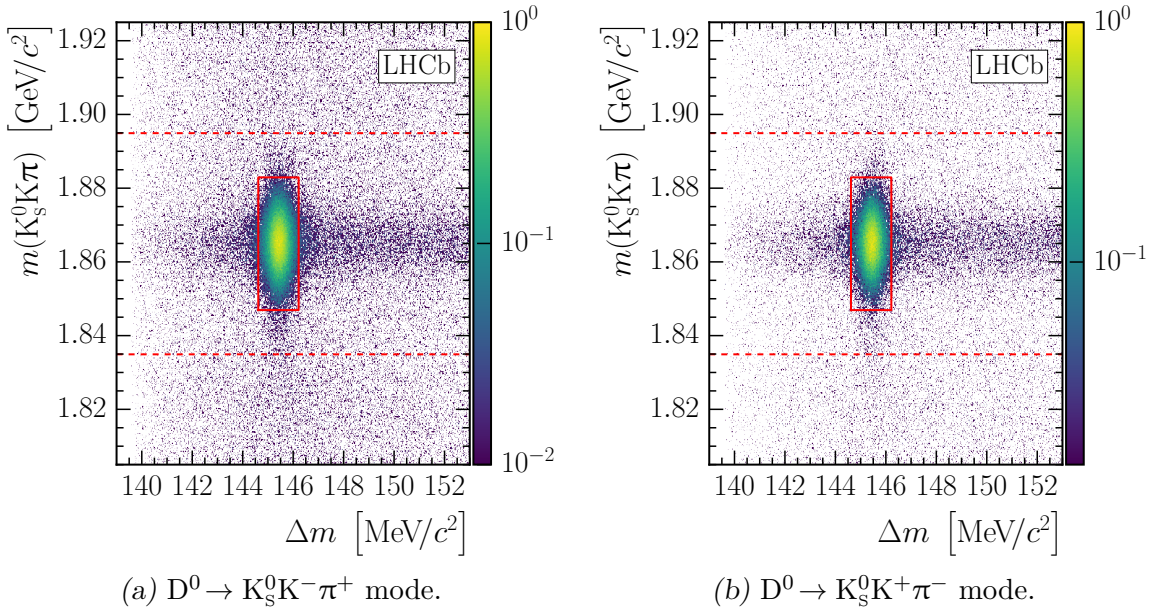


Figure 5.1: Distributions in $m(K_s^0 K\pi)$ and Δm of the signal candidates selected in the amplitude analysis of $D^0 \rightarrow K_s^0 K^\pm \pi^\mp$ decays. The signal region is indicated by the solid curve. The dashed lines indicate the sideband regions of $m(K_s^0 K\pi)$. The z -units are arbitrary.

band. The $m(K_s^0 K\pi)$ and Δm distributions are fitted to determine the D^0 and D^{*+} yields, respectively, in the two-dimensional signal region [166]. In each case the fit is performed using data in the signal region of the other variable. The D^{*+} (D^0) signal shape in the Δm ($m(K_s^0 K\pi)$) distribution is modelled using a Johnson S_U [167] (Cruijff [168]) function. In the $m(K_s^0 K\pi)$ distribution the combinatorial background is modelled with an exponential function, while in Δm a power law function is used,

$$f(\Delta m; m_\pi, p, P, b) = \left(\frac{\Delta m - m_\pi}{m_\pi} \right)^p - b^{p-P} \left(\frac{\Delta m - m_\pi}{m_\pi} \right)^P, \quad (5.1)$$

with the parameters p , P and b determined by a fit in the $m(\text{K}_s^0\text{K}\pi)$ sidebands. The small $\text{D}^0 \rightarrow \text{K}_s^0\pi^+\pi^-\pi^0$ contribution in the Δm distribution is described by a Gaussian function and absorbed into the combinatorial background yield. The fit component corresponding to D^0 mesons associated with a random slow pion is the sum of an exponential function and a linear term. These fits are shown in Fig. 5.2. The results of the fits are used to determine the yields of interest in the two-dimensional signal region. These yields are given in Table 5.3 for both decay modes, together with the fractions of backgrounds.

Table 5.3: Signal yields and estimated background rates in the two-dimensional signal region. The larger mistag rate in the $D^0 \rightarrow K_s^0 K^+ \pi^-$ mode is due to the different branching fractions for the two modes. Only statistical uncertainties are quoted.

Mode	Signal yield	Mistag background [%]	Combinatorial background [%]
$D^0 \rightarrow K_s^0 K^- \pi^+$	$113\,290 \pm 130$	0.89 ± 0.09	3.04 ± 0.14
$D^0 \rightarrow K_s^0 K^+ \pi^-$	$76\,380 \pm 120$	1.93 ± 0.16	2.18 ± 0.15

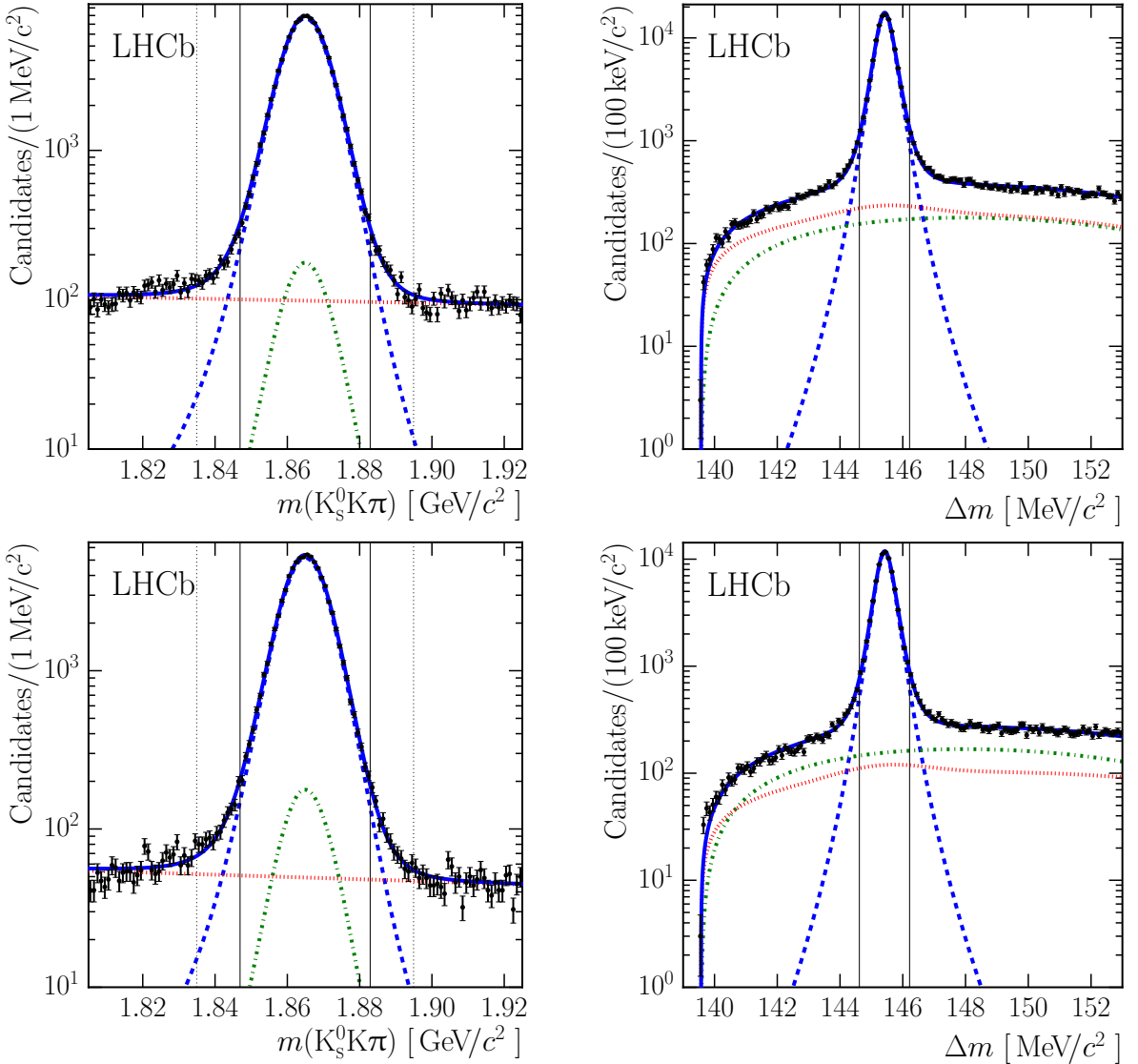


Figure 5.2: Mass (left) and Δm (right) distributions for the $D^0 \rightarrow K_s^0 K^- \pi^+$ (top) and $D^0 \rightarrow K_s^0 K^+ \pi^-$ (bottom) samples with fit results superimposed. The long-dashed (blue) curve represents the D^{*+} signal, the dash-dotted (green) curve represents the contribution of real D^0 mesons combined with incorrect π_{slow}^+ and the dotted (red) curve represents the combined combinatorial and $D^0 \rightarrow K_s^0 \pi^+ \pi^- \pi^0$ background contribution. The vertical solid lines show the signal region boundaries, and the vertical dotted lines show the sideband region boundaries. The residual distributions (not shown) indicate a good quality of fit, including in the peak.

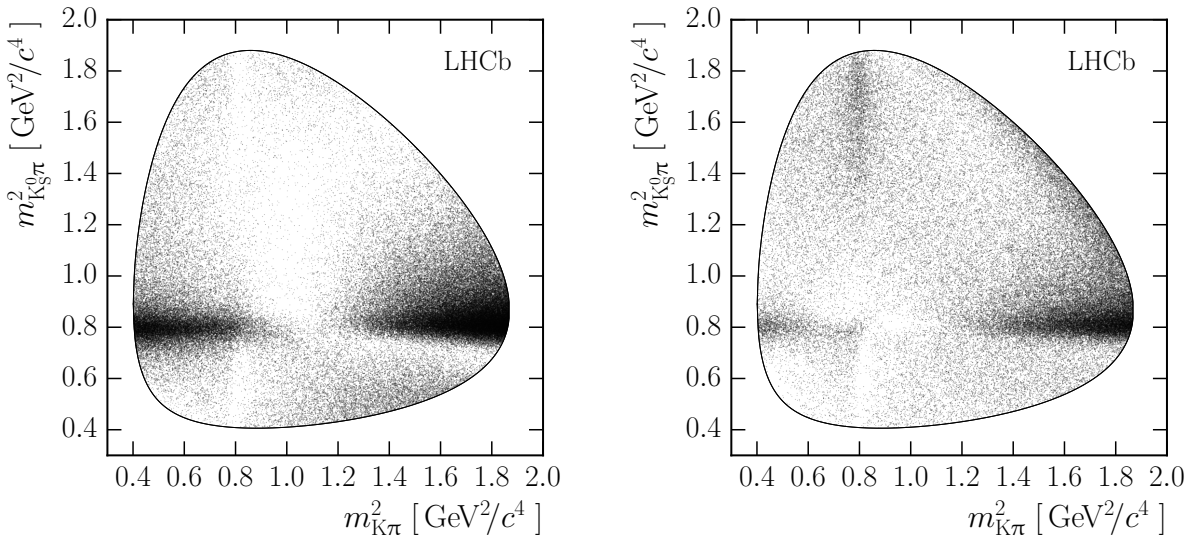


Figure 5.3: Dalitz plots of the $D^0 \rightarrow K_s^0 K^- \pi^+$ (left) and $D^0 \rightarrow K_s^0 K^+ \pi^-$ (right) candidates in the two-dimensional signal region.

A second kinematic fit that also constrains the D^0 mass to its known value is performed and used for all subsequent parts of the amplitude analysis of $D^0 \rightarrow K_s^0 K^\pm \pi^\mp$ decays. This fit further improves the resolution in the two-body invariant mass variables and forces all candidates to lie within the kinematically allowed region of the Dalitz plot. The Dalitz plots for data in the two-dimensional signal region are shown in Fig. 5.3, where the abbreviated notation $m_{K_s^0\pi}^2 \equiv m^2(K_s^0 \pi^\pm)$, $m_{K\pi}^2 \equiv m^2(K^\pm \pi^\mp)$ has been adopted. Both decays are dominated by a $K^*(892)^\pm$ structure. The $K^*(892)^0$ is also visible as a destructively interfering contribution in the $D^0 \rightarrow K_s^0 K^- \pi^+$ mode and the low- $m_{K_s^0\pi}^2$ region of the $D^0 \rightarrow K_s^0 K^+ \pi^-$ mode, while a clear excess is seen in the high- $m_{K_s^0\pi}^2$ region. Finally, a veto is applied to candidates close to the kinematic boundaries; this is detailed in Sect. 5.4.

5.4 $D^0 \rightarrow K_s^0 K^\pm \pi^\mp$ reconstruction efficiency

The trigger strategy described in Sect. 5.2, and to a lesser extent the offline selection, includes requirements on variables such as the IP and p_T of the various charged particles that are correlated with the two-body invariant masses $m_{K_s^0\pi}^2$ and $m_{K\pi}^2$. There is, therefore, a significant variation in reconstruction efficiency as a function of $m_{K_s^0\pi}^2$ and $m_{K\pi}^2$. This efficiency variation is modelled using simulated events generated with a uniform distribution in

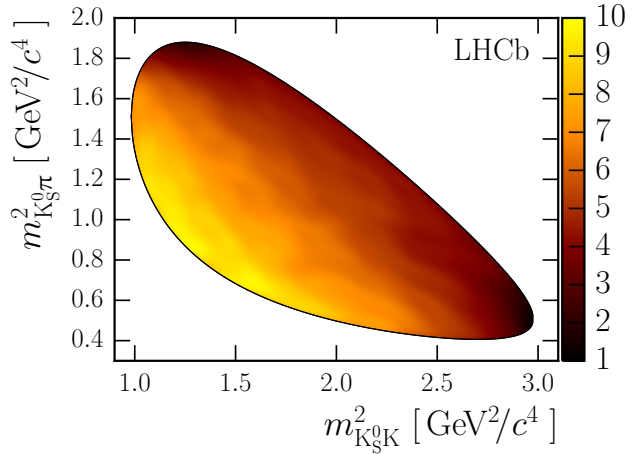


Figure 5.4: Efficiency function used in the isobar model fits, corresponding to the average efficiency over the full dataset. The coordinates $m_{K_s^0 \pi}^2$ and $m_{K_s^0 K}^2$ are used to highlight the approximate symmetry of the efficiency function. The z -units are arbitrary.

these variables and propagated through the full LHCb detector simulation, trigger emulation and offline selection. Weights are applied to the simulated events to ensure that various subsamples are present in the correct proportions. These weights correct for known discrepancies between the simulation and real data in the relative reconstruction efficiency for long and downstream tracks, and take into account the ratios of $\sqrt{s} = 7 \text{ TeV}$ to $\sqrt{s} = 8 \text{ TeV}$ and $D^0 \rightarrow K_s^0 K^- \pi^+$ to $D^0 \rightarrow K_s^0 K^+ \pi^-$ simulated events to improve the description of the data. The efficiencies of offline selection requirements based on information from the RICH detectors are calculated using a data-driven method based on calibration samples [116] of $D^{*+} \rightarrow D^0 \pi_{\text{slow}}^+$ decays, where $D^0 \rightarrow K^- \pi^+$ – these are the Run 1 counterparts of the calibration samples described in Sect. 4.4. These efficiencies are included as additional weights. A non-parametric kernel estimator [169] is used to produce a smooth function $\varepsilon(m_{K_s^0 \pi}^2, m_{K_s^0 K}^2)$ describing the efficiency variation in the isobar model fits. The average model corresponding to the full dataset recorded in 2011 and 2012, which is used unless otherwise noted, is shown in Fig. 5.4. Candidates very near to the boundary of the allowed kinematic region of the Dalitz plot are excluded, as the kinematics in this region lead to variations in efficiency that are difficult to model. It is required that $\max(|\cos(\theta_{K_s^0 \pi})|, |\cos(\theta_{\pi K})|, |\cos(\theta_{K_s^0 K})|) < 0.98$, where θ_{AB} is the angle between the A and B momenta in the AC rest frame. This criterion removes 5 % of the candidates. The simulated events are also used to verify that the resolution in $m_{K_s^0 \pi}^2$ and $m_{K_s^0 K}^2$ is around $0.004 \text{ GeV}^2/c^4$, corresponding to $\mathcal{O}(2 \text{ MeV}/c^2)$ resolution

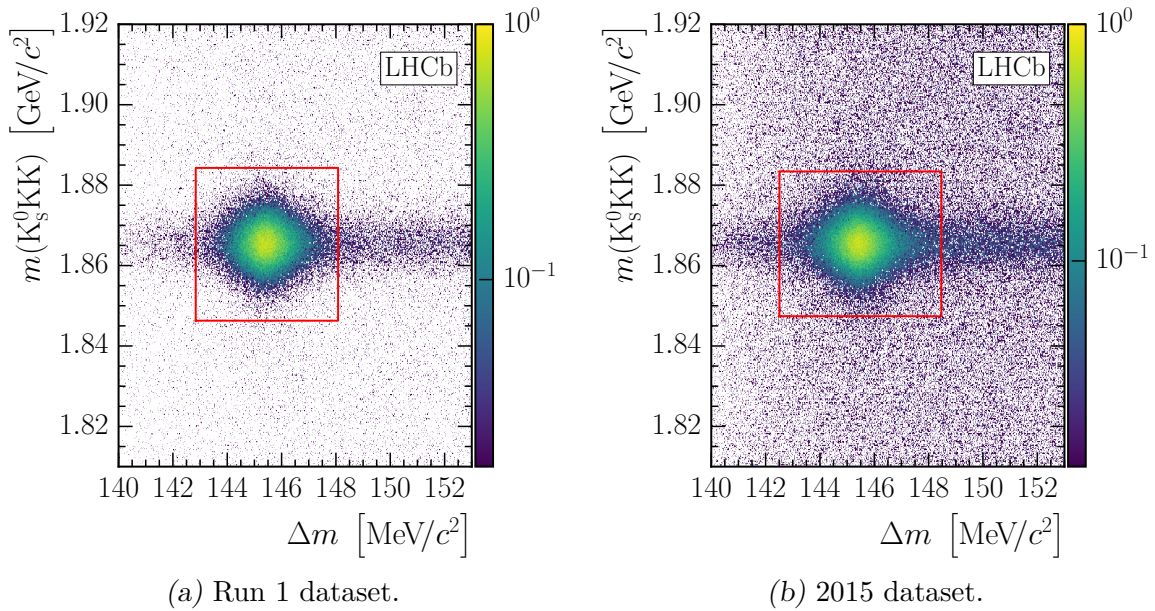


Figure 5.5: Distributions in $m(K_s^0 KK)$ and Δm of the $D^0 \rightarrow K_s^0 K^+ K^-$ signal candidates selected in the mixing and CP violation study. The signal region is indicated by the solid curve, and the z -units are arbitrary.

in $m(K_s^0 \pi^\pm)$. Although this is not explicitly accounted for in the isobar model fits, it has a small effect which is measurable only on the parameters of the $K^*(892)^\pm$ resonance and is accounted for in the systematic uncertainties.

5.5 $D^0 \rightarrow K_s^0 K^+ K^-$ mixing study yield extraction

Signal yields are determined using a two-dimensional maximum likelihood fit to the $m(K_s^0 KK)$ and Δm distributions. These distributions are shown in Fig. 5.5. The signal distribution in $m(K_s^0 KK)$ is described by the sum of a Crystal Ball [170] function and two Gaussian functions, where the three functions have the same peak position but different width and tail parameters. The combinatorial shape in $m(K_s^0 KK)$ is described by an exponential function. In Δm the signal distribution is described with the sum of a Johnson S_U [167] function and a Gaussian function with the same peak position. The combinatorial background distribution is described by the power law function defined in Eqn. 5.1. Finally, the Δm distribution of signal candidates formed from a D^0 meson and an incorrect π_{slow}^+ is modelled by the sum of a constant and exponential term.

Table 5.4: Signal yields and estimated background rates in the two-dimensional signal region for each Dalitz plot bin in the Run 1 dataset. Only statistical uncertainties are quoted.

Bin	Signal yield	Incorrect π_{slow}^+ background [%]	Combinatorial background [%]
-2	21319 ± 199	7.16 ± 0.27	2.30 ± 0.05
-1	25422 ± 224	6.64 ± 0.25	5.00 ± 0.06
+1	33965 ± 264	5.30 ± 0.22	3.98 ± 0.05
+2	28659 ± 234	5.63 ± 0.23	1.88 ± 0.04
-3	2460 ± 58	8.8 ± 0.6	14.04 ± 0.28
-2	20940 ± 192	6.87 ± 0.26	1.082 ± 0.033
-1	23382 ± 209	6.66 ± 0.25	4.86 ± 0.06
+1	30757 ± 243	5.36 ± 0.22	3.90 ± 0.05
+2	25095 ± 213	6.05 ± 0.24	0.927 ± 0.028
+3	6822 ± 93	3.95 ± 0.31	6.43 ± 0.12
-4	1040 ± 38	13.6 ± 1.0	21.2 ± 0.5
-3	16297 ± 145	7.09 ± 0.21	1.52 ± 0.04
-2	7923 ± 97	5.87 ± 0.27	2.55 ± 0.08
-1	21554 ± 172	6.46 ± 0.19	4.78 ± 0.06
+1	28258 ± 197	5.29 ± 0.17	3.83 ± 0.05
+2	7815 ± 97	6.28 ± 0.28	2.74 ± 0.08
+3	20442 ± 163	6.01 ± 0.19	1.34 ± 0.04
+4	6186 ± 84	2.83 ± 0.26	5.26 ± 0.12

A rectangular signal window of $\pm 19 \text{ MeV}/c^2$ in $m(K_s^0 \text{KK})$ and $\pm 2.62 \text{ MeV}/c^2$ in Δm is defined, where the dimensions correspond to three standard deviations of the signal distributions. The yields and background estimates in the two-dimensional signal region are given in Table 5.4. The fit results are illustrated in Figs. 5.6 and 5.7, where in each case the distributions are integrated over the signal region of the other variable. Note that, as discussed in Sect. 5.1, the kinematic fit used in this study does not constrain the D^{*+} decay vertex to coincide with the PV, which is responsible for the clear difference in Δm resolution between the $D^0 \rightarrow K_s^0 K^\pm \pi^\mp$ (Fig. 5.2) and $D^0 \rightarrow K_s^0 K^+ K^-$ distributions (Fig. 5.7). For brevity, only the $m(K_s^0 \text{KK})$ and Δm distributions corresponding to the $\mathcal{N} = 3$ binning scheme introduced in Sect. 2.5.1 are shown in this chapter. Numerical results for the $\mathcal{N} = 2$ and $\mathcal{N} = 4$ schemes are included in Table 5.4, but the corresponding figures are consigned to Appendix E.

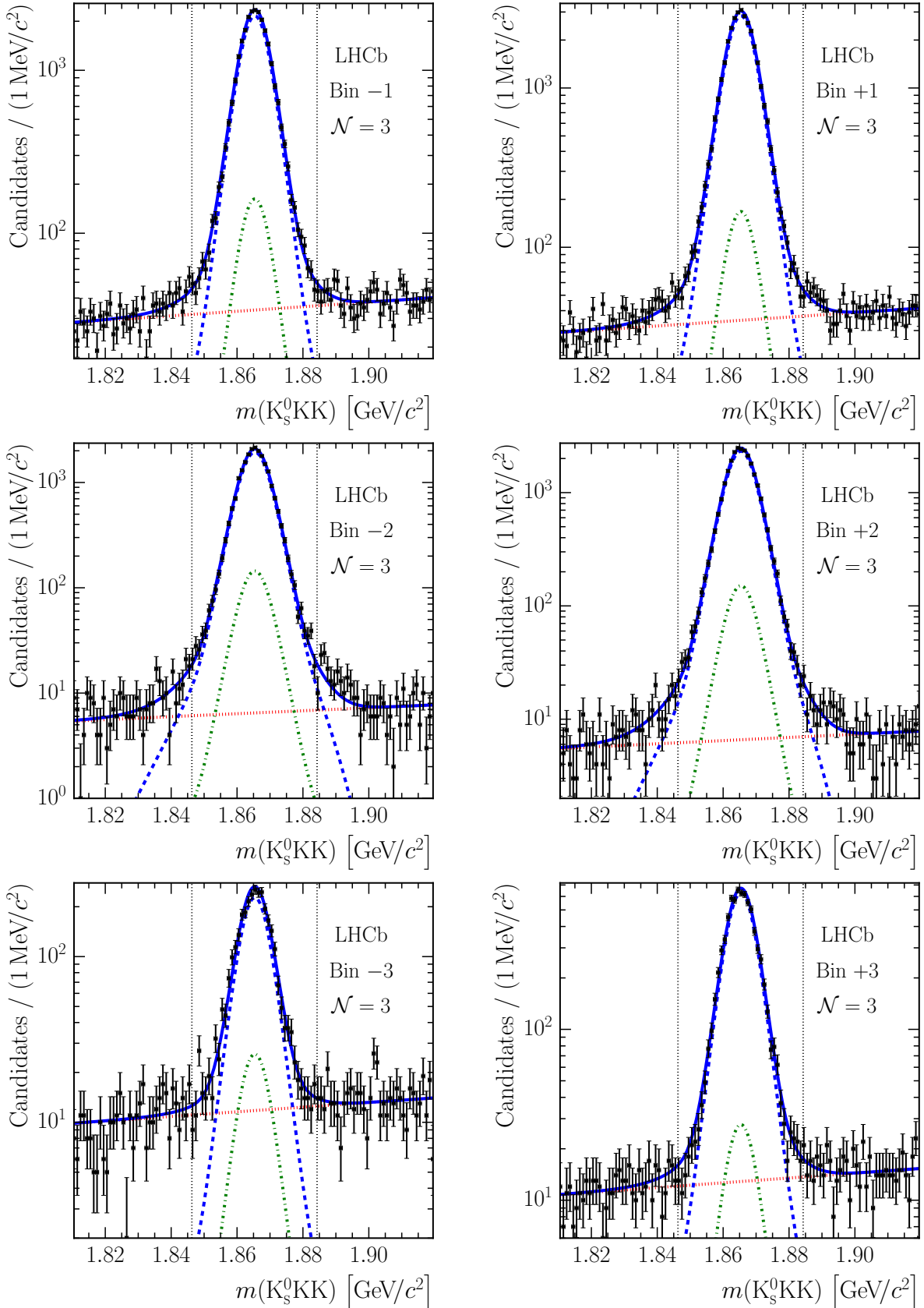


Figure 5.6: $m(K_s^0 KK)$ distributions for the $D^0 \rightarrow K_s^0 K^+ K^-$ samples with fit results superimposed. The $\mathcal{N}=3$ binning scheme results are shown. The long-dashed (blue) curve represents the D^{*+} signal, the dash-dotted (green) curve represents the contribution of real D^0 mesons combined with incorrect π_{slow}^+ and the dotted (red) curve represents the combinatorial background contribution. The vertical dotted lines indicate the signal window. The residual distributions (not shown) indicate a good quality of fit, including in the peak.

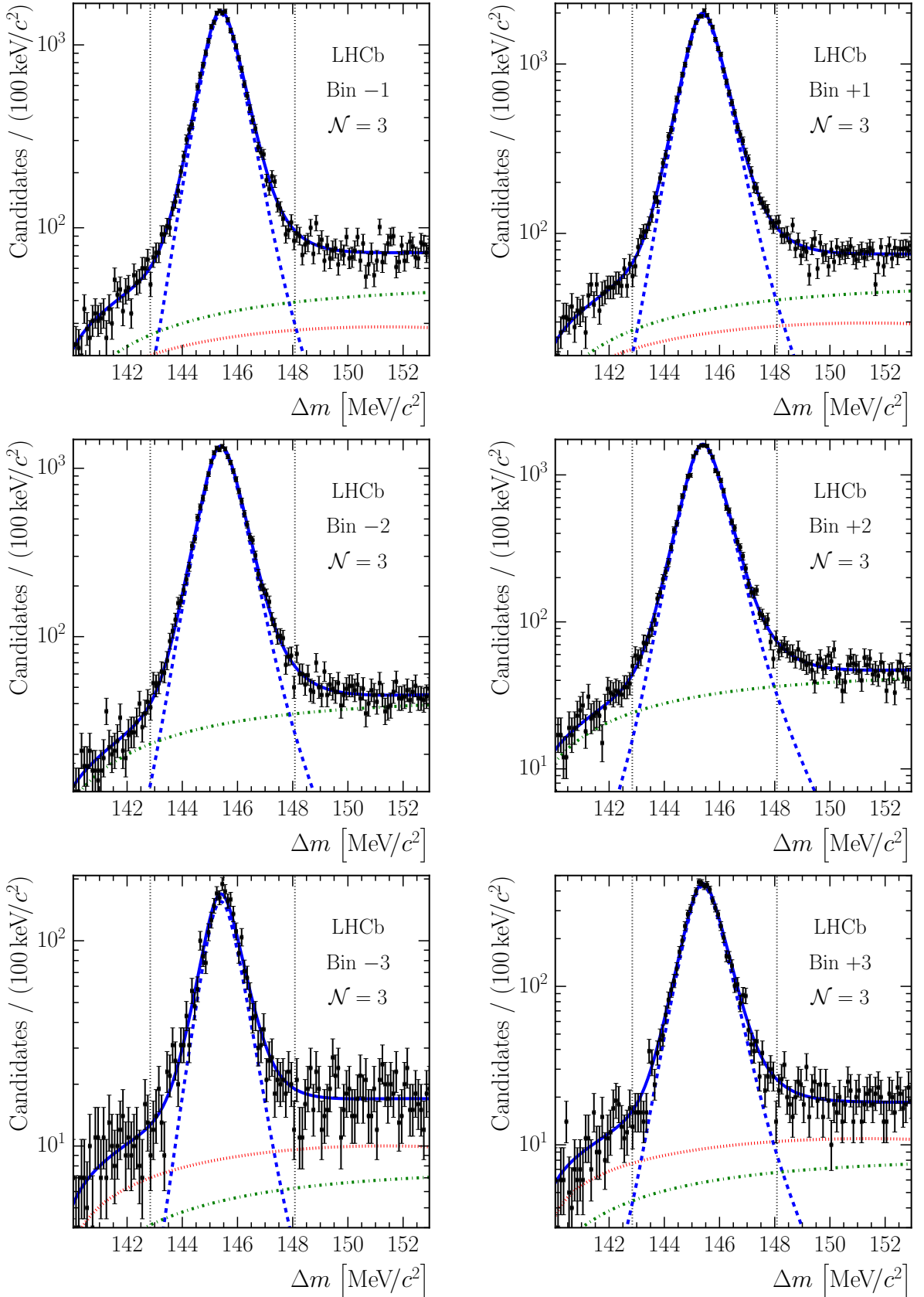


Figure 5.7: Δm distributions for the $D^0 \rightarrow K_s^0 K^+ K^-$ samples with fit results superimposed. The $\mathcal{N} = 3$ binning scheme results are shown. The long-dashed (blue) curve represents the D^{*+} signal, the dash-dotted (green) curve represents the contribution of real D^0 mesons combined with incorrect π_{slow}^+ and the dotted (red) curve represents the combinatorial background contribution. The vertical dotted lines indicate the signal window. The residual distributions (not shown) indicate a good quality of fit, including in the peak.

5.5.1 Run 2 $D^0 \rightarrow K_s^0 K^+ K^-$ yield estimates

The data collected in 2015, the first year of Run 2, have been processed in support of the mixing studies presented in Chapter 7. The 2015 dataset, which corresponds to an integrated luminosity of around 280 pb^{-1} , is used to estimate the total signal yield that will be recorded during Run 2. Estimates of the corresponding sensitivity to the charm mixing parameters are deferred to Chapter 7.

As in Run 1, the Run 2 HLT2 contains both exclusive selections for the $D^0 \rightarrow K_s^0 K^+ K^-$ decay mode and an inclusive $D^{*+} \rightarrow D^0 \pi_{\text{slow}}^+$ trigger. However, because the exclusive triggers operated efficiently from the start of data-taking, the inclusive trigger contributes negligible additional signal and is not considered further. As before, K_s^0 candidates are reconstructed both from pairs of long tracks and pairs of downstream tracks. In contrast to Run 1, the exclusive Run 2 HLT2 selections reconstruct the full, flavour-tagged, $D^{*+} \rightarrow D^0 \pi_{\text{slow}}^+$, $D^0 \rightarrow K_s^0 K^+ K^-$ decay chain. There are two sets of exclusive selections. The first of these are “lifetime biased”, contain IP thresholds and require that signal candidates also passed the one- and/or two-track inclusive beauty and charm HLT1 selections (*i.e.* TOS, as defined previously). The second set are “lifetime unbiased”, as outlined in Sect. 4.2.5. These require that the HLT1 decision was independent of the signal candidate (*i.e.* TIS), which is necessary because $D^0 \rightarrow K_s^0 h^+ h'^-$ candidates are not, at present, fully reconstructed in HLT1.

No significant offline selection requirements are imposed on the 2015 dataset, with the only additions to the HLT selections coming from the loose, centralised preselection described in Sect. 3.3. The two-dimensional PDFs used to fit $m(K_s^0 \text{KK})$ and Δm are similar to those used to fit the Run 1 $D^0 \rightarrow K_s^0 K^+ K^-$ dataset. The only change is that the Crystal Ball contribution is removed from the $m(K_s^0 \text{KK})$ signal PDF, leaving two Gaussian functions. The two-dimensional fit results are summarised in Table 5.5, and those for the $\mathcal{N} = 3$ binning scheme are illustrated in Figs. 5.8 and 5.9. As above, the corresponding distributions for the $\mathcal{N} = 2$ and $\mathcal{N} = 4$ binning schemes are given in Appendix E. The fit results are quoted both for the full dataset and for the “lifetime unbiased” subset, illustrating that this subset is significantly smaller and has somewhat worse signal purity. In the 2015 dataset around 15 %

Table 5.5: Signal yields and estimated background rates in the two-dimensional signal region for each Dalitz plot bin in the Run 2 dataset. The “Exclusive” heading denotes results from the combination of all exclusive HLT2 $D^{*+} \rightarrow D^0 \pi_{\text{slow}}^+$ selections, while “Unbiased” refers to the “lifetime unbiased” selections alone. Only statistical uncertainties are quoted.

Bin	Signal yield		Incorrect π_{slow}^+ background [%]		Combinatorial background [%]	
	Exclusive	Unbiased	Exclusive	Unbiased	Exclusive	Unbiased
-2	29100 ± 230	11300 ± 400	7.95 ± 0.24	8.6 ± 1.2	9.43 ± 0.07	16.28 ± 0.15
-1	33060 ± 260	12500 ± 400	7.29 ± 0.22	7.5 ± 1.1	18.49 ± 0.09	30.39 ± 0.18
+1	43120 ± 300	15800 ± 500	5.50 ± 0.21	5.6 ± 1.0	15.50 ± 0.07	26.71 ± 0.15
+2	38050 ± 270	14500 ± 500	6.16 ± 0.22	6.8 ± 1.2	7.94 ± 0.06	13.90 ± 0.13
-3	2790 ± 80	880 ± 40	8.0 ± 0.7	6.6 ± 0.9	45.5 ± 0.4	64.1 ± 0.7
-2	29300 ± 500	11570 ± 210	7.7 ± 0.6	8.9 ± 0.7	4.51 ± 0.05	8.38 ± 0.12
-1	30500 ± 500	11550 ± 220	7.1 ± 0.5	7.4 ± 0.6	18.36 ± 0.09	30.24 ± 0.19
+1	39400 ± 500	14490 ± 250	5.4 ± 0.5	5.5 ± 0.6	15.46 ± 0.08	26.54 ± 0.16
+2	34200 ± 500	13560 ± 240	6.6 ± 0.6	7.5 ± 0.7	4.13 ± 0.05	7.65 ± 0.11
+3	8000 ± 120	2320 ± 70	3.2 ± 0.4	3.1 ± 0.7	25.59 ± 0.20	44.6 ± 0.5
-4	1120 ± 50	350 ± 27	12.1 ± 0.9	7.5 ± 1.0	53.0 ± 0.5	72.2 ± 0.7
-3	21510 ± 170	8650 ± 200	9.90 ± 0.21	9.1 ± 0.9	6.38 ± 0.07	11.89 ± 0.13
-2	10700 ± 120	4340 ± 100	8.32 ± 0.28	7.0 ± 0.8	10.29 ± 0.12	19.54 ± 0.22
-1	27030 ± 200	10560 ± 240	9.08 ± 0.20	7.7 ± 0.7	16.94 ± 0.09	29.32 ± 0.16
+1	34880 ± 220	13120 ± 230	7.24 ± 0.17	5.6 ± 0.6	14.26 ± 0.08	25.85 ± 0.14
+2	10280 ± 110	4250 ± 100	8.62 ± 0.29	6.9 ± 0.9	11.14 ± 0.13	20.44 ± 0.22
+3	26880 ± 190	10870 ± 210	8.33 ± 0.18	7.2 ± 0.8	5.59 ± 0.06	10.39 ± 0.11
+4	6900 ± 90	2040 ± 50	5.01 ± 0.34	3.2 ± 0.6	19.30 ± 0.19	36.9 ± 0.4

of candidates are selected by both the “lifetime unbiased” and decay-time-biasing selections.

In general the signal yields in the 2015 dataset are similar to those in Run 1, despite the much smaller integrated luminosity, due to a combination of improved trigger efficiency and increased production cross-section [41]. The combinatorial background levels quoted in Table 5.5 are somewhat higher in the 2015 dataset than in Run 1 (Table 5.4), but it should be noted that the offline selection requirements applied to the 2015 dataset are much looser. The various HLT2 selections will be optimised during Run 2, and in any case offline selections can be applied, so this difference in background level is substantially artificial. The exception to this may be the “lifetime unbiased” selections, where the exclusion of decay-time-biasing selection requirements necessarily results in some degradation in performance.

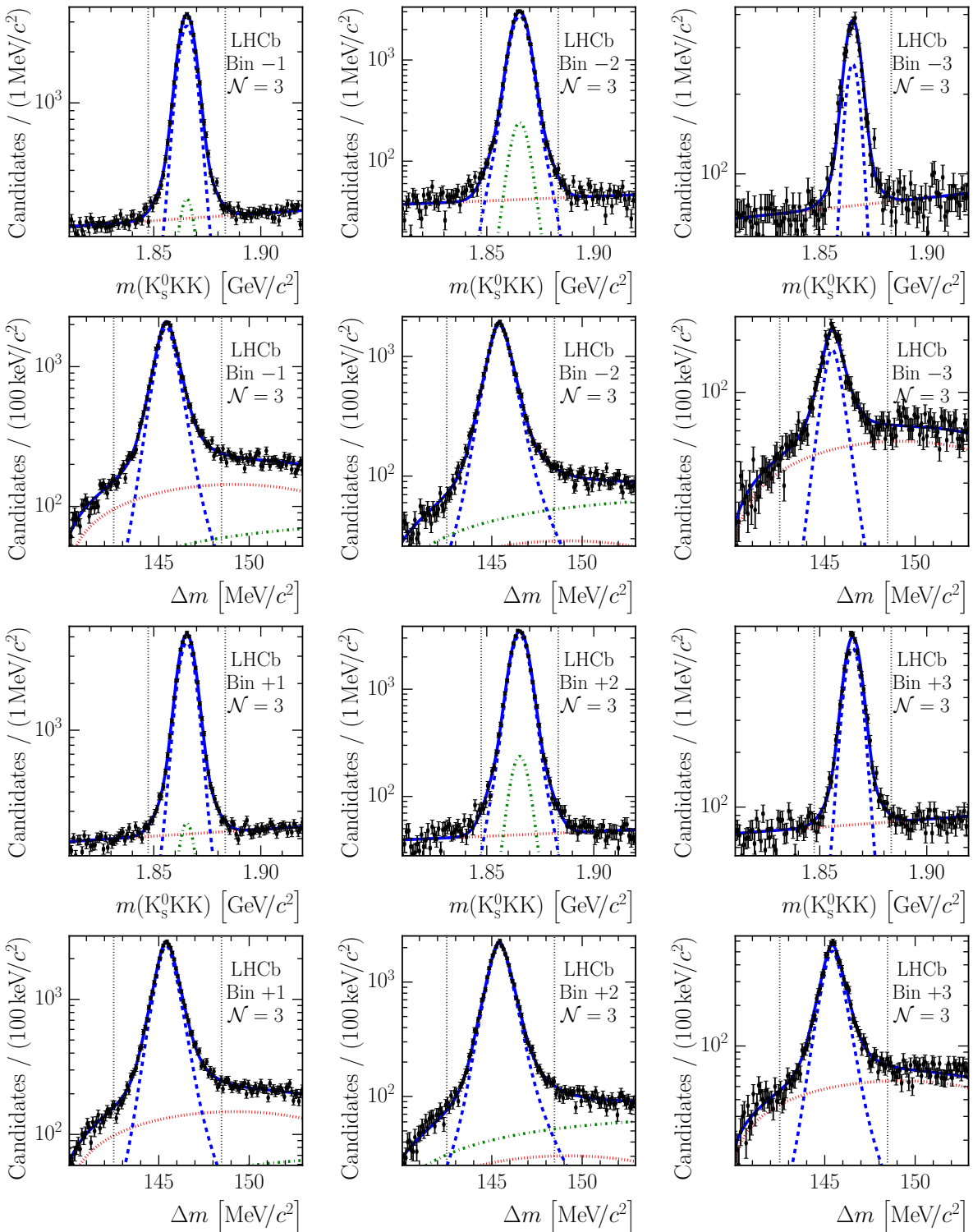


Figure 5.8: $m(K_s^0 KK)$ and Δm distributions for the Run 2 $D^0 \rightarrow K_s^0 K^+ K^-$ samples recorded in 2015. Fit results are superimposed. The $\mathcal{N} = 3$ binning scheme results are shown. The long-dashed (blue) curve represents the D^{*+} signal, the dash-dotted (green) curve represents the contribution of real D^0 mesons combined with incorrect π_{slow}^+ and the dotted (red) curve represents the combinatorial background contribution. The vertical dotted lines indicate the signal window. The residual distributions (not shown) indicate a good quality of fit, including in the peak.

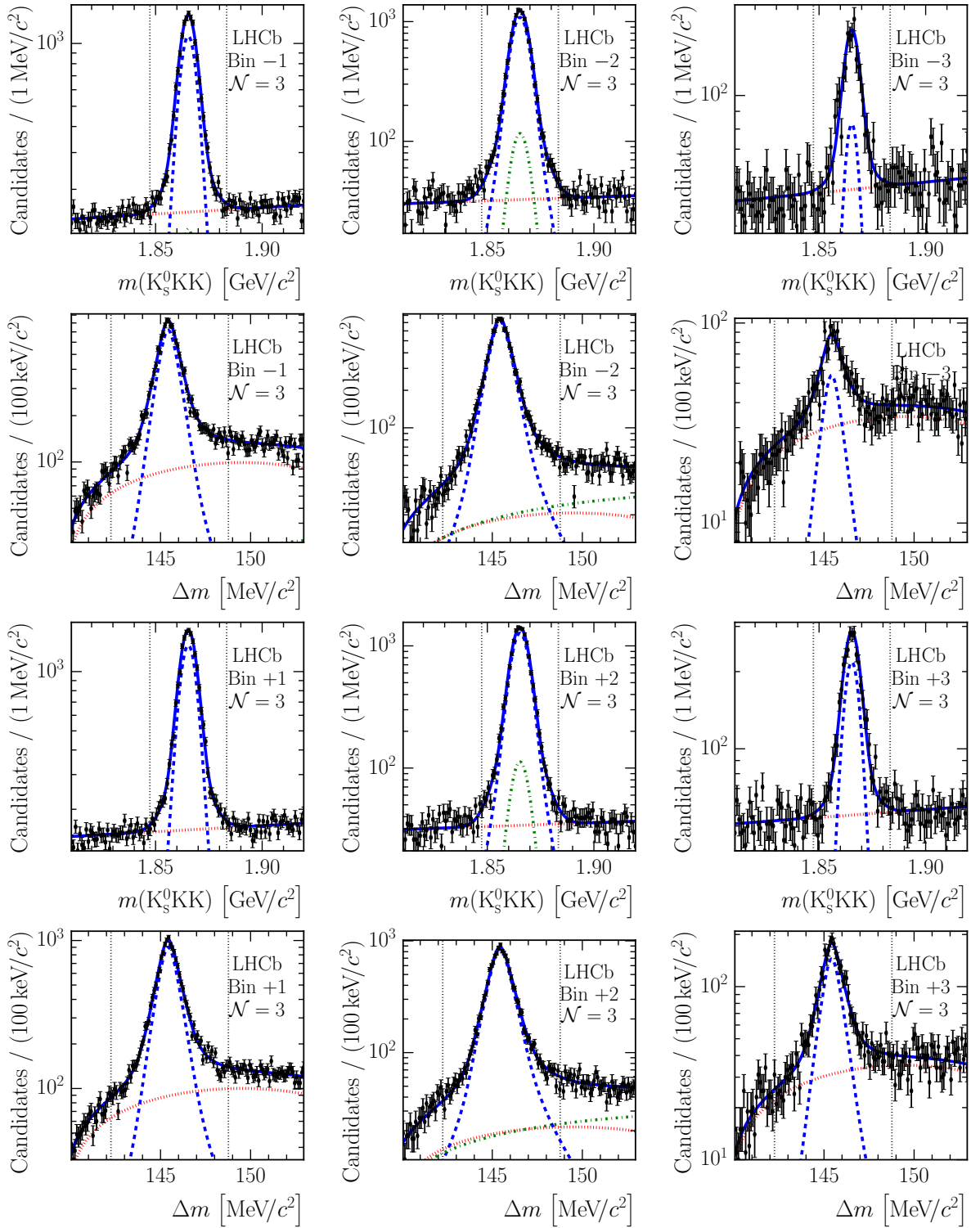


Figure 5.9: $m(K_s^0 K K)$ and Δm distributions for the “lifetime unbiased” Run 2 $D^0 \rightarrow K_s^0 K^+ K^-$ samples recorded in 2015 Fit results are superimposed. The $\mathcal{N} = 3$ binning scheme results are shown. The long-dashed (blue) curve represents the D^{*+} signal, the dash-dotted (green) curve represents the contribution of real D^0 mesons combined with incorrect π_{slow}^+ and the dotted (red) curve represents the combinatorial background contribution. The vertical dotted lines indicate the signal window. The residual distributions (not shown) indicate a good quality of fit, including in the peak.

LHCb is expected to record an integrated luminosity of around 5 fb^{-1} by the end of Run 2 in 2018 [171]. It is challenging to accurately predict what $D^0 \rightarrow K_s^0 K^+ K^-$ signal yield this will correspond to for three main reasons. Firstly, the hardware trigger (L0) thresholds are regularly updated according to the LHC beam intensity. These thresholds were relatively loose during 2015 data-taking, but will be tightened later in Run 2 as LHC commissioning proceeds, decreasing signal efficiencies. Secondly, the software trigger (HLT) is regularly improved and re-tuned, so it is reasonable to expect some performance improvement. Finally, while the signal yields quoted in Table 5.5 are background-subtracted, it is unlikely that a full mixing analysis would proceed without applying further selection requirements to improve the signal purity, which will incur some signal inefficiency. It will be assumed that these effects cancel one another for the projections included in this thesis, and the yields obtained in 2015 simply extrapolated by a factor $5\text{ fb}^{-1}/280\text{ pb}^{-1} \approx 18$ to obtain the full Run 2 yields.

Tables 5.4 and 5.5 illustrate that the overall trigger efficiency has increased substantially for the $D^0 \rightarrow K_s^0 K^+ K^-$ modes in Run 2, with this simple extrapolation indicating that the yield recorded during the full Run 2 will be around 20 times larger than the full Run 1 dataset, despite gaining a factor of just $\sim 2/3$ in integrated luminosity, and ~ 2 in cross-section. The upgraded LHCb detector is expected to record a total integrated luminosity of around 50 fb^{-1} in Run 3 and beyond, which is around an order of magnitude more than the Run 1 and Run 2 expectation. In addition, upgrades to the trigger and online system should increase hadronic signal yields by a further order of magnitude [172]. A significant fraction of this expected gain is due to the removal of the hardware trigger, with the full inelastic collision rate of 30 MHz processed by the software trigger. The expected signal yield with the full dataset to be recorded by the upgraded LHCb detector is, therefore, around two orders of magnitude larger than the combined Run 1 and Run 2 sample.

6. AMPLITUDE ANALYSIS OF $D^0 \rightarrow K_s^0 K^\pm \pi^\mp$ DECAYS

A large variety of physics can be accessed by studying the decays $D^0 \rightarrow K_s^0 K^- \pi^+$ and $D^0 \rightarrow K_s^0 K^+ \pi^-$. Analysis of the relative amplitudes of intermediate resonances contributing to these decays can help in understanding the behaviour of the strong interaction at low energies. These modes are also of interest for improving knowledge of the CKM matrix, and CP violation measurements and mixing studies in the $D^0-\bar{D}^0$ system. Both modes are singly Cabibbo-suppressed (SCS), with the $K_s^0 K^- \pi^+$ final state favoured by approximately $\times 1.7$ with respect to its $K_s^0 K^+ \pi^-$ counterpart [54]. The main classes of Feynman diagrams, and the sub-decays to which they contribute, are shown in Fig. 6.1. The process shown in Fig. 6.1d is expected to be suppressed due to the Okubo-Zweig-Iizuka (OZI) rule [173–175], as the initial and final states are connected only by internal gluon lines.

Flavour symmetries are an important phenomenological tool in the study of hadronic decays, and the presence of both charged and neutral K^* resonances in each $D^0 \rightarrow K_s^0 K^\pm \pi^\mp$ mode allows several tests of SU(3) flavour symmetry to be carried out [176, 177]. The $K_s^0 K^\pm \pi^\mp$ final states also provide opportunities to study the incompletely understood $K\pi$ S -wave systems [178], and to probe several resonances in the $K_s^0 K^\pm$ decay channels that are poorly established.

An important goal of flavour physics is to make a precise determination of the CKM unitarity-triangle angle $\gamma \equiv \arg(-V_{ud}V_{ub}^*/V_{cd}V_{cb}^*)$. Information on this parameter can be obtained by studying CP -violating observables in the decays $B^- \rightarrow (\bar{D}^0) K^-$, where the D^0 and \bar{D}^0 are reconstructed in a set of common final states [179, 180], such as the modes $D^0 \rightarrow K_s^0 K^- \pi^+$ and $D^0 \rightarrow K_s^0 K^+ \pi^-$ [181]. Optimum statistical power is achieved by studying the dependence of the CP asymmetry on where in three-body phase space the D-meson decay

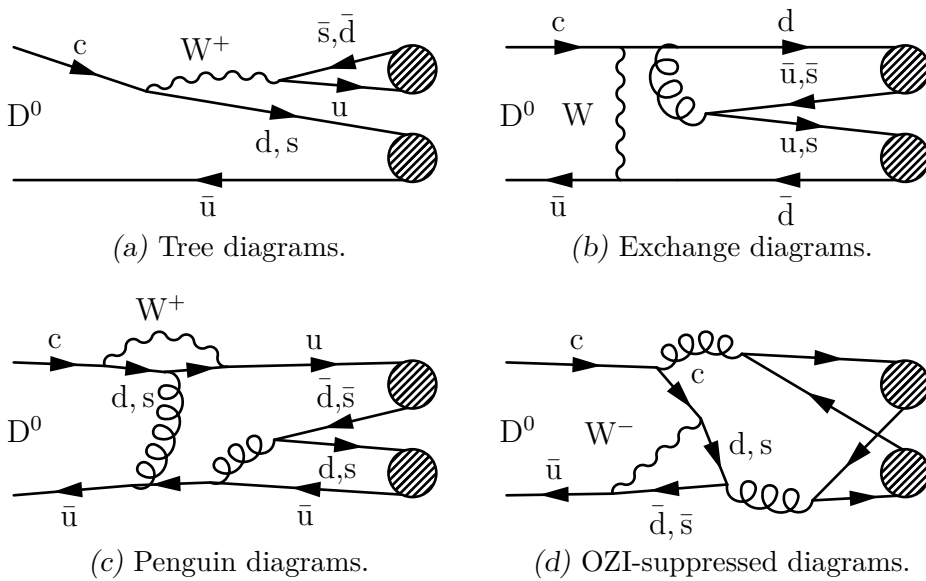


Figure 6.1: SCS classes of diagrams contributing to the decays $D^0 \rightarrow K_s^0 K^\pm \pi^\mp$. The colour-favoured (tree) diagrams (a) contribute to the $K_{0,1,2}^{*\pm} \rightarrow K_s^0 \pi^\pm$ and $(a_{0,2}, \rho)^\pm \rightarrow K_s^0 K^\pm$ channels, while the colour-suppressed exchange diagrams (b) contribute to the $(a_{0,2}, \rho)^\pm \rightarrow K_s^0 K^\pm$, $K_{0,1,2}^{*0} \rightarrow K^+ \pi^-$ and $\bar{K}_{0,1,2}^{*0} \rightarrow K^- \pi^+$ channels. Second-order loop (penguin) diagrams (c) contribute to the $(a_{0,2}, \rho)^\pm \rightarrow K_s^0 K^\pm$ and $K_{0,1,2}^{*\pm} \rightarrow K_s^0 \pi^\pm$ channels, and, finally, OZI-suppressed penguin annihilation diagrams (d) contribute to all decay channels.

occurs, provided that the decay amplitude from the intermediate resonances is sufficiently well described. Alternatively, an inclusive analysis may be pursued, as in Ref. [182], with a ‘coherence factor’ [183] parameterising the net effect of these resonances. The coherence factor of these decays has been measured by the CLEO collaboration using quantum-correlated D^0 decays at the open-charm threshold [61], but it may also be calculated from knowledge of the contributing resonances. In both cases, therefore, it is valuable to be able to model the variation of the magnitude and phase of the D^0 -decay amplitudes across phase space.

This chapter describes the construction of time-integrated amplitude models of the $D^0 \rightarrow K_s^0 K^\pm \pi^\mp$ decays, and the use of these models to test SU(3) flavour symmetry predictions, search for local CP violation, and compute coherence factors and associated parameters. In addition a precise measurement is performed of the ratio of branching fractions. Details concerning the data sample used for this analysis were presented in Chapter 5 and will only be discussed further when associated systematic uncertainties are evaluated. The majority of the theoretical background relevant to amplitude analysis and the isobar model has been

given in Chapter 2, with the exception of some details that are particularly specific to the analysis of $D^0 \rightarrow K_s^0 K^\pm \pi^\mp$. The amplitude model PDFs are given in Sect. 6.1; the calculation of additional quantities of interest, such as the CP -even fraction and coherence factor, is described in Sect. 6.2; and the model-finding procedure is outlined in Sect. 6.3. The application of this procedure is described in Sect. 6.4, with further details given in Sect. 6.5. The calculation of systematic uncertainties is described in Sect. 6.6, and the final models are presented in Sect. 6.7. Additional results are presented in the following sections, such as the search for direct CP violation (Sect. 6.8), measurement of the ratio of branching fractions (Sect. 6.9), computation of the CP -even fraction and coherence factor (Sect. 6.10), and tests of SU(3) flavour symmetry (Sect. 6.11). Finally, conclusions are given in Sect. 6.12.

This work is published in Ref. [162].

6.1 Amplitude model probability density functions

Amplitude models for the $D^0 \rightarrow K_s^0 K^\pm \pi^\mp$ decays are constructed using the isobar formalism, which was introduced in Chapter 2. Throughout this chapter the two-dimensional complex decay amplitudes for these decays will be expressed in terms of the squared invariant masses $m_{K_s^0 \pi}^2 \equiv m^2(K_s^0 \pi)$ and $m_{K\pi}^2 \equiv m^2(K\pi)$, as this choice highlights the dominant resonant structure of the $D^0 \rightarrow K_s^0 K^\pm \pi^\mp$ decay modes. Only resonances with spin $J \in \{0, 1, 2\}$ are considered in the models, as those with greater spin are not expected to contribute significantly to the $D^0 \rightarrow K_s^0 K^\pm \pi^\mp$ decays. The particle ordering convention chosen for this analysis is given in Table 6.1. This is important because the $J = 1$ spin factor, Ω_1 , is antisymmetric under exchange of the indices describing the resonance children. The meson radius parameters introduced in Sect. 2.4.1 are set to $d_{D^0} = 5.0\,c/\text{GeV}$ and $d_R = 1.5\,c/\text{GeV}$, following the literature [61, 62].

This analysis uses two different parameterisations for the $K\pi$ S -wave contributions, dubbed **GLASS** and **LASS**, with different motivations. These forms include both $K_0^*(1430)$ resonance and nonresonant $K\pi$ S -wave contributions. The **LASS** parameterisation's dynamical function

Table 6.1: Particle ordering conventions used in this analysis.

Decay	A	B	C
$D^0 \rightarrow K_s^0 \bar{K}^{*0}$,	$\bar{K}^{*0} \rightarrow K^\pm \pi^\mp$	π	K
$D^0 \rightarrow K^\mp K^{*\pm}$,	$K^{*\pm} \rightarrow K_s^0 \pi^\pm$	K_s^0	π
$D^0 \rightarrow \pi^\mp (\rho^\pm, a^\pm)$,	$\rho^\pm, a^\pm \rightarrow K_s^0 K^\pm$	K	K_s^0

takes the form

$$T_R = f \left(\frac{m_{K\pi}}{m_{K_0^*(1430)}} \right) \frac{m_{K\pi}}{q} \sin(\delta_S + \delta_F) e^{i(\delta_S + \delta_F)} \quad (6.1)$$

where q is the momentum of the resonance children in the resonance rest frame,

$$f(x) = A \exp(b_1 x + b_2 x^2 + b_3 x^3) \quad (6.2)$$

is an empirical real production form factor, and the phases are defined by

$$\tan \delta_F = \frac{2aq}{2 + arq^2}, \quad \tan \delta_S = \frac{m_R \Gamma_R(m_{K\pi})}{m_{K_0^*(1430)}^2 - m_{K\pi}^2}. \quad (6.3)$$

The scattering length a , effective range r and $K_0^*(1430)$ mass and width are taken from measurements [184] at the LASS experiment [185] and are tabulated in Appendix A. With the choice $f(x) = 1$ this form has been used in previous analyses, *e.g.* Refs. [186–188], and if δ_F is additionally set to zero the relativistic S -wave Breit-Wigner form is recovered. The Watson theorem [189] states that the phase motion, as a function of $K\pi$ invariant mass, is the same in elastic scattering and decay processes, in the absence of final-state interactions (*i.e.* in the isobar model). Studies of $K\pi$ scattering data indicate that the S -wave remains elastic up to the $K\eta'$ threshold [184]. The magnitude behaviour is not constrained by the Watson theorem, which motivates the inclusion of the form factor $f(x)$, but the LASS parameterisation preserves the phase behaviour measured in $K\pi$ scattering. The real form factor parameters are allowed to take different values for the neutral and charged $K_0^*(1430)$ resonances, as the production processes are not the same, but the parameters taken from LASS measurements, which specify the phase behaviour, are shared between both $K\pi$ channels. A transformed set $\mathbf{b}' = \mathbf{U}^{-1}\mathbf{b}$ of the parameters $\mathbf{b} = (b_1, b_2, b_3)$ defined in Eqn. 6.2 is also defined for use in the isobar model fit, which is described in detail in Sect. 6.5. The

constant matrix \mathbf{U} is chosen to minimise fit correlations, and the form factor is normalised to unity at the centre of the accessible kinematic range, *e.g.* $\frac{1}{2}(m_{K_s^0} + m_{\pi^\pm} + m_{D^0} - m_{K^\pm})$ for the charged $K\pi$ S -wave.

The GLASS (Generalised LASS) parameterisation has been used by several recent amplitude analyses, *e.g.* Refs. [36, 61, 67],

$$T_R = \left[F \sin(\delta_F + \phi_F) e^{i(\delta_F + \phi_F)} + \sin(\delta_S) e^{i(\delta_S + \phi_S)} e^{2i(\delta_F + \phi_F)} \right] \frac{m_{K\pi}}{q}, \quad (6.4)$$

where δ_F and δ_S are defined as before, and F , ϕ_F and ϕ_S are free parameters in the fit. It should be noted that this functional form can result in phase behaviour significantly different to that measured in LASS scattering data when its parameters are allowed to vary freely. This is illustrated in Fig. 6.9, Sect. 6.7.

6.1.1 Fit components

There are three event categories described in Sect. 5.3 that must be treated separately in the isobar model fits. The signal and mistagged components are described by terms proportional to $\varepsilon(m_{K_s^0\pi}^2, m_{K\pi}^2) |\bar{\mathcal{M}}_{K_s^0 K^\pm \pi^\mp}(m_{K_s^0\pi}^2, m_{K\pi}^2)|^2$, while the combinatorial component is described by a smooth function, $c_{K_s^0 K^\pm \pi^\mp}(m_{K_s^0\pi}^2, m_{K\pi}^2)$, obtained by applying to data in the $m(K_s^0 K\pi)$ sidebands the same non-parametric kernel estimator used to model the efficiency variation. The same combinatorial background model is used for both D^0 flavours, and the same efficiency function is used for both modes and D^0 flavours. The overall function used in the fit to $D^0 \rightarrow K_s^0 K^\pm \pi^\mp$ decays is therefore

$$\begin{aligned} P_{K_s^0 K^\pm \pi^\mp}(m_{K_s^0\pi}^2, m_{K\pi}^2) &= (1 - f_m - f_c) \varepsilon(m_{K_s^0\pi}^2, m_{K\pi}^2) |\mathcal{M}_{K_s^0 K^\pm \pi^\mp}(m_{K_s^0\pi}^2, m_{K\pi}^2)|^2 \\ &\quad + f_m \varepsilon(m_{K_s^0\pi}^2, m_{K\pi}^2) |\bar{\mathcal{M}}_{K_s^0 K^\pm \pi^\mp}(m_{K_s^0\pi}^2, m_{K\pi}^2)|^2 \\ &\quad + f_c c_{K_s^0 K^\pm \pi^\mp}(m_{K_s^0\pi}^2, m_{K\pi}^2), \end{aligned} \quad (6.5)$$

where the mistagged contribution consists of $\bar{D}^0 \rightarrow K_s^0 K^\pm \pi^\mp$ decays and f_m (f_c) denotes the mistagged (combinatorial) fraction tabulated in Table 5.3.

All parameters except the complex amplitudes $a_R e^{i\phi_R}$ are shared between the PDFs for both modes and both D^0 flavours. For the other parameters, Gaussian constraints are included unless stated otherwise. The nominal values used in the constraints are tabulated in Appendix A. No constraints are applied for the $K\pi$ S -wave parameters $b_{1..3}$, F , ϕ_S and ϕ_F , as these have no suitable nominal values. The $K\pi$ S -wave parameters a and r are treated differently in the **GLASS** and **LASS** models. In the **LASS** case these parameters are shared between the neutral and charged $K\pi$ channels and a Gaussian constraint to the **LASS** measurements [184] is included. In the **GLASS** case these are allowed to vary freely and take different values for the two channels.

6.2 Coherence factor and CP -even fraction

The coherence factor R_f and mean strong-phase difference δ_f for the multi-body decays $D \rightarrow f$ and $D \rightarrow \bar{f}$ quantify the similarity of the two decay structures [183]. In the limit $R_f \rightarrow 1$ the matrix elements for the two decays are identical. For $D^0 \rightarrow K_s^0 K^\pm \pi^\mp$ the coherence factor and mean strong-phase difference are defined by [61, 182]

$$R_{K_s^0 K\pi} e^{-i\delta_{K_s^0 K\pi}} \equiv \frac{\int \mathcal{M}_{K_s^0 K^+ \pi^-}(m_{K_s^0 \pi}^2, m_{K\pi}^2) \mathcal{M}_{K_s^0 K^- \pi^+}^*(m_{K_s^0 \pi}^2, m_{K\pi}^2) dm_{K_s^0 \pi}^2 dm_{K\pi}^2}{M_{K_s^0 K^+ \pi^-} M_{K_s^0 K^- \pi^+}}, \quad (6.6)$$

where

$$M_{K_s^0 K^\pm \pi^\mp}^2 \equiv \int |\mathcal{M}_{K_s^0 K^\pm \pi^\mp}(m_{K_s^0 \pi}^2, m_{K\pi}^2)|^2 dm_{K_s^0 \pi}^2 dm_{K\pi}^2, \quad (6.7)$$

and the integrals are over the entire available phase space. The restricted phase space coherence factor $R_{K^* K} e^{-i\delta_{K^* K}}$ is defined analogously but with all integrals restricted to an area of phase space close to the $K^*(892)^\pm$ resonance. The restricted area is defined by Ref. [61] as the region where the $K_s^0 \pi^\pm$ invariant mass is within $100 \text{ MeV}/c^2$ of the $K^*(892)^\pm$ mass. The four observables $R_{K_s^0 K\pi}$, $\delta_{K_s^0 K\pi}$, $R_{K^* K}$ and $\delta_{K^* K}$ have been measured using quantum-correlated $\psi(3770) \rightarrow D^0 \bar{D}^0$ decays by the CLEO collaboration [61], and the coherence was found to be large for both the full and the restricted regions. This LHCb amplitude analysis is not sensitive to the overall phase difference between $D^0 \rightarrow K_s^0 K^+ \pi^-$ and $\bar{D}^0 \rightarrow K_s^0 K^+ \pi^-$.

However, because this overall phase cancels, the combination $\delta_{K_S^0 K\pi} - \delta_{K^* K}$ can be calculated from the isobar models, along with $R_{K_S^0 K\pi}$ and $R_{K^* K}$. There are, therefore, three parameters that can be compared to CLEO results.

An associated parameter that it is interesting to consider is the CP -even fraction [92],

$$F_+ \equiv \frac{|\langle D_+ | K_S^0 K^\pm \pi^\mp \rangle|^2}{|\langle D_+ | K_S^0 K^\pm \pi^\mp \rangle|^2 + |\langle D_- | K_S^0 K^\pm \pi^\mp \rangle|^2} \quad (6.8)$$

where the CP eigenstates $|D_\pm\rangle$ are given by $\frac{1}{\sqrt{2}} [|D^0\rangle \pm |\bar{D}^0\rangle]$. The amplitude for one CP eigenstate, $|D_\pm\rangle$, is given by

$$\begin{aligned} |\langle D_\pm | K_S^0 K^- \pi^+ \rangle|^2 &= \frac{1}{2} \left| \langle D^0 | K_S^0 K^- \pi^+ \rangle \pm \langle \bar{D}^0 | K_S^0 K^- \pi^+ \rangle \right|^2 \\ &= \frac{1}{2} M_{K_S^0 K^- \pi^+}^2 \left[1 + \frac{M_{K_S^0 K^+ \pi^-}^2}{M_{K_S^0 K^- \pi^+}^2} \pm 2 \frac{M_{K_S^0 K^+ \pi^-}}{M_{K_S^0 K^- \pi^+}} R_{K_S^0 K\pi} \cos(\delta_{K_S^0 K\pi}) \right] \\ &= \frac{\alpha}{2} \left[1 + \mathcal{B}_{K_S^0 K\pi} \pm 2 \sqrt{\mathcal{B}_{K_S^0 K\pi}} R_{K_S^0 K\pi} \cos(\delta_{K_S^0 K\pi}) \right], \end{aligned} \quad (6.9)$$

where $\mathcal{B}_{K_S^0 K\pi}$ is the ratio of branching fractions of the two $D^0 \rightarrow K_S^0 K^\pm \pi^\mp$ modes, α is a constant, the effects of direct CP violation have been neglected and the $K_S^0 K^- \pi^+$ final state has been chosen for clarity. The CP -even fraction is given by

$$\begin{aligned} F_+ &= \frac{1}{2} \frac{1 + \mathcal{B}_{K_S^0 K\pi} + 2 \sqrt{\mathcal{B}_{K_S^0 K\pi}} R_{K_S^0 K\pi} \cos(\delta_{K_S^0 K\pi})}{1 + \mathcal{B}_{K_S^0 K\pi}} \\ &= \frac{1}{2} \left[1 + 2 R_{K_S^0 K\pi} \cos(\delta_{K_S^0 K\pi}) \sqrt{\mathcal{B}_{K_S^0 K\pi}} (1 + \mathcal{B}_{K_S^0 K\pi})^{-1} \right]. \end{aligned} \quad (6.10)$$

As stated above, the relative strong phase $\delta_{K_S^0 K\pi}$ is not predicted by the amplitude models and requires external input.

6.3 Model-finding procedure

Amplitude models are fitted using an unbinned maximum-likelihood method, using the GooFit [190] package to exploit massively-parallel Graphics Processing Unit (GPU) architectures. Where χ^2/bin values are quoted these are simply to indicate the fit quality.

Table 6.2: Resonances initially considered for inclusion in each isobar model.

$K^{*-} \rightarrow K_s^0 \pi^-$	$K^{*0} \rightarrow K^- \pi^+$	$\rho^+, a^+ \rightarrow K_s^0 K^+$
$K^*(892)^-$	$K^*(892)^0$	$a_0(980)^+$
$K^*(1410)^-$	$K^*(1410)^0$	$a_2(1320)^+$
$K_0^*(1430)^-$	$K_0^*(1430)^0$	$a_0(1450)^+$
$K_2^*(1430)^-$	$K_2^*(1430)^0$	$\rho(1450)^+$
$K^*(1680)^-$	$K^*(1680)^0$	$\rho(1700)^+$

Statistical uncertainties on derived quantities, such as the resonance fit fractions, are calculated using a pseudoexperiment method based on the fit covariance matrix.

Initially, 15 resonances are considered for inclusion in each isobar model. These are summarised in Table 6.2. Preliminary studies showed that models containing the $K^*(1680)$ resonances tend to include large interference terms, which are cancelled by other large components. Such fine-tuned interference effects are in general unphysical, and are therefore disfavoured in the model-finding procedure [66, 191]. It is worth noting that the large masses of the $K^*(1680)$ resonances imply that only their low-mass tails enter the kinematically-allowed regions of the $D^0 \rightarrow K_s^0 K^\pm \pi^\mp$ Dalitz plots. The $K^*(1680)$ resonances are not considered further, and additionally the absolute value of the sum of interference fractions [192] is required to be less than 30 % in all models. In the absence of the $K^*(1680)$ resonances, large interference terms are typically generated by the $K\pi$ S -wave contributions. The requirement on the sum of interference fractions, while arbitrary, allows an iterative procedure to be used to search for the best amplitude models. This procedure explores a large number of possible starting configurations and sets of resonances; it begins with the most general models containing all 13 resonances and considers progressively simpler configurations, trying a large number of initial fit configurations for each set of resonances, until no further improvement in fit quality is found among models simple enough to satisfy the interference fraction limit. Higher values of this limit lead to a large number of candidate models with similar fit quality.

A second procedure iteratively removes resonances from the models if they do not significantly improve the fit quality. In this step a resonance must improve the value of $-2 \log \mathcal{L}$, where \mathcal{L} is the likelihood of the full dataset, by at least 16 units in order to be retained. This threshold corresponds, approximately, to a change of 0.01 units in χ^2/bin for the model

in question. Up to this point, the $K^*(892)$ mass and width parameters and $K\pi$ S -wave parameters have been allowed to vary in the fit, but mass and width parameters for other resonances have been fixed. To improve the quality of fit further, in a third step, S - and P -wave resonance parameters are allowed to vary. The tensor resonance parameters are known precisely [54], so remain fixed. At this stage, resonances that no longer significantly improve the fit quality are removed, with the threshold tightened so that each resonance must increase $-2 \log \mathcal{L}$ by 25 units in order to be retained.

Finally, parameters that are consistent with their nominal values to within 1σ are fixed to the nominal value. The nominal values used are tabulated in Appendix A. The entire procedure is performed in parallel using the **GLASS** and **LASS** parameterisations of the $K\pi$ S -wave. Some additional adjustments are made to the final models; these are discussed in Sect. 6.5.

6.4 Application of model-finding procedure

This section will summarise the evolution of the amplitude models as the iterative procedure described in Sect. 6.3 is applied to the LHCb dataset.

For each new step in the procedure several starting configurations are generated by removing – or adding, if the resonance has already been removed – each resonance in turn from each mode. Every step also includes a “no change” configuration. The $K^*(892)$ resonances are excluded from this procedure and are present in all models. Ten copies are made of each new configuration and their parameter values are randomised by generating amplitudes log-uniform in the range $[e^{-2}, e^2]$ and phases uniform between $-\pi$ and π . This excludes the $K^*(892)^\pm$ complex amplitude, which is always fixed to unity. In the first iteration, the fits begin with the **LASS** form factor parameters $b_{1..3}$ at zero, as no other seed values are available, and the other **LASS** and **GLASS** parameters are started at the values given in Appendix A.

The results for the first iteration are shown in Tables 6.3 (**GLASS**) and 6.4 (**LASS**), where several selection requirements have been imposed to reject outliers. Each table shows which model is retained for the second iteration of the procedure, alongside the quantity “DFF”

Table 6.3: Fit results after the first iteration of the model-finding procedure using the **GLASS** $K\pi$ *S*-wave parameterisation.

Description	$D^0 \rightarrow K_s^0 K^- \pi^+$		$D^0 \rightarrow K_s^0 K^+ \pi^-$		$\Delta(-2 \log \mathcal{L})$	Retained
	χ^2/bin	DFF [%]	χ^2/bin	DFF [%]		
No $a_0(1450)^+$ in $D^0 \rightarrow K_s^0 K^+ \pi^-$	1.18	107.0	1.10	85.8	169.2	No
No $\bar{K}^*(1410)^0$ in $D^0 \rightarrow K_s^0 K^- \pi^+$	1.17	129.8	1.10	71.6	160.6	No
No $a_0(980)^-$ in $D^0 \rightarrow K_s^0 K^- \pi^+$	1.18	109.1	1.09	90.9	130.0	No
No $K_2^*(1430)^+$ in $D^0 \rightarrow K_s^0 K^- \pi^+$	1.13	105.0	1.08	71.7	—	Yes

Table 6.4: Fit results after the first iteration of the model-finding procedure using the **LASS** $K\pi$ *S*-wave parameterisation. The penultimate model is chosen in preference to the final row because its fit quality is not significantly different, but the DFF values are closer to 100 % and our theoretical prejudice is that neutral K^* contributions should be suppressed with respect to their charged counterparts. It will be shown that the $K_2^*(1430)^-$ state is removed from the $D^0 \rightarrow K_s^0 K^+ \pi^-$ model in a later iteration.

Description	$D^0 \rightarrow K_s^0 K^- \pi^+$		$D^0 \rightarrow K_s^0 K^+ \pi^-$		$\Delta(-2 \log \mathcal{L})$	Retained
	χ^2/bin	DFF [%]	χ^2/bin	DFF [%]		
No $a_2(1320)^-$ in $D^0 \rightarrow K_s^0 K^- \pi^+$	1.14	119.5	1.10	89.7	13.7	No
No $\bar{K}_2^*(1430)^0$ in $D^0 \rightarrow K_s^0 K^- \pi^+$	1.13	113.5	1.10	90.8	4.1	Yes
No $K_2^*(1430)^-$ in $D^0 \rightarrow K_s^0 K^+ \pi^-$	1.13	115.3	1.10	89.1	—	No

(diagonal fit fraction), which is the sum of fit fractions [192] from the various resonances, excluding interference terms. The important requirement, introduced in Sect. 6.3, that $70\% < \text{DFF} < 130\%$ is applied in these tables, while models must additionally have $\chi^2/\text{bin} < 1.3$ separately for each $D^0 \rightarrow K_s^0 K^\pm \pi^\mp$ decay mode, and the increase, $\Delta(-2 \log \mathcal{L})$, in negative log-likelihood with respect to the best model must be less than 200 units. Loose selection requirements are also applied to some fitted values in models using the **GLASS** parameterisation to exclude fits where these float excessively far. It is required that $a \in [10^{-4}, 99]$, $r \in [-99, +99]$ and $F \in [10^{-4}, 9.9]$. These ranges are slightly narrower than the parameter ranges imposed in the minimisation algorithm to mitigate poor behaviour in that regime.

The results for the second iteration are shown in Tables 6.5 (**GLASS**) and 6.6 (**LASS**), where the upper limit on χ^2/bin for each mode has been tightened from 1.3 to 1.2 for brevity. In the second iteration, $K\pi$ *S*-wave parameters that were floated freely during the first iteration are seeded with, but not constrained to, the values from the models retained in the first iteration. These parameters are tabulated in Appendix B. Parameters that were constrained in the fit, *i.e.* the $K^*(892)$, $K_0^*(1430)$ and – in the **LASS** case – the a and r $K\pi$ *S*-wave

Table 6.5: Fit results after the second iteration of the model-finding procedure using the **GLASS** $K\pi$ *S*-wave parameterisation. Descriptions are relative to the retained model in Table 6.3.

Description	$D^0 \rightarrow K_s^0 K^- \pi^+$		$D^0 \rightarrow K_s^0 K^+ \pi^-$		$\Delta(-2 \log \mathcal{L})$	Retained
	χ^2/bin	DFF [%]	χ^2/bin	DFF [%]		
No $\rho(1450)^+$ in $D^0 \rightarrow K_s^0 K^+ \pi^-$	1.17	125.4	1.08	79.1	97.9	No
No $K_2^*(1430)^0$ in $D^0 \rightarrow K_s^0 K^+ \pi^-$	1.13	98.1	1.10	73.3	68.5	No
No $a_0(1450)^+$ in $D^0 \rightarrow K_s^0 K^+ \pi^-$	1.14	104.2	1.10	73.8	64.7	No
No $\bar{K}_2^*(1430)^0$ in $D^0 \rightarrow K_s^0 K^- \pi^+$	1.13	113.1	1.09	70.3	41.4	No
No $K^*(1410)^-$ in $D^0 \rightarrow K_s^0 K^+ \pi^-$	1.12	100.6	1.09	73.0	33.9	No
No $a_2(1320)^-$ in $D^0 \rightarrow K_s^0 K^- \pi^+$	1.14	105.2	1.08	72.4	33.8	No
No $\rho(1450)^-$ in $D^0 \rightarrow K_s^0 K^+ \pi^-$	1.14	126.0	1.08	71.1	30.9	No
No $K_2^*(1430)^-$ in $D^0 \rightarrow K_s^0 K^+ \pi^-$	1.13	100.3	1.08	77.1	27.5	No
No $\rho(1700)^-$ in $D^0 \rightarrow K_s^0 K^- \pi^+$	1.14	106.8	1.08	70.1	25.7	No
No $\rho(1450)^+$ in $D^0 \rightarrow K_s^0 K^+ \pi^-$	1.13	101.8	1.08	73.3	16.1	No
No $a_0(980)^-$ in $D^0 \rightarrow K_s^0 K^- \pi^+$	1.13	102.0	1.08	72.7	11.1	No
No $a_2(1320)^+$ in $D^0 \rightarrow K_s^0 K^+ \pi^-$	1.13	105.9	1.08	71.1	1.8	Yes
No change	1.13	105.1	1.08	71.1	—	No

parameters, are reset to their nominal values in the new configurations. In the **GLASS** results (Table 6.5) the best-fitting model has the same resonance content as the seed model taken from Table 6.3, indicating that no further change is preferred and the first stage of the model-finding procedure has converged. However, the change in $-2 \log \mathcal{L}$ from the best model to the model which removes the $a_2(1320)^+$ resonance from the $D^0 \rightarrow K_s^0 K^+ \pi^-$ mode is only 1.8 units. This is not deemed significant, so the model with fewer resonances is preferred. Similarly the **LASS** results (Table 6.6) show a weak preference for a model that reverts the removal, in the first iteration, of the $\bar{K}_2^*(1430)^0$ resonance from the $D^0 \rightarrow K_s^0 K^- \pi^+$ model. Again, the model with the fewest resonances is preferred: the $K_2^*(1430)^+$ is removed from the $D^0 \rightarrow K_s^0 K^- \pi^+$ model, and the first stage of the model-finding procedure has converged.

The next stage in the model-finding procedure is to “clean” the models. This is similar to the previous iterations in that each resonance is removed in turn from the current best models, but differs in that no parameters are randomised or reset. The change in $-2 \log \mathcal{L}$ is evaluated with respect to the current best model, and the resonance that produces the smallest improvement in fit quality is removed until all remaining resonances improve $-2 \log \mathcal{L}$ by at least 16 units. This procedure converges after two iterations for the models using the **GLASS** $K\pi$ *S*-wave parameterisation, and after four iterations when the **LASS** parameterisa-

Table 6.6: Fit results after the second iteration of the model-finding procedure using the LASS $K\pi$ S -wave parameterisation. Descriptions are relative to the retained model in Table 6.4.

Description	$D^0 \rightarrow K_s^0 K^- \pi^+$		$D^0 \rightarrow K_s^0 K^+ \pi^-$		$\Delta(-2 \log \mathcal{L})$	Retained
	χ^2/bin	DFF [%]	χ^2/bin	DFF [%]		
No $a_0(1450)^-$ in $D^0 \rightarrow K_s^0 K^- \pi^+$	1.19	118.7	1.08	93.4	87.1	No
No $\rho(1700)^+$ in $D^0 \rightarrow K_s^0 K^+ \pi^-$	1.12	110.0	1.15	88.2	79.2	No
No $K^*(1410)^-$ in $D^0 \rightarrow K_s^0 K^+ \pi^-$	1.14	114.4	1.11	93.0	41.4	No
No $a_2(1320)^-$ in $D^0 \rightarrow K_s^0 K^- \pi^+$	1.14	122.9	1.10	91.3	27.4	No
No $K^*(1410)^0$ in $D^0 \rightarrow K_s^0 K^- \pi^+$	1.13	109.7	1.11	99.3	26.6	No
No $\rho(1700)^-$ in $D^0 \rightarrow K_s^0 K^- \pi^+$	1.14	119.5	1.10	91.6	24.9	No
No $\rho(1450)^+$ in $D^0 \rightarrow K_s^0 K^+ \pi^-$	1.13	113.2	1.11	82.6	21.6	No
No $K_2^*(1430)^-$ in $D^0 \rightarrow K_s^0 K^+ \pi^-$	1.14	115.5	1.10	89.2	11.0	No
No $K_2^*(1430)^0$ in $D^0 \rightarrow K_s^0 K^+ \pi^-$	1.13	112.4	1.10	91.6	9.6	No
No $a_2(1320)^+$ in $D^0 \rightarrow K_s^0 K^+ \pi^-$	1.13	115.1	1.10	90.7	6.8	No
No change	1.13	113.6	1.10	90.8	5.0	No
No $K_2^*(1430)^+$ in $D^0 \rightarrow K_s^0 K^- \pi^+$	1.13	113.4	1.10	90.6	4.9	Yes
Add $\bar{K}_2^*(1430)^0$ to $D^0 \rightarrow K_s^0 K^- \pi^+$	1.13	114.7	1.10	89.1	—	No

tion is used. These iterations are detailed in Appendix B.

The majority of resonance mass and decay width parameters, m_R and Γ_R , have remained fixed in the fits discussed thus far. The next stage in the model-finding procedure is to allow additional $J = 0$ and $J = 1$ resonance parameters to vary with Gaussian constraints to their nominal values. The freed parameters are the $a_0(980)^\pm$ mass and the $a_0(1450)^\pm$, $\rho(1450)^\pm$, $\rho(1700)^\pm$, $K^*(1410)^\pm$ and $K^*(1410)^0$ masses and widths. The $a_0(980)^\pm$ resonance is described by the coupled-channel Flatté dynamical function and lacks an appropriate width parameter to vary. This process is referred to as “refining” the models. The $J = 2$ resonance parameters are precisely known [54] and remain fixed in the fits. When this procedure is applied to the best model using the LASS $K\pi$ S -wave parameterisation a reasonable model with some tension in the $a_0(980)^\pm$ mass is produced. Applying the same procedure to the best model using the GLASS $K\pi$ S -wave parameterisation produces a model with the $a_0(980)^\pm$ mass nearly 4σ ($80 \text{ MeV}/c^2$) below the nominal value. If this parameter is fixed to the nominal value then the $\rho(1450)^\pm$ mass is forced to $1115 \text{ MeV}/c^2$, which is 2.2σ below the nominal value and well within one decay width of the $K_s^0 K^\pm$ kinematic threshold. The “refined” model using the GLASS parameterisation, therefore, fixes both the $a_0(980)^\pm$ and $\rho(1450)^\pm$ masses to the nominal values.

The additional degrees of freedom introduced in the refining procedure can reduce the significance of resonances in the models. To ensure the final models contain only resonances that significantly improve the description of the data, a second cleaning procedure is applied to the models. This differs from the first cleaning procedure in that the threshold in $\Delta (-2 \log \mathcal{L})$ is increased from 16 to 25 units, and the additional parameters that were set free in the refining stage remain free. This procedure converges after two iterations for the models using the GLASS $K\pi$ *S*-wave parameterisation, and requires three iterations when the LASS parameterisation is used. These iterations are described in Appendix B. Several minor adjustments made to the resulting models are described in Sect. 6.5, but none of these affect the resonance content or the qualitative results.

6.5 Model adjustments

Several checks are carried out on the final models described in Sect. 6.4, and minor adjustments are made in order to stabilise uncertainty calculations and remove redundant degrees of freedom. First, the models are re-fitted using polar coordinates, $a_R e^{i\phi_R}$, for the complex amplitudes in place of the cartesian parameterisation used throughout the model-finding process. This allows the minimisation algorithm, MINUIT, to calculate uncertainties directly on the polar coordinates, which are of greater physical interest than the cartesian forms. The cartesian parameterisation is superior for preliminary studies because it remains well-behaved when amplitudes approach zero.

The next adjustment is to fix parameters where a prior measurement exists and the fitted value lies within 1σ , as reported by the fit, of the known value. This typically affects parameters that were floated with Gaussian constraints but are not significantly constrained by the LHCb dataset. The adjustment is made for two reasons: first, it reduces the number of free parameters the minimisation algorithm must process, and, second, the values to be fixed are not independent measurements of the parameters in question and are not, therefore, suitable for inclusion in averages such as Ref. [54]. Nine parameters are fixed in the best model using the GLASS $K\pi$ *S*-wave parameterisation and eleven in the best model using the

LASS parameterisation. These are listed in Appendix B.

The data are found to prefer a solution where the **GLASS** parameterisation of the charged $K\pi$ *S*-wave has a poorly constrained degree of freedom, and large correlations are found between three parameters: the charged $K\pi$ *S*-wave amplitude parameters, a_R , in the two $D^0 \rightarrow K_s^0 K^\pm \pi^\mp$ decay modes, and the corresponding **GLASS** F parameter. The data favour a relatively large value of F , so the **GLASS** dynamical function is approximately proportional to F and there is, approximately, a redundant degree of freedom. The distribution of these three parameters in an ensemble of pseudoexperiments generated from the best isobar model is shown in Fig. 6.2. To stabilise the fit, and in particular the uncertainty calculation, the F parameter for the charged $K\pi$ *S*-wave is fixed to its central value, 1.785, in the best models using the **GLASS** parameterisation.

It was noted above, in Sect. 6.1, that a transformed set of LASS parameterisation form factor parameters, $b'_{1,2,3}$, is used to reduce correlations among the fit parameters used by the numerical minimisation algorithm. The transformation matrix is defined by $\mathbf{b}' = \mathbf{U}^{-1}\mathbf{b}$ and

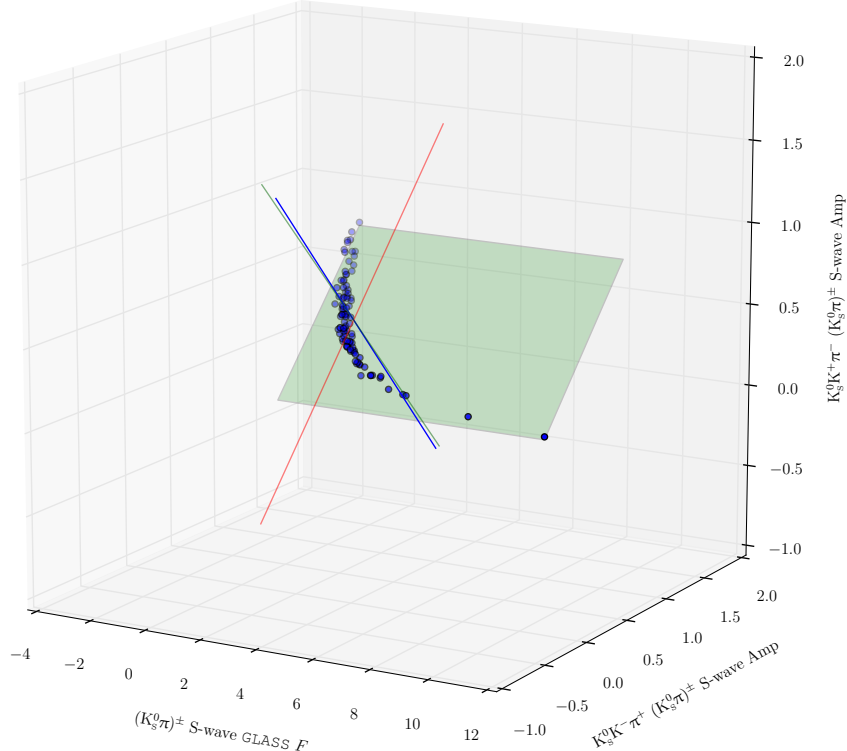


Figure 6.2: Three-dimensional scatter plot illustrating the large correlations seen between the **GLASS** $K\pi$ *S*-wave parameter F and the corresponding resonance amplitudes, a_R . Also shown are the best-fit plane and right-singular vectors of the distribution.

is derived from a singular value decomposition of $b_{1,2,3}$ values obtained in an ensemble of pseudoexperiments generated from the best isobar models. The transformation is illustrated in Fig. 6.3, while the transformation matrices are tabulated in Appendix C.

6.6 Systematic uncertainties

Several sources of systematic uncertainty are considered. Those due to experimental issues are described first, followed by uncertainties related to the amplitude model formalism. Unless otherwise stated, the uncertainty assigned to each parameter using an alternative fit is the absolute difference in its value between the nominal and alternative fit.

As mentioned in Sect. 5.4, candidates extremely close to the edges of the allowed kinematic region of the Dalitz plot are excluded. The requirement made is that the largest of the three $|\cos(\theta_{AB})|$ values is less than 0.98. A systematic uncertainty due to this process is estimated by changing the threshold to 0.96, as this excludes a similar additional area of the Dalitz plot as the original requirement.

The systematic uncertainty related to the efficiency model $\varepsilon(m_{K_S^0\pi}^2, m_{K\pi}^2)$ is evaluated in four ways. The first probes the process by which a smooth curve is produced from simulated events; this uncertainty is evaluated using an alternative fit that substitutes the non-parametric estimator with a polynomial parameterisation. The second uncertainty is due to the limited sample size of simulated events. This is evaluated by generating several alternative polynomial efficiency models according to the covariance matrix of the polynomial model parameters; the spread in parameter values from this ensemble is assigned as the uncertainty due to the limited sample size. The third contribution is due to possible imperfections in the description of the data by the simulation. This uncertainty is assigned using an alternative simultaneous fit that separates the sample into three categories according to the year in which the data were collected and the type of K_S^0 candidate used. As noted in Sect. 5.2, the sample recorded during 2011 does not include downstream K_S^0 candidates. These sub-samples have different kinematic distributions and $\varepsilon(m_{K_S^0\pi}^2, m_{K\pi}^2)$ behaviour, so

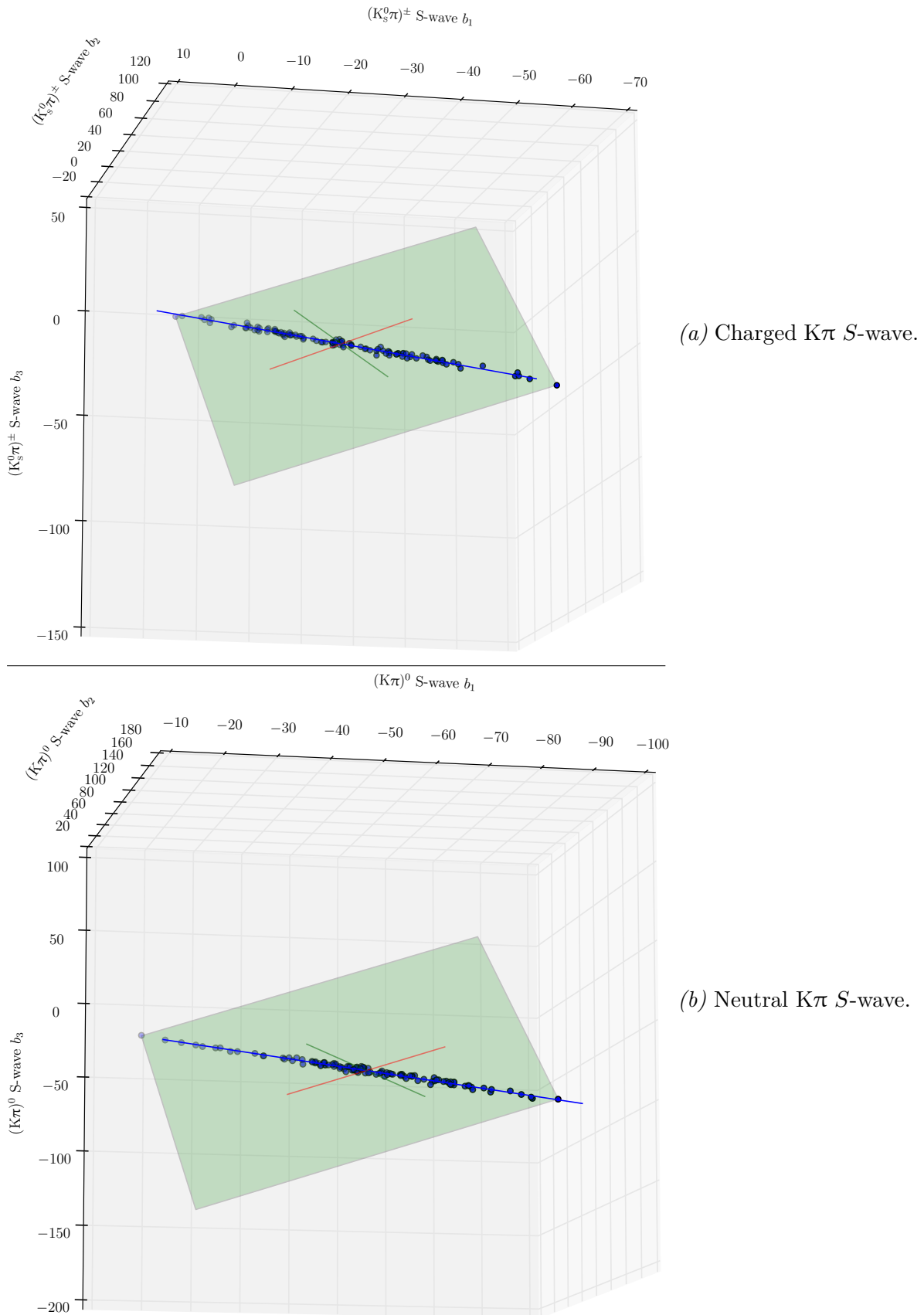


Figure 6.3: Three-dimensional scatter plots illustrating the large correlations seen among the LASS parameterisation form factor parameters for the charged (a) and neutral (b) $K\pi$ S-wave before they are transformed. Also shown are the best-fit plane and the right-singular vectors, which correspond to the new coordinates $b'_{1,2,3}$.

this procedure tests the ability of the simulation process to reproduce the variation seen in the data.

The final contribution is due to the re-weighting procedures used to include the effect of offline selection requirements based on information from the RICH detectors, and to correct for discrepancies between data and simulation in the reconstruction efficiencies of long and downstream K_s^0 candidates. This is evaluated using alternative efficiency models where the relative proportion of the track types is altered, and the weights describing the efficiency of selection requirements using information from the RICH detectors are modified to account for the limited calibration sample size. Additional robustness checks have been performed to probe the description of the efficiency function by the simulated events. In these checks the data are divided into two equally-populated bins of the D^0 meson p , p_T or pseudorapidity and the amplitude models are re-fitted using each bin separately. The fit results in each pair of bins are found to be compatible within the assigned uncertainties, indicating that the simulated D^0 kinematics adequately match the data.

An uncertainty is assigned due to the description of the hardware trigger efficiency in simulated events. Because the signal decay may not be responsible for firing the hardware trigger, it is important that the underlying pp interaction is well described, and a systematic uncertainty is assigned due to possible imperfections. This uncertainty is obtained using an alternative efficiency model generated from simulated events that have been weighted to adjust the fraction where the hardware trigger was fired by the signal candidate.

The uncertainty due to the description of the combinatorial background is evaluated by recomputing the $c_{K_s^0 K^\pm \pi^\mp}(m_{K_s^0 \pi}^2, m_{K\pi}^2)$ function using $m(K_s^0 K\pi)$ sideband events to which an alternative kinematic fit has been applied, without a constraint on the D^0 mass. The alternative model is expected to describe the edges of the phase space less accurately, while providing an improved description of peaking features.

An alternative set of models is produced using a threshold of 9 units in the value of $-2 \log \mathcal{L}$ instead of the thresholds of 16 and 25 used for the model-finding procedure. These models contain more resonances, as fewer are removed during the model-finding process. A

systematic uncertainty is assigned using these alternative models for those parameters which are common between the two sets of models.

Two parameters of the Flatté dynamical function, which is used to describe the $a_0(980)^\pm$ resonance, are fixed to nominal values in the isobar model fits. Alternative fits are performed, where these parameters are fixed to different values according to their quoted uncertainties, and the largest changes to the fit parameters are assigned as systematic uncertainties.

The effect of resolution in the $m_{K_s^0 \pi}^2$ and $m_{K\pi}^2$ coordinates is neglected in the isobar model fits, and this is expected to have an effect on the measured $K^*(892)^\pm$ decay width. An uncertainty is calculated using a pseudoexperiment method, and is found to be small.

The uncertainty due to the yield determination process described in Sect. 5.3 is measured by changing the fractions f_m and f_c in the isobar model fit according to their statistical uncertainties, and taking the largest changes with respect to the nominal result as the systematic uncertainty.

There are two sources of systematic uncertainty due to the amplitude model formalism considered. The first is that due to varying the meson radius parameters d_{D^0} and d_R , defined in Sect. 2.4. These are changed from $d_{D^0} = 5.0\,c/\text{GeV}$ and $d_R = 1.5\,c/\text{GeV}$ to $2.5\,c/\text{GeV}$ and $1.0\,c/\text{GeV}$, respectively [61, 67]. The second is due to the dynamical function T_R used to describe the $\rho(1450, 1700)^\pm$ resonances. These resonances are described by the Gounaris-Sakurai functional form in the nominal models, which is replaced with a relativistic P -wave Breit-Wigner function to calculate a systematic uncertainty due to this choice.

The uncertainties described above are added in quadrature to produce the total systematic uncertainty quoted for the various results. For most quantities the dominant systematic uncertainty is due to the meson radius parameters d_{D^0} and d_R . The largest sources of experimental uncertainty relate to the description of the efficiency variation across the Dalitz plot. The fit procedure and statistical uncertainty calculation have been validated using pseudo-experiments and no bias was found. Tables summarising the various sources of systematic uncertainty and their relative contributions are included in Appendix D.

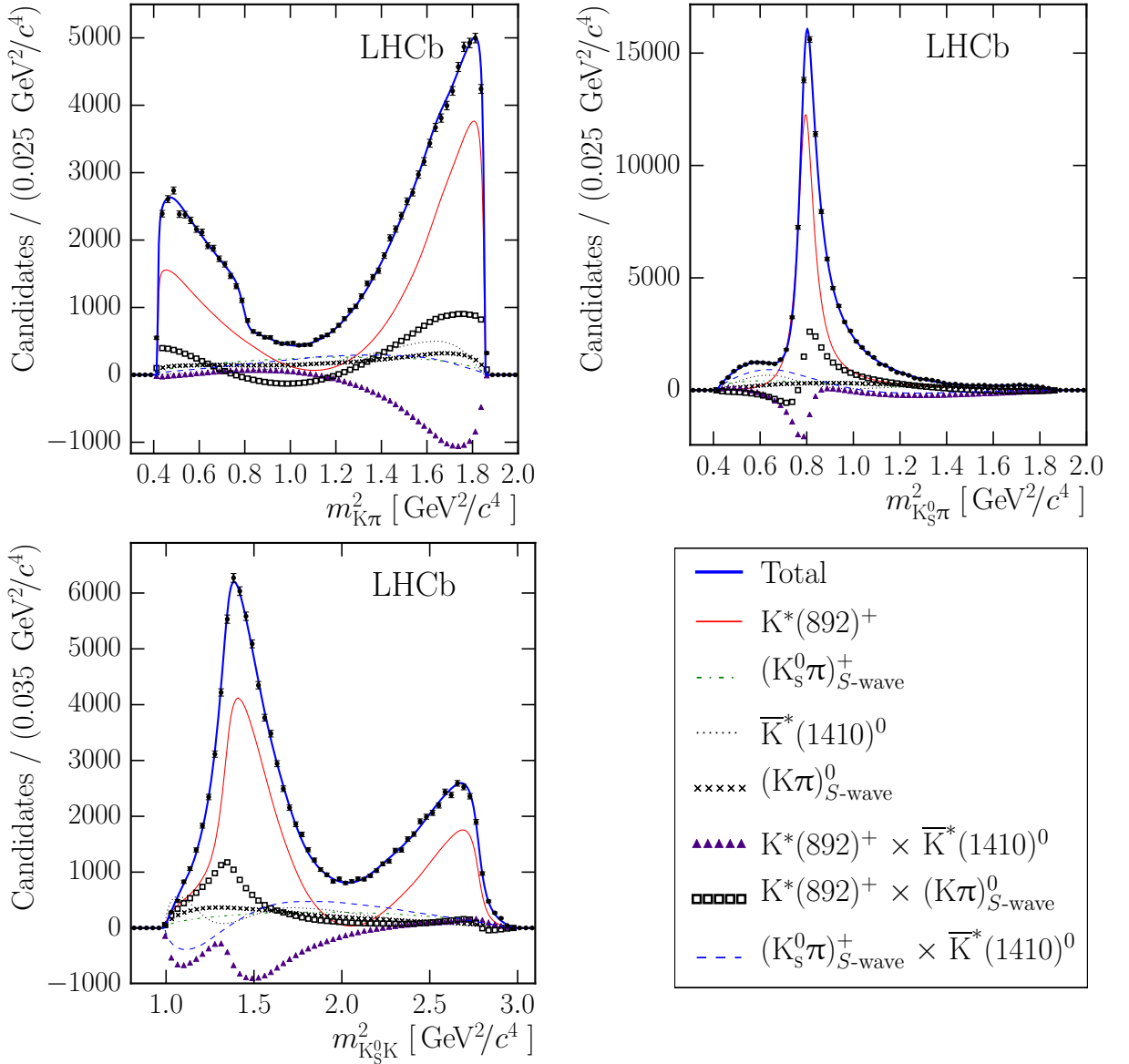


Figure 6.4: Distributions of $m_{K\pi}^2$ (upper left), $m_{K_S^0\pi}^2$ (upper right) and $m_{K_S^0K}^2$ (lower left) in the $D^0 \rightarrow K_S^0 K^- \pi^+$ mode with fit curves from the best **GLASS** model. The solid (blue) curve shows the full PDF $P_{K_S^0 K^- \pi^+}(m_{K_S^0\pi}^2, m_{K\pi}^2)$, while the other curves show the components with the largest integrated fractions. The solid black markers indicate the data.

6.7 Model results

The fit results for the best isobar models using the **GLASS** and **LASS** parameterisations of the $K\pi$ S -wave are given in Table 6.7. Distributions of $m_{K\pi}^2$, $m_{K_S^0\pi}^2$ and $m_{K_S^0K}^2$ are shown alongside the best model of the $D^0 \rightarrow K_S^0 K^- \pi^+$ mode using the **GLASS** parameterisation in Fig. 6.4. In Fig. 6.4 and elsewhere the nomenclature $R_1 \times R_2$ denotes interference terms. The corresponding distributions showing the best model using the **LASS** parameterisation

Chapter 6. Amplitude analysis of $D^0 \rightarrow K_s^0 K^\pm \pi^\mp$ decays

 Table 6.7: Isobar model fit results for the $D^0 \rightarrow K_s^0 K^\pm \pi^\mp$ modes. The first uncertainties are statistical and the second systematic.

Resonance	GLASS	a_R	$\phi_R [^\circ]$		Fit fraction [%]	
			LASS	GLASS	LASS	GLASS
$D^0 \rightarrow K_s^0 K^- \pi^+$						
$K^*(892)^+$	1.0 (fixed)		1.0 (fixed)	0.0 (fixed)	57.0 \pm 0.8 \pm 2.6	56.9 \pm 0.6 \pm 1.1
$K^*(1410)^+$	$4.3 \pm 0.3 \pm 0.7$		$5.83 \pm 0.29 \pm 0.29$	$-160 \pm 6 \pm 24$	$-143 \pm 3 \pm 6$	$9.6 \pm 1.1 \pm 2.9$
$(K_s^0 \pi)^+_{S\text{-wave}}$	$0.62 \pm 0.05 \pm 0.18$		$1.13 \pm 0.09 \pm 0.21$	$-67 \pm 5 \pm 15$	$-59 \pm 4 \pm 13$	$11.7 \pm 1.0 \pm 2.3$
$\bar{K}^*(892)^0$	$0.213 \pm 0.007 \pm 0.018$		$0.210 \pm 0.006 \pm 0.010$	$-108 \pm 2 \pm 4$	$-101.5 \pm 2.0 \pm 2.8$	$2.5 \pm 0.2 \pm 0.4$
$K^*(1410)^0$	$6.0 \pm 0.3 \pm 0.5$		$3.9 \pm 0.2 \pm 0.4$	$-179 \pm 4 \pm 17$	$-174 \pm 4 \pm 7$	$9 \pm 1 \pm 4$
$\bar{K}_2^*(1430)^0$	$3.2 \pm 0.3 \pm 1.0$		—	$-172 \pm 5 \pm 23$	—	$3.8 \pm 0.5 \pm 2.0$
$(K\pi)^0_{S\text{-wave}}$	$2.5 \pm 0.2 \pm 1.3$		$1.28 \pm 0.12 \pm 0.23$	$50 \pm 10 \pm 80$	$75 \pm 3 \pm 8$	$11 \pm 2 \pm 10$
$a_0(980)^-$	—		$1.07 \pm 0.09 \pm 0.14$	—	$82 \pm 5 \pm 7$	—
$a_2(1320)^-$	$0.19 \pm 0.03 \pm 0.09$		$0.17 \pm 0.03 \pm 0.05$	$-129 \pm 8 \pm 17$	$-128 \pm 10 \pm 8$	$0.20 \pm 0.06 \pm 0.21$
$a_0(1450)^-$	$0.52 \pm 0.04 \pm 0.15$		$0.43 \pm 0.05 \pm 0.10$	$-82 \pm 7 \pm 31$	$-49 \pm 11 \pm 19$	$1.2 \pm 0.2 \pm 0.6$
$\rho(1450)^-$	$1.6 \pm 0.2 \pm 0.5$		$1.3 \pm 0.1 \pm 0.4$	$-177 \pm 7 \pm 32$	$-144 \pm 7 \pm 9$	$1.3 \pm 0.3 \pm 0.7$
$\rho(1700)^-$	$0.38 \pm 0.08 \pm 0.15$		—	$-70 \pm 10 \pm 60$	—	$0.12 \pm 0.05 \pm 0.14$
$D^0 \rightarrow K_s^0 K^+ \pi^-$						
$K^*(892)^-$	1.0 (fixed)		1.0 (fixed)	0.0 (fixed)	$29.5 \pm 0.6 \pm 1.6$	$28.8 \pm 0.4 \pm 1.3$
$K^*(1410)^-$	$4.7 \pm 0.5 \pm 1.1$		$9.1 \pm 0.6 \pm 1.5$	$-106 \pm 6 \pm 25$	$-79 \pm 3 \pm 7$	$3.1 \pm 0.6 \pm 1.6$
$(K_s^0 \pi)^-_{S\text{-wave}}$	$0.58 \pm 0.05 \pm 0.11$		$1.16 \pm 0.11 \pm 0.32$	$-164 \pm 6 \pm 31$	$-101 \pm 6 \pm 21$	$5.4 \pm 0.9 \pm 1.7$
$K^*(892)^0$	$0.410 \pm 0.010 \pm 0.021$		$0.427 \pm 0.010 \pm 0.013$	$176 \pm 2 \pm 9$	$-175.0 \pm 1.7 \pm 1.4$	$4.82 \pm 0.23 \pm 0.35$
$K^*(1410)^0$	$6.2 \pm 0.5 \pm 1.4$		$4.2 \pm 0.5 \pm 0.9$	$175 \pm 4 \pm 14$	$165 \pm 5 \pm 10$	$5.2 \pm 0.7 \pm 1.6$
$K_2^*(1430)^0$	$6.3 \pm 0.5 \pm 1.7$		—	$-139 \pm 5 \pm 21$	—	$7 \pm 1 \pm 4$
$(K\pi)^0_{S\text{-wave}}$	$3.7 \pm 0.3 \pm 1.8$		$1.7 \pm 0.2 \pm 0.4$	$100 \pm 10 \pm 70$	$144 \pm 3 \pm 6$	$12 \pm 1 \pm 8$
$a_0(980)^+$	$1.8 \pm 0.1 \pm 0.6$		$3.8 \pm 0.2 \pm 0.7$	$64 \pm 5 \pm 24$	$126 \pm 3 \pm 6$	$11 \pm 1 \pm 6$
$a_0(1450)^+$	$0.44 \pm 0.05 \pm 0.13$		$0.86 \pm 0.10 \pm 0.12$	$-140 \pm 9 \pm 35$	$-110 \pm 8 \pm 7$	$0.45 \pm 0.09 \pm 0.34$
$\rho(1450)^+$	$2.3 \pm 0.4 \pm 0.8$		—	$-60 \pm 6 \pm 18$	—	$1.5 \pm 0.5 \pm 0.9$
$\rho(1700)^+$	$1.04 \pm 0.12 \pm 0.32$		$1.25 \pm 0.15 \pm 0.33$	$4 \pm 11 \pm 20$	$39 \pm 9 \pm 15$	$0.5 \pm 0.1 \pm 0.5$

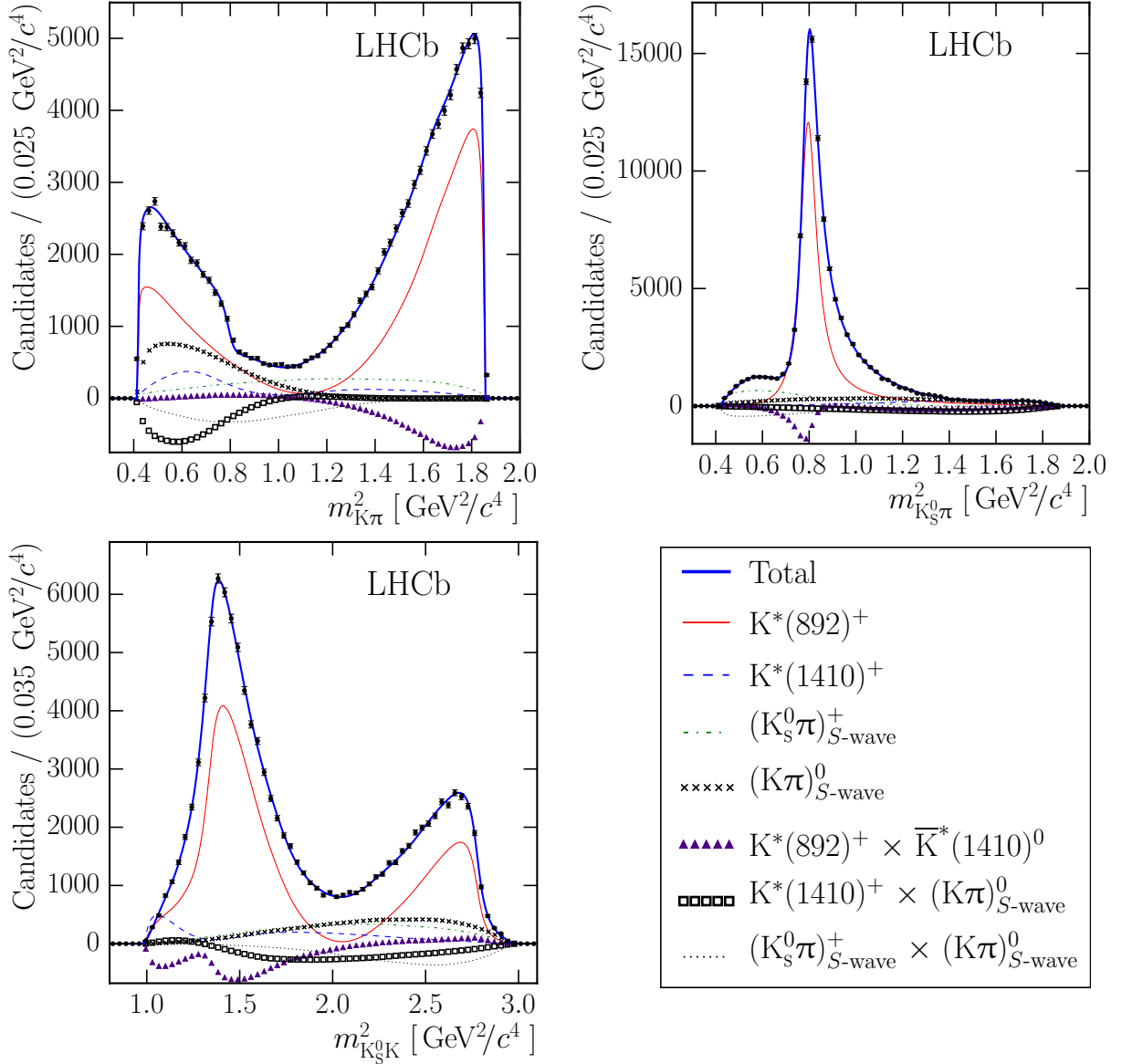


Figure 6.5: Distributions of $m_{K\pi}^2$ (upper left), $m_{K_S^0\pi}^2$ (upper right) and $m_{K_S^0K}^2$ (lower left) in the $D^0 \rightarrow K_S^0 K^- \pi^+$ mode with fit curves from the best LASS model. The solid (blue) curve shows the full PDF $P_{K_S^0 K^- \pi^+}(m_{K_S^0\pi}^2, m_{K\pi}^2)$, while the other curves show the components with the largest integrated fractions. The solid black markers indicate the data.

are shown in Fig. 6.5. Distributions for the $D^0 \rightarrow K_S^0 K^+ \pi^-$ mode are shown in Figs. 6.6 and 6.7. Figure 6.8 shows the GLASS isobar models in two dimensions, and demonstrates that the GLASS and LASS choices of $K\pi$ S -wave parameterisation both lead to similar descriptions of the overall phase variation. Lookup tables for the complex amplitude variation across the Dalitz plot in all four isobar models are available in the supplemental material of Ref. [162].

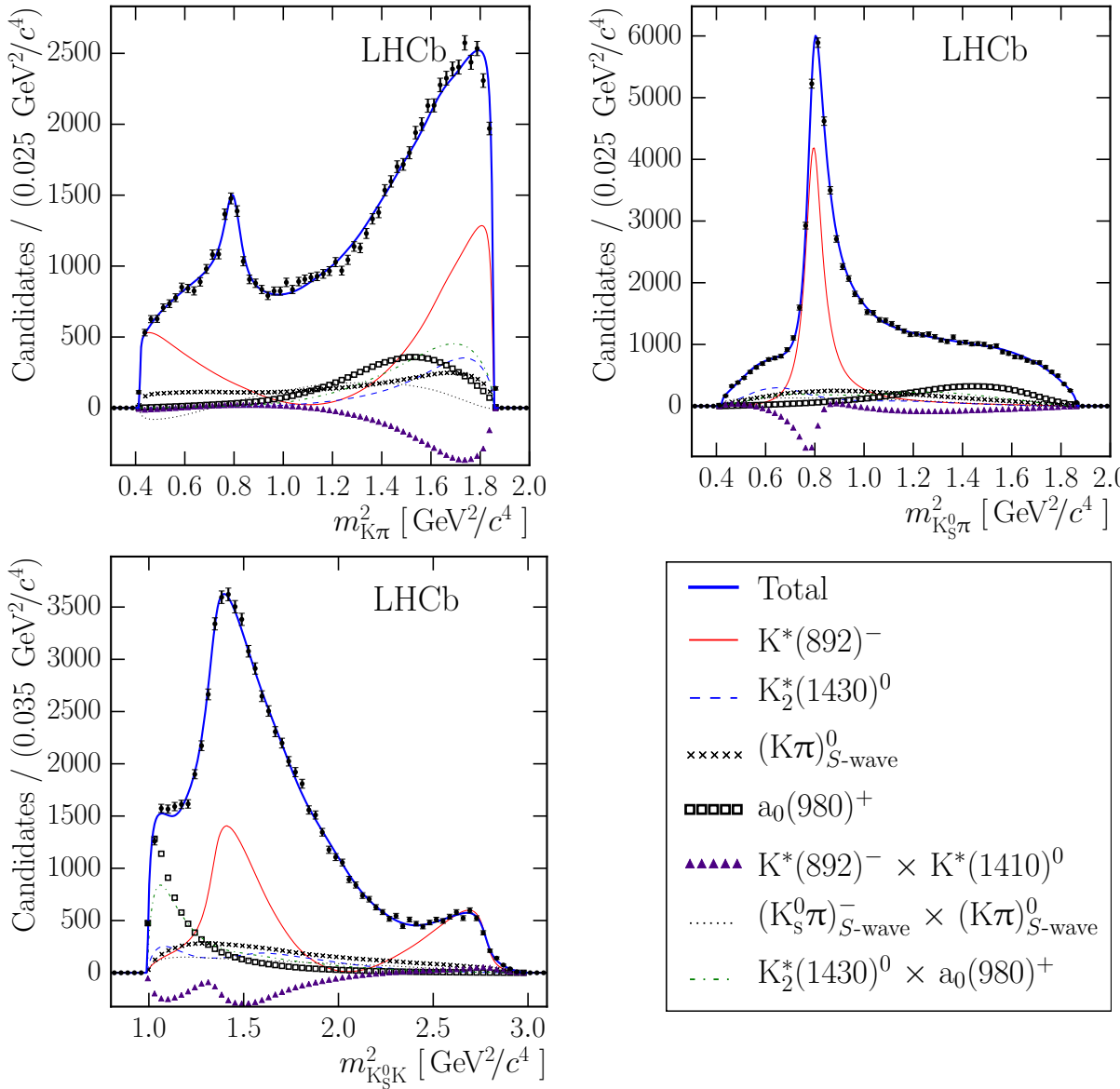


Figure 6.6: Distributions of $m_{K\pi}^2$ (upper left), $m_{K_S^0\pi}^2$ (upper right) and $m_{K_S^0K}^2$ (lower left) in the $D^0 \rightarrow K_S^0 K^\pm \pi^\mp$ mode with fit curves from the best **GLASS** model. The solid (blue) curve shows the full PDF $P_{K_S^0 K^\pm \pi^\mp}(m_{K_S^0\pi}^2, m_{K\pi}^2)$, while the other curves show the components with the largest integrated fractions. The solid black markers indicate the data.

The data are found to favour solutions that have a significant neutral $K\pi$ S -wave contribution, even though the exchange (Fig. 6.1b) and penguin annihilation (Fig. 6.1d) processes that contribute to the neutral channel are expected to be suppressed. The expected suppression is observed for the P -wave $K^*(892)$ resonances, with the neutral mode fit fractions substantially lower. The models using the **LASS** parameterisation additionally show this pattern for the $K^*(1410)$ states. The sums of the fit fractions [192], excluding interference terms, in the $D^0 \rightarrow K_S^0 K^- \pi^+$ and $D^0 \rightarrow K_S^0 K^+ \pi^-$ models are, respectively, 103 % (109 %) and

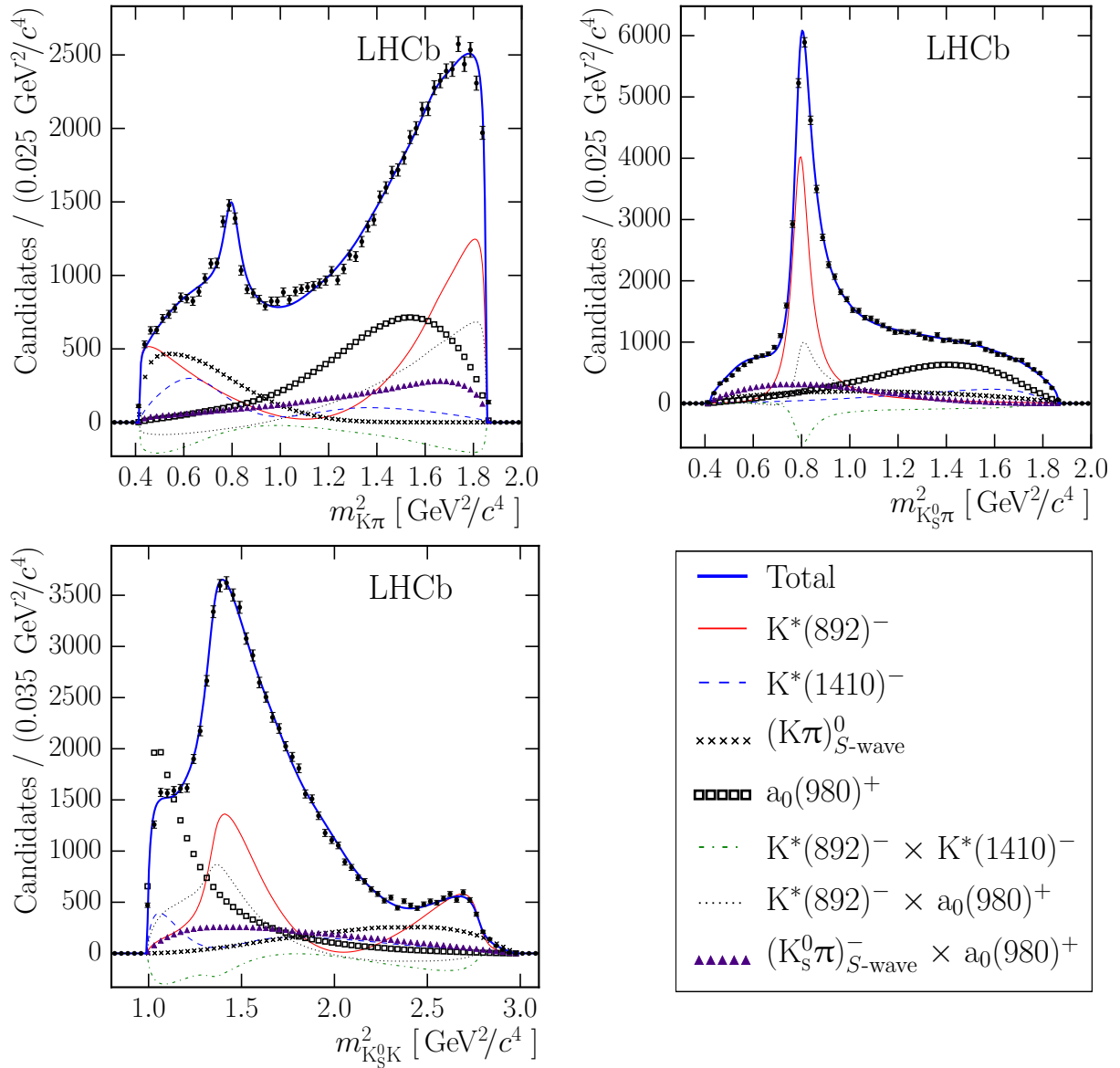


Figure 6.7: Distributions of $m_{K\pi}^2$ (upper left), $m_{K_s^0 \pi}^2$ (upper right) and $m_{K_s^0 K}^2$ (lower left) in the $D^0 \rightarrow K_s^0 K^+ \pi^-$ mode with fit curves from the best LASS model. The solid (blue) curve shows the full PDF $P_{K_s^0 K^+ \pi^-}(m_{K_s^0 \pi}^2, m_{K\pi}^2)$, while the other curves show the components with the largest integrated fractions. The solid black markers indicate the data.

81 % (99 %) using the GLASS (LASS) $K\pi$ S -wave parameterisation.

Using measurements of the mean strong-phase difference between the $D^0 \rightarrow K_s^0 K^\pm \pi^\mp$ modes available from $\psi(3770)$ decays [61], the relative complex amplitudes between each resonance in one D^0 decay mode and its conjugate contribution to the other D^0 decay mode are computed. These values are summarised in Table 6.8.

Additional information about the models is listed in Appendices C and D, including the

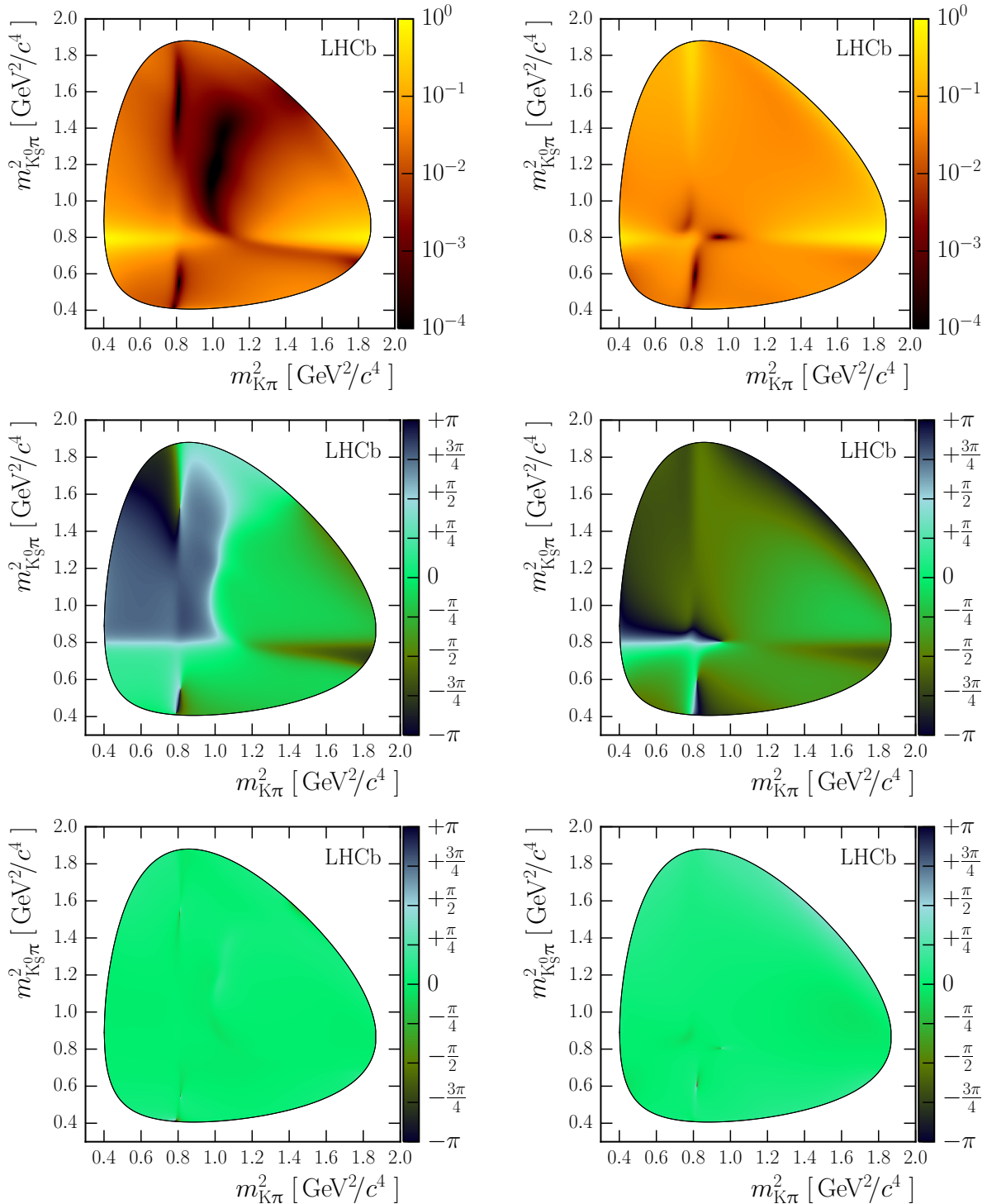


Figure 6.8: Decay rate and phase variation across the Dalitz plot. The top row shows $|\mathcal{M}_{K_s^0 K^\pm \pi^\mp}(m_{K_s^0 \pi}^2, m_{K \pi}^2)|^2$ in the best GLASS isobar models, the centre row shows the phase behaviour of the same models and the bottom row shows the same function subtracted from the phase behaviour in the best LASS isobar models. The left column shows the $D^0 \rightarrow K_s^0 K^- \pi^+$ mode with $D^0 \rightarrow K_s^0 K^+ \pi^-$ on the right. The small inhomogeneities that are visible in the bottom row relate to the GLASS and LASS models preferring slightly different values of the $K^*(892)^\pm$ mass and width.

Table 6.8: Modulus and phase of the relative amplitudes between resonances that appear in both the $D^0 \rightarrow K_s^0 K^- \pi^+$ and $D^0 \rightarrow K_s^0 K^+ \pi^-$ modes. Relative phases are calculated using the value of $\delta_{K^0 K \pi}$ measured in $\psi(3770)$ decays [61], and the uncertainty on this value is included in the statistical uncertainty. The first uncertainties are statistical and the second systematic.

Relative amplitude		GLASS	LASS
$\mathcal{A}(K^*(892)^-)$	mod	$0.582 \pm 0.007 \pm 0.008$	$0.576 \pm 0.005 \pm 0.010$
$\mathcal{A}(K^*(892)^+)$	arg [°]	$-2 \pm 15 \pm 2$	$-2 \pm 15 \pm 1$
$\mathcal{A}(K^*(1410)^-)$	mod	$0.64 \pm 0.08 \pm 0.22$	$0.90 \pm 0.08 \pm 0.15$
$\mathcal{A}(K^*(1410)^+)$	arg [°]	$52 \pm 17 \pm 20$	$62 \pm 16 \pm 6$
$\mathcal{A}((K_s^0 \pi)_{S-\text{wave}}^-)$	mod	$0.54 \pm 0.06 \pm 0.26$	$0.59 \pm 0.05 \pm 0.08$
$\mathcal{A}((K_s^0 \pi)_{S-\text{wave}}^+)$	arg [°]	$-100 \pm 20 \pm 40$	$-44 \pm 17 \pm 10$
$\mathcal{A}(K^*(892)^0)$	mod	$1.12 \pm 0.05 \pm 0.11$	$1.17 \pm 0.04 \pm 0.05$
$\mathcal{A}(\bar{K}^*(892)^0)$	arg [°]	$-78 \pm 16 \pm 10$	$-75 \pm 15 \pm 2$
$\mathcal{A}(K^*(1410)^0)$	mod	$0.60 \pm 0.05 \pm 0.12$	$0.62 \pm 0.09 \pm 0.12$
$\mathcal{A}(\bar{K}^*(1410)^0)$	arg [°]	$-9 \pm 16 \pm 14$	$-23 \pm 17 \pm 11$
$\mathcal{A}(K_2^*(1430)^0)$	mod	$1.1 \pm 0.1 \pm 0.5$	—
$\mathcal{A}(\bar{K}_2^*(1430)^0)$	arg [°]	$31 \pm 17 \pm 12$	—
$\mathcal{A}((K^+ \pi^-)_{S-\text{wave}})$	mod	$0.87 \pm 0.08 \pm 0.14$	$0.78 \pm 0.06 \pm 0.18$
$\mathcal{A}((K^- \pi^+)_{S-\text{wave}})$	arg [°]	$49 \pm 25 \pm 16$	$68 \pm 16 \pm 6$
$\mathcal{A}(a_0(980)^+)$	mod	—	$2.1 \pm 0.2 \pm 0.6$
$\mathcal{A}(a_0(980)^-)$	arg [°]	—	$42 \pm 16 \pm 5$
$\mathcal{A}(a_0(1450)^+)$	mod	$0.49 \pm 0.06 \pm 0.28$	$1.14 \pm 0.16 \pm 0.30$
$\mathcal{A}(a_0(1450)^-)$	arg [°]	$-60 \pm 19 \pm 34$	$-63 \pm 20 \pm 19$
$\mathcal{A}(\rho(1450)^+)$	mod	$0.86 \pm 0.16 \pm 0.26$	—
$\mathcal{A}(\rho(1450)^-)$	arg [°]	$110 \pm 20 \pm 50$	—
$\mathcal{A}(\rho(1700)^+)$	mod	$1.6 \pm 0.4 \pm 0.4$	—
$\mathcal{A}(\rho(1700)^-)$	arg [°]	$70 \pm 20 \pm 70$	—

interference fractions and decomposition of the systematic uncertainties. The best models contain contributions from the $\rho(1450)^\pm$ and $\rho(1700)^\pm$ resonances in the $K_s^0 K^\pm$ channels, supporting evidence in Ref. [73] of the $K\bar{K}$ decay modes for these states. Alternative models are fitted where one ρ^\pm contribution is removed from the best models; in these the value of $-2 \log \mathcal{L}$ is found to degrade by at least 162 units. Detailed results are tabulated in Appendix C.

The $K\pi$ *S*-wave systems are poorly understood [178], and there is no clear theoretical

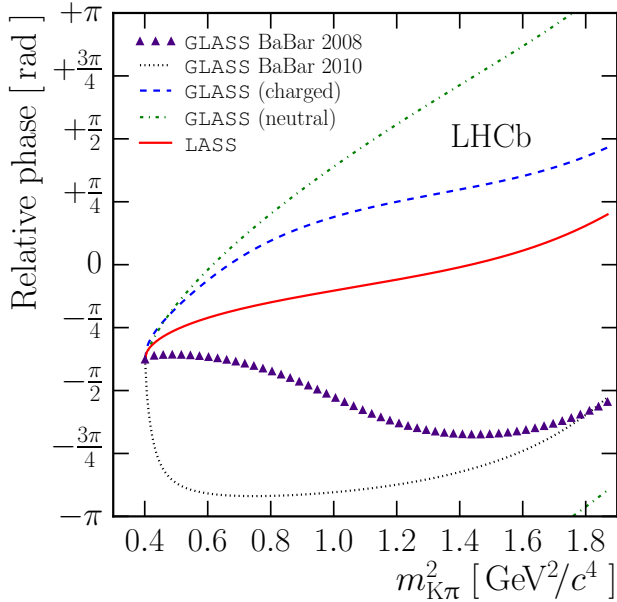


Figure 6.9: Comparison of the phase behaviour of the various $K\pi$ S -wave parameterisations used. The solid (red) curve shows the **LASS** parameterisation, while the dashed (blue) and dash-dotted (green) curves show, respectively, the **GLASS** functional form fitted to the charged and neutral S -wave channels. The final two curves show the **GLASS** forms fitted to the charged $K\pi$ S -wave in $D^0 \rightarrow K_s^0 \pi^+ \pi^-$ decays in Ref. [67] (triangular markers, purple) and Ref. [36] (dotted curve, black). The latter of these was used in the analysis of $D^0 \rightarrow K_s^0 K^\pm \pi^\mp$ decays by the CLEO collaboration [61].

guidance regarding the correct description of these systems in an isobar model. As introduced in Sect. 6.1, the **LASS** parameterisation is motivated by the Watson theorem, but this assumes that three-body interactions are negligible and is not, therefore, expected to be precisely obeyed in nature.

The isobar models using the **GLASS** parameterisation favour solutions with qualitatively similar phase behaviour to those using the **LASS** parameterisation. This is illustrated in Fig. 6.9, which also shows the **GLASS** forms obtained in fits to $D^0 \rightarrow K_s^0 \pi^+ \pi^-$ decays by the BaBar collaboration [36, 67] and previously used in fits to the $D^0 \rightarrow K_s^0 K^\pm \pi^\mp$ decay modes [61]. This figure shows that the **GLASS** functional form has substantial freedom to produce different phase behaviour to the **LASS** form, but that this is not strongly favoured in the $D^0 \rightarrow K_s^0 K^\pm \pi^\mp$ decays. The good quality of fit obtained using the **LASS** parameterisation indicates that large differences in phase behaviour with respect to $K\pi$ scattering data [184, 185] are not required in order to describe the $D^0 \rightarrow K_s^0 K^\pm \pi^\mp$ decays. A similar conclusion was drawn in Ref. [193] for the decay $D^+ \rightarrow K^- \pi^+ \pi^+$, while Ref. [194] found behaviour

Table 6.9: Values of χ^2/bin indicating the fit quality obtained using both $K\pi$ *S*-wave parameterisations in the two decay modes. The binning scheme for the $D^0 \rightarrow K_s^0 K^- \pi^+$ ($D^0 \rightarrow K_s^0 K^+ \pi^-$) mode contains 2191 (2573) bins.

	Isobar model	
	GLASS	LASS
$D^0 \rightarrow K_s^0 K^- \pi^+$	1.12	1.10
$D^0 \rightarrow K_s^0 K^+ \pi^-$	1.07	1.09

inconsistent with scattering data using the same D^+ decay mode but a slightly different technique. Ref. [195] studied the $K\pi$ *S*-wave in $\tau^- \rightarrow K_s^0 \pi^- \nu_\tau$ decays and found that a parameterisation based on the LASS $K\pi$ scattering data, but without a real production form factor, gave a poor description of the τ^- decay data.

The quality of fit for each model is quantified by calculating χ^2 using a dynamic binning scheme. The values are summarised in Table 6.9, while the binning scheme and two-dimensional quality of fit are shown in Appendix C. This binning scheme is generated by iteratively sub-dividing the Dalitz plot to produce new bins of approximately equal population until further sub-division would result in a bin population of fewer than 15 candidates, or a bin dimension smaller than $0.02 \text{ GeV}^2/c^4$ in $m_{K_s^0 \pi}^2$ or $m_{K\pi}^2$. This minimum size corresponds to five times the average resolution in these variables.

The overall fit quality is slightly better in the isobar models using the GLASS $K\pi$ *S*-wave parameterisation, but this is not a significant effect and it should be noted that these models contain more degrees of freedom, with 57 parameters fitted in the final GLASS model compared to 50 when using the LASS parameterisation.

The resonance amplitudes in the two models for each decay mode can be compared graphically using a modified argand diagram, where the radial coordinate is taken to be the fit fraction rather than the amplitude a_R . This is easier to interpret as the overall scale of the a_R parameters is arbitrary. Figure 6.10 illustrates the best isobar models in this way.

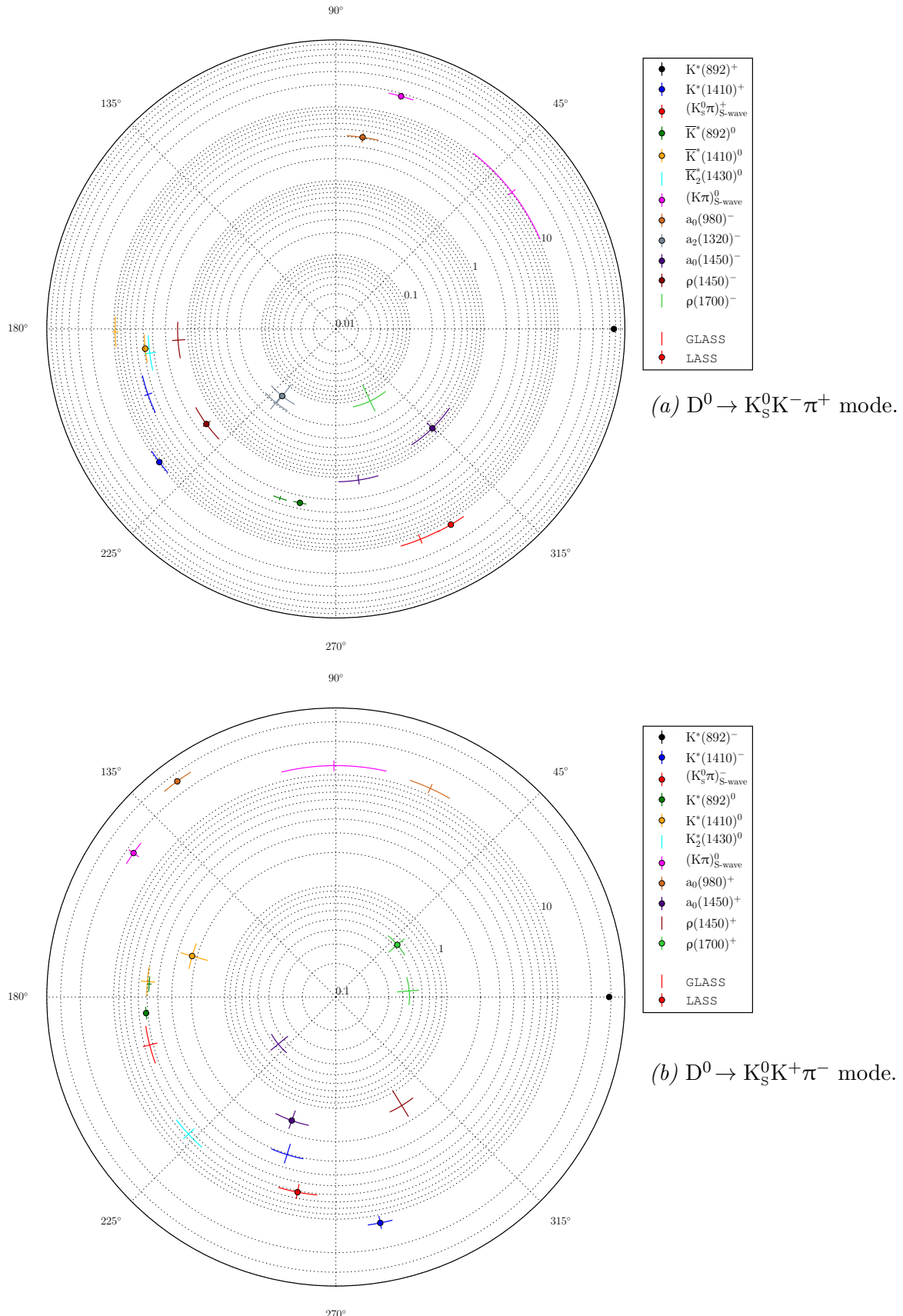


Figure 6.10: Diagram showing the best isobar models of the $D^0 \rightarrow K_s^0 K^- \pi^+$ (a) and $D^0 \rightarrow K_s^0 K^+ \pi^-$ (b) decay modes for each of the two $K\pi$ S -wave parameterisations, GLASS and LASS. The radial coordinate is the resonance fit fraction in percent.

6.8 *CP* violation tests

Searches for time-integrated *CP*-violating effects in the resonant structure of these decays are performed using the best isobar models. The resonance amplitude and phase parameters a_R and ϕ_R are substituted with $a_R(1 \pm \Delta a_R)$ and $\phi_R \pm \Delta \phi_R$, respectively, where the signs are set by the flavour tag. The convention adopted is that a positive sign produces the \bar{D}^0 complex amplitude. The fitted values of the Δ parameters are given in Table 6.10, while full fit results are tabulated in Appendix C.

A subset of the Δ parameters is used to perform a χ^2 test against the no-*CP*-violation hypothesis: only those parameters corresponding to resonances that are present in the best isobar models using both the **GLASS** and **LASS** $K\pi$ *S*-wave parameterisations are included. The absolute difference $|\Delta_{\text{GLASS}} - \Delta_{\text{LASS}}|$ is assigned as the systematic uncertainty due to dependence on the choice of isobar model. This subset of parameters is shown in Table 6.10, where the change in fit fraction between the D^0 and \bar{D}^0 solutions is included for illustrative purposes. In the χ^2 test the statistical and systematic uncertainties are added in quadrature.

Using the best **GLASS** (**LASS**) isobar models the test result is $\chi^2/\text{ndf} = 30.5/32 = 0.95$ ($32.3/32 = 1.01$), corresponding to a *p*-value of 0.54 (0.45). Therefore, the data are compatible with the hypothesis of *CP* conservation.

6.9 Ratio of branching fractions measurement

The ratio of branching fractions

$$\mathcal{B}_{K_S^0 K\pi} \equiv \frac{\mathcal{B}(D^0 \rightarrow K_S^0 K^+ \pi^-)}{\mathcal{B}(D^0 \rightarrow K_S^0 K^- \pi^+)}, \quad (6.11)$$

and the restricted region ratio $\mathcal{B}_{K^* K}$, defined in the same region near the $K^*(892)^\pm$ resonance as the coherence factor $R_{K^* K}$ (Sect. 6.2), are also measured. The efficiency correction due to the reconstruction efficiency $\varepsilon(m_{K_S^0 \pi}^2, m_{K\pi}^2)$ is evaluated using the best isobar models, and the difference between the results obtained with the two $K\pi$ *S*-wave parameterisations is taken

Chapter 6. Amplitude analysis of $D^0 \rightarrow K_s^0 K^\pm \pi^\mp$ decays

Table 6.10: CP violation fit results. Results are only shown for those resonances that appear in both the GLASS and LASS models. The first uncertainties are statistical and the second systematic; the only systematic uncertainty is that due to the choice of isobar model.

Resonance	Δa_R		$\Delta\phi_R$ [°]		$\Delta(\text{Fit fraction})$ [%]	
	GLASS	LASS	GLASS	LASS	GLASS	LASS
$D^0 \rightarrow K_s^0 K^- \pi^+$						
$K^*(892)^+$	0.0 (fixed)	0.0 (fixed)	0.0 (fixed)	0.0 (fixed)	0.6 ± 1.0 ± 0.3	0.9 ± 1.0 ± 0.3
$K^*(1410)^+$	0.07 ± 0.06 ± 0.04	0.03 ± 0.06 ± 0.04	3.9 ± 3.5 ± 1.9	2.0 ± 2.9 ± 1.9	1.4 ± 0.8 ± 0.2	1.2 ± 1.6 ± 0.2
$(K_s^0 \pi^+)_S\text{-wave}$	0.02 ± 0.08 ± 0.07	-0.05 ± 0.08 ± 0.07	2.0 ± 1.7 ± 0.0	2.0 ± 1.7 ± 0.0	1 ± 4 ± 3	-2.3 ± 3.5 ± 3.3
$\bar{K}^*(892)^0$	-0.046 ± 0.031 ± 0.005	-0.051 ± 0.030 ± 0.005	1.2 ± 1.6 ± 0.3	1.5 ± 1.7 ± 0.3	-0.43 ± 0.30 ± 0.03	-0.47 ± 0.29 ± 0.03
$\bar{K}^*(1410)^0$	0.006 ± 0.034 ± 0.017	0.02 ± 0.04 ± 0.02	2 ± 5 ± 5	-3 ± 6 ± 5	0.3 ± 1.0 ± 0.1	0.4 ± 0.7 ± 0.1
$(K\pi^0_S)_S\text{-wave}$	0.05 ± 0.04 ± 0.02	0.03 ± 0.04 ± 0.02	0.4 ± 1.6 ± 0.6	1.0 ± 1.4 ± 0.6	2.2 ± 1.3 ± 0.4	2.6 ± 2.2 ± 0.4
$a_2(1320)^-$	-0.25 ± 0.14 ± 0.01	-0.24 ± 0.13 ± 0.01	2 ± 9 ± 3	-1 ± 9 ± 3	-0.20 ± 0.13 ± 0.05	-0.15 ± 0.10 ± 0.05
$a_0(1450)^-$	-0.01 ± 0.14 ± 0.12	-0.13 ± 0.14 ± 0.12	0 ± 5 ± 4	-4 ± 6 ± 4	-0.0 ± 0.4 ± 0.4	-0.4 ± 0.4 ± 0.4
$\rho(1450)^-$	0.06 ± 0.13 ± 0.11	-0.05 ± 0.12 ± 0.11	-13 ± 10 ± 9	-5 ± 9 ± 9	0.3 ± 0.7 ± 0.6	-0.3 ± 0.7 ± 0.6
$D^0 \rightarrow K_s^0 K^+ \pi^-$						
$K^*(892)^-$	0.0 (fixed)	0.0 (fixed)	0.0 (fixed)	0.0 (fixed)	-1.1 ± 0.7 ± 0.2	-0.9 ± 0.7 ± 0.2
$K^*(1410)^-$	0.05 ± 0.12 ± 0.08	-0.03 ± 0.10 ± 0.08	-6 ± 4 ± 3	-3.0 ± 3.6 ± 2.8	0.6 ± 2.7 ± 2.4	-2 ± 4 ± 2
$(K_s^0 \pi^-)_{S\text{-wave}}$	0.10 ± 0.25 ± 0.24	-0.14 ± 0.25 ± 0.24	-7.7 ± 3.4 ± 0.0	-8 ± 4 ± 0	2 ± 6 ± 6	-4 ± 6 ± 6
$K^*(892)^0$	-0.010 ± 0.024 ± 0.001	-0.012 ± 0.022 ± 0.001	-1.4 ± 2.9 ± 2.2	0.8 ± 2.8 ± 2.2	-0.4 ± 0.4 ± 0.0	-0.4 ± 0.4 ± 0.0
$K^*(1410)^0$	0.10 ± 0.10 ± 0.09	0.19 ± 0.13 ± 0.09	-1 ± 9 ± 8	-9 ± 9 ± 8	1.9 ± 1.1 ± 0.2	1.6 ± 0.8 ± 0.2
$(K\pi^0_S)_S\text{-wave}$	-0.07 ± 0.06 ± 0.05	-0.12 ± 0.06 ± 0.05	-2 ± 4 ± 4	2 ± 4 ± 4	-4 ± 5 ± 5	-9 ± 6 ± 5
$a_0(980)^+$	0.06 ± 0.04 ± 0.01	0.052 ± 0.025 ± 0.008	-3 ± 5 ± 2	-0.9 ± 3.1 ± 2.2	2.2 ± 2.8 ± 2.4	4.6 ± 3.3 ± 2.4
$a_0(1450)^+$	-0.11 ± 0.10 ± 0.04	-0.07 ± 0.07 ± 0.04	10 ± 8 ± 5	5 ± 6 ± 5	-0.21 ± 0.30 ± 0.23	-0.4 ± 0.4 ± 0.2
$\rho(1700)^+$	-0.03 ± 0.13 ± 0.09	4 ± 6 ± 2	2 ± 5 ± 2	-0.07 ± 0.25 ± 0.19	-0.27 ± 0.27 ± 0.19	

Table 6.11: Coherence factor observables to which the isobar models are sensitive. The third column summarises the CLEO results measured in quantum-correlated decays [61], where the uncertainty on $\delta_{K_S^0 K\pi} - \delta_{K^* K}$ is calculated assuming maximal correlation between $\delta_{K_S^0 K\pi}$ and $\delta_{K^* K}$. The first uncertainties are statistical and where quoted, the second are systematic.

Variable	GLASS	LASS	CLEO
$R_{K_S^0 K\pi}$	$0.573 \pm 0.007 \pm 0.019$	$0.571 \pm 0.005 \pm 0.019$	0.73 ± 0.08
$R_{K^* K}$	$0.831 \pm 0.004 \pm 0.010$	$0.835 \pm 0.003 \pm 0.011$	1.00 ± 0.16
$\delta_{K_S^0 K\pi} - \delta_{K^* K}$ [°]	$0.2 \pm 0.6 \pm 1.1$	$-0.0 \pm 0.5 \pm 0.7$	-18 ± 31

as a systematic uncertainty in addition to those effects described in Sect. 6.6. This efficiency correction modifies the ratio of yields quoted in Table 5.3 by approximately 3 %.

The two ratios are measured to be

$$\mathcal{B}_{K_S^0 K\pi} = 0.655 \pm 0.004 \text{ (stat)} \pm 0.006 \text{ (syst)},$$

$$\mathcal{B}_{K^* K} = 0.370 \pm 0.003 \text{ (stat)} \pm 0.012 \text{ (syst)}.$$

These are the most precise measurements to date.

6.10 Coherence factor and CP -even fraction results

The amplitude models are used to calculate the coherence factors $R_{K_S^0 K\pi}$ and $R_{K^* K}$, and the strong-phase difference $\delta_{K_S^0 K\pi} - \delta_{K^* K}$, as described in Sect. 6.2. The results are summarised in Table 6.11, alongside the corresponding values measured in $\psi(3770)$ decays by the CLEO collaboration. Lower, but compatible, coherence is calculated using the isobar models than was measured at CLEO, with the discrepancy larger for the coherence factor calculated over the full phase space. The results from the GLASS and LASS isobar models are very similar, showing that the coherence variables are not sensitive to the $K\pi$ S -wave parameterisation.

The coherence factor $R_{K_S^0 K\pi}$, and the ratio of branching fractions $\mathcal{B}_{K_S^0 K\pi}$, are combined with the mean phase difference between the two final states measured in $\psi(3770)$ decays [61]

to calculate the CP -even fraction F_+ , defined in Sect. 6.2, which is determined to be

$$F_+ = 0.777 \pm 0.003 \text{ (stat)} \pm 0.009 \text{ (syst)},$$

using the **GLASS** amplitude models. A consistent result is obtained using the alternative (**LASS**) amplitude models. This model-dependent value is compatible with the direct measurement using only $\psi(3770)$ decay data [61, 92].

6.11 $SU(3)$ flavour symmetry tests

$SU(3)$ flavour symmetry can be used to relate decay amplitudes in several D-meson decays, such that a global fit to many such amplitudes can provide predictions for the neutral and charged $K^*(892)$ complex amplitudes in $D^0 \rightarrow K_s^0 K^\pm \pi^\mp$ decays [176, 177]. Predictions are available for the K^+K^- , K^-K^+ , $K^{*0}\bar{K}^0$ and $\bar{K}^{*0}K^0$ complex amplitudes, where K^* refers to the $K^*(892)$ resonances. There are, therefore, three relative amplitudes and two relative phases that can be determined from the isobar models, with an additional relative phase accessible if the isobar results are combined with the CLEO measurement of the mean strong-phase difference, $\delta_{K_s^0 K\pi}$ [61]. The results are summarised in Table 6.12.

The isobar model results are found to follow broadly the patterns predicted by $SU(3)$ flavour symmetry. The amplitude ratio between the $K^*(892)^+$ and $\bar{K}^*(892)^0$ resonances, which is derived from the $D^0 \rightarrow K_s^0 K^- \pi^+$ isobar model alone, shows good agreement. The two other amplitude ratios additionally depend on the ratio $\mathcal{B}_{K_s^0 K\pi}$, and these are more discrepant with the $SU(3)$ predictions. The relative phase between the charged and neutral $K^*(892)$ resonances shows better agreement with the flavour symmetry prediction in the $D^0 \rightarrow K_s^0 K^+ \pi^-$ mode, where both resonances have clear peaks in the data. The **GLASS** and **LASS** isobar models are found to agree well, suggesting the problems are not related to the $K\pi$ S -wave.

Table 6.12: SU(3) flavour symmetry predictions [177] and results. The uncertainties on phase difference predictions are calculated from the quoted magnitude and phase uncertainties. Note that some theoretical predictions depend on the $\eta-\eta'$ mixing angle $\theta_{\eta-\eta'}$ and are quoted for two different values. The bottom entry in the table relies on the CLEO measurement [61] of the coherence factor phase $\delta_{K_s^0 K\pi}$, and the uncertainty on this phase is included in the statistical uncertainty, while the other entries are calculated directly from the isobar models and ratio of branching fractions. Where two uncertainties are quoted the first is statistical and the second systematic.

Ratio	Theory		Experiment	
	$\theta_{\eta-\eta'} = 19.5^\circ$	$\theta_{\eta-\eta'} = 11.7^\circ$	GLASS	LASS
$\frac{ \mathcal{A}(K^*(892)^- K^+) }{ \mathcal{A}(K^*(892)^+ K^-) }$	0.685 ± 0.032	0.685 ± 0.032	$0.582 \pm 0.007 \pm 0.007$	$0.576 \pm 0.005 \pm 0.010$
$\frac{ \mathcal{A}(\bar{K}^*(892)^0 K^0) }{ \mathcal{A}(K^*(892)^+ K^-) }$	0.138 ± 0.033	0.307 ± 0.035	$0.297 \pm 0.010 \pm 0.024$	$0.295 \pm 0.009 \pm 0.014$
$\frac{ \mathcal{A}(K^*(892)^0 \bar{K}^0) }{ \mathcal{A}(K^*(892)^+ K^-) }$	0.138 ± 0.033	0.307 ± 0.035	$0.333 \pm 0.008 \pm 0.016$	$0.345 \pm 0.007 \pm 0.010$
Argument	Theory [°]		Experiment [°]	
$\frac{\mathcal{A}(\bar{K}^*(892)^0 K^0)}{\mathcal{A}(K^*(892)^+ K^-)}$	151 ± 14	112 ± 8	$72 \pm 2 \pm 4$	$78.5 \pm 2.0 \pm 2.8$
$\frac{\mathcal{A}(K^*(892)^0 \bar{K}^0)}{\mathcal{A}(K^*(892)^- K^+)}$	-9 ± 13	-37 ± 6	$-4 \pm 2 \pm 9$	$5.0 \pm 1.7 \pm 1.4$
$\frac{\mathcal{A}(K^*(892)^0 \bar{K}^0)}{\mathcal{A}(\bar{K}^*(892)^0 K^0)}$	180	180	$-78 \pm 16 \pm 10$	$-75 \pm 15 \pm 2$

6.12 Conclusions

The decay modes $D^0 \rightarrow K_s^0 K^\pm \pi^\mp$ have been studied using unbinned, time-integrated, fits to a high purity sample of 189 670 candidates, and two amplitude models have been constructed for each decay mode. These models are compared to data in a large number of bins in the relevant Dalitz plots and a χ^2 test indicates a good description of the data.

Models are presented using two different parameterisations of the $K\pi$ *S*-wave systems, which have been found to be an important component of these decays. These systems are poorly understood, and comparisons have been made to previous results and alternative parameterisations, but the treatment of the $K\pi$ *S*-wave is found to have little impact on the other results presented in this thesis. The large fractions attributed to the neutral $K\pi$ *S*-wave channels could indicate larger than expected contributions from the penguin annihilation diagrams shown in Fig. 6.1d.

The models are seen to favour small, but significant, contributions from the $\rho(1450)^\pm$ and $\rho(1700)^\pm$ resonances in the $K_s^0 K^\pm$ channel, modes which may have been seen by the OBELIX

experiment [73] but are not well established. All models contain clear contributions from both the $K^*(892)^\pm$ and $K^*(892)^0$ resonances, with the $K^*(892)^0$ contribution found to be suppressed as expected from the diagrams shown in Fig. 6.1. This allows the full set of amplitudes in these decays that are predicted by SU(3) flavour symmetry to be tested, in contrast to the previous analysis by the CLEO collaboration [61]. Partial agreement is found with these predictions.

The ratio of branching fractions between the two $D^0 \rightarrow K_s^0 K^\pm \pi^\mp$ modes is also measured, both across the full Dalitz plot area and in a restricted region near the $K^*(892)^\pm$ resonance, with much improved precision compared to previous results.

Values for the $D^0 \rightarrow K_s^0 K\pi$ coherence factor are computed using the amplitude models, again both for the whole Dalitz plot area and in the restricted region, and are found to be in reasonable agreement with direct measurements by CLEO [61] using quantum-correlated $\Psi(3770) \rightarrow D^0 \bar{D}^0$ decays. The CP -even fraction of the $D^0 \rightarrow K_s^0 K\pi$ decays is also computed, using input from the quantum-correlated decays, and is found to be in agreement with the direct measurement [61, 92]. A search for time-integrated CP violation is carried out using the amplitude models, but no evidence is found with either choice of parameterisation for the $K\pi$ S -wave.

The models presented here will be useful for future $D^0 - \bar{D}^0$ mixing, indirect CP violation and CKM angle γ studies, where knowledge of the strong-phase variation across the Dalitz plot can improve the attainable precision. These improvements will be particularly valuable for studies of the large dataset that is expected to be accumulated in Run 2 of the LHC.

7. MIXING STUDIES USING $D^0 \rightarrow K_s^0 K^+ K^-$ DECAYS

Neutral meson mixing is a powerful probe of physics beyond the SM. Mixing is well established in the charm system, notably by several recent LHCb results [196–198] that show the mixing parameters are small. This means it is challenging to measure the effects of indirect CP violation, and hence significant violation at a higher level than expected in the SM has not yet been excluded. An overview of the relevant methods for measuring mixing and probing for indirect CP violation was given in Chapter 1, and the theoretical background to the model-independent technique has been outlined in Sect. 2.5. This chapter is dedicated to model-independent mixing and indirect CP violation studies [40] using $D^0 \rightarrow K_s^0 K^+ K^-$ decays and the swimming technique described in Sect. 4.3. One similar measurement has been carried out [101], using the sample of promptly-produced $D^0 \rightarrow K_s^0 \pi^+ \pi^-$ decays recorded in 2011 by the LHCb experiment.

The key result of the theoretical derivation in Sect. 2.5.1 is that the squared modulus of the decay amplitude in bin i of the Dalitz plot is given by

$$|\mathcal{A}_\pm(t)|_i^2 = e^{-\Gamma t} \left[T_i + \frac{(\Gamma t)^2}{4} \left[T_i \Re(z_{CP}^2 - \Delta z^2) + T_{-i} |z_{CP} \pm \Delta z|^2 \right] + \Gamma t \sqrt{T_i T_{-i}} \Re(X_i (z_{CP} \pm \Delta z)) \right], \quad (2.28)$$

where the positive (negative) sign gives the decay time distribution in bin i of the Dalitz plot of a D^0 (\bar{D}^0) signal decay to $K_s^0 K^+ K^-$. The index i runs from $-\mathcal{N}$ to $+\mathcal{N}$, excluding zero. Binning schemes and measurements of the strong-phase parameters, X_i , are available for $\mathcal{N} \in \{2, 3, 4\}$. The quantity T_i represents the fraction of flavour-specific decays that fall in bin i in the absence of mixing effects, while X_i represents the weighted average of

the strong-phase difference between the amplitude in bin i and that in the opposite bin, $-i$. The effects of mixing and indirect CP violation are parameterised by z_{CP} and Δz , where $z(q/p)^{\pm 1} \equiv z_{CP} \pm \Delta z$. The real and imaginary components of z correspond to the absorptive and dispersive components of mixing, respectively, while Δz is related to indirect CP violation. Precise definitions were given in Sect. 2.5.1.

The swimming technique described in Sect. 4.3 produces per-event decay time efficiency functions, $\varepsilon(t)$, which are approximately a series of top-hat functions. The normalised decay time PDF for a signal candidate n , evaluated at the measured decay time for that candidate, t_n , is, therefore,

$$P_n(t_n) = \frac{|\mathcal{A}_{\pm(n)}(t_n)|_{i(n)}^2}{\sum_i \int_0^\infty \varepsilon_n(t') |\mathcal{A}_{\pm(n)}(t')|_i^2 dt'}, \quad (7.1)$$

where the term $\varepsilon_n(t_n)$ in the numerator is not shown, as it is nonzero by definition and can be chosen to be unity. An unbinned maximum likelihood fit to N candidates typically minimises the quantity

$$-2 \log \mathcal{L} = -2 \log \left(\prod_n^N P_n(t_n) \right). \quad (7.2)$$

The variation in reconstruction and selection efficiency as a function of decay time can, therefore, be incorporated into such a fit simply by normalising the PDF for each candidate separately. This, unfortunately, forbids the widely-used optimisation

$$\log(\mathcal{L}) = \sum_n^N \log(p(t_n)) - \sum_n^N \log \left(\alpha \equiv \int_0^\infty p(t') dt' \right) \quad (7.3)$$

$$= \sum_n^N \log(p(t_n)) - N \log(\alpha), \quad (7.4)$$

where $p(t)/\alpha$ is some normalised PDF including the averaged result of decay time acceptance effects, as the normalisation integrals in Eqn. 7.2 depend on the index n and must be evaluated a factor N times more frequently each time \mathcal{L} is computed. There is, therefore, a strong motivation to construct analytically integrable fit PDFs.

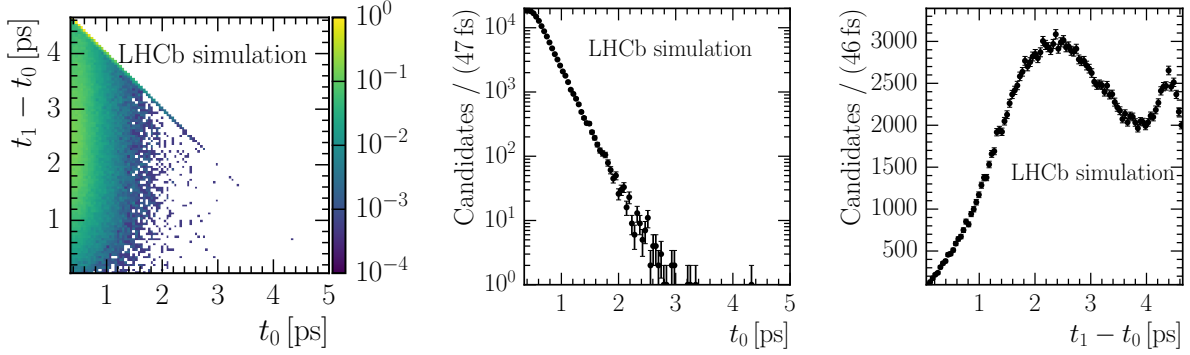


Figure 7.1: Distributions of the turning point positions t_0 and t_1 , which are defined in Eqn. 7.5, in a sample of simulated, promptly-produced $D^0 \rightarrow K_s^0 \pi^+ \pi^-$ and $D^0 \rightarrow K_s^0 K^+ K^-$ decays. The z -units are arbitrary in the left-most figure.

The full PDF in the presence of non-zero background contributions requires so-called Punzi corrections [199] if the efficiency functions $\varepsilon_n(t)$ differ, on average, between signal decays and background contributions. These are not included in the study presented in this chapter, which consists only of fits to pure simulated signal samples.

7.1 Idealised sensitivity studies

This section contains idealised studies of the sensitivity to the D^0 – \bar{D}^0 mixing and indirect CP violation parameters z_{CP} and Δz , and the mean D^0 lifetime $\tau_{D^0} = 1/\Gamma$. The sensitivities that are, and will be, achievable using the LHCb dataset of $D^0 \rightarrow K_s^0 K^+ K^-$ decays are estimated.

For these sensitivity studies only a simplified form of the per-candidate decay time efficiency functions $\varepsilon(t)$ are considered: a single top-hat function of unit height,

$$\varepsilon(t) = \begin{cases} 1, & t_0 < t < t_1 \\ 0, & \text{otherwise.} \end{cases} \quad (7.5)$$

The position (t_0) and width ($t_1 - t_0$) of this function are sampled, including their correlations, from their distributions in a sample of simulated $D^0 \rightarrow K_s^0 \pi^+ \pi^-$ and $D^0 \rightarrow K_s^0 K^+ K^-$ decays¹ when emulating decay-time-biasing selections, and a constant $\varepsilon(t) = 1$ is used to simulate the “lifetime unbiased” samples. These distributions are shown in Fig. 7.1.

¹ $D^0 \rightarrow K_s^0 \pi^+ \pi^-$ candidates, selected using the same strategy, are included to increase the sample size.

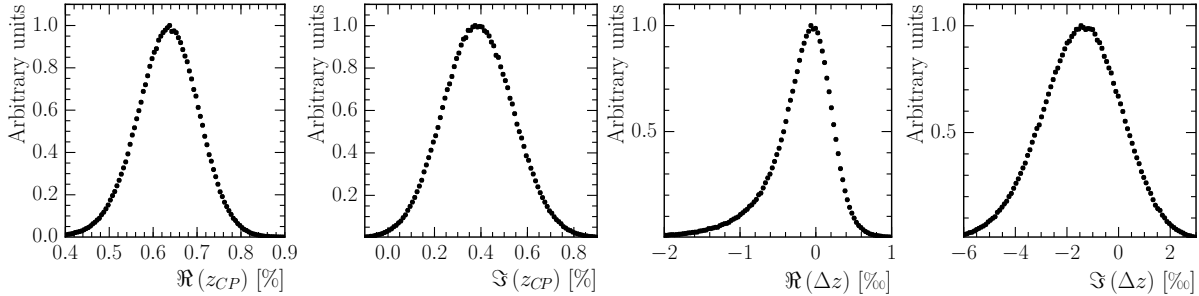


Figure 7.2: Values of z_{CP} and Δz sampled from the correlated world-average results for x , y and q/p [35]. The same sampling procedure is used to produce the generated values of z_{CP} and Δz used in the sensitivity studies.

Sensitivity to the observables of interest is evaluated using a large number of pseudoexperiments. In each pseudoexperiment, values for the mixing and CP violation parameters z_{CP} and Δz are drawn from the world-average fit results [35]. Because values and correlations between the observables z_{CP} and Δz are not explicitly given by Ref. [35], these are derived from the best-fit values and correlation matrix for the related parameters x , y and q/p , assuming Gaussian behaviour. The resulting distributions for the real and imaginary parts of z_{CP} and Δz are shown in Fig. 7.2, while numerical values are given in Table 7.1. These distributions illustrate the same features as were seen in Sect. 2.5.1: mixing ($z_{CP} \neq 0$) is well established, with the absorptive component ($y \approx \Re(z_{CP})$) more precisely measured, and CP violation ($\Delta z \neq 0$) in mixing is neither observed nor strongly constrained. It should be noted that Δz is, by construction, numerically small. For example, a value for q/p of $0.8e^{-i(20^\circ)}$, which would be considered large indirect CP violation, lies within the 1σ contour of the current world-average results, and corresponds to $\Delta z \approx (-0.3 - 3.2i)\%$.

Values for the binned parameters T_i and X_i are, for each pseudoexperiment, drawn from the CLEO results [38], which are listed in Table 7.2. If the drawn set $\{X_i\}$ contains

Table 7.1: Average values of z_{CP} and Δz sampled from the correlated world-average results for x , y and q/p [35]. These are simply taken from the distributions shown in Fig. 7.2.

Observable	Value
$\Re(z_{CP})$	0.63 ± 0.07 [%]
$\Im(z_{CP})$	0.39 ± 0.15 [%]
$\Re(\Delta z)$	-0.2 ± 0.4 [%]
$\Im(\Delta z)$	-1.5 ± 1.6 [%]

Table 7.2: Values for the binned parameters T_i and $X_i \equiv c_i - is_i$ measured by the CLEO collaboration [38]. Correlation information is not shown here, but is included when values for these parameters are sampled in the pseudoexperiments.

\mathcal{N}	i	T_i	T_{-i}	c_i	s_i
2	1	0.355 ± 0.019	0.239 ± 0.016	0.818 ± 0.107	-0.445 ± 0.215
	2	0.233 ± 0.017	0.173 ± 0.015	-0.746 ± 0.083	-0.229 ± 0.220
3	1	0.330 ± 0.017	0.220 ± 0.015	0.793 ± 0.063	-0.431 ± 0.222
	2	0.228 ± 0.016	0.181 ± 0.014	-0.566 ± 0.092	-0.413 ± 0.234
	3	0.030 ± 0.006	0.012 ± 0.004	-0.096 ± 0.329	0.461 ± 0.432
4	1	0.305 ± 0.017	0.200 ± 0.015	0.858 ± 0.059	-0.309 ± 0.248
	2	0.076 ± 0.013	0.072 ± 0.011	0.176 ± 0.223	-0.992 ± 0.472
	3	0.177 ± 0.014	0.133 ± 0.014	-0.819 ± 0.095	-0.307 ± 0.267
	4	0.028 ± 0.006	0.008 ± 0.004	0.376 ± 0.329	0.133 ± 0.659

unphysical elements with $|X_i| > 1$, the set is re-drawn until a physical set is obtained. The number of simulated signal candidates is, for each pseudoexperiment, drawn from a Poisson distribution. Correlated uncertainties from the CLEO measurement of the strong-phase parameters, X_i , are included in the pseudoexperiment fits as a multivariate Gaussian constraint term, and the full set of X_i and T_i is allowed to vary. An alternative set of pseudoexperiments, where values of X_i are drawn in the same manner but not allowed to vary in the fit, is used to evaluate the contribution to the final uncertainties on z_{CP} and Δz that is due to the precision of the CLEO measurements of $\{X_i\}$. The normalisation condition $\sum_i T_i = 1$ is imposed using a recursive fraction parameterisation, and an unbinned maximum likelihood fit is carried out in each pseudoexperiment to estimate the mixing and CP violation parameters. The decay time distribution of an illustrative pseudoexperiment is shown in Fig. 7.3.

The uncertainties on the CLEO measurements of the fractions T_i are fairly large, and, as quantum-correlated data are not required to measure these quantities, one might worry that an unduly large uncertainty is injected into the pseudoexperiments by the use of CLEO measurements. An alternative set of pseudoexperiments, where no smearing is applied to the values of T_i used for generation, is used to evaluate the variation in sensitivity to z_{CP} and Δz as a function of the absolute values $\{T_i\}$. No such effect is found, despite the imprecise nature of the CLEO measurements of $\{T_i\}$. Two conclusions can be drawn. First,

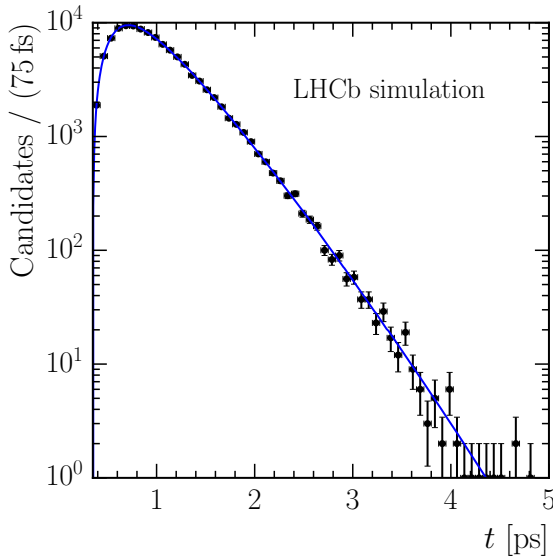


Figure 7.3: Decay time distribution and fit result obtained in an illustrative pseudoexperiment using the “2012 biased” configuration, *i.e.* the configuration that corresponds to the LHCb dataset recorded during 2012. Although the dominant efficiency effect is the turn-on at low decay times, a reduction in efficiency at large decay times is also visible.

this exercise shows that the sensitivities quoted below are not artificially degraded by the use of CLEO results for T_i instead of the more precise values that could be obtained from an amplitude model, or from the results of Chapter 5. Second, and more importantly, it shows that the effects of a non-uniform selection efficiency across the $D^0 \rightarrow K_s^0 K^+ K^-$ Dalitz plot, which must be accounted for in an analysis of real data, will not be large. Such a non-uniform selection efficiency has the effect of modifying the statistical power available in each of the $2\mathcal{N}$ Dalitz plot bins, which has a similar effect to changing the values T_i .

The effect of non-uniform selection efficiency on the averaged strong-phase differences, X_i , must also be accounted for, as these are defined assuming a uniform efficiency. One approach, which has the advantage that the analysis could not only measure z_{CP} and Δz , but also improve the knowledge of $\{T_i, X_i\}$ for use in other analyses, is to reduce the weight given to signal candidates in high-efficiency regions of the Dalitz plot. An alternative approach is to use an amplitude model, and knowledge of the variation in selection efficiency across the Dalitz plot, to compute an alternative set of parameters T'_i and X'_i that incorporate efficiency effects. The latter approach incurs some model-dependence, but allows the full statistical power of the LHCb dataset to be exploited. In both cases some knowledge of

Table 7.3: Estimates of $D^{*+} \rightarrow D^0\pi_{\text{slow}}^+$, $D^0 \rightarrow K_s^0 K^+ K^-$ signal yields recorded by the LHCb detector in various data-taking periods. This summarises results obtained in Chapter 5.

Data collection period	Yield
2012 (~Run 1)	1.1×10^5
2015 (Exclusive)	1.4×10^5
2015 (Unbiased)	5.4×10^4
Run 2 (Exclusive)	2.6×10^6
Run 2 (Unbiased)	9.7×10^5
Upgrade	$\sim 10^8$

the efficiency variation is required, and once again there are two possible strategies. First, simulated events could be used, as in the amplitude analysis of $D^0 \rightarrow K_s^0 K^\pm \pi^\mp$ decays presented earlier. Alternatively, an existing amplitude model of $D^0 \rightarrow K_s^0 K^+ K^-$ decays may be used to obtain the efficiency variation from the LHCb dataset, by weighting with the inverse squared magnitude of the amplitude model. This approach would incur no significant model-dependence, as it depends only on the absolute value of the decay amplitude, which the amplitude models are known to describe accurately.

Chapter 5 contains estimates of $D^0 \rightarrow K_s^0 K^+ K^-$ signal yields in the datasets recorded in 2012 and 2015, and extrapolations of these results to the full Run 2 data-taking period, and the end of the LHCb upgrade programme. These estimates are summarised in Table 7.3.

Sensitivity studies are carried out using four configurations. The first of these corresponds to the dataset recorded in 2012, using decay-time-biasing selections. As noted in Chapter 5, this corresponds to the vast majority of data recorded during Run 1. The second configuration does not correspond to any anticipated dataset, but is rather intended to illustrate the differences between the biased and unbiased selection strategies. It produces the same size of dataset as the first configuration, but produces flat acceptance functions $\varepsilon(t) = 1$. The third and fourth configurations estimate the sensitivity expected with the full dataset recorded by LHCb during Run 2 using both biased and unbiased selection strategies. These strategies are considered separately, which is reasonable given the small 15 % overlap between samples reported in Sect. 5.5.1. In contrast to the first two configurations, differently sized datasets are generated for the two selection strategies, according to the yields given in Table 7.3.

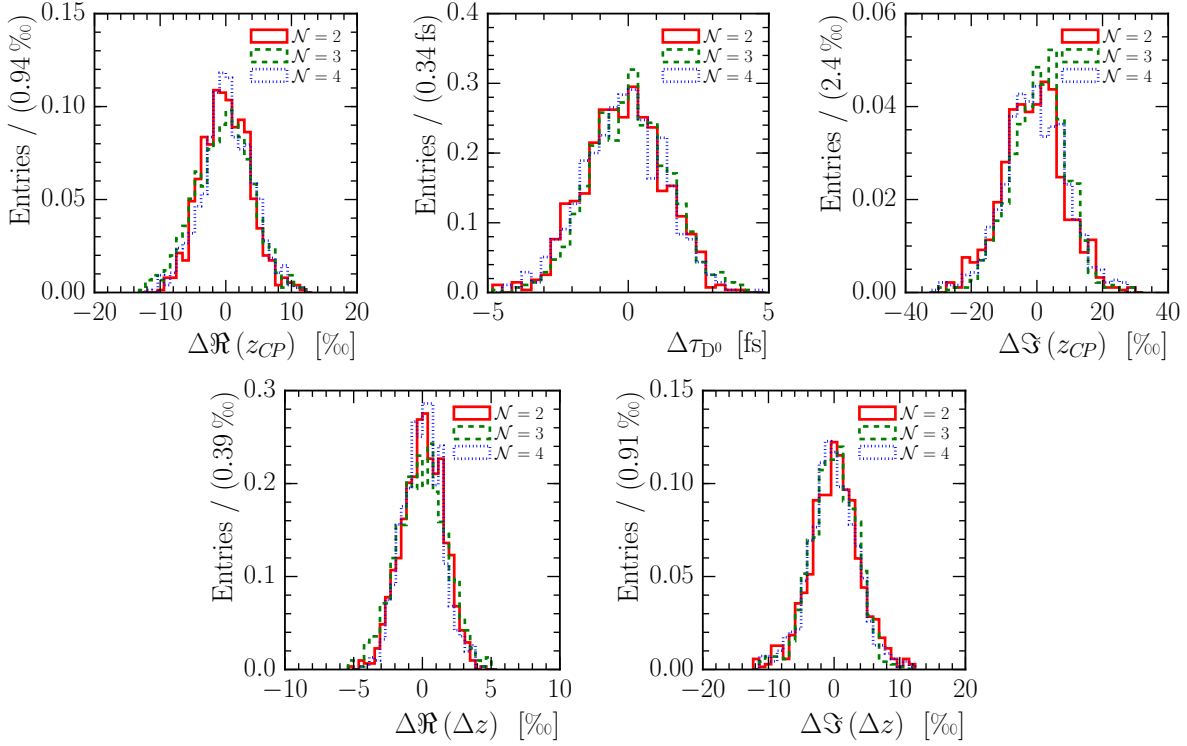


Figure 7.4: Distributions of $\Delta X \equiv X_{\text{fitted}} - X_{\text{generated}}$ obtained in pseudoexperiment studies emulating the $D^0 \rightarrow K_s^0 K^+ K^-$ dataset recorded during 2012. Distributions for the three binning schemes, $N \in \{2, 3, 4\}$, are overlaid. The widths of these distributions are tabulated in Table 7.4.

In each study the sensitivity is extracted by fitting a Gaussian function to the distributions of $\Delta X \equiv X_{\text{fitted}} - X_{\text{generated}}$, where X represents the real or imaginary part of z_{CP} or Δz , or the mean D^0 lifetime τ_{D^0} . Examples of these distributions are shown in Fig. 7.4. Some outlier removal is performed before populating these distributions. This removes the results of pseudoexperiments where the fit did not converge, or where the negative log-likelihood (NLL) has multiple minima and the fit did not converge to the correct one. Typically the minima are related to one another by a change of sign in one or more of the real and imaginary components of z_{CP} and Δz . In an analysis of real data, scans could be performed to fully describe these multiple minima, but in the pseudoexperiment studies outlying values of ΔX are simply discarded.

No large bias is observed in the various pseudoexperiment studies. In nine of the twelve (four configurations \times three binning schemes) configurations considered, the mean values of the Gaussian functions fitted to the ΔX distributions for the real and imaginary components

of z_{CP} and Δz are compatible with zero, while in the remaining three configurations (Run 2 biased $\mathcal{N} \in \{2, 3\}$, 2012 biased $\mathcal{N} = 2$) one or two of these observables show a bias of 10–20 % of the expected uncertainty. The full set of estimated biases is given in Appendix E.1.

Because each pseudoexperiment draws new values for z_{CP} and Δz from the world-average values, it is possible to study the variation in sensitivity as a function of the true values of these observables. This is done by splitting the set of pseudoexperiment results in half according to the true value of $|z_{CP}|$ or $|\Delta z|$, and comparing the sensitivities found in each half. In general, large variations in sensitivity are not seen: the largest changes are seen in those pseudoexperiments simulating larger datasets, and the sensitivity is degraded in those pseudoexperiments with larger true values of $|z_{CP}|$ or $|\Delta z|$. In most cases the change in sensitivity between the two subsets of pseudoexperiments is a few percent (*i.e.* $\sigma(\text{high } |\Delta z|)/\sigma(\text{low } |\Delta z|) \sim 1.02$), but larger variations are seen in those pseudoexperiments simulating the full Run 2 samples, in particular for the observable $\Im(\Delta z)$ when the results are split according to $|\Delta z|$. Here, the sensitivity to $\Im(\Delta z)$ degrades by around 50 % (10 %) with larger values of $|\Delta z|$ when the decay-time-biasing (unbiased) selection strategy is used. Full results showing the sensitivity to mixing and CP violation parameters for large and small values of $|z_{CP}|$ and $|\Delta z|$ are given in Appendix E.1.

The full set of twelve estimated sensitivities for each observable are given in Table 7.4. The left-most two sections of this table are based on the same dataset size, so the differences between them illustrate the effects of the biased and unbiased selections. It can be seen that the unbiased selections result in decreased sensitivity to the mixing and CP violation parameters z_{CP} and Δz per signal candidate, which is expected, as the average decay time of signal candidates is smaller in the unbiased than in the biased samples, and as a result the effects of mixing are smaller. The right-most sections of Table 7.4 also compare the biased and unbiased techniques, but in this case the reduced selection efficiency of the unbiased triggers is included.

As outlined above, the component of the total uncertainty due to knowledge of the strong-phase parameters X_i is evaluated using an alternative set of pseudoexperiments where these

Table 7.4: Estimated sensitivities to the observables z_{CP} , Δz and τ_{D^0} using different binning schemes, \mathcal{N} , and configurations. The configurations are described in the main text. In brief, they correspond to the dataset collected during 2012, or to dataset that is expected at the end of Run 2, and in each case both the normal, decay-time-biasing, selection and the “lifetime unbiased” selection described in Chapter 4 are simulated. In each case both the total uncertainty and the component of it due to uncertainties in the CLEO measurement of the strong-phase parameters X_i is given. When this component is small, the procedure used to extract it does not always succeed.

Observable	\mathcal{N}	2012 biased				2012 unbiased				Run 2 biased		Run 2 unbiased	
		Total	CLEO	Total	CLEO	Total	CLEO	Total	CLEO	Total	CLEO	Total	CLEO
τ_{D^0}	2	1.45 ± 0.04	0.50 ± 0.13	1.35 ± 0.04	0.36 ± 0.16	0.329 ± 0.009	0.173 ± 0.019	0.467 ± 0.013	0.10 ± 0.07	[fs]	[fs]	[fs]	[fs]
	3	1.46 ± 0.04	—	1.318 ± 0.035	—	0.329 ± 0.009	0.160 ± 0.021	0.471 ± 0.012	0.04 ± 0.17	[fs]	[fs]	[fs]	[fs]
$\Re(z_{CP})$	2	3.73 ± 0.10	—	4.11 ± 0.10	0.8 ± 0.7	0.924 ± 0.025	0.53 ± 0.05	1.54 ± 0.04	0.76 ± 0.10	[%]	[%]	[%]	[%]
	3	4.40 ± 0.12	1.2 ± 0.6	4.87 ± 0.14	0.9 ± 0.9	0.994 ± 0.026	0.48 ± 0.06	1.73 ± 0.05	0.67 ± 0.15	[%]	[%]	[%]	[%]
$\Im(z_{CP})$	2	10.29 ± 0.26	1.4 ± 2.5	11.95 ± 0.30	4.3 ± 1.0	2.70 ± 0.07	1.81 ± 0.11	4.16 ± 0.11	0.9 ± 0.6	[%]	[%]	[%]	[%]
	3	8.93 ± 0.23	4.2 ± 0.6	9.94 ± 0.27	4.6 ± 0.7	2.14 ± 0.06	1.41 ± 0.09	3.86 ± 0.10	2.49 ± 0.17	[%]	[%]	[%]	[%]
$\Re(\Delta z)$	2	1.53 ± 0.04	—	1.95 ± 0.05	0.2 ± 0.6	0.299 ± 0.008	—	0.605 ± 0.015	—	[%]	[%]	[%]	[%]
	3	1.80 ± 0.05	0.44 ± 0.25	2.29 ± 0.06	0.67 ± 0.26	0.361 ± 0.009	0.11 ± 0.04	0.777 ± 0.021	0.20 ± 0.10	[%]	[%]	[%]	[%]
$\Im(\Delta z)$	2	4.26 ± 0.11	0.9 ± 0.7	5.79 ± 0.15	2.0 ± 0.5	1.136 ± 0.029	0.74 ± 0.05	2.01 ± 0.05	0.98 ± 0.12	[%]	[%]	[%]	[%]
	3	3.64 ± 0.09	1.57 ± 0.25	4.32 ± 0.12	1.5 ± 0.4	1.002 ± 0.026	0.74 ± 0.04	1.75 ± 0.04	1.09 ± 0.08	[%]	[%]	[%]	[%]
$\Im(\Delta z)$	4	4.20 ± 0.11	2.55 ± 0.20	5.40 ± 0.14	3.24 ± 0.26	0.974 ± 0.025	0.70 ± 0.04	2.02 ± 0.05	1.44 ± 0.08	[%]	[%]	[%]	[%]

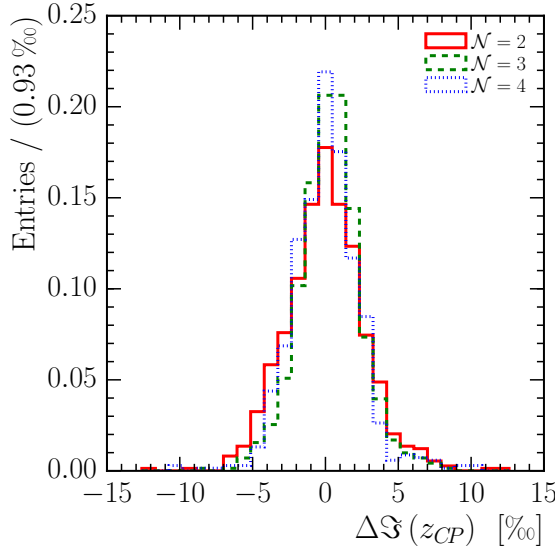


Figure 7.5: $\Delta\Im(z_{CP})$ distribution in pseudoexperiments using the “Run 2 biased” configuration.

values are fixed. The ΔX distribution is fitted as before, and the width obtained is subtracted in quadrature to obtain the uncertainties quoted under the “CLEO” heading in Table 7.4. This procedure is unstable in cases where the contribution to the total uncertainty is small, as fluctuations can lead to the uncertainty estimated with fixed $\{X_i\}$ being larger than when these parameters are allowed to vary. This could be solved by performing additional pseudoexperiments, but, as the conclusions are fairly clear, this has not been pursued.

Some variation is seen in the sensitivity to mixing and CP violation with the choice of binning scheme, \mathcal{N} . This is not typically a simple scaling in the width of ΔX . Instead, in some cases, the distribution of ΔX gains heavier tails, which increases the average width quoted in Table 7.4. For example, Fig. 7.5 shows the distribution of $\Delta\Im(z_{CP})$ in the “Run 2 biased” pseudoexperiments, where the $\mathcal{N} = 2$ contribution has broader tails than the $\mathcal{N} \in \{3, 4\}$ distributions. These tails contain pseudoexperiments where the fit favours values $\Im(X_i) \approx 0$, which makes the fit insensitive to $\Im(z_{CP})$ at leading order in decay time (Eqn. 2.28) and allows $\Im(z_{CP})$ to take large values. This behaviour is only observed in pseudoexperiments where the generated dataset is large enough to overcome the penalty terms constraining the set $\{X_i\}$ to the CLEO measurements. As noted above, scans could be performed in an analysis of real data to identify alternative NLL minima with $\{X_i\}_{\text{fitted}} \approx \{X_i\}_{\text{CLEO}}$.

Figure 7.6 illustrates the impact on the world-average results of the two of the scenarios

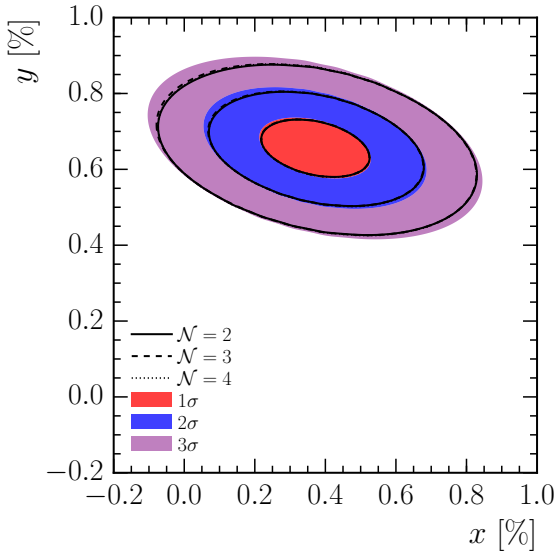
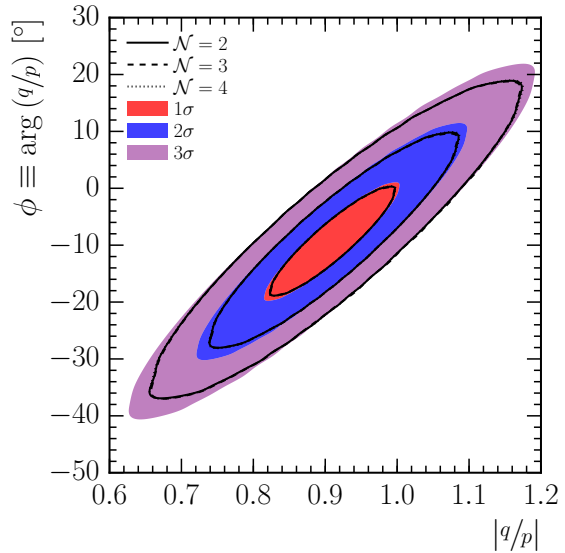
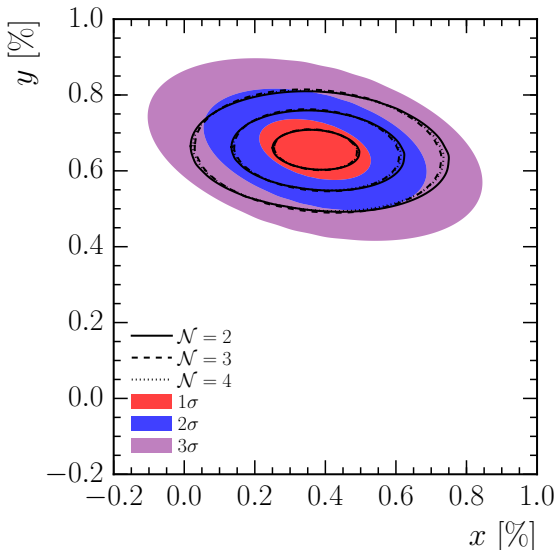
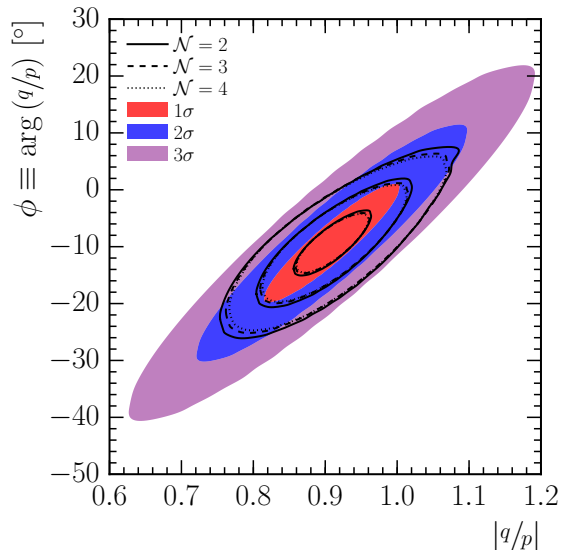
(a) 2012 biased, x vs. y .(b) 2012 biased, q/p modulus and phase.(c) Run 2 biased, x vs. y .(d) Run 2 biased, q/p modulus and phase.

Figure 7.6: Illustrations of the world-average fit results before (shaded contours) and after (black lines) the addition of new results with uncertainties corresponding to the “2012 biased” and “Run 2 biased” entries in Table 7.4. It is assumed that the new results favour the same central values. Results for the three choices of binning scheme $\mathcal{N} \in \{2, 3, 4\}$ are shown in each case using different line styles, although these typically fall very close to one another. The solid contours shown in these figures are based on a multivariate Gaussian approximation to the world-average results, and as a result fail to reproduce some of the complex features in the full results of Ref. [35] (Fig. 2.7, Chapter 2).

considered above using decay-time-biasing selections. For ease of comparison, the results have been transformed back to the usual basis of $(x, y, q/p)$ and away from the observables $(z_{CP}, \Delta z)$ that are used elsewhere in this thesis. The equivalent illustrations for the anticipated Run 2 dataset selected using the unbiased strategy are shown in Appendix E.1. There are several interesting features in these figures. Figure 7.6c clearly shows, by the rotation of the black ellipses with respect to the solid contours, that the approach outlined in this chapter is sensitive to x and y separately. The same figure shows that a more substantial reduction in uncertainty is achieved for x . Figures 7.6b and 7.6d illustrate the sensitivity to the indirect CP violation parameter q/p , showing a clear reduction in uncertainty, but no large change in the orientation of the error ellipse.

7.2 Additional corrections and validation

The swimming technique outlined in Sect. 4.3 is powerful, but nonetheless has some limitations. Several additional corrections are required if unbiased results are to be obtained. This section will describe these corrections and apply them to a sample of simulated events that have been propagated through the full LHCb detector simulation described in Sect. 3.3.

The corrections arise because of an approximation that is central to the swimming technique: alternative lifetimes are simulated by moving the set of PVs in each event, not by moving the tracking detector hits created by the charged particles that form each signal candidate. The decay time efficiency functions $\varepsilon(t)$ produced by the swimming algorithm do not, therefore, account for variations in reconstruction efficiency with the position of charged particles in the detector. The dominant variation is that tracks which are off-axis, *i.e.* with a large IP to the LHC beam line (**DOCAz**, distance of closest approach [to the] z -axis), are less likely to be reconstructed than those originating near the beam line. This effect is most pronounced in the HLT1 track reconstruction, but also exists in the HLT2 and offline reconstructions. It typically translates into a decrease in efficiency at large D^0 decay times.

These effects can be corrected by modifying the efficiency functions produced by the

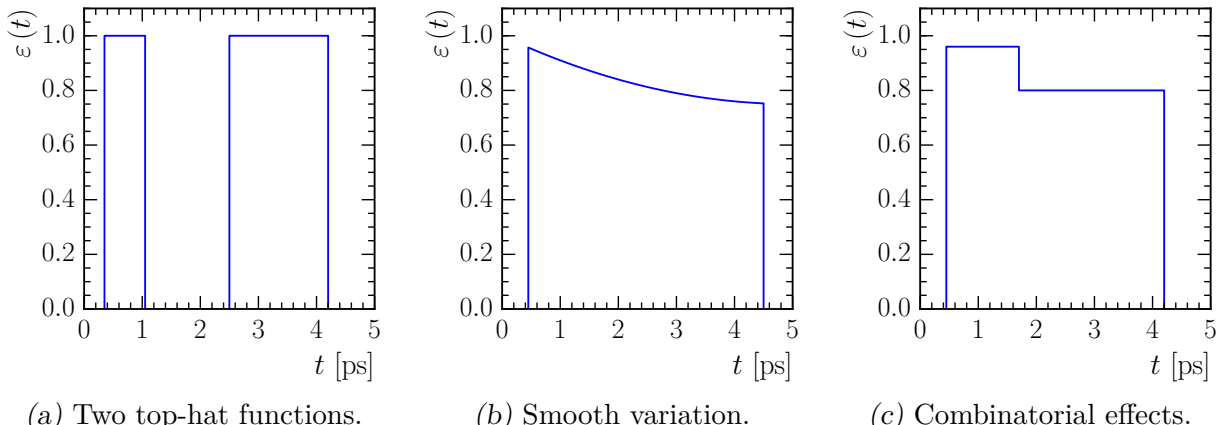


Figure 7.7: Examples of per-candidate decay time efficiency functions $\varepsilon(t)$. These are exaggerated for illustrative purposes.

swimming algorithm, which are initially a simple set of top-hat functions (Fig. 7.7a). As introduced in Sect. 4.3, the decay time values bounding these top-hat functions are known as turning points. The reconstruction effects described above can be incorporated by multiplying the initial efficiency function $\varepsilon(t)$ by a new reconstruction efficiency function $\varepsilon_{\text{eff.}}(t)$. The resulting efficiency function contains both smooth variations between turning points (Fig. 7.7b), and additional turning points where the efficiency changes between two nonzero values as a result of combinatorial effects (Fig. 7.7c).

The reconstruction efficiency functions $\varepsilon_{\text{eff.}}(t)$ are calculated for each candidate from several ingredients. The various conditional reconstruction efficiencies are parameterised as functions of **DOCAz** [200]. Examples of these curves are shown in Fig. 7.8, which contains the distributions for charged D^0 child particles (K^\pm). Different functions are used for K_s^0 child particles (π^\pm) reconstructed as long and downstream tracks, which are shown in Appendix E.2. All the tracking efficiencies shown are calculated using simulated events. The LHC beam position, which is measured by the VELO detector, determines the coefficients α_i and β_i that linearly relate **DOCAz** to the D^0 decay time, t , for each charged particle, i , in the D^0 decay final state, $\text{DOCAz}_i(t) = |\alpha_i + \beta_i t|$. The final ingredient, required to account for combinatorial effects, is the list of particles and particle combinations that satisfy the various selection thresholds at each value of t . This list is calculated by the swimming algorithm.

The combinatorial effects noted above arise because both the HLT1 and inclusive $D^{*+} \rightarrow$

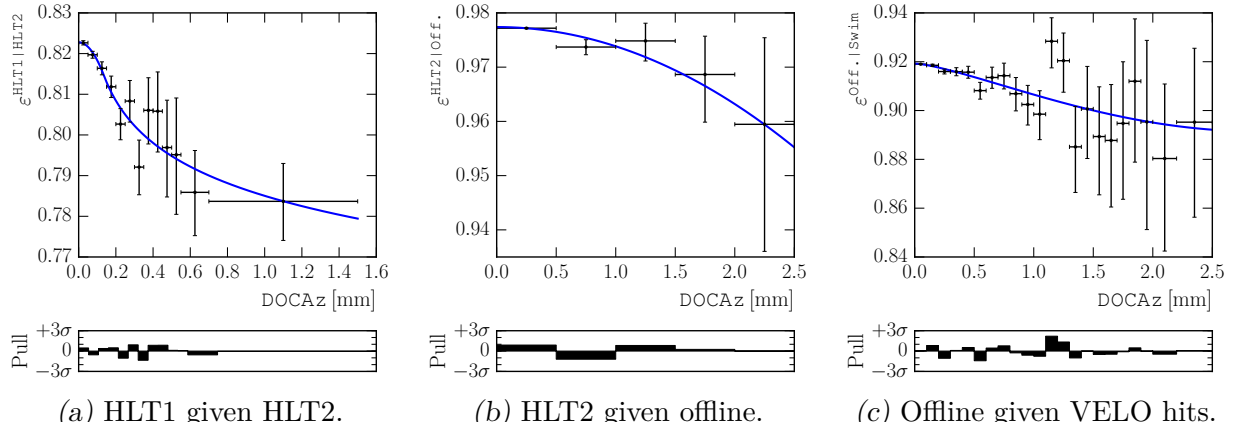


Figure 7.8: Conditional reconstruction efficiencies as a function of **DOCAz** for D⁰ child tracks (h^\pm).

The swimming algorithm contains a model of the VELO detector geometry, which allows the requirement to be imposed that, at a particular D^0 decay time, a child particle traverses enough VELO stations that it can be reconstructed. Note that both the x - and y -axis limits differ significantly between the three figures. The parameterisations used for the blue fit curves are listed in Appendix E.2.

$D^0\pi_{\text{slow}}^+$ HLT2 triggers do not require that the full set of D^0 child particles are reconstructed, and the conditional track reconstruction efficiencies are less than 100 %. For example, if the probability that a track reconstructed in HLT2 is also reconstructed in HLT1 is a constant $\bar{\varepsilon}$, and N of the four charged particles in the D^0 decay final state satisfy the HLT1 selection requirements, a combinatorial term $\varepsilon_N = 1 - (1 - \bar{\varepsilon})^N$ is required, which is the probability that at least one particle is reconstructed in HLT1. A similar expression is required for the inclusive $D^{*+} \rightarrow D^0\pi_{\text{slow}}^+$ trigger, as there are $\binom{4}{2} = 6$ possible 2-body combinations that may be used to partially reconstruct the D^0 signal candidate, and the Run 1 HLT2 track reconstruction is slightly less efficient than the Run 1 offline reconstruction. The swimming algorithm stores the set of tracks that satisfy the HLT1 kinematic requirements (four Boolean values) and the set of long track combinations that satisfy the $D^{*+} \rightarrow D^0\pi_{\text{slow}}^+$ inclusive HLT2 trigger (six Boolean values), and stores additional turning points at decay times where these sets of Boolean values change.

Between each pair of turning points, the full efficiency function $\varepsilon_{\text{eff.}}(t)$ is, therefore,

$$\varepsilon_{\text{eff.}}(t) = \varepsilon_{\text{Offline}}(t) \varepsilon_{\text{HLT2}}(t) \varepsilon_{\text{HLT1}}(t) \quad (7.6)$$

where

$$\varepsilon_{\text{Offline}}(t) = \prod_i \varepsilon_i^{\text{Off.} | \text{swim}}(\text{DOCAz}_i(t)), \quad (7.7)$$

and the index i runs over all four D^0 descendant particles. The other terms are given by

$$\varepsilon_{\text{HLT2}}(t) = \sum_p^P \left\{ \prod_i^{R_{\text{HLT2}}(p)} \varepsilon_i^{\text{HLT2} | \text{Off.}}(\text{DOCAz}_i(t)) \prod_j^{S_{\text{HLT2}}(p)} \left(1 - \varepsilon_j^{\text{HLT2} | \text{Off.}}(\text{DOCAz}_j(t))\right) \right\}, \quad (7.8)$$

$$\varepsilon_{\text{HLT1}}(t) = \sum_p^P \left\{ \prod_i^{R_{\text{HLT1}}(p)} \varepsilon_i^{\text{HLT1} | \text{HLT2}}(\text{DOCAz}_i(t)) \prod_j^{S_{\text{HLT1}}(p)} \left(1 - \varepsilon_j^{\text{HLT1} | \text{HLT2}}(\text{DOCAz}_j(t))\right) \right\}, \quad (7.9)$$

where the index p represents the permutation where the set of charged D^0 descendant particles $R_X(p)$ are reconstructed in X and $S_X(p)$ are not², and the range of the sum, P , is defined by the ten Boolean values defined above.

The full expression for $\varepsilon_{\text{eff.}}(t)$ is cumbersome, but conceptually simple. The expression is constructed using a symbolic algebra package [201], and a Taylor expansion is computed about the midpoint of the t range for which the full function was constructed. This range is never more than a few picoseconds, as the full range of t considered is [0.35 ps, 5 ps], and a first-order Taylor expansion is sufficient to approximate $\varepsilon_{\text{eff.}}(t)$. In other words, while the variation and curvature of the functions in Fig. 7.8 is significant over the full ranges, only small ranges of these functions are relevant for each signal candidate. This Taylor expansion significantly simplifies the normalisation integral Eqn. 7.1, improving performance.

The eventual result of the swimming is a list of $3n - 2$ floating point numbers for each candidate with n turning points. For example with $n = 2$ the final result is of the form

$$\varepsilon(t) = \begin{cases} a_0 + b_0 t, & t_0 < t < t_1 \\ 0, & \text{otherwise.} \end{cases} \quad (7.10)$$

Several examples of decay time efficiency functions $\varepsilon(t)$ for simulated events are illustrated in Fig. 7.9, while Fig. 7.10 illustrates the result of a fit to around 49 000 simulated,

² i.e. $R_X(p) \cup S_X(p) = \{K^+, K^-, \pi^+, \pi^-\} \forall p$.

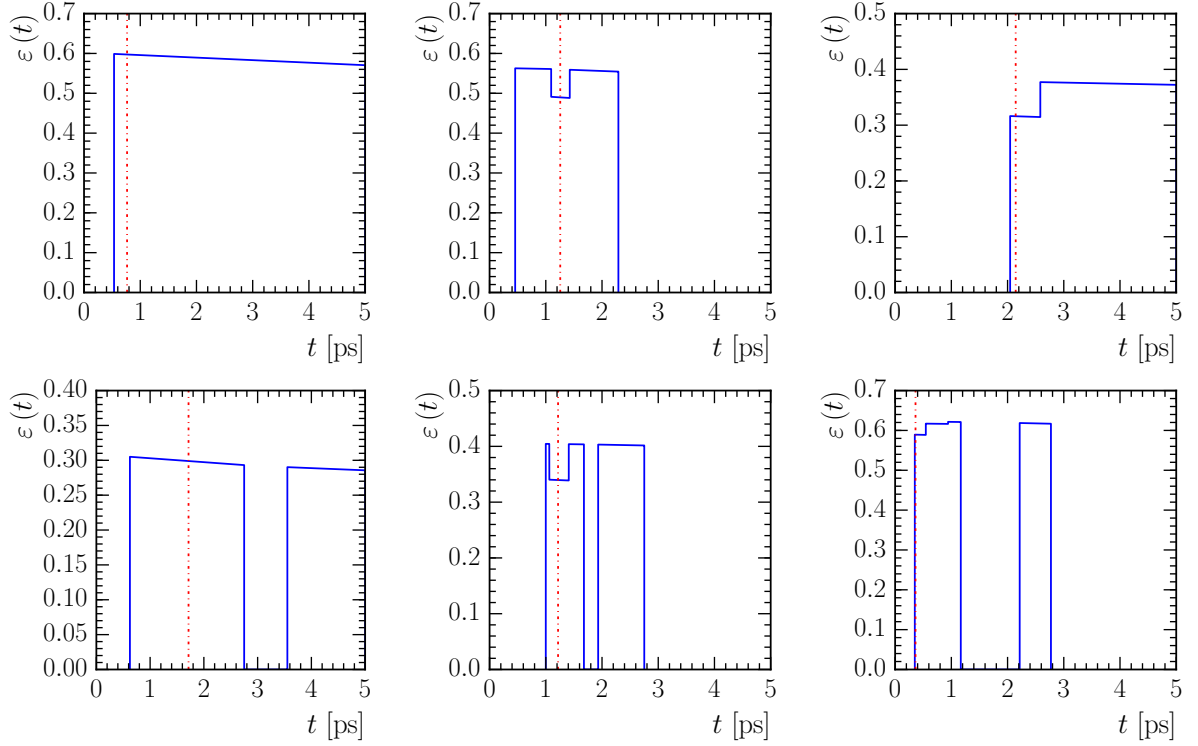


Figure 7.9: Examples of decay time acceptance functions $\varepsilon(t)$, taken from simulated decays. The vertical dash-dotted (red) line shows the measured decay time in each case. These examples have been chosen to illustrate the different features, and as such are not a representative sample.

promptly-produced $D^0 \rightarrow K_s^0 K^+ K^-$ signal events using the full swimming procedure outlined above and a single exponential function fit model. This fit produces a value of $\tau_{D^0} = 409.5 \pm 2.1$ fs for the average D^0 lifetime, consistent with the generated value of 410.1 fs. If the additional corrections to the decay time efficiency functions $\varepsilon(t)$ that have been described above are neglected, so $\varepsilon(t)$ consists simply of unit-height top-hat functions, a result of $\tau_{D^0} = 413.4 \pm 2.1$ fs is obtained.

There are several additional technicalities relating to swimming the trigger selections discussed in Chapter 5, but these do not affect the general discussion above. For example, selection requirements applied only to the π_{slow}^+ in a $D^{*+} \rightarrow D^0 \pi_{\text{slow}}^+$ decay chain do not typically bias the D^0 decay time, but if the swimming algorithm is applied naively then, because the PVs are displaced to simulate alternative D^0 decay times, the π_{slow}^+ selection would erroneously affect the simulated trigger decision. The correct turning points are calculated for the inclusive $D^{*+} \rightarrow D^0 \pi_{\text{slow}}^+$ trigger by disabling the D^{*+} part of the trigger

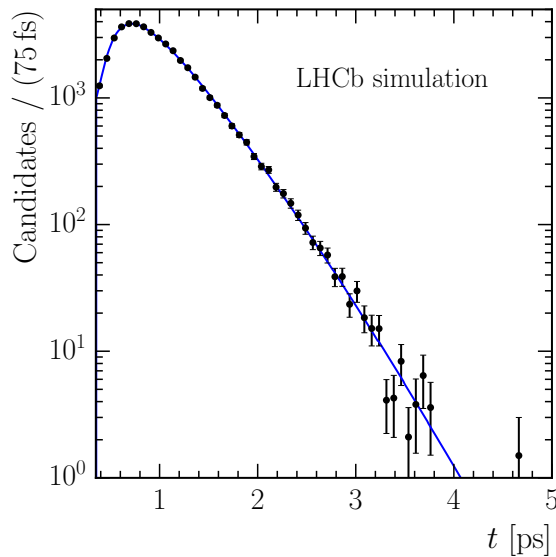


Figure 7.10: Fit with a single exponential function to simulated $D^0 \rightarrow K_s^0 K^+ K^-$ candidates.

selection and emulating one residual decay-time-biasing requirement – that the π_{slow}^+ and both reconstructed D^0 child particles are associated with the same PV – in an additional swimming iteration. Additional swimming iterations are also used to calculate turning points for offline selection requirements, such as a requirement that D^0 candidates are consistent with originating at a PV (to suppress background from b-hadron decays), an upper limit on the flight distance from the LHC beam line to suppress material interactions in the VELO, and additional requirements to mitigate software issues in the Run 1 HLT.

The additional corrections discussed in this section are not expected to have any significant impact on the expected sensitivities quoted above, but are nonetheless important to consider if an unbiased measurement is to be achieved.

7.3 Prospects for $D^0 \rightarrow K_s^0 K^+ K^-$ mixing measurements

A powerful, model-independent method for probing mixing and CP violation in the D^0 – \bar{D}^0 system has been outlined above, which can provide stringent constraints on the observables z_{CP} and Δz with no systematic uncertainty due to the use of an amplitude model. The data-driven swimming technique for the measurement of decay time efficiency functions has also been described, including the details of its application to the LHCb dataset of $D^0 \rightarrow K_s^0 K^+ K^-$

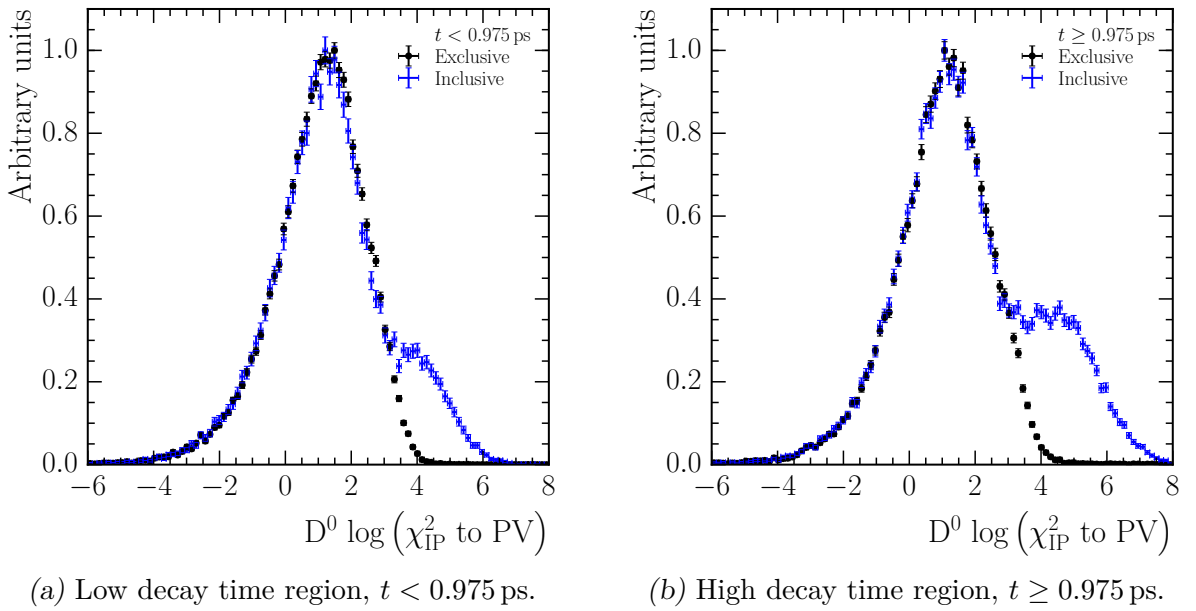


Figure 7.11: Distributions for D^0 signal candidates in the LHCb dataset recorded in 2012 of the quantity $\log(\chi^2_{IP}$ to PV), which measures how consistent the D^0 signal candidate is with originating at the nearest PV. The subsidiary peak on the right hand side of the distribution, which is more prominent at large decay times (right) than small decay times (left) corresponds to D^0 candidates produced in b-hadron decays. Distributions are shown for both the exclusive HLT2 triggers (black), which fully reconstruct the decay $D^0 \rightarrow K_s^0 h^+ h'^-$, and the inclusive $D^{*+} \rightarrow D^0 \pi_{slow}^+$ trigger (blue).

decays. This is a valuable technique for extracting unbiased decay time distributions, which can be applied to the datasets recorded by LHCb in both Run 1 and Run 2.

Unfortunately, in the LHCb dataset recorded during 2012 there are several issues with the trigger selections, which make such an analysis of this dataset particularly challenging. The primary issue is that some selections include stringent requirements that D^0 signal candidates are consistent with originating at a primary vertex, as illustrated in Fig. 7.11. While this is an effective way of increasing signal purity, it also tends to reject D^0 candidates produced in b-hadron decays at large measured D^0 decay times³. This means it is difficult to measure both the fraction of the dataset that consists of D^0 mesons produced in b-hadron decays, and the other properties of these decays, such as their decay time and turning point distributions. The latter point is important, as these distributions must be incorporated into the fit as so-called Punzi corrections. The distribution of measured decay time for these candidates, $f(t)$, is approximately the convolution of two exponential decays. However, due

³ The measured decay time contains components of both the b-hadron and D^0 meson decay times.

to the partial reconstruction of the b-hadron, an integral over $\beta \equiv \frac{m_B p_{D^0}}{m_{D^0} p_B}$ is also required,

$$f(t) \sim \int d\beta p(\beta) \left| e^{-\Gamma t} - e^{-\beta \Gamma_B t} \right|. \quad (7.11)$$

Some input from data is, therefore, required in order to obtain an accurate distribution for use in a mixing and CP violation study. This is challenging to extract from the Run-1 LHCb dataset for the reasons outlined above.

The LHCb dataset of $D^{*+} \rightarrow D^0 \pi_{\text{slow}}^+$, $D^0 \rightarrow K_s^0 h^+ h'^-$ decays recorded in Run 2 is already larger than that collected in Run 1, and the modifications that have been made to the trigger strategy are expected to both mitigate the problems outlined above, and simplify the treatment outlined in Sect. 7.2. For example, the fact that the offline and HLT2 track reconstruction algorithms are identical in Run 2 implies that the expression given in Eqn. 7.8 for the conditional reconstruction efficiency in HLT2 is simply unity, rather than a cumbersome function. In addition to these incremental improvements, the addition of “lifetime unbiased” triggers in HLT2 opens the possibility of performing an analysis on this subset of the data without using the swimming technique. As outlined in the introduction to this chapter, analysis using the per-candidate efficiency functions produced by the swimming algorithm incurs a performance penalty, so as ever-larger datasets are accumulated it may become preferable to use less computationally intensive analysis techniques.

For example, analyses of the Run 2 and LHCb upgrade datasets could use a hybrid technique, whereby the “lifetime unbiased” dataset is analysed using the full decay time PDF outlined above, while the larger dataset using decay-time-biasing selections is simultaneously analysed using a simplified method with inferior per-candidate sensitivity that does not rely on a precise determination of the selection efficiency as a function of decay time. In the LHCb upgrade era it may prove optimal to invest in more computing resources for the software trigger, allowing it to select larger and less biased datasets, and accept as a consequence that the eventual data analysis be simplified and less sensitive per-candidate in order to fit within computational constraints. It will be important to study this in detail, and ensure that the upgraded trigger system selects as optimal a dataset for these studies as possible.

In addition to the methods discussed in this thesis that probe mixing and CP violation in the $D^0-\bar{D}^0$ system using $D^0 \rightarrow K_s^0 h^+ h^-$ decays, there are several other decay modes that can provide important supplementary information. For example, the inclusive $D^0 \rightarrow K_s^0 K^- \pi^+$ and $D^0 \rightarrow K_s^0 K^+ \pi^-$ final states can constrain $\Re(z_{CP}) \approx y$ and, to a lesser extent, $\Im(z_{CP}) \approx x$ by using external measurements of the coherence factor discussed in Sects. 6.2 and 6.10 [39]. A large value of this coherence factor enhances the sensitivity to mixing effects. Decays to self-conjugate, multi-body final states whose fractional CP -even content is known (F_+ as defined in Sect. 6.2) can also be exploited in a similar, inclusive manner [202]. Final states that are close to CP -odd or CP -even, *i.e.* with F_+ near zero or unity, offer the best sensitivity if such an approach is pursued. The $D^0 \rightarrow \pi^+ \pi^- \pi^0$ decay mode is a particularly attractive prospect for such an analysis, as it has a large branching fraction and is almost entirely CP -even, with $F_+ = 0.973 \pm 0.017$ [203].

Figure 7.6 shows that a study of the $D^0 \rightarrow K_s^0 K^+ K^-$ decay mode using the dataset expected to be recorded by LHCb during Run 2 (Figs. 7.6c and 7.6d) would have an appreciable impact on the knowledge of mixing and indirect CP violation parameters in the charm system, but that studies of additional modes – such as those outlined above – will be required to conclusively answer the major outstanding questions regarding the charm system, for example: is $x \neq 0$ and what is its sign? Is the current, large, best-fit value for the indirect CP violation parameter q/p supported by new data?

It should, however, be stressed that the $D^0 \rightarrow K_s^0 h^+ h^-$ modes are particularly important probes of the charm system because they allow the full set of mixing and indirect CP violation parameters to be accessed simultaneously. The model-independent technique that has been described in this chapter is a very attractive way of analysing the sample of these decays recorded by LHCb, and the results of Sect. 7.1 show that the uncertainty due to external measurements of the strong-phase parameters X_i scales favourably with the signal yield, and future measurements of these parameters by the BES-III collaboration using quantum-correlated D-meson decays could reduce this uncertainty still further.

8. CONCLUSIONS

Several studies of the neutral charm meson system have been presented in this thesis, encompassing searches for direct CP violation, detailed study of the resonance content of exclusive decay modes, and the measurement of D^0 - \bar{D}^0 mixing and indirect CP violation. In addition to these physics analyses, the LHCb software trigger has been described in detail, in particular those changes made to it ahead of the current period of LHC operation, Run 2.

The amplitude analysis of the $D^0 \rightarrow K_s^0 K^- \pi^+$ and $D^0 \rightarrow K_s^0 K^+ \pi^-$ decay modes presented in Chapter 6 is, by far, the most precise analysis of these modes to date. Isobar models, which describe the strong-phase variation across the Dalitz plot, have been produced for each decay mode, and will be useful for future D^0 - \bar{D}^0 mixing, CP violation and CKM angle γ studies. Detailed knowledge of the variation of the complex decay amplitude across the phase space of important decay modes, such as $D^0 \rightarrow K_s^0 K^\pm \pi^\mp$, will be particularly valuable for studies of the large datasets LHCb is expected to accumulate in Run 2 and beyond.

Several other interesting results are derived from the $D^0 \rightarrow K_s^0 K^\pm \pi^\mp$ isobar models. Estimates of the contributions of different intermediate resonances, such as $K^{*+} \rightarrow K_s^0 \pi^+$, to each decay mode are used to test SU(3) flavour symmetry predictions, finding marginal agreement. The models also provide evidence for poorly-established $\rho^\pm \rightarrow K_s^0 K^\pm$ decay modes, and are used to compute the CP -even fraction and coherence factor of these decays.

The $D^0 \rightarrow K_s^0 K^\pm \pi^\mp$ decay modes are singly Cabibbo-suppressed (SCS), and are expected to receive significant contributions from loop diagrams. New Physics theories often include new particles that can contribute to these loop diagrams, enhancing the small levels of direct CP violation predicted by the SM. A search for direct CP violation was performed using the isobar models of the $D^0 \rightarrow K_s^0 K^\pm \pi^\mp$ decays, but no CP violation was found.

A model-independent technique for the measurement of mixing and indirect CP violation parameters using the sample of $D^0 \rightarrow K_s^0 K^+ K^-$ decays accumulated by LHCb was studied in Chapter 7. These data can provide constraints on the full set of D^0 - \bar{D}^0 mixing and indirect CP violation parameters, making their analysis a key component of the LHCb physics programme, alongside studies of the closely-related $D^0 \rightarrow K_s^0 \pi^+ \pi^-$ decay mode. Although recent results, including several from LHCb, have conclusively established mixing in the D^0 - \bar{D}^0 system, the world averages are dominated by two-body D-decay results, and neither large indirect CP violation nor a zero value of the dispersive component of mixing, x , has been excluded. Charm mixing will, therefore, remain an interesting topic of study in the coming years, in particular as new results utilising multi-body decay modes are published, which are sensitive to different combinations of the mixing and CP violation parameters.

The LHCb experiment has performed exceptionally well throughout Run 1 and into the early period of Run 2 of the LHC, despite the significant challenges inherent in attempting precision flavour physics measurements in the complex hadronic environment of a proton-proton collider. The changes made to the software trigger between Run 1 and Run 2 were discussed in Chapter 4, and have led to substantial improvements in signal efficiency in Run 2, as demonstrated in the study of $D^0 \rightarrow K_s^0 K^+ K^-$ signal yields presented in Chapter 5.

The upgraded LHCb experiment will operate at an instantaneous luminosity five times larger than the current detector, significantly increasing the average number of inelastic collisions per bunch crossing, and consequently the fraction of events that contain one or more interesting signal decays. The role of the LHCb trigger will, therefore, become one of signal categorisation rather than background rejection. Several key steps in this direction have been taken in Run 2, with the introduction of real-time alignment and calibration, and the “Turbo” concept of performing physics analysis directly within the software trigger, while simultaneously reducing the complexity and systematic uncertainties of these measurements.

The role of the trigger system is critical in ensuring that sufficiently large datasets are accumulated to precisely measure mixing and CP violation effects in the charm system, and to allow further precision measurements and constraints on physics beyond the SM.

APPENDIX

A. ADDITIONAL ISOBAR FORMALISM INFORMATION

This appendix contains Table A.1, which summarises the nominal values used for the various resonance and form factor parameters in the amplitude analysis of $D^0 \rightarrow K_s^0 K^\pm \pi^\mp$ decays.

Table A.1: Nominal values for isobar model parameters that are fixed in the model fits, or used in constraint terms. These values are taken from Refs. [54, 65, 73, 184] as described in Chapters 2 and 6.

	Parameter	Value
$K^*(892)^\pm$	m_R	891.66 ± 0.26 MeV/ c^2
	Γ_R	50.8 ± 0.9 MeV/ c^2
$K^*(1410)^\pm$	m_R	1.414 ± 0.015 GeV/ c^2
	Γ_R	0.232 ± 0.021 GeV/ c^2
$(K_s^0 \pi)_{S\text{-wave}}^\pm$	m_R	1.435 ± 0.005 GeV/ c^2
	Γ_R	0.279 ± 0.006 GeV/ c^2
$K^*(892)^0$	m_R	895.94 ± 0.22 MeV/ c^2
	Γ_R	48.7 ± 0.8 MeV/ c^2
$K^*(1410)^0$	m_R	1.414 ± 0.015 GeV/ c^2
	Γ_R	0.232 ± 0.021 GeV/ c^2
$K_2^*(1430)^0$	m_R	1.4324 ± 0.0013 GeV/ c^2
	Γ_R	0.109 ± 0.005 GeV/ c^2
$(K\pi)_{S\text{-wave}}^0$	m_R	1.435 ± 0.005 GeV/ c^2
	Γ_R	0.279 ± 0.006 GeV/ c^2
$K\pi$ S -wave	r	1.8 ± 0.4 c/GeV
	a	1.95 ± 0.09 c/GeV
$a_0(980)^\pm$	m_R	0.980 ± 0.020 GeV/ c^2
	$g_{\eta\pi}$	324 ± 15 MeV
	$g_{K\bar{K}}^2/g_{\eta\pi}^2$	1.03 ± 0.14
$a_2(1320)^\pm$	m_R	1.3181 ± 0.0007 GeV/ c^2
	Γ_R	0.1098 ± 0.0024 GeV/ c^2
$a_0(1450)^\pm$	m_R	1.474 ± 0.019 GeV/ c^2
	Γ_R	0.265 ± 0.013 GeV/ c^2
$\rho(1450)^\pm$	m_R	1.182 ± 0.030 GeV/ c^2
	Γ_R	0.389 ± 0.020 GeV/ c^2
$\rho(1700)^\pm$	m_R	1.594 ± 0.020 GeV/ c^2
	Γ_R	0.259 ± 0.020 GeV/ c^2

B. $D^0 \rightarrow K_s^0 K^\pm \pi^\mp$ ISOBAR MODEL EVOLUTION

This appendix concerns the amplitude analysis of $D^0 \rightarrow K_s^0 K^\pm \pi^\mp$ decays, and contains additional information about the amplitude models found in Chapter 6, and in particular the model-finding procedure described in Sect. 6.3. First, Table B.1 lists parameters that are fixed to their known value in the final models as a result of having a fitted value within 1σ of that value. This adjustment was described in Sect. 6.5.

Tables B.2 (GLASS) and B.3 (LASS), which show how the unconstrained $K\pi$ *S*-wave parameters evolve as the model-finding procedure progresses. Additional tables (B.4–B.14) are also included, which show how the resonance content of the various models changes throughout the procedure. The sequence of models found for each $K\pi$ *S*-wave parameterisation is tabulated in Tables B.2 and B.3, alongside the $K\pi$ *S*-wave parameters. The “refined” models were discussed in Sect. 6.4 and are not revisited here.

Table B.1: Parameters that are fixed to nominal values because no significant deviation was found. One list is given for each $K\pi$ *S*-wave parameterisation, and the corresponding increase in $-2 \log \mathcal{L}$ is given in each case.

(a) LASS parameterisation.	(b) GLASS parameterisation.
$K_0^*(1430)^{0,\pm}$ mass and width	$K_0^*(1430)^{0,\pm}$ mass and width
$K^*(1410)^{0,\pm}$ width	$K^*(892)^0$ mass and width
$K^*(892)^0$ mass and width	$a_0(1450)^\pm$ width
$\rho(1450, 1700)^\pm$ width	$\rho(1700)^\pm$ width
LASS a	$K^*(1410)^\pm$ mass
$\Delta(-2 \log \mathcal{L}) = 6.20.$	$\Delta(-2 \log \mathcal{L}) = 5.10.$

Table B.2: Evolution of GLASS $K\pi$ S -wave parameters during the model-finding procedure. There is no “2nd cleaning” heading corresponding to Table B.5, or “4th cleaning” heading corresponding to Table B.11, because these steps marked the end of the cleaning procedures, and thus the selected model is the same as its predecessor.

Table reference		6.3	6.5	B.4	—	B.10
Channel	Parameter	<i>1st iteration</i>	<i>2nd iteration</i>	<i>1st cleaning</i>	<i>Refined</i>	<i>3rd cleaning</i>
$(K_s^0 \pi)^\pm$	F	1.12	1.22	1.46	1.10	1.75
	a [c/GeV]	4.86	4.95	4.72	4.52	4.58
	r [c/GeV]	-5.62	-5.33	-5.51	-6.02	-5.45
	ϕ_R [rad]	2.80	2.84	2.79	2.71	2.83
	ϕ_F [rad]	0.35	0.33	0.34	0.33	0.30
$(K\pi)^0$	F	0.22	0.25	0.18	0.16	0.16
	a [c/GeV]	4.63	4.58	4.50	4.21	4.16
	r [c/GeV]	-3.80	-3.84	-3.61	-3.31	-3.12
	ϕ_R [rad]	-1.69	-1.69	-1.45	-1.11	-1.06
	ϕ_F [rad]	-2.64	-2.70	-2.70	-2.61	-2.55

Table B.3: Evolution of LASS $K\pi$ S -wave parameters during the model-finding procedure. There is no “4th cleaning” heading corresponding to Table B.9, because this step marked the end of the cleaning procedure, and this the selected model is the same as the “3rd cleaning” heading. The final cleaning iterations (Tables B.13 and B.14) are not shown, as no significant variation is observed.

Table reference		6.4	6.6	B.6	B.7	B.8	—	B.12
Channel	Parameter	<i>1st iteration</i>	<i>2nd iteration</i>	<i>1st cleaning</i>	<i>2nd cleaning</i>	<i>3rd cleaning</i>	<i>Refined</i>	<i>5th cleaning</i>
$(K_s^0 \pi)^\pm$	b_1	-14.52	-14.25	-14.48	-14.35	-11.47	-22.59	-22.94
	b_2	26.97	26.88	26.95	26.88	20.64	39.56	39.58
	b_3	-20.02	-20.27	-20.13	-20.29	-16.03	-27.10	-27.02
$(K\pi)^0$	b_1	-26.26	-26.05	-26.30	-26.08	-32.34	-65.00	-64.81
	b_2	48.81	48.81	48.89	48.81	59.28	114.51	114.40
	b_3	-33.47	-33.57	-33.41	-33.60	-39.49	-71.68	-71.84
a [c/GeV]		2.04	2.05	2.04	2.03	2.06	2.02	1.99
r [c/GeV]		0.95	0.88	0.88	0.99	0.81	1.11	1.20

Table B.4: Fit results after the first cleaning iteration using the GLASS $K\pi$ S -wave parameterisation. Descriptions are relative to the retained model in Table 6.5.

Description	$D^0 \rightarrow K_s^0 K^- \pi^+$		$D^0 \rightarrow K_s^0 K^+ \pi^-$		$\Delta(-2 \log \mathcal{L})$	Retained
	χ^2/bin	DFF [%]	χ^2/bin	DFF [%]		
No $K^*(1410)^-$ in $D^0 \rightarrow K_s^0 K^+ \pi^-$	1.12	101.5	1.10	72.3	36.9	No
No $a_2(1320)^-$ in $D^0 \rightarrow K_s^0 K^- \pi^+$	1.14	105.5	1.08	72.3	34.9	No
No $\rho(1450)^-$ in $D^0 \rightarrow K_s^0 K^- \pi^+$	1.14	127.8	1.08	71.5	32.2	No
No $\rho(1450)^+$ in $D^0 \rightarrow K_s^0 K^+ \pi^-$	1.13	101.7	1.08	72.7	27.2	No
No $\rho(1700)^0$ in $D^0 \rightarrow K_s^0 K^- \pi^+$	1.14	107.5	1.08	70.3	24.2	No
No $a_0(980)^-$ in $D^0 \rightarrow K_s^0 K^- \pi^+$	1.13	103.1	1.08	72.6	11.8	Yes
No change	1.13	105.9	1.08	71.1	—	No

Table B.5: Fit results after the second cleaning iteration using the GLASS $K\pi$ S -wave parameterisation. Descriptions are relative to the retained model in Table B.4.

Description	$D^0 \rightarrow K_s^0 K^- \pi^+$		$D^0 \rightarrow K_s^0 K^+ \pi^-$		$\Delta(-2 \log \mathcal{L})$	Retained
	χ^2/bin	DFF [%]	χ^2/bin	DFF [%]		
No $K^*(1410)^0$ in $D^0 \rightarrow K_s^0 K^+ \pi^-$	1.14	120.4	1.11	79.1	129.53	No
No $K_2^*(1430)^0$ in $D^0 \rightarrow K_s^0 K^+ \pi^-$	1.15	96.3	1.12	75.0	121.82	No
No $a_0(980)^+$ in $D^0 \rightarrow K_s^0 K^+ \pi^-$	1.13	129.4	1.12	84.7	92.79	No
No $a_0(1450)^+$ in $D^0 \rightarrow K_s^0 K^+ \pi^-$	1.13	121.6	1.12	83.5	75.45	No
No $K^*(1410)^-$ in $D^0 \rightarrow K_s^0 K^+ \pi^-$	1.13	100.0	1.10	74.1	44.31	No
No $a_2(1320)^-$ in $D^0 \rightarrow K_s^0 K^- \pi^+$	1.15	101.5	1.09	74.6	42.24	No
No $\rho(1700)^+$ in $D^0 \rightarrow K_s^0 K^+ \pi^-$	1.13	107.7	1.09	70.3	37.32	No
No $\rho(1450)^+$ in $D^0 \rightarrow K_s^0 K^+ \pi^-$	1.14	99.3	1.08	75.0	28.64	No
No $\rho(1700)^-$ in $D^0 \rightarrow K_s^0 K^- \pi^+$	1.14	105.3	1.08	71.9	19.08	No
No change	1.13	103.1	1.08	72.6	—	Yes

Table B.6: Fit results after the first cleaning iteration using the LASS $K\pi$ S -wave parameterisation. Descriptions are relative to the retained model in Table 6.6.

Description	$D^0 \rightarrow K_s^0 K^- \pi^+$		$D^0 \rightarrow K_s^0 K^+ \pi^-$		$\Delta(-2 \log \mathcal{L})$	Retained
	χ^2/bin	DFF [%]	χ^2/bin	DFF [%]		
No $a_0(1450)^-$ in $D^0 \rightarrow K_s^0 K^- \pi^+$	1.19	112.1	1.09	95.2	119.27	No
No $\rho(1700)^-$ in $D^0 \rightarrow K_s^0 K^+ \pi^-$	1.13	113.8	1.13	82.3	80.93	No
No $K^*(1410)^-$ in $D^0 \rightarrow K_s^0 K^+ \pi^-$	1.13	114.1	1.12	88.4	39.76	No
No $K^*(1410)^0$ in $D^0 \rightarrow K_s^0 K^+ \pi^-$	1.13	109.7	1.11	101.1	31.48	No
No $a_2(1320)^-$ in $D^0 \rightarrow K_s^0 K^- \pi^+$	1.14	120.1	1.10	89.4	26.57	No
No $\rho(1450)^+$ in $D^0 \rightarrow K_s^0 K^+ \pi^-$	1.13	112.8	1.12	82.5	22.21	No
No $\rho(1700)^-$ in $D^0 \rightarrow K_s^0 K^+ \pi^-$	1.13	115.8	1.11	90.7	20.80	No
No $K_2^*(1430)^-$ in $D^0 \rightarrow K_s^0 K^+ \pi^-$	1.13	114.6	1.11	85.5	6.71	No
No $K_2^*(1430)^0$ in $D^0 \rightarrow K_s^0 K^+ \pi^-$	1.13	113.1	1.10	91.7	4.91	No
No $a_2(1320)^+$ in $D^0 \rightarrow K_s^0 K^+ \pi^-$	1.13	114.0	1.10	90.6	1.47	Yes
No change	1.13	113.4	1.10	90.6	—	No

Table B.7: Fit results after the second cleaning iteration using the LASS $K\pi$ S -wave parameterisation. Descriptions are relative to the retained model in Table B.6.

Description	$D^0 \rightarrow K_s^0 K^- \pi^+$		$D^0 \rightarrow K_s^0 K^+ \pi^-$		$\Delta(-2 \log \mathcal{L})$	Retained
	χ^2/bin	DFF [%]	χ^2/bin	DFF [%]		
No $a_0(1450)^-$ in $D^0 \rightarrow K_s^0 K^- \pi^+$	1.20	112.8	1.09	94.7	121.36	No
No $\rho(1700)^+$ in $D^0 \rightarrow K_s^0 K^+ \pi^-$	1.13	116.6	1.13	81.5	81.93	No
No $K^*(1410)^-$ in $D^0 \rightarrow K_s^0 K^+ \pi^-$	1.13	117.4	1.13	86.9	51.77	No
No $K^*(1410)^0$ in $D^0 \rightarrow K_s^0 K^+ \pi^-$	1.13	110.6	1.11	101.0	33.47	No
No $a_2(1320)^-$ in $D^0 \rightarrow K_s^0 K^- \pi^+$	1.14	120.7	1.10	89.4	25.37	No
No $\rho(1450)^+$ in $D^0 \rightarrow K_s^0 K^+ \pi^-$	1.13	113.6	1.12	82.6	22.15	No
No $\rho(1700)^-$ in $D^0 \rightarrow K_s^0 K^- \pi^+$	1.13	116.3	1.11	90.1	20.42	No
No $K_2^*(1430)^-$ in $D^0 \rightarrow K_s^0 K^+ \pi^-$	1.13	115.8	1.11	85.9	7.08	No
No $K_2^*(1430)^0$ in $D^0 \rightarrow K_s^0 K^+ \pi^-$	1.13	113.4	1.10	91.7	3.94	Yes

Table B.8: Fit results after the third cleaning iteration using the LASS $K\pi$ S -wave parameterisation. Descriptions are relative to the retained model in Table B.7.

Description	$D^0 \rightarrow K_s^0 K^- \pi^+$		$D^0 \rightarrow K_s^0 K^+ \pi^-$		$\Delta(-2 \log \mathcal{L})$	Retained
	χ^2/bin	DFF [%]	χ^2/bin	DFF [%]		
No $K^*(1410)^-$ in $D^0 \rightarrow K_s^0 K^+ \pi^-$	1.12	112.6	1.17	73.2	130.23	No
No $a_0(1450)^-$ in $D^0 \rightarrow K_s^0 K^- \pi^+$	1.19	112.6	1.10	94.7	120.53	No
No $\rho(1700)^+$ in $D^0 \rightarrow K_s^0 K^+ \pi^-$	1.14	118.1	1.13	80.8	85.63	No
No $K^*(1410)^0$ in $D^0 \rightarrow K_s^0 K^+ \pi^-$	1.14	114.3	1.11	106.7	49.35	No
No $\rho(1450)^+$ in $D^0 \rightarrow K_s^0 K^+ \pi^-$	1.13	112.8	1.12	87.0	37.27	No
No $a_2(1320)^-$ in $D^0 \rightarrow K_s^0 K^- \pi^+$	1.13	118.1	1.11	90.9	28.33	No
No $\rho(1700)^-$ in $D^0 \rightarrow K_s^0 K^- \pi^+$	1.13	115.8	1.11	90.9	17.58	No
No $K_2^*(1430)^-$ in $D^0 \rightarrow K_s^0 K^+ \pi^-$	1.13	112.5	1.11	84.5	10.06	Yes
No change	1.13	112.8	1.10	91.7	—	No

Table B.9: Fit results after the fourth cleaning iteration using the LASS $K\pi$ S -wave parameterisation. Descriptions are relative to the retained model in Table B.8.

Description	$D^0 \rightarrow K_s^0 K^- \pi^+$		$D^0 \rightarrow K_s^0 K^+ \pi^-$		$\Delta(-2 \log \mathcal{L})$	Retained
	χ^2/bin	DFF [%]	χ^2/bin	DFF [%]		
No $K^*(1410)^-$ in $D^0 \rightarrow K_s^0 K^+ \pi^-$	1.12	111.2	1.17	75.4	141.93	No
No $a_0(1450)^-$ in $D^0 \rightarrow K_s^0 K^- \pi^+$	1.19	111.5	1.10	89.5	117.13	No
No $\rho(1700)^+$ in $D^0 \rightarrow K_s^0 K^+ \pi^-$	1.13	114.8	1.14	79.3	77.82	No
No $K^*(1410)^0$ in $D^0 \rightarrow K_s^0 K^+ \pi^-$	1.14	117.0	1.13	103.5	73.66	No
No $a_2(1320)^-$ in $D^0 \rightarrow K_s^0 K^- \pi^+$	1.13	117.2	1.12	83.8	30.32	No
No $\rho(1450)^+$ in $D^0 \rightarrow K_s^0 K^+ \pi^-$	1.13	112.8	1.13	86.0	29.26	No
No $\rho(1700)^-$ in $D^0 \rightarrow K_s^0 K^- \pi^+$	1.13	115.6	1.11	84.6	16.53	No
No change	1.13	112.5	1.11	84.5	—	Yes

Table B.10: Fit results after the third cleaning iteration using the GLASS $K\pi$ *S*-wave parameterisation. Descriptions are relative to the refined model described in the text.

Description	$D^0 \rightarrow K_s^0 K^- \pi^+$		$D^0 \rightarrow K_s^0 K^+ \pi^-$		$\Delta (-2 \log \mathcal{L})$	Retained
	χ^2/bin	DFF [%]	χ^2/bin	DFF [%]		
No $K^*(1410)^0$ in $D^0 \rightarrow K_s^0 K^+ \pi^-$	1.14	94.9	1.09	82.2	128.76	No
No $a_0(1450)^+$ in $D^0 \rightarrow K_s^0 K^+ \pi^-$	1.12	107.9	1.11	78.5	88.58	No
No $\bar{K}_2^*(1430)^0$ in $D^0 \rightarrow K_s^0 K^- \pi^+$	1.16	93.5	1.07	73.5	86.93	No
No $a_0(980)^+$ in $D^0 \rightarrow K_s^0 K^+ \pi^-$	1.12	121.5	1.10	84.0	80.23	No
No $K_2^*(1430)^0$ in $D^0 \rightarrow K_s^0 K^+ \pi^-$	1.11	98.6	1.10	82.7	74.78	No
No $\rho(1450)^-$ in $D^0 \rightarrow K_s^0 K^- \pi^+$	1.15	114.7	1.07	70.5	69.82	No
No $\rho(1700)^+$ in $D^0 \rightarrow K_s^0 K^+ \pi^-$	1.12	108.0	1.09	70.9	53.46	No
No $a_2(1320)^-$ in $D^0 \rightarrow K_s^0 K^- \pi^+$	1.12	102.1	1.08	76.2	35.16	No
No $\rho(1450)^+$ in $D^0 \rightarrow K_s^0 K^+ \pi^-$	1.12	98.2	1.07	73.9	29.58	No
No $K^*(1410)^-$ in $D^0 \rightarrow K_s^0 K^+ \pi^-$	1.11	101.3	1.09	73.4	29.01	No
No $\rho(1700)^-$ in $D^0 \rightarrow K_s^0 K^- \pi^+$	1.13	101.5	1.07	71.8	25.38	No
No $K_2^*(1430)^-$ in $D^0 \rightarrow K_s^0 K^+ \pi^-$	1.12	101.2	1.07	80.2	12.45	Yes
No change	1.11	102.2	1.07	73.6	—	No

Table B.11: Fit results after the fourth cleaning iteration using the GLASS $K\pi$ *S*-wave parameterisation. Descriptions are relative to the retained model in Table B.10.

Description	$D^0 \rightarrow K_s^0 K^- \pi^+$		$D^0 \rightarrow K_s^0 K^+ \pi^-$		$\Delta (-2 \log \mathcal{L})$	Retained
	χ^2/bin	DFF [%]	χ^2/bin	DFF [%]		
No $K^*(1410)^0$ in $D^0 \rightarrow K_s^0 K^+ \pi^-$	1.14	87.6	1.11	83.7	159.17	No
No $\rho(1700)^+$ in $D^0 \rightarrow K_s^0 K^+ \pi^-$	1.14	109.4	1.09	74.7	97.14	No
No $\bar{K}_2^*(1430)^0$ in $D^0 \rightarrow K_s^0 K^- \pi^+$	1.17	92.5	1.07	77.5	94.68	No
No $K^*(1410)^-$ in $D^0 \rightarrow K_s^0 K^+ \pi^-$	1.11	105.6	1.12	82.4	94.14	No
No $a_0(1450)^+$ in $D^0 \rightarrow K_s^0 K^+ \pi^-$	1.12	106.8	1.11	87.7	85.44	No
No $K_2^*(1430)^0$ in $D^0 \rightarrow K_s^0 K^+ \pi^-$	1.13	107.1	1.09	71.1	79.88	No
No $\rho(1450)^-$ in $D^0 \rightarrow K_s^0 K^- \pi^+$	1.15	114.4	1.08	81.3	79.54	No
No $\rho(1450)^+$ in $D^0 \rightarrow K_s^0 K^+ \pi^-$	1.13	95.1	1.08	80.6	42.76	No
No $a_2(1320)^-$ in $D^0 \rightarrow K_s^0 K^- \pi^+$	1.13	101.8	1.07	82.8	34.27	No
No $\rho(1700)^-$ in $D^0 \rightarrow K_s^0 K^- \pi^+$	1.13	100.3	1.07	79.1	26.15	No
No change	1.12	101.2	1.07	80.2	—	Yes

Table B.12: Fit results after the fifth cleaning iteration using the LASS $K\pi$ *S*-wave parameterisation. Descriptions are relative to the refined model described in the text.

Description	$D^0 \rightarrow K_s^0 K^- \pi^+$		$D^0 \rightarrow K_s^0 K^+ \pi^-$		$\Delta (-2 \log \mathcal{L})$	Retained
	χ^2/bin	DFF [%]	χ^2/bin	DFF [%]		
No $(K_s^0 \pi^-)_{S\text{-wave}}$ in $D^0 \rightarrow K_s^0 K^+ \pi^-$	1.09	112.7	1.15	91.8	157.16	No
No $a_0(980)^-$ in $D^0 \rightarrow K_s^0 K^- \pi^+$	1.16	103.0	1.10	96.1	145.57	No
No $K^*(1410)^-$ in $D^0 \rightarrow K_s^0 K^+ \pi^-$	1.09	110.3	1.14	75.8	145.46	No
No $a_0(1450)^-$ in $D^0 \rightarrow K_s^0 K^- \pi^+$	1.15	113.0	1.08	95.0	82.49	No
No $\rho(1700)^+$ in $D^0 \rightarrow K_s^0 K^+ \pi^-$	1.09	108.2	1.12	88.5	76.91	No
No $a_0(1450)^+$ in $D^0 \rightarrow K_s^0 K^+ \pi^-$	1.14	106.2	1.08	116.3	72.54	No
No $K^*(1410)^0$ in $D^0 \rightarrow K_s^0 K^+ \pi^-$	1.10	112.5	1.10	114.2	41.21	No
No $a_2(1320)^-$ in $D^0 \rightarrow K_s^0 K^- \pi^+$	1.10	114.2	1.09	92.5	28.35	No
No $\rho(1450)^+$ in $D^0 \rightarrow K_s^0 K^+ \pi^-$	1.10	107.7	1.09	98.5	15.32	No
No $\rho(1700)^-$ in $D^0 \rightarrow K_s^0 K^- \pi^+$	1.10	109.4	1.09	94.1	2.35	Yes
No change	1.10	108.6	1.09	93.7	—	No

Table B.13: Fit results after the sixth cleaning iteration using the LASS $K\pi$ S -wave parameterisation. Descriptions are relative to the retained model in Table. B.12.

Description	$D^0 \rightarrow K_s^0 K^- \pi^+$		$D^0 \rightarrow K_s^0 K^+ \pi^-$		$\Delta(-2 \log \mathcal{L})$	Retained
	χ^2/bin	DFF [%]	χ^2/bin	DFF [%]		
No $(K_s^0 \pi)^-$ wave in $D^0 \rightarrow K_s^0 K^+ \pi^-$	1.09	113.6	1.15	92.1	155.39	No
No $K^*(1410)^-$ in $D^0 \rightarrow K_s^0 K^+ \pi^-$	1.09	111.4	1.14	76.1	147.52	No
No $a_0(980)^-$ in $D^0 \rightarrow K_s^0 K^- \pi^+$	1.16	102.6	1.10	97.2	141.52	No
No $a_0(1450)^-$ in $D^0 \rightarrow K_s^0 K^- \pi^+$	1.15	115.3	1.08	96.1	89.15	No
No $a_0(1450)^-$ in $D^0 \rightarrow K_s^0 K^+ \pi^-$	1.13	108.4	1.10	120.7	84.29	No
No $\rho(1700)^+$ in $D^0 \rightarrow K_s^0 K^+ \pi^-$	1.09	108.5	1.12	89.3	74.80	No
No $K^*(1410)^0$ in $D^0 \rightarrow K_s^0 K^+ \pi^-$	1.10	115.7	1.10	115.5	49.81	No
No $a_2(1320)^-$ in $D^0 \rightarrow K_s^0 K^- \pi^+$	1.10	115.1	1.10	92.5	30.26	No
No $\rho(1450)^+$ in $D^0 \rightarrow K_s^0 K^+ \pi^-$	1.10	108.9	1.09	99.3	16.18	Yes
No change	1.10	109.4	1.09	94.1	—	No

Table B.14: Fit results after the seventh cleaning iteration using the LASS $K\pi$ S -wave parameterisation. Descriptions are relative to the retained model in Table B.13.

Description	$D^0 \rightarrow K_s^0 K^- \pi^+$		$D^0 \rightarrow K_s^0 K^+ \pi^-$		$\Delta(-2 \log \mathcal{L})$	Retained
	χ^2/bin	DFF [%]	χ^2/bin	DFF [%]		
No $a_0(980)^-$ in $D^0 \rightarrow K_s^0 K^- \pi^+$	1.16	103.0	1.10	101.3	137.53	No
No $\rho(1700)^+$ in $D^0 \rightarrow K_s^0 K^+ \pi^-$	1.10	110.0	1.12	91.9	97.21	No
No $a_0(1450)^-$ in $D^0 \rightarrow K_s^0 K^- \pi^+$	1.15	115.8	1.08	102.2	91.71	No
No $a_0(1450)^+$ in $D^0 \rightarrow K_s^0 K^+ \pi^-$	1.14	106.9	1.10	122.8	77.99	No
No $K^*(1410)^0$ in $D^0 \rightarrow K_s^0 K^+ \pi^-$	1.10	114.9	1.11	117.8	61.20	No
No $a_2(1320)^-$ in $D^0 \rightarrow K_s^0 K^- \pi^+$	1.10	114.0	1.10	98.3	31.69	No
No change	1.10	108.9	1.09	99.3	—	Yes

C. ADDITIONAL $D^0 \rightarrow K_s^0 K^\pm \pi^\mp$ ISOBAR MODEL INFORMATION

This appendix contains additional information about the various isobar model parameters that are used and allowed to vary freely in the $D^0 \rightarrow K_s^0 K^\pm \pi^\mp$ amplitude model fits, *e.g.* resonance mass and width parameter values, and parameters of the **GLASS** and **LASS** $K\pi$ *S*-wave functional forms. It also contains supplementary results, such as those of the search for *CP* violation in $D^0 \rightarrow K_s^0 K^\pm \pi^\mp$ decays.

Tables C.1 and C.2 summarise the most significant interference terms in the $D^0 \rightarrow K_s^0 K^- \pi^+$ and $D^0 \rightarrow K_s^0 K^+ \pi^-$ models, respectively. Table C.3 defines the matrices **U** used to define the **LASS** $K\pi$ *S*-wave form factor. Tables C.4 (**GLASS**) and C.5 (**LASS**) summarise the various resonance and form factor parameters. The nominal values that are used in Gaussian constraint terms are given in Appendix A.

Figure C.1 illustrates the two-dimensional quality of fit achieved in the four isobar models and shows the binning scheme used to derive χ^2/bin values.

The changes in $-2 \log \mathcal{L}$ obtained in alternative models where one ρ contribution is removed are given in Table C.6.

Finally, Table C.7 summarises the full fit results of the searches for *CP* violation described in Sect. 6.8.

Table C.1: Interference fractions for the $D^0 \rightarrow K_s^0 K^- \pi^+$ mode. The first uncertainties are statistical and the second systematic. Only the 25 largest terms are shown.

(a) Best GLASS isobar model.		(b) Best LASS isobar model.			
Resonances	Fit fraction [%]	Resonances	Fit fraction [%]		
$(K\pi)_S^0$	$\times K^*(892)^+$	$12 \pm 1 \pm 4$	$(K\pi)_S^0$	$\times K^*(892)^+$	$11.7 \pm 0.5 \pm 1.5$
$(K_s^0\pi)_S^+$	$\times \bar{K}^*(1410)^0$	$10.4 \pm 0.7 \pm 2.0$	$(K\pi)_S^0$	$\times K^*(1410)^+$	$-11.5 \pm 1.7 \pm 3.4$
$\bar{K}^*(1410)^0$	$\times K^*(892)^+$	$-9.0 \pm 0.4 \pm 1.0$	$(K_s^0\pi)_S^+$	$\times (K\pi)_S^0$	$-10.8 \pm 1.6 \pm 3.4$
$(K_s^0\pi)_S^+$	$\times (K\pi)_S^0$	$-8 \pm 2 \pm 11$	$\bar{K}^*(1410)^0$	$\times K^*(892)^+$	$-5.7 \pm 0.4 \pm 0.8$
$(K_s^0\pi)_S^+$	$\times \bar{K}^*(1430)^0$	$-7.8 \pm 1.1 \pm 1.6$	$(K_s^0\pi)_S^+$	$\times K^*(892)^+$	$5.6 \pm 0.4 \pm 1.2$
$K^*(1410)^+$	$\times \bar{K}^*(1410)^0$	$-4.6 \pm 0.5 \pm 3.4$	$(K_s^0\pi)_S^+$	$\times \bar{K}^*(1410)^0$	$5.2 \pm 0.5 \pm 0.9$
$\bar{K}^*(1430)^0$	$\times \bar{K}^*(1410)^0$	$-4 \pm 1 \pm 4$	$(K\pi)_S^0$	$\times a_0(980)^-$	$-5.1 \pm 0.8 \pm 0.8$
$(K_s^0\pi)_S^+$	$\times K^*(892)^+$	$4.0 \pm 0.4 \pm 2.4$	$K^*(892)^+$	$\times \rho(1450)^-$	$4.0 \pm 0.3 \pm 1.2$
$(K_s^0\pi)_S^+$	$\times K^*(1410)^+$	$-4.0 \pm 0.5 \pm 2.1$	$K^*(1410)^+$	$\times \bar{K}^*(1410)^0$	$-3.7 \pm 0.4 \pm 2.0$
$K^*(892)^+$	$\times \rho(1450)^-$	$3.7 \pm 0.4 \pm 1.0$	$(K\pi)_S^0$	$\times \rho(1450)^-$	$3.1 \pm 0.4 \pm 0.9$
$(K\pi)_S^0$	$\times \bar{K}^*(1410)^0$	$-3.4 \pm 0.5 \pm 3.5$	$K^*(892)^+$	$\times a_0(1450)^-$	$2.7 \pm 0.3 \pm 0.5$
$K^*(892)^+$	$\times a_0(1450)^-$	$3.2 \pm 0.3 \pm 1.3$	$(K_s^0\pi)_S^+$	$\times \rho(1450)^-$	$2.5 \pm 0.2 \pm 0.8$
$\bar{K}^*(1410)^0$	$\times \bar{K}^*(892)^0$	$-2.7 \pm 0.2 \pm 0.5$	$(K_s^0\pi)_S^+$	$\times K^*(1410)^+$	$-2.5 \pm 0.4 \pm 0.9$
$\bar{K}^*(1410)^0$	$\times a_0(1450)^-$	$2.6 \pm 0.2 \pm 0.8$	$K^*(1410)^+$	$\times a_0(1450)^-$	$-2.1 \pm 0.2 \pm 0.9$
$(K_s^0\pi)_S^+$	$\times a_0(1450)^-$	$2.3 \pm 0.4 \pm 1.6$	$K^*(1410)^+$	$\times \bar{K}^*(892)^0$	$1.91 \pm 0.12 \pm 0.14$
$(K\pi)_S^0$	$\times \rho(1450)^-$	$2.1 \pm 0.3 \pm 1.2$	$K^*(1410)^+$	$\times a_0(980)^-$	$-1.76 \pm 0.27 \pm 0.28$
$(K\pi)_S^0$	$\times K^*(1410)^+$	$1.9 \pm 0.5 \pm 2.9$	$(K_s^0\pi)_S^+$	$\times \bar{K}^*(892)^0$	$-1.75 \pm 0.10 \pm 0.19$
$K^*(1410)^+$	$\times a_0(1450)^-$	$-1.8 \pm 0.2 \pm 1.1$	$(K_s^0\pi)_S^+$	$\times a_0(1450)^-$	$1.7 \pm 0.5 \pm 1.5$
$K^*(1410)^+$	$\times K^*(892)^+$	$1.7 \pm 0.7 \pm 3.5$	$\bar{K}^*(892)^0$	$\times a_0(980)^-$	$-1.68 \pm 0.14 \pm 0.29$
$(K_s^0\pi)_S^+$	$\times a_2(1320)^-$	$-1.6 \pm 0.3 \pm 1.5$	$\bar{K}^*(1410)^0$	$\times \bar{K}^*(892)^0$	$-1.7 \pm 0.1 \pm 0.5$
$K^*(1410)^+$	$\times \bar{K}^*(892)^0$	$1.36 \pm 0.11 \pm 0.32$	$\bar{K}^*(1410)^0$	$\times a_0(980)^-$	$1.49 \pm 0.16 \pm 0.21$
$\bar{K}^*(1430)^0$	$\times a_0(1450)^-$	$-1.3 \pm 0.2 \pm 1.0$	$K^*(1410)^+$	$\times K^*(892)^+$	$-1.5 \pm 0.9 \pm 1.2$
$\bar{K}^*(1430)^0$	$\times K^*(1410)^+$	$-1.3 \pm 0.2 \pm 0.5$	$(K\pi)_S^0$	$\times a_0(1450)^-$	$1.3 \pm 0.8 \pm 1.8$
$K^*(892)^+$	$\times \bar{K}^*(892)^0$	$1.2 \pm 0.2 \pm 0.4$	$(K_s^0\pi)_S^+$	$\times a_2(1320)^-$	$-1.2 \pm 0.3 \pm 0.8$
$(K_s^0\pi)_S^+$	$\times \rho(1450)^-$	$1.1 \pm 0.3 \pm 0.9$	$(K\pi)_S^0$	$\times \bar{K}^*(892)^0$	$1.21 \pm 0.07 \pm 0.19$

Table C.2: Interference fractions for the $D^0 \rightarrow K_s^0 K^+ \pi^-$ mode. The first uncertainties are statistical and the second systematic. Only the 25 largest terms are shown.

(a) Best GLASS isobar model.		(b) Best LASS isobar model.	
Resonances	Fit fraction [%]	Resonances	Fit fraction [%]
$K_2^*(1430)^0 \times a_0(980)^+$	$10.3 \pm 0.7 \pm 3.5$	$(K_s^0 \pi)^-_{S\text{-wave}} \times (K\pi)^0_{S\text{-wave}}$	$\times a_0(980)^+ \times (K\pi)^-_{S\text{-wave}} \times K^*(1410)^-$
$(K_s^0 \pi)^-_{S\text{-wave}} \times (K\pi)^0_{S\text{-wave}}$	$6 \pm 1 \pm 5$	$K^*(892)^- \times a_0(980)^+$	$\times a_0(980)^+ \times K^*(892)^-$
$K^*(892)^- \times a_0(980)^+$	$-5 \pm 1 \pm 4$	$K^*(892)^- \times a_0(980)^+$	$\times a_0(980)^+ \times K^*(892)^-$
$K^*(1410)^0 \times K^*(892)^-$	$-5.0 \pm 0.3 \pm 1.0$	$K^*(1410)^- \times a_0(1450)^+$	$\times a_0(1450)^+ \times K^*(892)^-$
$(K\pi)^0_{S\text{-wave}} \times K^*(892)^-$	$5 \pm 1 \pm 4$	$a_0(1450)^+ \times a_0(980)^+$	$\times a_0(980)^+ \times K^*(892)^-$
$K^*(1430)^0 \times K^*(1410)^0$	$-4.1 \pm 0.7 \pm 2.2$	$(K\pi)^0_{S\text{-wave}} \times a_0(980)^+$	$\times a_0(980)^+ \times K^*(892)^-$
$K_2^*(1410)^0 \times a_0(980)^+$	$3.8 \pm 0.2 \pm 1.0$	$(K_s^0 \pi)^-_{S\text{-wave}} \times (K\pi)^0_{S\text{-wave}}$	$\times (K\pi)^0_{S\text{-wave}} \times a_0(1450)^+$
$(K_s^0 \pi)^-_{S\text{-wave}} \times K_2^*(1430)^0$	$4 \pm 1 \pm 7$	$(K\pi)^0_{S\text{-wave}} \times a_0(1450)^+$	$\times a_0(1450)^+ \times K^*(1410)^-$
$K^*(892)^- \times K^*(892)^0$	$3.61 \pm 0.10 \pm 0.32$	$(K_s^0 \pi)^-_{S\text{-wave}} \times K^*(1410)^-$	$\times K^*(1410)^- \times K^*(892)^-$
$(K\pi)^0_{S\text{-wave}} \times p(1450)^+$	$3.4 \pm 0.6 \pm 1.4$	$K^*(892)^- \times a_0(980)^+$	$\times a_0(980)^+ \times K^*(892)^0$
$K^*(1410)^- \times K^*(892)^-$	$-3.4 \pm 0.4 \pm 0.6$	$K^*(892)^0 \times a_0(980)^+$	$\times a_0(980)^+ \times K^*(892)^-$
$K^*(1430)^0 \times K^*(892)^-$	$3.2 \pm 0.4 \pm 1.3$	$K^*(1410)^- \times a_0(980)^+$	$\times a_0(980)^+ \times K^*(892)^-$
$(K\pi)^0_{S\text{-wave}} \times K_2^*(1430)^0$	$-3.1 \pm 1.2 \pm 1.7$	$K^*(1410)^0 \times a_0(980)^+$	$\times a_0(980)^+ \times K^*(892)^-$
$K_2^*(1430)^0 \times p(1450)^+$	$-2.6 \pm 0.5 \pm 1.6$	$(K\pi)^0_{S\text{-wave}} \times K^*(1410)^0$	$\times K^*(1410)^- \times a_0(1450)^+$
$K_2^*(1410)^0 \times p(1450)^+$	$2.3 \pm 0.4 \pm 0.8$	$(K_s^0 \pi)^-_{S\text{-wave}} \times a_0(1450)^+$	$\times a_0(1450)^+ \times K^*(892)^-$
$(K_s^0 \pi)^-_{S\text{-wave}} \times K^*(892)^-$	$1.9 \pm 0.2 \pm 1.3$	$(K\pi)^0_{S\text{-wave}} \times K^*(892)^0$	$\times K^*(892)^0 \times a_0(1450)^+$
$(K_s^0 \pi)^-_{S\text{-wave}} \times K^*(1410)^0$	$-1.9 \pm 0.6 \pm 2.6$	$K^*(1410)^- \times a_0(1450)^+$	$\times a_0(1450)^+ \times K^*(892)^-$
$K^*(892)^0 \times a_0(980)^+$	$-1.8 \pm 0.3 \pm 1.8$	$(K_s^0 \pi)^-_{S\text{-wave}} \times K^*(892)^0$	$\times K^*(892)^0 \times a_0(1450)^+$
$a_0(1450)^+ \times a_0(980)^+$	$1.7 \pm 0.4 \pm 0.8$	$K^*(892)^- \times a_0(1450)^+$	$\times a_0(1450)^+ \times K^*(892)^-$
$(K_s^0 \pi)^-_{S\text{-wave}} \times K^*(1410)^-$	$1.7 \pm 0.3 \pm 1.1$	$(K_s^0 \pi)^-_{S\text{-wave}} \times K^*(892)^-$	$\times K^*(892)^- \times a_0(1450)^+$
$(K\pi)^0_{S\text{-wave}} \times a_0(980)^+$	$-1 \pm 1 \pm 4$	$K^*(1410)^- \times \rho(1700)^+$	$\times \rho(1700)^+ \times K^*(1410)^-$
$(K_s^0 \pi)^-_{S\text{-wave}} \times p(1450)^+$	$-1.4 \pm 0.2 \pm 0.4$	$K^*(892)^- \times \rho(1700)^+$	$\times \rho(1700)^+ \times K^*(892)^-$
$K^*(1410)^0 \times K^*(892)^0$	$-1.3 \pm 0.2 \pm 0.8$	$K^*(1410)^- \times K^*(892)^0$	$\times K^*(892)^0 \times K^*(1410)^-$
$(K_s^0 \pi)^-_{S\text{-wave}} \times a_0(1450)^+$	$1.33 \pm 0.17 \pm 0.29$	$K^*(1410)^- \times K^*(1410)^0$	$\times K^*(1410)^0 \times K^*(892)^0$
$K_2^*(1430)^0 \times \rho(1700)^+$	$-1.3 \pm 0.2 \pm 1.2$		

Table C.3: Matrices \mathbf{U} relating the fit coordinates \mathbf{b}' to the LASS form factor coordinates $\mathbf{b} = \mathbf{Ub}'$ defined in Sect. 6.1.

$$\begin{array}{c} (K_s^0 \pi)_{S\text{-wave}}^\pm \\ \left(\begin{array}{ccc} -0.460 & 0.702 & -0.543 \\ 0.776 & 0.197 & -0.631 \\ -0.433 & -0.711 & -0.554 \end{array} \right) \end{array} \quad \begin{array}{c} (K\pi)_S^0 \text{-wave} \\ \left(\begin{array}{ccc} -0.452 & -0.676 & -0.582 \\ 0.776 & 0.0243 & -0.631 \\ -0.440 & 0.737 & -0.513 \end{array} \right) \end{array}$$

Figure C.1: Two-dimensional quality-of-fit distributions illustrating the dynamic binning scheme used to evaluate χ^2 . The variable shown is $\frac{d_i - p_i}{\sqrt{p_i}}$ where d_i and p_i are the number of events and the fitted value, respectively, in bin i . The $D^0 \rightarrow K_s^0 K^- \pi^+$ ($D^0 \rightarrow K_s^0 K^+ \pi^-$) mode is shown in the left (right) column, and the GLASS (LASS) isobar models are shown in the top (bottom) row.

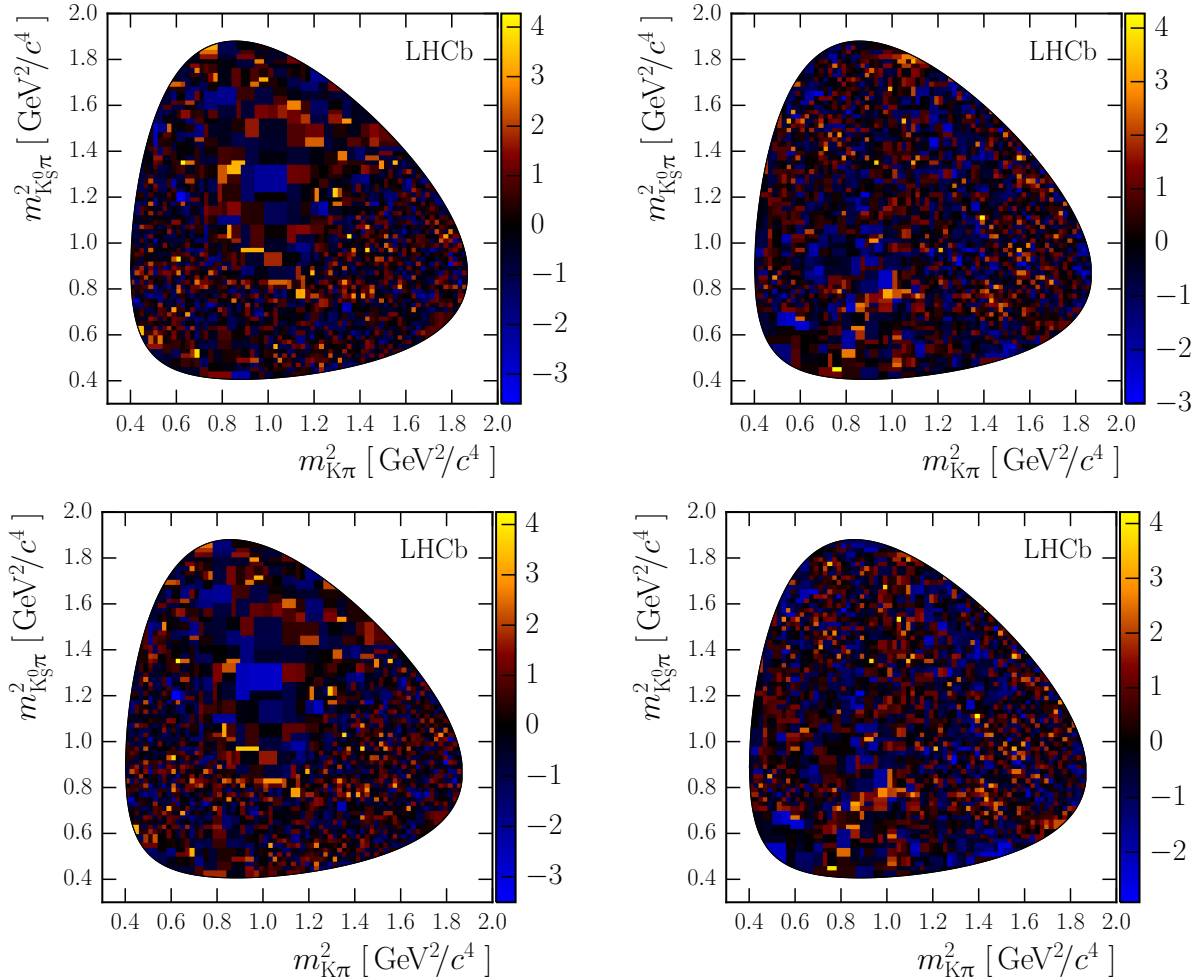


Table C.4: Additional fit parameters for GLASS models. This table does not include parameters that are fixed to their nominal values. The first uncertainties are statistical and the second systematic.

Parameter		Value	
$K^*(892)^\pm$	m_R	$893.1 \pm 0.1 \pm 0.9$	MeV/c^2
	Γ_R	$46.9 \pm 0.3 \pm 2.5$	MeV/c^2
$K^*(1410)^\pm$	Γ_R	$210 \pm 20 \pm 60$	MeV/c^2
$(K_S^0 \pi)_{S\text{-wave}}^\pm$	F	1.785 (fixed)	
	a	$4.7 \pm 0.4 \pm 1.0$	c/GeV
	ϕ_F	$0.28 \pm 0.05 \pm 0.19$	rad
	ϕ_S	$2.8 \pm 0.2 \pm 0.5$	rad
$K^*(1410)^0$	r	$-5.3 \pm 0.4 \pm 1.9$	c/GeV
	m_R	$1426 \pm 8 \pm 24$	MeV/c^2
	Γ_R	$270 \pm 20 \pm 40$	MeV/c^2
	F	$0.15 \pm 0.03 \pm 0.14$	
$(K\pi)_{S\text{-wave}}^0$	a	$4.2 \pm 0.3 \pm 2.8$	c/GeV
	ϕ_F	$-2.5 \pm 0.2 \pm 1.0$	rad
	ϕ_S	$-1.1 \pm 0.6 \pm 1.3$	rad
	r	$-3.0 \pm 0.4 \pm 1.7$	c/GeV
$a_0(1450)^\pm$	m_R	$1430 \pm 10 \pm 40$	MeV/c^2
$\rho(1450)^\pm$	Γ_R	$410 \pm 19 \pm 35$	MeV/c^2
$\rho(1700)^\pm$	m_R	$1530 \pm 10 \pm 40$	MeV/c^2

Table C.5: Additional fit parameters for LASS models. This table does not include parameters that are fixed to their nominal values. The first uncertainties are statistical and the second systematic.

Parameter	Value		
$K^*(892)^\pm$	m_R	$893.4 \pm 0.1 \pm 1.1$	MeV/c^2
	Γ_R	$47.4 \pm 0.3 \pm 2.0$	MeV/c^2
$K^*(1410)^\pm$	m_R	$1437 \pm 8 \pm 16$	MeV/c^2
	b'_1	$60 \pm 30 \pm 40$	
$(K_s^0 \pi)_{S\text{-wave}}^\pm$	b'_2	$4 \pm 1 \pm 5$	
	b'_3	$3.0 \pm 0.2 \pm 0.7$	
	m_R	$1404 \pm 9 \pm 22$	MeV/c^2
$(K\pi)_{S\text{-wave}}^0$	b'_1	$130 \pm 30 \pm 80$	
	b'_2	$-6 \pm 1 \pm 14$	
	b'_3	$2.5 \pm 0.1 \pm 1.4$	
$K\pi S\text{-wave}$	r	$1.2 \pm 0.3 \pm 0.4$	c/GeV
$a_0(980)^\pm$	m_R	$925 \pm 5 \pm 8$	MeV/c^2
$a_0(1450)^\pm$	m_R	$1458 \pm 14 \pm 15$	MeV/c^2
	Γ_R	$282 \pm 12 \pm 13$	MeV/c^2
$\rho(1450)^\pm$	m_R	$1208 \pm 8 \pm 9$	MeV/c^2
$\rho(1700)^\pm$	m_R	$1552 \pm 13 \pm 26$	MeV/c^2

Table C.6: Change in $-2 \log \mathcal{L}$ value when removing a ρ resonance from one of the models.

K π S-wave parameterisation	Decay mode	Removed resonance	$\Delta(-2 \log \mathcal{L})$
LASS	$D^0 \rightarrow K_s^0 K^- \pi^+$	$\rho(1450)^-$	338
	$D^0 \rightarrow K_s^0 K^+ \pi^-$	$\rho(1700)^+$	235
GLASS	$D^0 \rightarrow K_s^0 K^- \pi^+$	$\rho(1450)^-$	238
		$\rho(1700)^-$	162
	$D^0 \rightarrow K_s^0 K^- \pi^+$	$\rho(1450)^+$	175
		$\rho(1700)^+$	233

Table C.7: Full CP violation fit results as described in Sect. 6.8. The only uncertainties included are statistical.

Resonance	GLASS	a_R	LASS	$D^0 \rightarrow K_s^0 K^- \pi^+$				$\Delta\phi_R$	LASS
				Δa_R	GLASS	LASS	GLASS		
$D^0 \rightarrow K_s^0 K^- \pi^+$									
$K^*(892)^+$	1.0 (fixed)	1.0 (fixed)	0.0 (fixed)	0.0 (fixed)	0.03 ± 0.05	-160 ± 6	-143.1 ± 3.4	3.9 ± 2.9	2.0 ± 2.1
$K^*(1410)^+$	4.24 ± 0.30	5.83 ± 0.30	0.07 ± 0.05	0.03 ± 0.05	-66 ± 5	-59 ± 4	2.0 ± 1.7	2.0 ± 1.7	
$(K_s^0 \pi)_{S\text{-wave}}^+$	0.63 ± 0.05	1.12 ± 0.09	0.018 ± 0.034	-0.053 ± 0.030	-0.051 ± 0.029	-108.2 ± 2.2	-101.5 ± 2.0	1.2 ± 1.6	1.5 ± 1.6
$\bar{K}^*(892)^0$	0.213 ± 0.007	0.210 ± 0.006	-0.046 ± 0.031	0.006 ± 0.029	0.02 ± 0.04	-179 ± 4	-174 ± 4	1.9 ± 1.3	-3.3 ± 2.1
$\bar{K}^*(1410)^0$	6.04 ± 0.27	3.93 ± 0.19	—	-0.05 ± 0.04	—	-171 ± 5	—	1.8 ± 2.4	—
$\bar{K}_2^*(1430)^0$	3.31 ± 0.29	—	0.051 ± 0.031	0.032 ± 0.031	47 ± 13	74.9 ± 2.9	82 ± 5	0.4 ± 1.4	1.0 ± 1.3
$(K\pi)_{S\text{-wave}}^0$	2.48 ± 0.23	1.28 ± 0.11	—	-0.01 ± 0.06	—	—	—	—	7.0 ± 2.8
$a_0(980)^-$	—	1.07 ± 0.09	—	-0.24 ± 0.13	-128 ± 9	-128 ± 10	2 ± 8	-1 ± 9	
$a_2(1320)^-$	0.195 ± 0.030	0.169 ± 0.030	-0.25 ± 0.14	-0.13 ± 0.08	-84 ± 7	-52 ± 10	0.2 ± 2.7	-4 ± 4	
$a_0(1450)^-$	0.51 ± 0.04	0.44 ± 0.05	-0.01 ± 0.07	-0.05 ± 0.07	-175 ± 7	-144 ± 7	-13 ± 4	-4.7 ± 2.9	
$\rho(1450)^-$	1.58 ± 0.18	1.30 ± 0.11	0.06 ± 0.07	—	-65 ± 12	—	7 ± 8	—	
$\rho(1700)^-$	0.39 ± 0.08	—	-0.08 ± 0.15	—	—	—	—	—	
$D^0 \rightarrow K_s^0 K^+ \pi^-$									
$K^*(892)^-$	1.0 (fixed)	1.0 (fixed)	0.0 (fixed)	0.0 (fixed)	-105 ± 6	-78.5 ± 3.0	-5.8 ± 3.3	-3.0 ± 2.2	
$K^*(1410)^-$	4.8 ± 0.5	9.1 ± 0.6	0.05 ± 0.09	-0.03 ± 0.06	-163 ± 6	-102 ± 6	-7.7 ± 3.4	-8 ± 4	
$(K_s^0 \pi)_{S\text{-wave}}^-$	0.59 ± 0.05	1.14 ± 0.11	0.10 ± 0.06	-0.14 ± 0.07	176.2 ± 2.2	-174.6 ± 1.7	-1.4 ± 1.8	0.8 ± 1.6	
$K^*(892)^0$	0.409 ± 0.010	0.427 ± 0.010	-0.010 ± 0.024	-0.012 ± 0.022	0.19 ± 0.09	175 ± 4	165 ± 5	-0.6 ± 3.3	-9 ± 4
$K^*(1410)^0$	6.2 ± 0.5	4.2 ± 0.5	0.10 ± 0.05	-0.09 ± 0.05	—	-139 ± 5	—	6 ± 4	—
$\bar{K}_2^*(1430)^0$	6.2 ± 0.5	—	—	-0.12 ± 0.04	96 ± 12	145.4 ± 3.0	-1.9 ± 2.4	1.9 ± 2.3	
$(K\pi)_{S\text{-wave}}^0$	3.66 ± 0.29	1.72 ± 0.16	-0.075 ± 0.034	0.052 ± 0.024	65 ± 5	127.4 ± 3.5	-3 ± 5	-0.9 ± 2.3	
$a_0(980)^+$	1.74 ± 0.10	3.79 ± 0.20	0.06 ± 0.04	-0.11 ± 0.09	-0.07 ± 0.06	-139 ± 9	-112 ± 7	10 ± 6	5 ± 4
$a_0(1450)^+$	0.44 ± 0.05	0.87 ± 0.10	—	-0.06 ± 0.10	—	-60 ± 6	—	5 ± 4	—
$\rho(1450)^+$	2.4 ± 0.4	—	—	-0.03 ± 0.09	-0.12 ± 0.09	2 ± 11	40 ± 9	4 ± 6	2 ± 5
$\rho(1700)^+$	1.01 ± 0.12	1.23 ± 0.15	—	—	—	—	—	—	

D. $D^0 \rightarrow K_s^0 K^\pm \pi^\mp$ ISOBAR MODEL SYSTEMATIC UNCERTAINTIES

This appendix includes tables summarising the various contributions to the systematic uncertainties assigned to the various results in the amplitude analysis of $D^0 \rightarrow K_s^0 K^\pm \pi^\mp$ decays. The table headings correspond to the uncertainties discussed in Sect. 6.6 with some abbreviations to allow the tables to be typeset compactly. Definitions of the various abbreviations are given in Table D.1. The quantity ‘DFF’ listed in the tables is the sum of fit fractions [192] from the various resonances, excluding interference terms. Tables D.2 (GLASS) and D.3 (LASS) show the results for the complex amplitudes and fit fractions in the $D^0 \rightarrow K_s^0 K^- \pi^+$ models, Tables D.4 (GLASS) and D.5 (LASS) show the corresponding values for the $D^0 \rightarrow K_s^0 K^+ \pi^-$ models and Tables D.6 and D.7 summarise the uncertainties for the parameters that are not specific to a decay mode.

In each of these tables the parameter in question is listed on the left, followed by the central value and the corresponding statistical (first) and systematic (second) uncertainty. The subsequent columns list the contributions to this systematic uncertainty, and are approximately ordered in decreasing order of significance from left to right.

Table D.1: Listing of abbreviations required to typeset the systematic uncertainty tables.

Abbreviation	Description
$\max(\cos)$	Variation of the cut that excludes the boundary regions of the Dalitz plot.
Efficiency	Two efficiency-modelling uncertainties added in quadrature: using an alternative parameterisation, and accounting for the limited size of the simulated event sample.
Joint	Uncertainty obtained by simultaneously fitting disjoint sub-sets of the dataset, separated by the year of data-taking and type of K_s^0 daughter track, with distinct efficiency models.
Weights	Three uncertainties related to the re-weighting of simulated events used to generate the efficiency model $\varepsilon(m_{K_s^0 \pi}^2, m_{K \pi}^2)$, added in quadrature. These account for: incorrect simulation of the underlying pp interaction, uncertainty in the relative yield of long and downstream K_s^0 candidates, and uncertainty in the efficiency of selection requirements using information from the RICH detectors.
Comb.	Using an alternative combinatorial background model.
$-2 \log \mathcal{L}$	Using a more complex alternative model where the threshold in $\Delta(-2 \log \mathcal{L})$ for a resonance to be retained is reduced to 9 units.
Flatté	Variation of the Flatté lineshape parameters for the $a_0(980)^\pm$ resonance according to their nominal uncertainties.
f_m, f_c	Variation of the mistag and combinatorial background rates according to their uncertainties in the mass fit.
d_{D^0}, d_R	Variation of the meson radius parameters.
T_{ρ^\pm}	Switching to a Breit-Wigner dynamical function to describe the $\rho(1450, 1700)^\pm$ resonances.

Table D.2: Systematic uncertainties for complex amplitudes and fit fractions in the $D^0 \rightarrow K_S^0 K^- \pi^+$ model using the GLASS parameterisation. The headings are defined in Table D.1.

Resonance	Var	Baseline	$\Delta\phi_{\text{obs}}$	$\zeta_{\text{eff}}^{\text{obs}}$	$\zeta_{\text{eff}}^{\text{sim}}$	$\log_{10}(\text{Weights})$	Efficiency	$\zeta_{\text{eff}}^{\text{sim}}$	$\zeta_{\text{eff}}^{\text{obs}}$	$\log_{10}(\text{Weights})$	Efficiency	$\zeta_{\text{eff}}^{\text{sim}}$	$\zeta_{\text{eff}}^{\text{obs}}$	$\log_{10}(\text{Weights})$
$K^*(892)^+$	FF [%]	$57.0 \pm 0.8 \pm 2.6$	1.76	1.48	0.56	0.37	0.23	0.13	0.66	0.03	0.14	0.75	—	—
$K^*(1410)^+$	a_R	$4.3 \pm 0.3 \pm 0.7$	0.39	0.32	0.16	0.18	0.30	0.14	0.22	0.01	0.04	0.06	—	—
	ϕ_R [°]	$-160 \pm 6 \pm 24$	6.7	11.3	13.7	14.4	0.4	0.2	3.0	1.4	1.5	0.3	—	—
	FF [%]	$5 \pm 1 \pm 4$	4.08	1.01	0.84	0.84	0.65	0.30	0.36	0.05	0.08	0.14	—	—
$(K_S^0\pi_S^+)_S$ -wave	a_R	$0.62 \pm 0.05 \pm 0.18$	0.12	0.08	0.07	0.05	0.03	0.02	0.02	0.03	0.02	0.01	—	—
	ϕ_R [°]	$-67 \pm 5 \pm 15$	12.2	2.8	6.7	2.2	1.4	0.8	2.4	2.6	1.6	0.5	—	—
	FF [%]	$12 \pm 2 \pm 9$	4.61	4.14	4.26	4.17	2.33	1.26	1.39	1.39	1.04	0.43	—	—
$\bar{K}^*(892)^0$	a_R	$0.213 \pm 0.007 \pm 0.018$	0.01	0.00	0.01	0.00	0.00	0.00	0.00	0.00	0.00	0.00	—	—
	ϕ_R [°]	$-108 \pm 2 \pm 4$	2.4	1.0	1.5	0.6	1.3	0.2	1.8	0.2	0.2	0.2	—	—
	FF [%]	$2.5 \pm 0.2 \pm 0.4$	0.19	0.26	0.07	0.16	0.07	0.07	0.05	0.05	0.06	0.06	—	—
$\bar{K}^*(1410)^0$	a_R	$6.0 \pm 0.3 \pm 0.5$	0.16	0.17	0.00	0.06	0.44	0.07	0.08	0.09	0.07	0.00	—	—
	ϕ_R [°]	$-179 \pm 4 \pm 17$	4.8	9.1	6.7	9.1	6.8	2.2	2.1	0.9	1.4	0.7	—	—
	FF [%]	$9 \pm 1 \pm 4$	3.15	0.86	0.30	0.61	1.66	0.30	0.46	0.23	0.19	0.28	—	—
$\bar{K}_2^*(1430)^0$	a_R	$3.2 \pm 0.3 \pm 1.0$	0.44	0.57	0.29	0.42	0.34	0.16	0.17	0.02	0.03	0.00	—	—
	ϕ_R [°]	$-172 \pm 5 \pm 23$	17.2	7.8	1.4	0.6	10.5	5.7	3.8	1.1	1.2	1.9	—	—
	FF [%]	$3.4 \pm 0.6 \pm 2.7$	1.99	1.14	0.59	0.84	0.68	0.36	0.32	0.05	0.07	0.13	—	—
$(K\pi)_S^0$ -wave	a_R	$2.5 \pm 0.2 \pm 1.3$	0.90	0.18	0.60	0.56	0.35	0.13	0.16	0.08	0.04	0.06	—	—
	ϕ_R [°]	$50 \pm 10 \pm 80$	71.0	13.6	5.5	2.6	5.4	21.9	10.7	13.9	8.8	0.8	—	—
	FF [%]	$11 \pm 2 \pm 10$	5.28	4.42	4.67	4.49	0.13	1.27	0.76	0.98	0.44	0.29	—	—
$a_2(1320)^-$	a_R	$0.19 \pm 0.03 \pm 0.09$	0.01	0.06	0.04	0.04	0.00	0.01	0.03	0.00	0.00	0.00	—	—
	ϕ_R [°]	$-129 \pm 8 \pm 17$	5.7	8.5	5.8	8.7	5.8	2.5	3.4	1.3	1.6	1.3	—	—
	FF [%]	$0.20 \pm 0.06 \pm 0.21$	0.06	0.14	0.08	0.10	0.00	0.01	0.06	0.01	0.00	0.00	—	—
$a_0(1450)^-$	a_R	$0.52 \pm 0.04 \pm 0.15$	0.01	0.08	0.07	0.07	0.03	0.05	0.04	0.02	0.01	0.01	—	—
	ϕ_R [°]	$-82 \pm 7 \pm 31$	3.7	12.1	19.9	18.0	3.2	3.6	8.5	0.9	0.9	1.6	—	—
	FF [%]	$1.2 \pm 0.2 \pm 0.6$	0.00	0.33	0.24	0.27	0.15	0.24	0.14	0.07	0.06	0.03	—	—
$\rho(1450)^-$	a_R	$1.6 \pm 0.2 \pm 0.5$	0.06	0.15	0.03	0.35	0.28	0.07	0.11	0.04	0.01	0.04	—	—
	ϕ_R [°]	$-177 \pm 7 \pm 32$	2.5	15.7	15.9	19.5	8.3	4.1	4.7	2.2	1.9	1.5	—	—
	FF [%]	$1.3 \pm 0.3 \pm 0.7$	0.21	0.28	0.04	0.27	0.32	0.13	0.22	0.08	0.03	0.24	—	—
$\rho(1700)^-$	a_R	$0.38 \pm 0.08 \pm 0.15$	0.11	0.03	0.06	0.02	0.06	0.01	0.03	0.01	0.00	0.02	—	—
	ϕ_R [°]	$-70 \pm 10 \pm 60$	50.1	28.3	17.0	17.6	6.1	7.3	5.6	3.2	1.0	0.8	—	—
	FF [%]	$0.12 \pm 0.05 \pm 0.14$	0.12	0.01	0.04	0.00	0.02	0.01	0.02	0.00	0.00	0.04	—	—
χ^2/bin		1.12	1.12	1.08	1.11	1.10	—	—	—	1.11	1.11	1.20	—	—
DFF [%]		103.0	103.7	110.6	111.7	111.8	103.7	—	—	101.0	102.1	102.3	—	—

Table D.3: Systematic uncertainties for complex amplitudes and fit fractions in the $D^0 \rightarrow K_s^0 K^\pm \pi^\mp$ model using the LASS parameterisation. The headings are defined in Table D.1.

Resonance	Var	Baseline	d_{D^0}, d_R	$-2 \log \mathcal{L}$	Efficiency	$\max(\cos)$	Weights	Comb.	Flatté	T_{ρ^\pm}	f_m, f_c	Joint
$K^*(892)^+$	FF [%]	$56.9 \pm 0.6 \pm 1.1$	0.03	0.10	0.40	0.10	0.19	0.07	0.06	0.16	0.17	1.00
$K^*(1410)^+$	a_R ϕ_R [°] FF [%]	$5.83 \pm 0.29 \pm 0.29$ $-143 \pm 3 \pm 6$ $9.6 \pm 1.1 \pm 2.9$	0.04 1.9 2.79	0.02 0.2 0.06	0.26 3.7 0.80	0.05 2.8 0.22	0.06 1.6 0.15	0.02 1.6 0.14	0.06 0.7 0.23	0.02 0.7 0.02	0.02 0.1 0.18	0.06
$(K_s^0 \pi)^+_{S\text{-wave}}$	a_R ϕ_R [°] FF [%]	$1.13 \pm 0.09 \pm 0.21$ $-59 \pm 4 \pm 13$ $11.7 \pm 1.0 \pm 2.3$	0.11 10.6 0.68	0.11 6.2 0.53	0.03 3.2 0.35	0.09 0.9 1.35	0.06 0.6 0.87	0.04 0.1 0.90	0.04 0.5 0.33	0.04 0.5 0.71	0.03 0.8 0.30	0.02
$\bar{K}^*(892)^0$	a_R ϕ_R [°] FF [%]	$0.210 \pm 0.006 \pm 0.010$ $-101.5 \pm 2.0 \pm 2.8$ $2.47 \pm 0.15 \pm 0.23$	0.01 0.2 0.16	0.00 1.8 0.00	0.00 2.0 0.06	0.01 0.0 0.10	0.00 0.2 0.03	0.00 0.3 0.09	0.00 0.4 0.03	0.00 0.4 0.03	0.00 0.2 0.04	0.00
$\bar{K}^*(1410)^0$	a_R ϕ_R [°] FF [%]	$3.9 \pm 0.2 \pm 0.4$ $-174 \pm 4 \pm 7$ $3.8 \pm 0.5 \pm 2.0$	0.13 0.4 1.75	0.07 3.5 0.38	0.24 2.3 0.70	0.24 3.3 0.38	0.17 4.0 0.08	0.05 1.9 0.00	0.07 0.4 0.15	0.05 0.4 0.01	0.05 0.3 0.10	0.09
$(K\pi)^0_{S\text{-wave}}$	a_R ϕ_R [°] FF [%]	$1.28 \pm 0.12 \pm 0.23$ $75 \pm 3 \pm 8$ $18 \pm 2 \pm 4$	0.10 3.7 2.36	0.07 3.7 0.57	0.13 3.1 1.97	0.07 2.5 1.10	0.10 3.0 1.08	0.06 1.6 0.54	0.03 1.2 0.30	0.03 1.4 0.72	0.03 0.9 0.22	0.01
$a_0(980)^-$	a_R ϕ_R [°] FF [%]	$1.07 \pm 0.09 \pm 0.14$ $82 \pm 5 \pm 7$ $4.0 \pm 0.7 \pm 1.1$	0.12 2.5 0.91	0.02 2.1 0.19	0.07 4.6 0.50	0.02 1.2 0.06	0.01 0.9 0.06	0.01 0.9 0.20	0.02 0.6 0.03	0.02 0.6 0.17	0.01 0.6 0.18	0.02
$a_2(1320)^-$	a_R ϕ_R [°] FF [%]	$0.17 \pm 0.03 \pm 0.05$ $-128 \pm 10 \pm 8$ $0.15 \pm 0.06 \pm 0.13$	0.02 3.9 0.09	0.01 3.9 0.02	0.04 2.9 0.08	0.00 2.8 0.01	0.01 1.9 0.01	0.01 2.5 0.02	0.00 1.0 0.01	0.01 0.5 0.01	0.00 1.1 0.01	0.01
$a_0(1450)^-$	a_R ϕ_R [°] FF [%]	$0.43 \pm 0.05 \pm 0.10$ $-49 \pm 11 \pm 19$ $0.74 \pm 0.15 \pm 0.34$	0.07 3.0 0.25	0.06 12.5 0.18	0.03 8.2 0.10	0.02 5.7 0.07	0.00 7.1 0.08	0.00 1.2 0.00	0.00 4.0 0.00	0.01 2.2 0.04	0.01 4.1 0.01	0.01
$\rho(1450)^-$	a_R ϕ_R [°] FF [%]	$1.3 \pm 0.1 \pm 0.4$ $-144 \pm 7 \pm 9$ $1.4 \pm 0.2 \pm 0.7$	0.27 1.5 0.63	0.05 6.0 0.21	0.06 3.2 0.13	0.01 2.8 0.06	0.05 2.2 0.12	0.01 3.3 0.05	0.03 1.0 0.07	0.04 3.7 0.10	0.01 1.0 0.04	0.00
χ^2/bin DFF [%]		1.10 114.1 109.1	1.11 108.5 —	1.10 — 107.0	— — —	1.08 — —	1.08 — —	1.08 — —	1.10 110.8 109.4	1.10 110.8 110.0	1.10 110.4 110.0	1.17

Table D.4: Systematic uncertainties for complex amplitudes and fit fractions in the $D^0 \rightarrow K_s^0 K^+ \pi^-$ model using the GLASS parameterisation. The headings are defined in Table D.1.

Resonance	Var	Baseline	ρ_{loss}	ζ_{comb}	$\max_{\text{cos}}(\zeta_{\text{f}})$	Efficiency	Weights	Fitter	ζ_{f}	Joint		
$K^*(892)^-$	FF [%]	$29.5 \pm 0.6 \pm 1.6$	1.30	0.15	0.32	0.49	0.27	0.25	0.41	0.26	0.25	0.47
$K^*(1410)^-$	a_R	$4.7 \pm 0.5 \pm 1.1$	0.30	0.81	0.29	0.28	0.45	0.22	0.09	0.06	0.04	0.05
	ϕ_R [°]	$-106 \pm 6 \pm 25$	6.3	18.1	11.0	8.0	7.4	5.3	0.9	1.9	1.5	0.6
	FF [%]	$3.1 \pm 0.6 \pm 1.6$	1.13	0.99	0.13	0.22	0.36	0.21	0.11	0.06	0.07	0.11
$(K_S^0\pi^-)_{S\text{-wave}}$	a_R	$0.58 \pm 0.05 \pm 0.11$	0.07	0.07	0.01	0.01	0.05	0.02	0.00	0.01	0.00	0.00
	ϕ_R [°]	$-164 \pm 6 \pm 31$	19.0	2.0	13.2	13.0	12.3	7.7	1.8	3.2	2.5	0.2
	FF [%]	$5.4 \pm 0.9 \pm 1.7$	1.16	0.94	0.33	0.59	0.06	0.33	0.23	0.11	0.14	0.12
$K^*(892)^0$	a_R	$0.410 \pm 0.010 \pm 0.021$	0.01	0.01	0.00	0.00	0.00	0.01	0.00	0.00	0.00	0.01
	ϕ_R [°]	$176 \pm 2 \pm 9$	4.4	2.4	4.4	4.7	3.6	2.4	0.2	0.4	0.3	0.2
	FF [%]	$4.82 \pm 0.23 \pm 0.35$	0.02	0.27	0.15	0.08	0.08	0.08	0.06	0.04	0.02	0.03
$K^*(1410)^0$	a_R	$6.2 \pm 0.5 \pm 1.4$	1.13	0.09	0.38	0.22	0.07	0.17	0.54	0.26	0.13	0.03
	ϕ_R [°]	$175 \pm 4 \pm 14$	0.9	13.4	1.9	2.9	1.4	1.1	1.2	1.8	0.2	0.7
	FF [%]	$5.2 \pm 0.7 \pm 1.6$	0.25	0.37	0.83	0.62	0.32	0.24	0.90	0.44	0.22	0.09
$K^*_2(1430)^0$	a_R	$6.3 \pm 0.5 \pm 1.7$	1.17	0.82	0.72	0.35	0.32	0.13	0.23	0.27	0.15	0.09
	ϕ_R [°]	$-139 \pm 5 \pm 21$	16.2	3.8	6.5	7.4	4.8	2.7	4.4	2.5	2.2	0.3
	FF [%]	$7 \pm 1 \pm 4$	2.84	1.66	1.60	0.71	0.69	0.30	0.37	0.55	0.25	0.41
$(K\pi)_S^0$	a_R	$3.7 \pm 0.3 \pm 1.8$	1.46	0.65	0.55	0.03	0.45	0.12	0.11	0.09	0.03	0.01
	ϕ_R [°]	$100 \pm 10 \pm 70$	57.6	13.1	9.0	13.6	3.2	10.6	20.4	11.9	7.0	0.4
	FF [%]	$12 \pm 1 \pm 8$	6.60	0.83	2.75	2.68	2.20	0.54	0.92	1.00	0.22	0.15
$a_0(980)^+$	a_R	$1.8 \pm 0.1 \pm 0.6$	0.25	0.44	0.11	0.14	0.06	0.10	0.04	0.20	0.03	0.01
	ϕ_R [°]	$64 \pm 5 \pm 24$	14.6	14.9	5.9	1.7	2.4	3.2	6.1	6.7	1.7	0.3
	FF [%]	$11 \pm 1 \pm 6$	2.43	4.86	1.42	1.75	0.81	1.15	0.68	1.40	0.36	0.27
$a_0(1450)^+$	a_R	$0.44 \pm 0.05 \pm 0.13$	0.10	0.01	0.01	0.06	0.03	0.02	0.03	0.01	0.01	0.00
	ϕ_R [°]	$-140 \pm 9 \pm 35$	26.9	3.9	13.7	9.2	13.3	6.2	3.7	1.0	1.1	2.6
	FF [%]	$0.45 \pm 0.09 \pm 0.34$	0.27	0.01	0.00	0.15	0.09	0.03	0.08	0.03	0.02	0.00
$\rho(1450)^+$	a_R	$2.3 \pm 0.4 \pm 0.8$	0.16	0.26	0.29	0.14	0.52	0.30	0.02	0.23	0.15	0.08
	ϕ_R [°]	$-60 \pm 6 \pm 18$	10.0	8.3	4.3	10.1	1.7	3.2	2.8	4.0	1.4	1.4
	FF [%]	$1.5 \pm 0.5 \pm 0.9$	0.08	0.16	0.38	0.23	0.30	0.35	0.03	0.25	0.16	0.51
$\rho(1700)^+$	a_R	$1.04 \pm 0.12 \pm 0.32$	0.23	0.09	0.07	0.15	0.09	0.05	0.06	0.02	0.01	0.01
	ϕ_R [°]	$4 \pm 11 \pm 20$	4.6	13.9	7.3	2.4	8.4	6.9	2.2	1.6	1.8	2.5
	FF [%]	$0.5 \pm 0.1 \pm 0.5$	0.39	0.12	0.07	0.13	0.02	0.06	0.05	0.02	0.01	0.11
χ^2/bin		1.07	1.09	1.07	1.06	1.04	1.06	—	—	1.07	1.12	1.12
DFF [%]		80.7	78.5	71.3	84.9	83.4	82.9	—	—	79.9	80.5	81.5

Table D.5: Systematic uncertainties for complex amplitudes and fit fractions in the $D^0 \rightarrow K_s^0 K^\pm \pi^\mp$ model using the LASS parameterisation. The headings are defined in Table D.1.

Resonance	Var	Baseline	$\frac{dD^0}{d\phi_R}$	$\sqrt{-2 \log \chi^2}$	$\max(\cos)$	Weights	Efficiency	Flatte $_{\text{C}}$	Joint	Comb.	f_{p^\pm}	f_m, f_c
$K^*(892)^-$	FF [%]	$28.8 \pm 0.4 \pm 1.3$	0.07	0.08	0.32	0.21	0.15	0.08	1.21	0.01	0.01	0.19
$K^*(1410)^-$	a_R	$9.1 \pm 0.6 \pm 1.5$	1.21	0.06	0.58	0.41	0.39	0.08	0.19	0.09	0.01	0.03
$K^*(1410)^-$	ϕ_R [°]	$-79 \pm 3 \pm 7$	5.2	4.1	2.7	0.8	0.6	0.9	0.2	0.2	0.0	0.4
$K^*(1410)^-$	FF [%]	$11.9 \pm 1.5 \pm 2.2$	0.15	0.00	1.42	1.11	1.04	0.17	0.71	0.15	0.10	0.08
$(K_s^0 \pi)^-$ S-wave	a_R	$1.16 \pm 0.11 \pm 0.32$	0.20	0.21	0.10	0.04	0.04	0.04	0.01	0.04	0.02	0.03
$(K_s^0 \pi)^-$ S-wave	ϕ_R [°]	$-101 \pm 6 \pm 21$	19.3	6.2	5.7	2.7	1.6	2.3	0.4	0.0	0.8	0.6
$(K_s^0 \pi)^-$ S-wave	FF [%]	$6.3 \pm 0.9 \pm 2.1$	1.30	1.31	0.81	0.24	0.42	0.20	0.19	0.26	0.20	0.11
$K^*(892)^0$	a_R	$0.427 \pm 0.010 \pm 0.013$	0.01	0.01	0.00	0.00	0.00	0.00	0.00	0.00	0.00	0.00
$K^*(892)^0$	ϕ_R [°]	$-175.0 \pm 1.7 \pm 1.4$	0.2	1.2	0.3	0.2	0.2	0.3	0.1	0.5	0.3	0.2
$K^*(892)^0$	FF [%]	$5.17 \pm 0.21 \pm 0.32$	0.16	0.20	0.04	0.08	0.08	0.01	0.10	0.10	0.00	0.02
$K^*(1410)^0$	a_R	$4.2 \pm 0.5 \pm 0.9$	0.33	0.20	0.71	0.16	0.13	0.15	0.03	0.08	0.02	0.06
$K^*(1410)^0$	ϕ_R [°]	$165 \pm 5 \pm 10$	1.3	7.1	3.6	4.3	2.5	0.7	0.2	1.8	1.1	0.6
$K^*(1410)^0$	FF [%]	$2.2 \pm 0.6 \pm 2.1$	1.82	0.36	0.77	0.34	0.19	0.16	0.12	0.03	0.07	0.07
$(K\pi)_S^0$ S-wave	a_R	$1.7 \pm 0.2 \pm 0.4$	0.18	0.29	0.17	0.06	0.09	0.04	0.00	0.08	0.00	0.03
$(K\pi)_S^0$ S-wave	ϕ_R [°]	$144 \pm 3 \pm 6$	3.6	0.9	2.2	2.3	3.3	0.4	0.9	0.5	0.7	0.3
$(K\pi)_S^0$ S-wave	FF [%]	$17 \pm 2 \pm 6$	3.76	4.31	2.30	0.70	0.56	0.60	1.37	0.54	0.00	0.32
$a_0(980)^+$	a_R	$3.8 \pm 0.2 \pm 0.7$	0.30	0.64	0.03	0.11	0.17	0.06	0.02	0.10	0.01	0.03
$a_0(980)^+$	ϕ_R [°]	$126 \pm 3 \pm 6$	4.3	0.4	0.8	1.3	1.9	2.7	0.2	0.6	0.5	0.5
$a_0(980)^+$	FF [%]	$26 \pm 2 \pm 10$	3.61	8.83	0.01	1.67	1.44	0.27	1.12	0.92	0.15	0.15
$a_0(1450)^+$	a_R	$0.86 \pm 0.10 \pm 0.12$	0.06	0.00	0.04	0.07	0.02	0.03	0.04	0.01	0.02	
$a_0(1450)^+$	ϕ_R [°]	$-110 \pm 8 \pm 7$	1.7	2.5	3.5	1.2	3.9	1.8	1.1	1.1	0.5	1.0
$a_0(1450)^+$	FF [%]	$1.5 \pm 0.3 \pm 0.4$	0.22	0.07	0.02	0.15	0.25	0.06	0.05	0.13	0.03	0.05
$\rho(1700)^+$	a_R	$1.25 \pm 0.15 \pm 0.33$	0.22	0.12	0.07	0.12	0.02	0.02	0.04	0.11	0.02	
$\rho(1700)^+$	ϕ_R [°]	$39 \pm 9 \pm 15$	9.5	8.4	5.1	4.0	2.0	1.3	0.1	0.4	2.1	1.1
$\rho(1700)^+$	FF [%]	$0.53 \pm 0.11 \pm 0.23$	0.15	0.08	0.06	0.07	0.10	0.01	0.07	0.03	0.02	0.01
χ^2/bin		1.09	1.10	1.07	1.08	—	—	1.09	1.14	1.09	1.09	1.09
DFF [%]		99.0	99.1	104.8	95.6	—	—	98.9	100.7	99.3	99.3	99.4

Table D.6: Systematic uncertainties for shared parameters, coherence and relative branching ratio observables in the **GLASS** models. The systematic uncertainty on the $K^*(892)^\pm$ width due to neglecting resolution effects in the nominal models is $0.5 \text{ MeV}/c^2$.

Resonance	Var	Baseline	$\delta_{D^0}^{sig}$	Comb.	ζ_{π^0}	ζ_{K^0}	$\zeta_{\bar{K}^0}$	ζ_{Total}	Efficiency	Meffits	Frate	ζ_{π^0}
Coherence	$R_{K_S^0 K \pi}$	$0.573 \pm 0.007 \pm 0.019$	0.000	0.004	0.001	0.003	0.017	0.004	0.002	0.004	0.004	[°]
	$\delta_{K_S^0 K \pi} -$	$0.2 \pm 0.6 \pm 1.1$	0.03	0.32	0.45	0.39	0.69	0.35	0.23	0.21	0.09	0.22
	$R_{K^* K}$	$0.831 \pm 0.004 \pm 0.011$	0.002	0.004	0.002	0.002	0.007	0.002	0.004	0.003	0.001	0.002
\mathcal{B}	$\mathcal{B}_{K^* K}$	$0.372 \pm 0.001 \pm 0.009$	0.001	0.001	0.000	0.001	0.008	0.000	0.002	0.001	0.001	0.001
	$\mathcal{B}_{K_S^0 K \pi}$	$0.655 \pm 0.001 \pm 0.006$	0.001	0.002	0.003	0.001	0.002	0.000	0.003	0.003	0.000	0.000
CP -even fraction	F_+	$0.777 \pm 0.003 \pm 0.009$	0.000	0.002	0.000	0.001	0.008	0.002	0.001	0.002	0.001	0.002
	m_R	$893.1 \pm 0.1 \pm 0.9$	0.3	0.1	0.1	0.1	0.9	0.0	0.1	0.0	0.0	0.0
$K^*(892)^\pm$	Γ_R	$46.9 \pm 0.3 \pm 2.5$	0.5	0.4	0.5	0.4	2.2	0.1	0.2	0.2	0.1	0.1
	$K^*(1410)^\pm$	$210 \pm 20 \pm 60$	8.8	41.0	27.0	36.2	11.0	4.1	12.5	2.9	7.1	5.9
$(K_S^0 \pi)^{\pm}_{S\text{-wave}}$	a	$4.7 \pm 0.4 \pm 1.0$	0.209	0.168	0.606	0.311	0.092	0.470	0.095	0.360	0.114	0.150
	ϕ_F	$0.28 \pm 0.05 \pm 0.19$	0.1	0.0	0.1	0.0	0.0	0.0	0.0	0.0	0.0	[c/GeV]
	ϕ_S	$-3.5 \pm 0.2 \pm 0.5$	0.2	0.1	0.0	0.4	0.1	0.1	0.1	0.1	0.1	[rad]
	r	$-5.3 \pm 0.4 \pm 1.9$	0.68	0.84	0.87	1.08	0.15	0.49	0.37	0.29	0.19	0.24
$K^*(1410)^0$	m_R	$1426 \pm 8 \pm 24$	2.3	11.8	5.8	13.0	10.6	—	7.4	5.6	2.9	2.0
	Γ_R	$270 \pm 20 \pm 40$	26.2	5.4	17.6	1.4	23.6	8.2	4.6	3.0	4.9	0.9
$(K\pi)^0_{S\text{-wave}}$	F	$0.15 \pm 0.03 \pm 0.14$	0.06	0.02	0.06	0.03	0.02	0.08	0.05	0.03	0.00	0.00
	a	$4.2 \pm 0.3 \pm 2.8$	1.074	1.563	1.092	1.548	0.649	0.260	0.607	0.143	0.090	0.030
	ϕ_F	$-2.5 \pm 0.2 \pm 1.0$	0.8	0.2	0.2	0.0	0.1	0.3	0.2	0.1	0.1	[rad]
	ϕ_S	$-1.1 \pm 0.6 \pm 1.3$	0.7	0.3	0.8	0.4	0.2	0.3	0.5	0.3	0.0	0.0
$a_0(1450)^\pm$	m_R	$1430 \pm 10 \pm 40$	4.1	26.9	16.6	23.8	12.6	1.8	7.1	3.1	0.8	0.9
	Γ_R	$410 \pm 19 \pm 35$	11.1	1.6	4.1	2.2	31.3	—	8.1	2.7	2.6	1.5
$\rho(1450)^\pm$	m_R	$1530 \pm 10 \pm 40$	6.4	2.6	4.0	0.8	36.3	14.7	3.0	4.3	2.4	2.6

Table D.7: Systematic uncertainties for shared parameters, coherence and relative branching ratio observables in the LASS models. The systematic uncertainty on the $K^*(892)^\pm$ width due to neglecting resolution effects in the nominal models is $0.6 \text{ MeV}/c^2$.

Resonance	Var	Baseline	Joint	$-2\log \mathcal{L}$	d_{D^0}, d_R	Weights	Efficiency	$\max(\cos)$	Comb.	Flatte	f_m, f_c	T_{ρ^\pm}
B	$R_{K_s^0 K\pi}$	$0.571 \pm 0.005 \pm 0.019$	0.015	0.011	0.005	0.003	0.002	0.001	0.001	0.002	0.003	0.000
	$\delta_{K_s^0 K\pi^-}$	$-0.0 \pm 0.5 \pm 0.8$	0.00	0.01	0.58	0.30	0.24	0.09	0.16	0.12	0.19	0.00
	$\delta_{K^* K}$	$0.835 \pm 0.003 \pm 0.011$	0.009	0.001	0.003	0.003	0.003	0.001	0.001	0.001	0.002	0.000
CP -even fraction	$\mathcal{B}_{K^* K}$	$0.368 \pm 0.001 \pm 0.011$	0.010	0.001	0.001	0.001	0.002	0.000	0.000	0.001	0.001	0.000
	$\mathcal{B}_{K_s^0 K\pi}$	$0.656 \pm 0.001 \pm 0.006$	0.003	0.001	0.000	0.003	0.003	0.001	0.000	0.000	0.000	0.000
	m_R	$893.4 \pm 0.1 \pm 1.1$	1.0	0.1	0.2	0.0	0.1	0.0	0.0	0.0	0.0	0.0
$K^*(892)^\pm$	Γ_R	$47.4 \pm 0.3 \pm 2.0$	1.9	0.1	0.1	0.2	0.2	0.3	0.1	0.1	0.1	0.0
	$K^*(1410)^\pm$	$1437 \pm 8 \pm 16$	8.8	5.8	8.9	1.9	5.6	5.4	3.3	1.3	1.2	2.0
	b'_1	$60 \pm 30 \pm 40$	14	16	20	10	22	8	6	6	6	2
$(K_s^0 \pi)_{S\text{-wave}}^\pm$	b'_2	$4 \pm 1 \pm 5$	4.8	1.2	0.6	0.4	0.6	0.1	0.4	0.3	0.2	0.3
	b'_3	$3.0 \pm 0.2 \pm 0.7$	0.4	0.4	0.3	0.1	0.1	0.1	0.1	0.1	0.1	0.0
	$K^*(1410)^0$	m_R	$1404 \pm 9 \pm 22$	7.1	—	14.9	10.7	6.6	4.5	3.5	0.7	3.4
$(K\pi)_S^0$	b'_1	$130 \pm 30 \pm 80$	49	28	2	39	13	32	12	6	5	1
	b'_2	$-6 \pm 1 \pm 14$	0.7	14.2	1.4	1.2	1.3	0.2	0.2	0.1	0.3	0.3
	b'_3	$2.5 \pm 0.1 \pm 1.4$	0.1	1.3	0.1	0.3	0.2	0.1	0.1	0.1	0.1	0.0
$K\pi$ S-wave r	$1.2 \pm 0.3 \pm 0.4$		0.04	0.23	0.28	0.11	0.10	0.06	0.03	0.04	0.04	0.04
	$a_0(980)^\pm$	m_R	$925 \pm 5 \pm 8$	3.7	1.6	3.8	1.6	3.4	3.3	1.9	2.0	0.5
	$a_0(1450)^\pm$	Γ_R	$1458 \pm 14 \pm 15$	4.4	—	4.2	6.0	8.2	7.1	2.2	4.4	4.1
$\rho(1450)^\pm$	m_R	$1208 \pm 8 \pm 9$	2.7	5.2	3.5	0.7	4.7	2.7	1.9	1.2	0.8	—
	$\rho(1700)^\pm$	m_R	$1552 \pm 13 \pm 26$	19.0	5.1	14.9	7.0	3.5	3.2	0.1	2.5	2.0

[MeV/ c^2]

[MeV/ c^2]

[MeV/ c^2]

[MeV/ c^2]

E. ADDITIONAL $D^0 \rightarrow K_s^0 K^+ K^-$ INFORMATION

This appendix contains supplementary information supporting the CP violation and mixing analysis presented in Chapter 7. Typically illustrative examples of the relevant figures have been included in the main body of the thesis, and the remainder are given in this appendix.

Figure E.1 shows the $\mathcal{N} = 2$ binning scheme for $D^0 \rightarrow K_s^0 K^+ K^-$ decays. The binning schemes for $\mathcal{N} \in \{3, 4\}$ were given in Sect. 2.5.1.

Fits to the $m(K_s^0 KK)$ and Δm distribution in the datasets recorded in 2012 and 2015 were described in Sects. 5.5 and 5.5.1. For brevity only the distributions for the $\mathcal{N} = 3$ binning scheme were shown there. The corresponding distributions for $\mathcal{N} \in \{2, 4\}$ are shown in Figs. E.2 and E.3 (2012), Figs. E.4 and E.5 (2015), and Figs. E.6 and E.7 (2015, “lifetime unbiased”).

Section E.1 of this appendix contains supplementary information about the pseudoexperiment studies presented in Sect. 7.1, and Sect. E.2 contains additional information about the tracking efficiency curves described in Sect. 7.2.

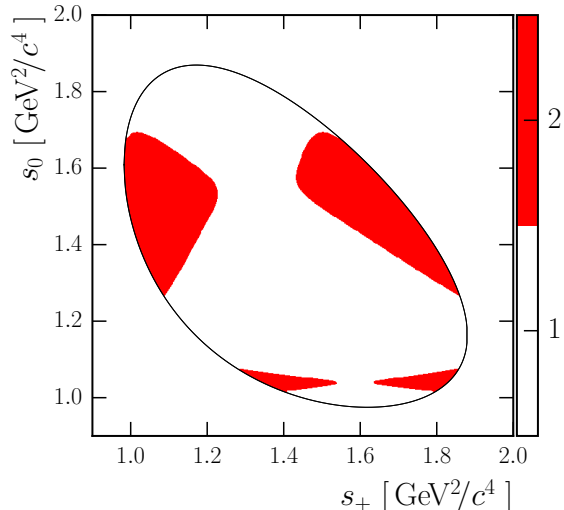


Figure E.1: Binning scheme [38] for $D^0 \rightarrow K_s^0 K^+ K^-$ decays with two bins in each half of the Dalitz plot, *i.e.* $\mathcal{N} = 2$. The variable $s_0 \equiv m_{K^+ K^-}^2$, and $s_+ + s_- + s_0 = m_{D^0}^2 + m_{K_s^0}^2 + 2m_{K^\pm}^2$.

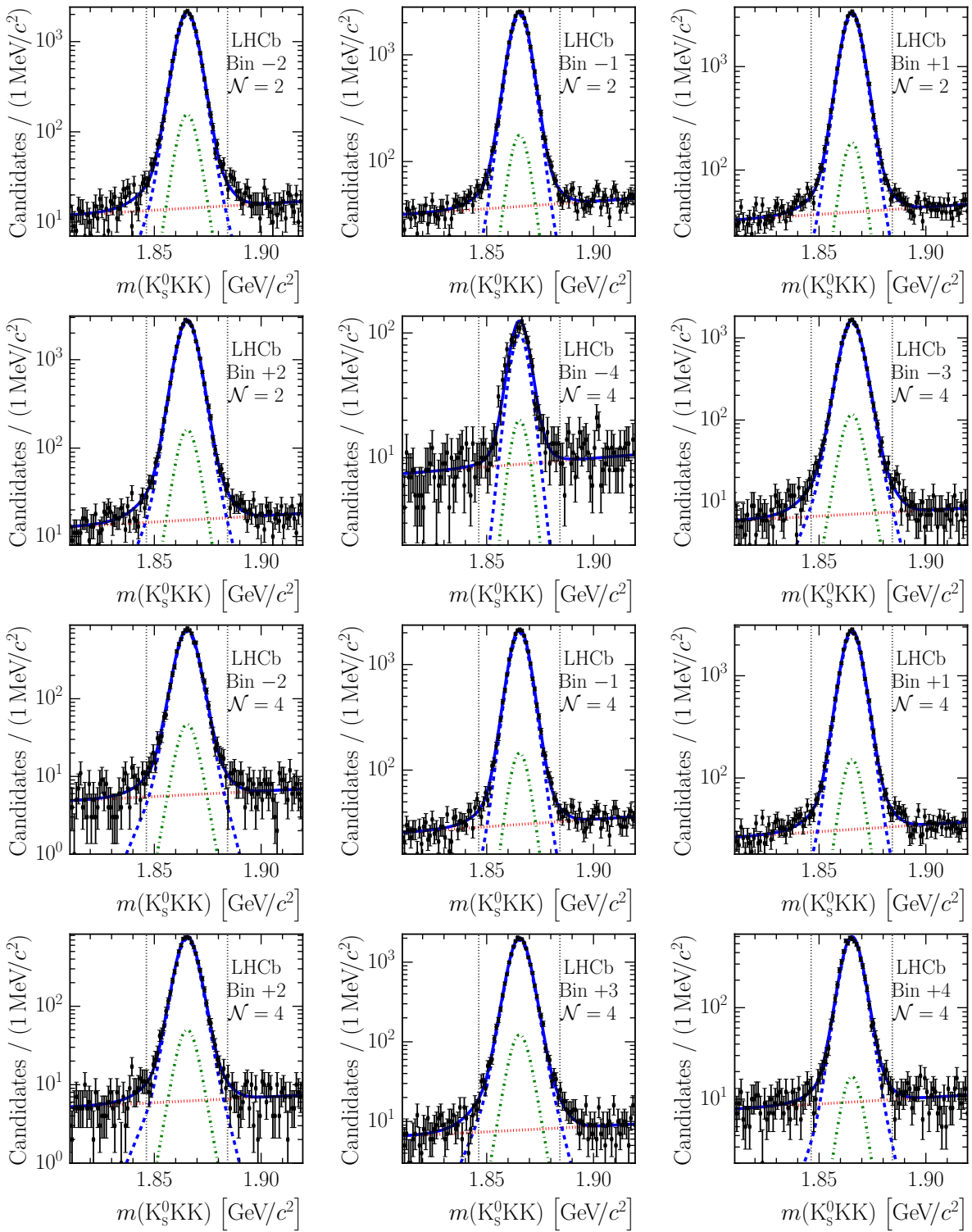


Figure E.2: $m(K_s^0 KK)$ distributions in the Run 1 $D^0 \rightarrow K_s^0 K^+ K^-$ samples binned using $\mathcal{N} = 2$ and $\mathcal{N} = 4$ binning schemes. Fit results are superimposed. The long-dashed (blue) curve represents the D^{*+} signal, the dash-dotted (green) curve represents the contribution of real D^0 mesons combined with incorrect π_{slow}^+ and the dotted (red) curve represents the combinatorial background contribution. The vertical dotted lines indicate the signal window.

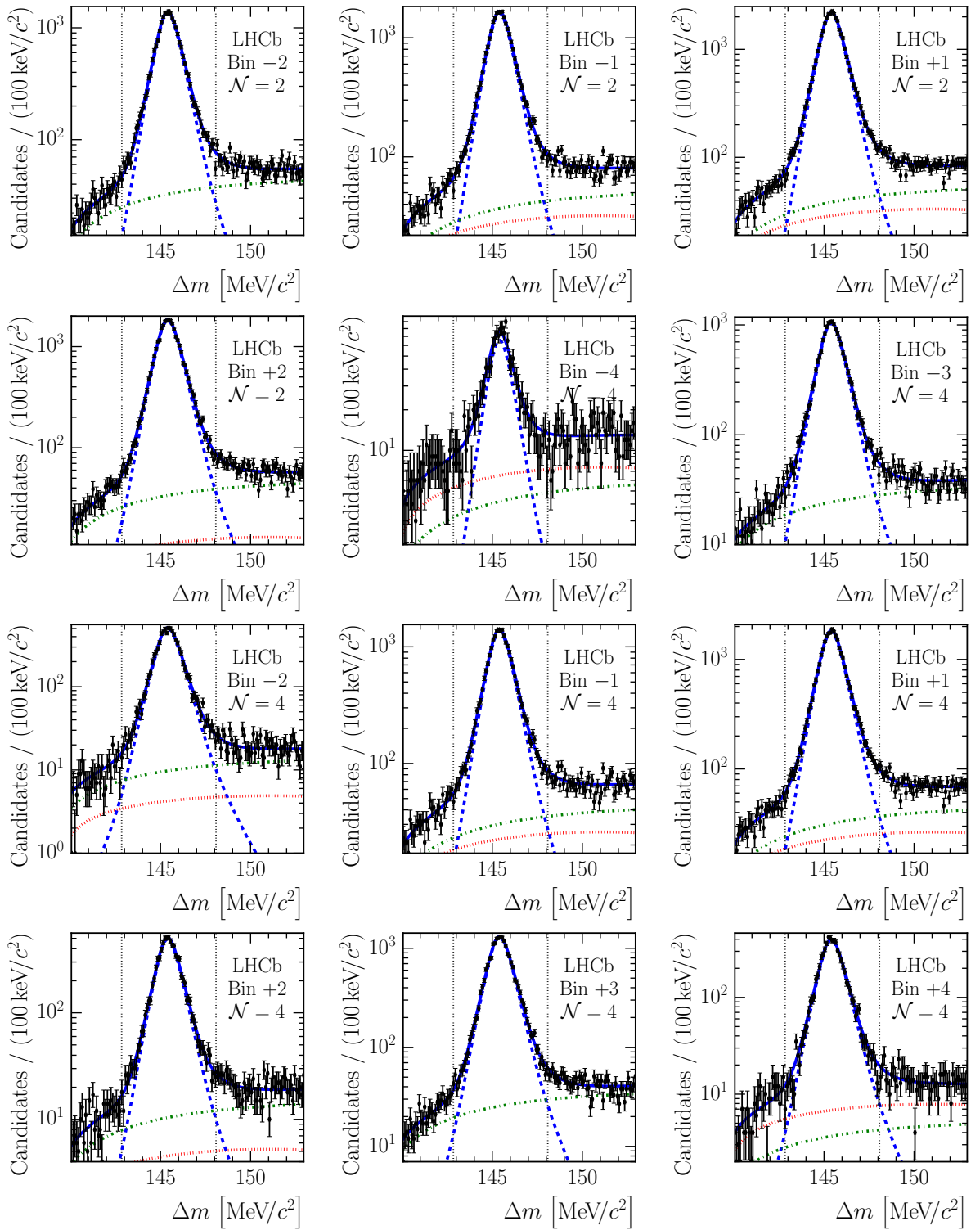


Figure E.3: Δm distributions in the Run 1 $D^0 \rightarrow K_s^0 K^+ K^-$ samples binned using $\mathcal{N} = 2$ and $\mathcal{N} = 4$ binning schemes. Fit results are superimposed. The long-dashed (blue) curve represents the D^{*+} signal, the dash-dotted (green) curve represents the contribution of real D^0 mesons combined with incorrect π_{slow}^+ and the dotted (red) curve represents the combinatorial background contribution. The vertical dotted lines indicate the signal window.

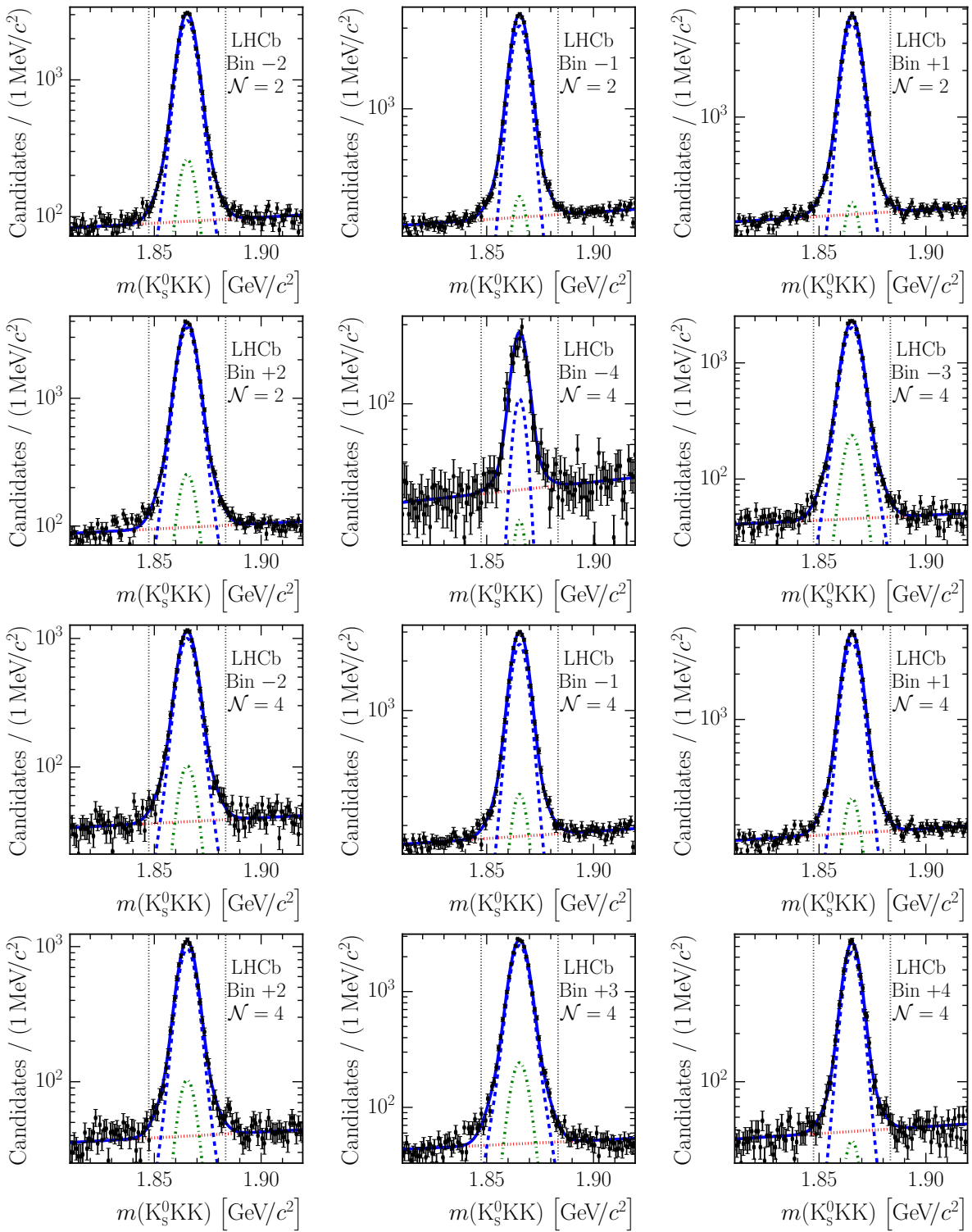


Figure E.4: $m(K_s^0 KK)$ distributions in the Run 2 $D^0 \rightarrow K_s^0 K^+ K^-$ samples binned using $\mathcal{N} = 2$ and $\mathcal{N} = 4$ binning schemes. Fit results are superimposed. The long-dashed (blue) curve represents the D^{*+} signal, the dash-dotted (green) curve represents the contribution of real D^0 mesons combined with incorrect π_s^+ and the dotted (red) curve represents the combinatorial background contribution. The vertical dotted lines indicate the signal window.

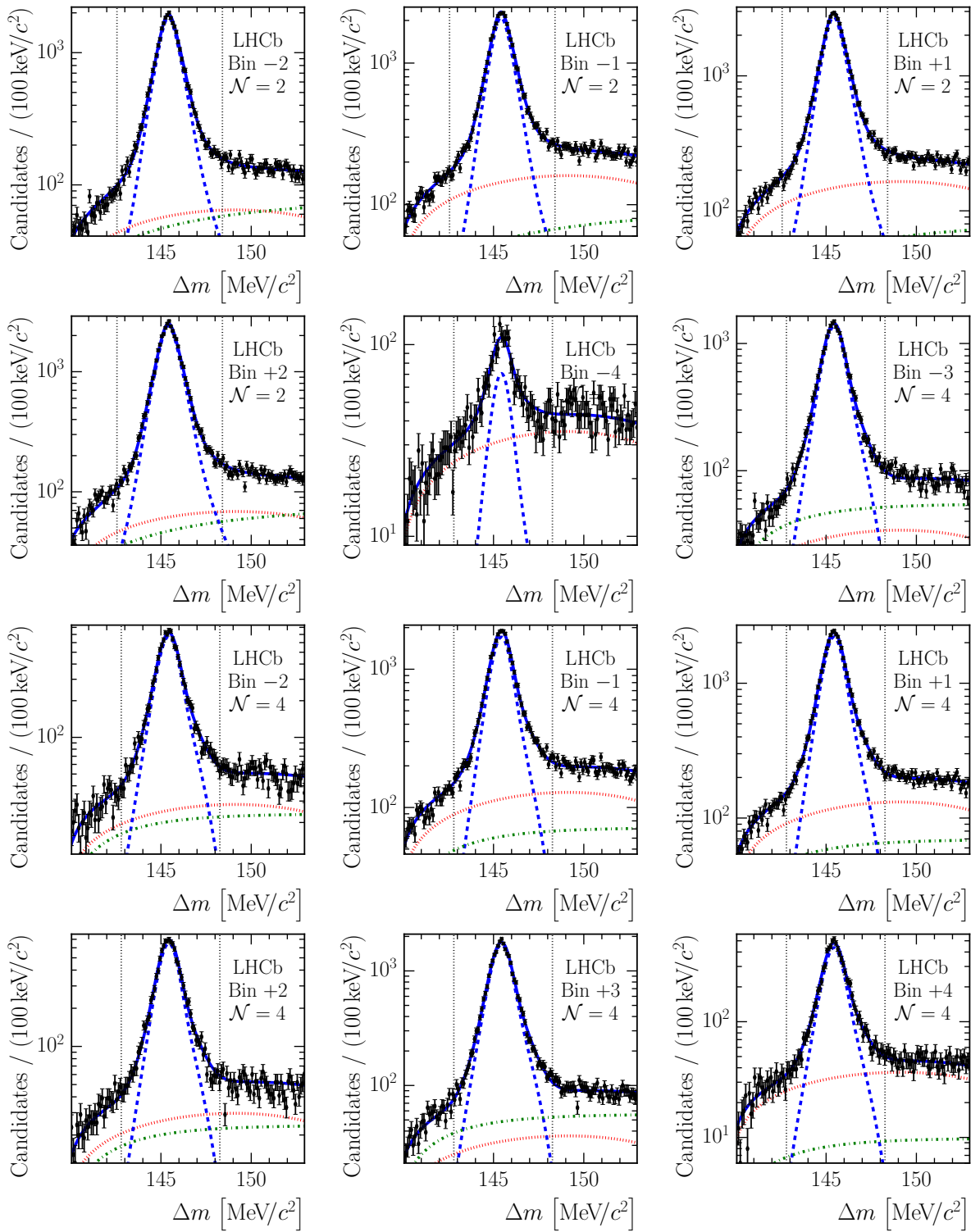


Figure E.5: Δm distributions in the Run 2 $D^0 \rightarrow K_s^0 K^+ K^-$ samples binned using $\mathcal{N} = 2$ and $\mathcal{N} = 4$ binning schemes. Fit results are superimposed. The long-dashed (blue) curve represents the D^{*+} signal, the dash-dotted (green) curve represents the contribution of real D^0 mesons combined with incorrect π_{slow}^+ and the dotted (red) curve represents the combinatorial background contribution. The vertical dotted lines indicate the signal window.

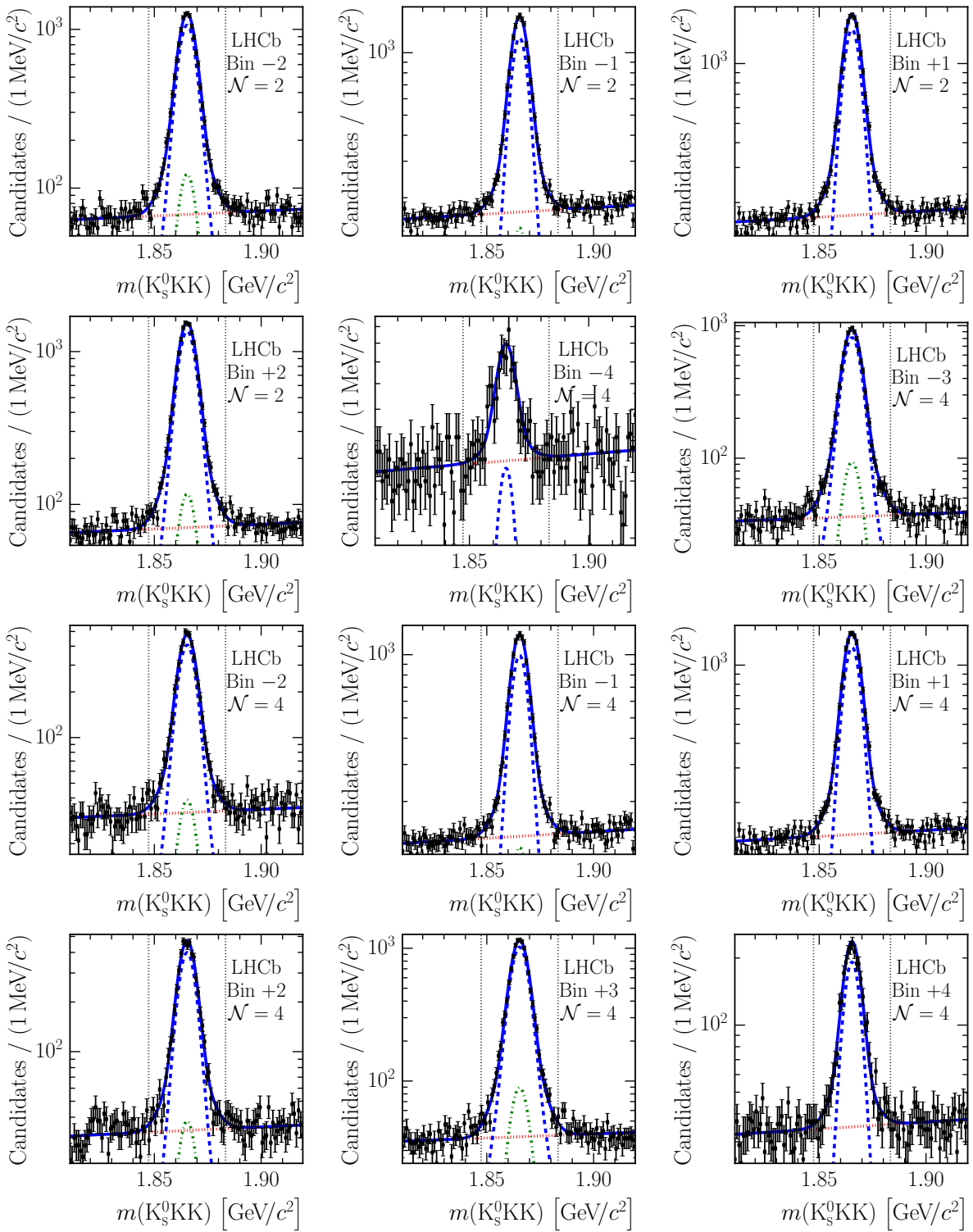


Figure E.6: $m(K_s^0 KK)$ distributions in the “lifetime unbiased” Run 2 $D^0 \rightarrow K_s^0 K^+ K^-$ samples binned using $\mathcal{N} = 2$ and $\mathcal{N} = 4$ binning schemes. Fit results are superimposed. The long-dashed (blue) curve represents the D^{*+} signal, the dash-dotted (green) curve represents the contribution of real D^0 mesons combined with incorrect π_{slow}^+ and the dotted (red) curve represents the combinatorial background contribution. The vertical dotted lines indicate the signal window.

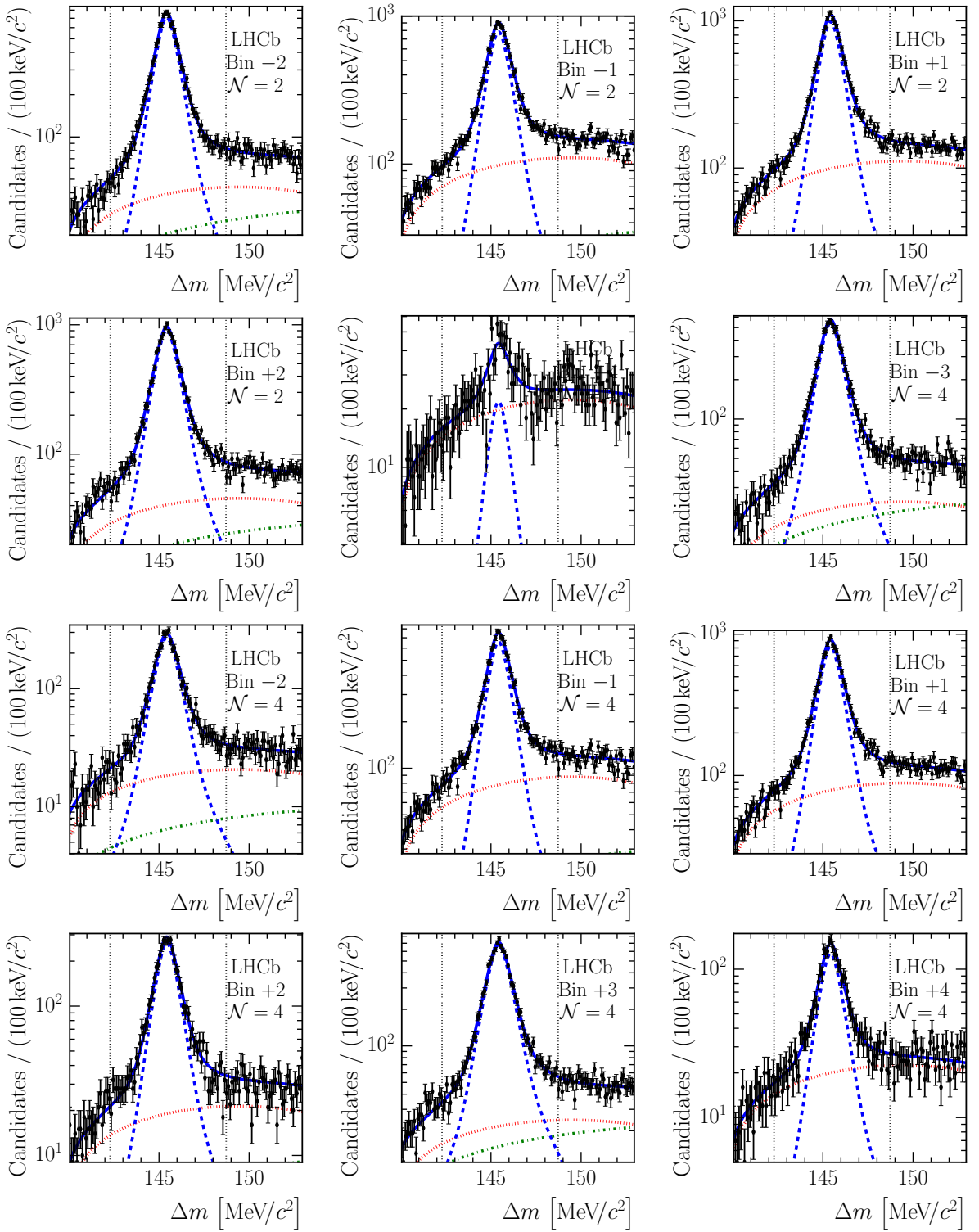


Figure E.7: Δm distributions in the “lifetime unbiased” Run 2 $D^0 \rightarrow K_s^0 K^+ K^-$ samples binned using $\mathcal{N} = 2$ and $\mathcal{N} = 4$ binning schemes. Fit results are superimposed. The long-dashed (blue) curve represents the D^{*+} signal, the dash-dotted (green) curve represents the contribution of real D^0 mesons combined with incorrect π_{slow}^+ and the dotted (red) curve represents the combinatorial background contribution. The vertical dotted lines indicate the signal window.

E.1 Pseudoexperiment results

This section includes additional information about the idealised pseudoexperiment studies presented in Sect. 7.1. Figure E.8 illustrates the improvement in the world-average results for the mixing and indirect CP violation parameters x , y and q/p in the event that an analysis of the anticipated dataset recorded by LHCb in Run 2 using the unbiased selection strategy found the same central values as the current world-averages.

Table E.1 shows the estimated biases for the observables z_{CP} , Δz and τ_{D^0} that have been extracted from ensembles of pseudoexperiments. Table E.2 shows the full sensitivity results, including the “CLEO fixed” ensembles used to evaluate the impact of the limited precision of the CLEO measurements of the strong-phase parameters X_i . Tables E.3 and E.4 show the impact of the absolute values of $|z_{CP}|$ and $|\Delta z|$, respectively, on the sensitivity to the mixing and indirect CP violation parameters.

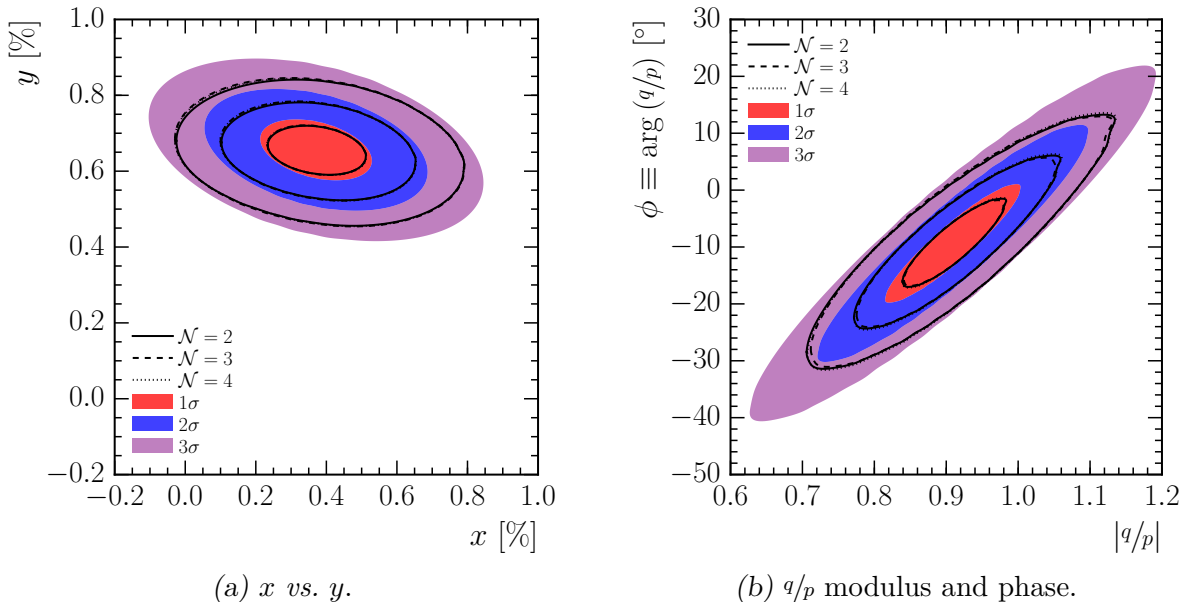


Figure E.8: Illustrations of the world-average fit results before (shaded contours) and after (black lines) the addition of new results with uncertainties corresponding to the “Run 2 unbiased” entries in Table 7.4. It is assumed that the new results favour the same central values. Results for the three choices of binning scheme $N \in \{2, 3, 4\}$ are shown in each case using different line styles, although these typically fall very close to one another. The solid contours shown in these figures are based on a multivariate Gaussian approximation to the world-average results, and as a result fail to reproduce some of the complex features in the full results of Ref. [35] (Fig. 2.7, Chapter 2).

Table E.1: Estimated biases in the observables z_{CP} , Δz and τ_{D^0} using different binning schemes, \mathcal{N} , and configurations discussed in Sect. 7.1. The bias is given by the peak position in the various ΔX distributions discussed in Sect. 7.1. In each case the peak position and its uncertainty are given, and the peak position is also quoted in units of the ΔX distribution width, σ .

Observable	\mathcal{N}	ΔX peak position			
		2012 biased	2012 unbiased	Run 2 biased	Run 2 unbiased
τ_{D^0}	2	-0.16 ± 0.05 (-0.11 σ)	-0.11 ± 0.05 (-0.08 σ)	-0.034 ± 0.012 (-0.10 σ)	-0.080 ± 0.017 (-0.17 σ) [fs]
	3	0.03 ± 0.05 (+0.02 σ)	-0.08 ± 0.05 (-0.06 σ)	0.001 ± 0.012 (+0.00 σ)	-0.017 ± 0.017 (-0.04 σ) [fs]
	4	-0.19 ± 0.05 (-0.13 σ)	-0.04 ± 0.05 (-0.03 σ)	-0.010 ± 0.012 (-0.03 σ)	-0.024 ± 0.017 (-0.05 σ) [fs]
$\Re(z_{CP})$	2	-0.06 ± 0.13 (-0.02 σ)	-0.25 ± 0.15 (-0.06 σ)	-0.163 ± 0.033 (-0.18 σ)	-0.12 ± 0.06 (-0.08 σ) [%oo]
	3	-0.34 ± 0.16 (-0.08 σ)	-0.17 ± 0.19 (-0.03 σ)	-0.05 ± 0.04 (-0.05 σ)	-0.06 ± 0.06 (-0.03 σ) [%oo]
	4	0.24 ± 0.14 (+0.06 σ)	-0.03 ± 0.15 (-0.01 σ)	-0.062 ± 0.033 (-0.07 σ)	-0.02 ± 0.06 (-0.01 σ) [%oo]
$\Im(z_{CP})$	2	-1.3 ± 0.4 (-0.13 σ)	-0.5 ± 0.4 (+0.06 σ)	-0.04 ± 0.10 (+0.02 σ)	0.10 ± 0.15 (+0.02 σ) [%oo]
	3	0.55 ± 0.32 (-0.04 σ)	0.1 ± 0.4 (+0.02 σ)	0.30 ± 0.08 (+0.14 σ)	0.19 ± 0.14 (+0.05 σ) [%oo]
	4	-0.4 ± 0.4 (-0.04 σ)	0.2 ± 0.4 (+0.02 σ)	0.07 ± 0.09 (+0.03 σ)	-0.06 ± 0.14 (-0.02 σ) [%oo]
$\Re(\Delta z)$	2	0.04 ± 0.05 (+0.03 σ)	-0.02 ± 0.07 (+0.02 σ)	-0.001 ± 0.011 (-0.00 σ)	0.022 ± 0.021 (+0.04 σ) [%oo]
	3	-0.05 ± 0.07 (-0.03 σ)	0.04 ± 0.09 (+0.02 σ)	0.018 ± 0.013 (+0.05 σ)	-0.003 ± 0.028 (-0.00 σ) [-0.02 σ) [%oo]
	4	-0.00 ± 0.05 (-0.00 σ)	-0.09 ± 0.07 (-0.05 σ)	-0.009 ± 0.013 (-0.03 σ)	-0.011 ± 0.024 (-0.02 σ) [%oo]
$\Im(\Delta z)$	2	0.01 ± 0.15 (+0.00 σ)	-0.10 ± 0.21 (-0.08 σ)	-0.03 ± 0.04 (-0.13 σ)	-0.08 ± 0.07 (-0.04 σ) [%oo]
	3	-0.16 ± 0.13 (-0.04 σ)	-0.34 ± 0.16 (+0.05 σ)	-0.13 ± 0.04 (-0.03 σ)	-0.06 ± 0.06 (-0.03 σ) [%oo]
	4	-0.18 ± 0.15 (-0.04 σ)	0.25 ± 0.19 (+0.05 σ)	-0.03 ± 0.04 (-0.03 σ)	-0.08 ± 0.07 (-0.04 σ) [%oo]

Appendix E Additional $D^0 \rightarrow K_s^0 K^+ K^-$ information

Table E.2: Estimated sensitivities to the observables z_{CP} , Δz and τ_{D^0} using different binning schemes, \mathcal{N} , and configurations. The configurations are described in the main text of Sect. 7.1. This table is very similar to Table 7.4, and differs only in that here the results of pseudoexperiment studies with the strong-phase parameters X_i are shown directly under the heading “CLEO fixed”, while in Table 7.4 these values were subtracted in quadrature from those under the heading “Total” to produce the values labelled “CLEO”.

Observable	\mathcal{N}	2012 biased		2012 unbiased		Run 2 biased		Run 2 unbiased		Uncertainty
		Total	CLEO fixed	Total	CLEO fixed	Total	CLEO fixed	Total	CLEO fixed	
τ_{D^0}	2	1.45 ± 0.04	1.363 ± 0.028	1.35 ± 0.04	1.301 ± 0.028	0.329 ± 0.009	0.279 ± 0.006	0.467 ± 0.013	0.456 ± 0.010	[fs]
	3	1.46 ± 0.04	1.473 ± 0.030	1.318 ± 0.035	1.360 ± 0.029	0.329 ± 0.009	0.287 ± 0.006	0.471 ± 0.012	0.4693 ± 0.0100	[fs]
	4	1.45 ± 0.04	1.426 ± 0.031	1.338 ± 0.035	1.314 ± 0.029	0.321 ± 0.009	0.293 ± 0.006	0.479 ± 0.012	0.446 ± 0.009	[fs]
$\Re(z_{CP})$	2	3.73 ± 0.10	3.84 ± 0.08	4.11 ± 0.10	4.03 ± 0.08	0.924 ± 0.025	0.755 ± 0.016	1.54 ± 0.04	1.335 ± 0.028	[%]
	3	4.40 ± 0.12	4.23 ± 0.09	4.87 ± 0.14	4.79 ± 0.10	0.994 ± 0.026	0.871 ± 0.018	1.73 ± 0.05	1.594 ± 0.034	[%]
	4	3.92 ± 0.11	3.84 ± 0.08	4.27 ± 0.11	4.29 ± 0.09	0.904 ± 0.024	0.769 ± 0.016	1.54 ± 0.04	1.444 ± 0.030	[%]
$\Im(z_{CP})$	2	10.29 ± 0.26	10.20 ± 0.21	11.95 ± 0.30	11.13 ± 0.23	2.70 ± 0.07	2.00 ± 0.04	4.16 ± 0.11	4.05 ± 0.08	[%]
	3	8.93 ± 0.23	7.86 ± 0.16	9.94 ± 0.27	8.82 ± 0.18	2.14 ± 0.06	1.606 ± 0.032	3.86 ± 0.10	2.94 ± 0.06	[%]
	4	11.05 ± 0.28	7.99 ± 0.16	11.48 ± 0.29	9.18 ± 0.18	2.39 ± 0.06	1.682 ± 0.034	3.88 ± 0.10	3.12 ± 0.06	[%]
$\Re(\Delta z)$	2	1.53 ± 0.04	1.557 ± 0.032	1.95 ± 0.05	1.94 ± 0.04	0.299 ± 0.008	0.311 ± 0.007	0.605 ± 0.015	0.662 ± 0.014	[%]
	3	1.80 ± 0.05	1.75 ± 0.04	2.29 ± 0.06	2.19 ± 0.05	0.361 ± 0.009	0.344 ± 0.008	0.777 ± 0.021	0.751 ± 0.016	[%]
	4	1.45 ± 0.04	1.510 ± 0.031	1.96 ± 0.05	1.91 ± 0.04	0.345 ± 0.010	0.318 ± 0.007	0.665 ± 0.017	0.668 ± 0.014	[%]
$\Im(\Delta z)$	2	4.26 ± 0.11	4.17 ± 0.08	5.79 ± 0.15	5.42 ± 0.11	1.136 ± 0.029	0.857 ± 0.018	2.01 ± 0.05	1.75 ± 0.04	[%]
	3	3.64 ± 0.09	3.28 ± 0.07	4.32 ± 0.12	4.04 ± 0.08	1.002 ± 0.026	0.671 ± 0.014	1.75 ± 0.04	1.371 ± 0.028	[%]
	4	4.20 ± 0.11	3.34 ± 0.07	5.40 ± 0.14	4.33 ± 0.09	0.974 ± 0.025	0.681 ± 0.014	2.02 ± 0.05	1.423 ± 0.029	[%]

Table E.3: Estimated sensitivities to the observables z_{CP} , Δz and τ_{D^0} using different binning schemes, \mathcal{N} , and configurations, with the ensemble of pseudoexperiments for each binning scheme and configuration split in half according to the value of $|z_{CP}|$. These are the total expected uncertainties, including the contribution due to uncertainties in the CLEO measurements of the strong-phase parameters X_i .

		Uncertainty											
Observable	\mathcal{N}	2012 biased			2012 unbiased			Run 2 biased			Run 2 unbiased		
		Low $ z_{CP} $	High $ z_{CP} $	Low $ z_{CP} $	High $ z_{CP} $	Low $ z_{CP} $	High $ z_{CP} $	Low $ z_{CP} $	High $ z_{CP} $	Low $ z_{CP} $	High $ z_{CP} $	Low $ z_{CP} $	High $ z_{CP} $
τ_{D^0}	2	1.42 ± 0.05	1.61 ± 0.07	1.38 ± 0.06	1.37 ± 0.05	0.320 ± 0.012	0.341 ± 0.013	0.466 ± 0.018	0.471 ± 0.018	[fs]	[fs]	[fs]	[fs]
	3	1.51 ± 0.06	1.37 ± 0.05	1.32 ± 0.05	1.35 ± 0.05	0.318 ± 0.012	0.341 ± 0.013	0.491 ± 0.018	0.455 ± 0.017	[fs]	[fs]	[fs]	[fs]
	4	1.46 ± 0.06	1.47 ± 0.06	1.44 ± 0.05	1.29 ± 0.05	0.328 ± 0.013	0.323 ± 0.013	0.517 ± 0.019	0.449 ± 0.018	[fs]	[fs]	[fs]	[fs]
$\Re(z_{CP})$	2	3.79 ± 0.15	3.71 ± 0.15	4.14 ± 0.15	4.11 ± 0.15	0.94 ± 0.04	0.94 ± 0.04	1.46 ± 0.05	1.63 ± 0.07	[%]	[%]	[%]	[%]
	3	4.33 ± 0.17	4.53 ± 0.19	4.64 ± 0.19	5.18 ± 0.23	0.98 ± 0.04	1.01 ± 0.04	1.79 ± 0.07	1.70 ± 0.07	[%]	[%]	[%]	[%]
	4	3.86 ± 0.15	4.09 ± 0.17	4.29 ± 0.17	4.50 ± 0.19	0.94 ± 0.04	0.888 ± 0.034	1.54 ± 0.06	1.65 ± 0.07	[%]	[%]	[%]	[%]
$\Im(z_{CP})$	2	10.6 ± 0.4	9.79 ± 0.35	12.9 ± 0.5	11.5 ± 0.4	2.38 ± 0.09	2.90 ± 0.11	4.13 ± 0.15	4.21 ± 0.16	[%]	[%]	[%]	[%]
	3	9.01 ± 0.32	8.89 ± 0.33	10.0 ± 0.4	9.9 ± 0.4	2.05 ± 0.07	2.31 ± 0.09	3.64 ± 0.13	4.16 ± 0.16	[%]	[%]	[%]	[%]
	4	11.3 ± 0.4	10.8 ± 0.4	10.7 ± 0.4	12.2 ± 0.4	2.24 ± 0.08	2.47 ± 0.09	3.55 ± 0.13	4.19 ± 0.15	[%]	[%]	[%]	[%]
$\Re(\Delta z)$	2	1.57 ± 0.07	1.54 ± 0.06	2.00 ± 0.08	1.91 ± 0.08	0.296 ± 0.011	0.305 ± 0.011	0.657 ± 0.029	0.586 ± 0.021	[%]	[%]	[%]	[%]
	3	1.76 ± 0.07	1.84 ± 0.07	2.27 ± 0.09	2.34 ± 0.09	0.362 ± 0.014	0.367 ± 0.014	0.786 ± 0.032	0.780 ± 0.030	[%]	[%]	[%]	[%]
	4	1.43 ± 0.05	1.48 ± 0.06	1.91 ± 0.08	2.09 ± 0.09	0.351 ± 0.014	0.345 ± 0.014	0.667 ± 0.025	0.686 ± 0.027	[%]	[%]	[%]	[%]
$\Im(\Delta z)$	2	4.06 ± 0.15	4.27 ± 0.15	5.47 ± 0.20	6.08 ± 0.22	1.10 ± 0.04	1.19 ± 0.04	2.00 ± 0.07	2.06 ± 0.08	[%]	[%]	[%]	[%]
	3	3.77 ± 0.13	3.57 ± 0.14	4.57 ± 0.18	4.11 ± 0.16	0.928 ± 0.035	1.07 ± 0.04	1.92 ± 0.07	1.63 ± 0.06	[%]	[%]	[%]	[%]
	4	4.13 ± 0.15	4.37 ± 0.16	5.33 ± 0.19	5.46 ± 0.20	0.97 ± 0.04	0.98 ± 0.04	2.05 ± 0.07	2.01 ± 0.08	[%]	[%]	[%]	[%]

Appendix E Additional $D^0 \rightarrow K_s^0 K^+ K^-$ information

Table E.4: Estimated sensitivities to the observables z_{CP} , Δz and τ_{D^0} using different binning schemes, \mathcal{N} , and configurations, with the ensemble of pseudoexperiments for each binning scheme and configuration split in half according to the value of $|\Delta z|$. These are the total expected uncertainties, including the contribution due to uncertainties in the CLEO measurements of the strong-phase parameters X_i .

Uncertainty									
Observable	\mathcal{N}	2012 biased		2012 unbiased		Run 2 biased		Run 2 unbiased	
		Low $ \Delta z $	High $ \Delta z $	Low $ \Delta z $	High $ \Delta z $	Low $ \Delta z $	High $ \Delta z $	Low $ \Delta z $	High $ \Delta z $
τ_{D^0}	2	1.48 ± 0.06	1.46 ± 0.06	1.37 ± 0.06	1.36 ± 0.05	0.323 ± 0.012	0.339 ± 0.013	0.450 ± 0.018	0.499 ± 0.020
	3	1.46 ± 0.06	1.44 ± 0.06	1.30 ± 0.05	1.36 ± 0.05	0.344 ± 0.014	0.315 ± 0.012	0.477 ± 0.018	0.474 ± 0.018
$\Re(z_{CP})$	4	1.51 ± 0.06	1.44 ± 0.05	1.40 ± 0.06	1.31 ± 0.05	0.325 ± 0.013	0.319 ± 0.012	0.473 ± 0.017	0.492 ± 0.019
	2	3.69 ± 0.14	3.81 ± 0.16	3.98 ± 0.15	4.26 ± 0.16	0.94 ± 0.04	0.925 ± 0.035	1.54 ± 0.06	1.55 ± 0.06
$\Im(z_{CP})$	3	4.66 ± 0.21	4.31 ± 0.17	4.98 ± 0.22	4.84 ± 0.20	1.02 ± 0.04	0.98 ± 0.04	1.74 ± 0.07	1.74 ± 0.07
	4	3.91 ± 0.16	3.98 ± 0.15	4.36 ± 0.19	4.41 ± 0.16	0.90 ± 0.04	0.93 ± 0.04	1.53 ± 0.06	1.66 ± 0.08
$\Re(\Delta z)$	2	10.5 ± 0.4	10.0 ± 0.4	12.0 ± 0.4	11.9 ± 0.4	2.79 ± 0.10	2.61 ± 0.10	4.22 ± 0.15	4.19 ± 0.16
	3	9.00 ± 0.32	8.87 ± 0.32	10.0 ± 0.4	9.8 ± 0.4	2.03 ± 0.08	2.28 ± 0.08	4.03 ± 0.16	3.65 ± 0.14
$\Im(\Delta z)$	4	11.0 ± 0.4	11.1 ± 0.4	13.1 ± 0.5	10.9 ± 0.4	2.50 ± 0.09	2.28 ± 0.09	4.10 ± 0.16	3.72 ± 0.14
	2	1.56 ± 0.06	1.55 ± 0.06	1.98 ± 0.08	1.93 ± 0.08	0.296 ± 0.011	0.305 ± 0.011	0.622 ± 0.023	0.604 ± 0.023
$\Re(\Delta z)$	3	1.80 ± 0.07	1.80 ± 0.07	2.32 ± 0.09	2.28 ± 0.09	0.369 ± 0.014	0.355 ± 0.013	0.762 ± 0.029	0.801 ± 0.032
	4	1.47 ± 0.05	1.44 ± 0.05	2.06 ± 0.09	1.93 ± 0.08	0.356 ± 0.015	0.343 ± 0.013	0.647 ± 0.025	0.692 ± 0.026
$\Im(\Delta z)$	2	4.21 ± 0.15	4.34 ± 0.16	5.80 ± 0.21	5.80 ± 0.21	0.891 ± 0.032	1.45 ± 0.05	1.76 ± 0.06	2.18 ± 0.09
	3	3.63 ± 0.14	3.82 ± 0.14	4.06 ± 0.16	4.68 ± 0.19	0.766 ± 0.029	1.26 ± 0.05	1.62 ± 0.06	1.89 ± 0.07
$\Im(\Delta z)$	4	4.37 ± 0.16	4.13 ± 0.15	5.30 ± 0.19	5.38 ± 0.19	0.844 ± 0.032	1.12 ± 0.04	1.97 ± 0.07	2.09 ± 0.08

E.2 Tracking efficiency parameterisations

This section contains additional information about the tracking efficiency curves described in Sect. 7.2. The various efficiencies for the charged kaons in the decay $D^0 \rightarrow K_s^0 K^+ K^-$ were shown in that section, parameterised as functions of the IP of the particle to the LHC beam line, **DOCAz**. The corresponding distributions for the charged pions produced by the K_s^0 meson decay are given in Fig. E.9, and the various parameterisations used are listed below.

Four different parameterisations are used to describe the various conditional track reconstruction efficiencies, $\varepsilon(d_z)$, where $d_z \equiv \text{DOCAz}$. All four are chosen to satisfy $\varepsilon'(d_z = 0) = 0$, to avoid discontinuities. The HLT2-given-offline efficiency for the charged kaons, given in Fig. 7.8b, is parameterised with a simple quadratic expression

$$\varepsilon(d_z) = p_0 + p_1 d_z^2. \quad (\text{E.1})$$

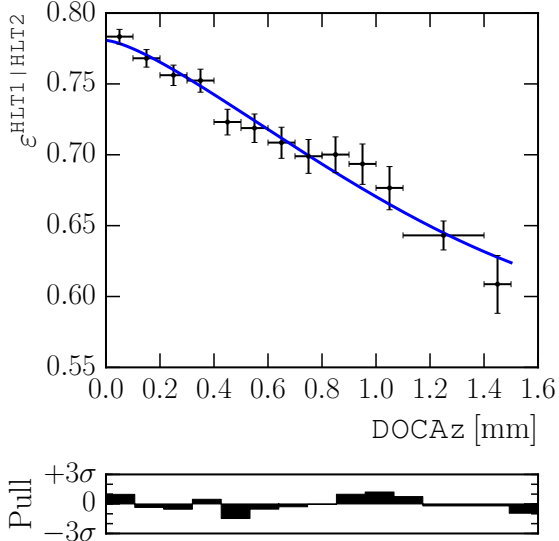
An additional term is required to describe the offline-given-VELO-hits efficiency for charged kaons (Fig. 7.8c), and the HLT1-given-HLT2 efficiency for charged pions produced in K_s^0 decays (Fig. E.9a)

$$\varepsilon(d_z) = p_0 + (p_1 - p_2) d_z^{3/2} + (p_1 + p_2) d_z^2. \quad (\text{E.2})$$

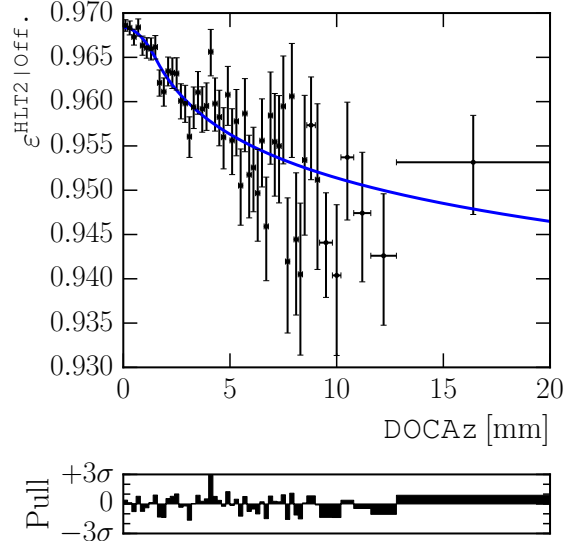
The offline reconstruction efficiency for long (Fig. E.9c) and downstream (Fig. E.9d) charged pions produced in K_s^0 decays are described by a two-part function

$$\varepsilon(d_z) = \begin{cases} \sum_{i=0}^n p_i d_z^i & d_z < p_{n+1}, \\ \alpha d_z^{-\beta} & d_z \geq p_{n+1}, \end{cases} \quad (\text{E.3})$$

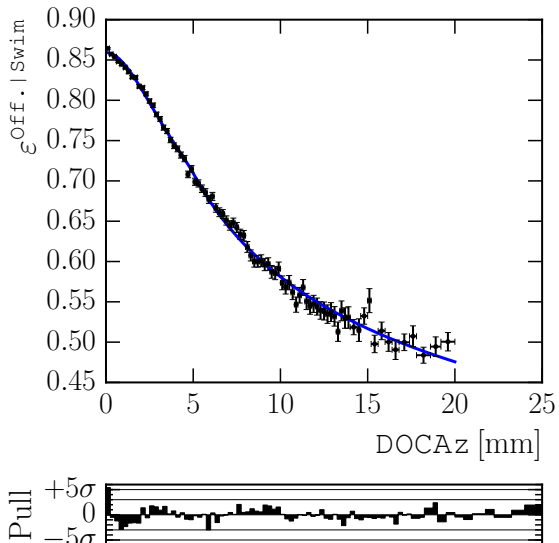
where the parameters α and β are set by the requirement that the function and its first derivative are continuous at $d_z = p_{n+1}$. Finally, the Crystal Ball function [170] is used to model the HLT1-given-HLT2 efficiency for charged kaons (Fig. 7.8a), and the HLT2-given-offline efficiency for charged pions, shown in Fig. E.9b.



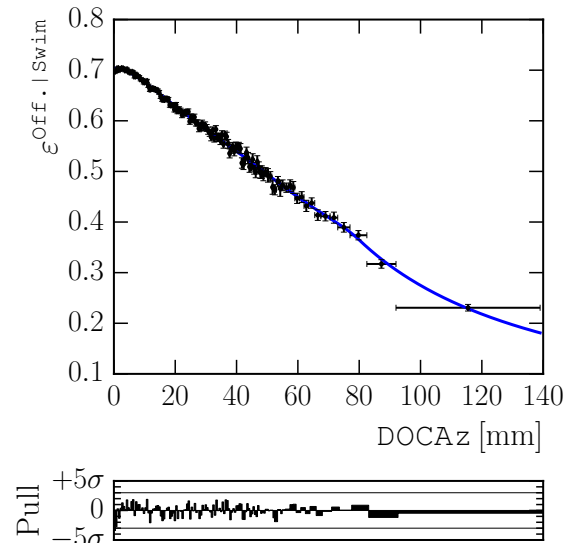
(a) HLT1 given HLT2.



(b) HLT2 given offline.



(c) Offline given VELO hits.



(d) Offline using downstream tracks.

Figure E.9: Conditional reconstruction efficiencies as a function of DOCAz for charged pions produced in K_s^0 decays. These are long tracks except where noted.

BIBLIOGRAPHY

- [1] S. L. Glashow, J. Iliopoulos, and L. Maiani, *Weak interactions with lepton-hadron symmetry*, Phys. Rev. **D2** (1970) 1285.
- [2] ATLAS collaboration, *Observation of a new particle in the search for the Standard Model Higgs boson with the ATLAS detector at the LHC*, Phys. Lett. **B716** (2012) 1, [arXiv:1207.7214](https://arxiv.org/abs/1207.7214).
- [3] CMS collaboration, *Observation of a new boson at a mass of 125 GeV with the CMS experiment at the LHC*, Phys. Lett. **B716** (2012) 30, [arXiv:1207.7235](https://arxiv.org/abs/1207.7235).
- [4] E598 collaboration, *Experimental observation of a heavy particle J*, Phys. Rev. Lett. **33** (1974) 1404.
- [5] J. E. Augustin *et al.*, *Discovery of a narrow resonance in e^+e^- annihilation*, Phys. Rev. Lett. **33** (1974) 1406.
- [6] E288 collaboration, *Observation of a dimuon resonance at 9.5 GeV in 400 GeV proton-nucleus collisions*, Phys. Rev. Lett. **39** (1977) 252.
- [7] CDF collaboration, *Observation of top quark production in $\bar{p}p$ collisions*, Phys. Rev. Lett. **74** (1995) 2626, [arXiv:hep-ex/9503002](https://arxiv.org/abs/hep-ex/9503002).
- [8] DØ collaboration, *Observation of the top quark*, Phys. Rev. Lett. **74** (1995) 2632, [arXiv:hep-ex/9503003](https://arxiv.org/abs/hep-ex/9503003).
- [9] M. L. Perl *et al.*, *Evidence for anomalous lepton production in e^+e^- annihilation*, Phys. Rev. Lett. **35** (1975) 1489.
- [10] DONUT collaboration, *Observation of tau neutrino interactions*, Phys. Lett. **B504** (2001) 218, [arXiv:hep-ex/0012035](https://arxiv.org/abs/hep-ex/0012035).
- [11] SLD Electroweak Group, DELPHI, ALEPH, SLD, SLD Heavy Flavour Group, OPAL, LEP Electroweak Working Group, L3, *Precision electroweak measurements on the Z resonance*, Phys. Rep. **427** (2006) 257, [arXiv:hep-ex/0509008](https://arxiv.org/abs/hep-ex/0509008).
- [12] L3 collaboration, *Determination of the number of light neutrino species from single photon production at LEP*, Phys. Lett. **B431** (1998) 199.
- [13] DELPHI collaboration, *Search for new phenomena using single photon events in the DELPHI detector at LEP*, Z. Phys. **C74** (1997) 577.
- [14] OPAL collaboration, *Measurement of single photon production in e^+e^- collisions near the Z^0 resonance*, Z. Phys. **C65** (1995) 47.
- [15] ALEPH collaboration, *A direct measurement of the invisible width of the Z from single photon counting*, Phys. Lett. **B313** (1993) 520.

- [16] J. H. Christenson, J. W. Cronin, V. L. Fitch, and R. Turlay, *Evidence for the 2π decay of the K_2^0 meson*, Phys. Rev. Lett. **13** (1964) 138.
- [17] M. Kobayashi and T. Maskawa, *CP-violation in the renormalizable theory of weak interaction*, Prog. Theor. Phys. **49** (1973) 652.
- [18] B. W. Lee, C. Quigg, and H. B. Thacker, *Weak interactions at very high energies: the role of the Higgs boson mass*, Phys. Rev. **D16** (1977) 1519.
- [19] W. Marciano, G. Valencia, and S. Willenbrock, *Renormalization group improved unitarity bounds on the Higgs boson and top quark masses*, Phys. Rev. **D40** (1989) 1725.
- [20] A. D. Sakharov, *Violation of CP invariance, C asymmetry, and baryon asymmetry of the universe*, Pisma Zh. Eksp. Teor. Fiz. **5** (1967) 32, [Usp. Fiz. Nauk 161, 61 (1991)].
- [21] LHCb collaboration, *Angular analysis of the $B^0 \rightarrow K^{*0} \mu^+ \mu^-$ decay using 3fb^{-1} of integrated luminosity*, JHEP **02** (2016) 104, LHCb-PAPER-2015-051, CERN-PH-EP-2015-314, [arXiv:1512.04442](https://arxiv.org/abs/1512.04442).
- [22] Belle collaboration, *Angular analysis of $B^0 \rightarrow K^*(892)^0 \ell^+ \ell^-$* , [arXiv:1604.04042](https://arxiv.org/abs/1604.04042).
- [23] Winter 2016 update to Ref. [93] semileptonic section.
- [24] BaBar collaboration, *Evidence for an excess of $\bar{B} \rightarrow D^{(*)} \tau^- \bar{\nu}_\tau$ decays*, Phys. Rev. Lett. **109** (2012) 101802, [arXiv:1205.5442](https://arxiv.org/abs/1205.5442).
- [25] BaBar collaboration, *Measurement of an excess of $\bar{B} \rightarrow D^{(*)} \tau^- \bar{\nu}_\tau$ decays and implications for charged Higgs bosons*, Phys. Rev. **D88** (2013), no. 7 072012, [arXiv:1303.0571](https://arxiv.org/abs/1303.0571).
- [26] Belle collaboration, *Measurement of the branching ratio of $\bar{B} \rightarrow D^{(*)} \tau^- \bar{\nu}_\tau$ relative to $\bar{B} \rightarrow D^{(*)} \ell^- \bar{\nu}_\ell$ decays with hadronic tagging at Belle*, Phys. Rev. **D92** (2015), no. 7 072014, [arXiv:1507.03233](https://arxiv.org/abs/1507.03233).
- [27] LHCb collaboration, *Measurement of the ratio of branching fractions $\mathcal{B}(\bar{B}^0 \rightarrow D^{*+} \tau^- \bar{\nu}_\tau)/\mathcal{B}(\bar{B}^0 \rightarrow D^{*+} \mu^- \bar{\nu}_\mu)$* , Phys. Rev. Lett. **115** (2015) 111803, LHCb-PAPER-2015-025, CERN-PH-EP-2015-150, [arXiv:1506.08614](https://arxiv.org/abs/1506.08614).
- [28] Belle collaboration, *Measurement of the branching ratio of $\bar{B}^0 \rightarrow D^{(*)} \tau^- \bar{\nu}_\tau$ relative to $\bar{B}^0 \rightarrow D^{(*)} \ell^- \bar{\nu}_\ell$ decays with a semileptonic tagging method*, [arXiv:1603.06711](https://arxiv.org/abs/1603.06711).
- [29] ATLAS collaboration, *Search for resonances in diphoton events with the ATLAS detector at $\sqrt{s} = 13\text{ TeV}$* , ATLAS-CONF-2016-018.
- [30] CMS collaboration, *Search for new physics in high mass diphoton events in 3.3fb^{-1} of proton-proton collisions at $\sqrt{s} = 13\text{ TeV}$ and combined interpretation of searches at 8 TeV and 13 TeV* , CMS-PAS-EXO-16-018.
- [31] S. Bianco, F. L. Fabbri, D. Benson, and I. Bigi, *A Cicerone for the physics of charm*, Riv. Nuovo Cim. **26N7** (2003) 1, [arXiv:hep-ex/0309021](https://arxiv.org/abs/hep-ex/0309021).
- [32] M. Artuso, B. Meadows, and A. A. Petrov, *Charm meson decays*, Ann. Rev. Nucl. Part. Sci. **58** (2008) 249, [arXiv:0802.2934](https://arxiv.org/abs/0802.2934).

- [33] F. Buccella, M. Lusignoli, A. Pugliese, and P. Santorelli, *CP violation in D meson decays: Would it be a sign of new physics?*, Phys. Rev. **D88** (2013) 074011, [arXiv:1305.7343](#).
- [34] Y. Grossman, A. L. Kagan, and Y. Nir, *New physics and CP violation in singly Cabibbo suppressed D decays*, Phys. Rev. **D75** (2007) 036008, [arXiv:hep-ph/0609178](#).
- [35] Summer 2015 update to Ref. [93] charm section.
- [36] BaBar collaboration, *Measurement of D^0 - \bar{D}^0 mixing parameters using $D^0 \rightarrow K_S^0\pi^+\pi^-$ and $D^0 \rightarrow K_S^0K^+K^-$ decays*, Phys. Rev. Lett. **105** (2010) 081803, [arXiv:1004.5053](#).
- [37] Belle collaboration, *Measurement of D^0 - \bar{D}^0 mixing and search for indirect CP violation using $D^0 \rightarrow K_S^0\pi^+\pi^-$ decays*, Phys. Rev. **D89** (2014), no. 9 091103, [arXiv:1404.2412](#).
- [38] CLEO collaboration, *Model-independent determination of the strong-phase difference between D^0 and $\bar{D}^0 \rightarrow K_{S,L}^0 h^+h^- (h = \pi, K)$ and its impact on the measurement of the CKM angle γ/ϕ_3* , Phys. Rev. **D82** (2010) 112006, [arXiv:1010.2817](#).
- [39] S. Malde and G. Wilkinson, *D^0 - \bar{D}^0 mixing studies with the decays $D^0 \rightarrow K_S^0K^\mp\pi^\pm$* , Phys. Lett. **B701** (2011) 353, [arXiv:1104.2731](#).
- [40] C. Thomas and G. Wilkinson, *Model-independent D^0 - \bar{D}^0 and CP violation studies with $D^0 \rightarrow K_S^0\pi^+\pi^-$ and $D^0 \rightarrow K_S^0K^+K^-$* , JHEP **1210** (2012) 185, [arXiv:1209.0172](#).
- [41] LHCb collaboration, *Measurements of prompt charm production cross-sections in pp collisions at $\sqrt{s} = 13$ TeV*, JHEP **03** (2016) 159, LHCb-PAPER-2015-041, CERN-PH-EP-2015-272, [arXiv:1510.01707](#).
- [42] LHCb collaboration, *Measurement of forward J/ψ production cross-sections in pp collisions at $\sqrt{s} = 13$ TeV*, JHEP **10** (2015) 172, LHCb-PAPER-2015-037, CERN-PH-EP-2015-222, [arXiv:1509.00771](#).
- [43] F. Englert and R. Brout, *Broken symmetry and the mass of gauge vector mesons*, Phys. Rev. Lett. **13** (1964) 321.
- [44] P. W. Higgs, *Broken symmetries and the masses of gauge bosons*, Phys. Rev. Lett. **13** (1964) 508.
- [45] J. Kim, *Light pseudoscalars, particle physics and cosmology*, Phys. Rep. **150** (1987) 1.
- [46] N. Cabibbo, *Unitary symmetry and leptonic decays*, Phys. Rev. Lett. **10** (1963) 531.
- [47] L.-L. Chau and W.-Y. Keung, *Comments on the parametrization of the Kobayashi-Maskawa matrix*, Phys. Rev. Lett. **53** (1984) 1802.
- [48] B. Pontecorvo, *Mesonium and anti-mesonium*, Sov. Phys. JETP **6** (1957) 429, [Zh. Eksp. Teor. Fiz. 33, 549 (1957)].
- [49] Z. Maki, M. Nakagawa, and S. Sakata, *Remarks on the unified model of elementary particles*, Prog. Theor. Phys. **28** (1962) 870.

- [50] J. Charles *et al.*, *Current status of the Standard Model CKM fit and constraints on $\Delta F = 2$ New Physics*, Phys. Rev. **D91** (2015), no. 7 073007, [arXiv:1501.05013](#), and July 2015 update.
- [51] M. C. Gonzalez-Garcia, M. Maltoni, and T. Schwetz, *Updated fit to three neutrino mixing: status of leptonic CP violation*, JHEP **11** (2014) 052, [arXiv:1409.5439](#).
- [52] J. L. Feng *et al.*, *Evidence for a protophobic fifth force from ${}^8\text{Be}$ nuclear transitions*, [arXiv:1604.07411](#).
- [53] A. J. Krasznahorkay *et al.*, *Observation of anomalous internal pair creation in ${}^8\text{Be}$: A possible indication of a light, neutral boson*, Phys. Rev. Lett. **116** (2016), no. 4 042501, [arXiv:1504.01527](#).
- [54] Particle Data Group, *Review of particle physics*, Chin. Phys. **C38** (2014) 090001.
- [55] Belle collaboration, *Dalitz analysis of $B \rightarrow K\pi^+\psi'$ decays and the $Z(4430)^+$* , Phys. Rev. **D80** (2009) 031104, [arXiv:0905.2869](#).
- [56] LHCb collaboration, *Observation of the resonant character of the $Z(4430)^-$ state*, Phys. Rev. Lett. **112** (2014) 222002, LHCb-PAPER-2014-014, CERN-PH-EP-2014-061, [arXiv:1404.1903](#).
- [57] LHCb collaboration, *A model-independent confirmation of the $Z(4430)^-$ state*, Phys. Rev. **D92** (2015) 112009, LHCb-PAPER-2015-038, CERN-PH-EP-2015-244, [arXiv:1510.01951](#).
- [58] LHCb collaboration, *Observation of $J/\psi p$ resonances consistent with pentaquark states in $\Lambda_b^0 \rightarrow J/\psi p K^-$ decays*, Phys. Rev. Lett. **115** (2015) 072001, LHCb-PAPER-2015-029, CERN-PH-EP-2015-153, [arXiv:1507.03414](#).
- [59] R. H. Dalitz, *On the analysis of τ -meson data and the nature of the τ -meson*, Phil. Mag. **44** (1953) 1068.
- [60] J. Blatt and V. Weisskopf, *Theoretical Nuclear Physics*, John Wiley & Sons, 1952.
- [61] CLEO collaboration, *Studies of the decays $D^0 \rightarrow K_S^0 K^- \pi^+$ and $D^0 \rightarrow K_S^0 K^+ \pi^-$* , Phys. Rev. **D85** (2012) 092016, [arXiv:1203.3804](#).
- [62] CLEO collaboration, *Dalitz analysis of the decay $D^0 \rightarrow K^- \pi^+ \pi^0$* , Phys. Rev. **D63** (2001) 092001, [arXiv:hep-ex/0011065](#).
- [63] S. M. Flatté, *Coupled-channel analysis of the $\pi\eta$ and $K\bar{K}$ systems near $K\bar{K}$ threshold*, Phys. Lett. **B63** (1976) 224.
- [64] S. M. Flatté, *On the nature of 0^+ mesons*, Phys. Lett. **B63** (1976) 228.
- [65] A. Abele *et al.*, *$p\bar{p}$ annihilation at rest into $K_L K^\pm \pi^\mp$* , Phys. Rev. **D57** (1998) 3860.
- [66] BaBar collaboration, *Dalitz plot analysis of $D^0 \rightarrow \bar{K}^0 K^+ K^-$* , Phys. Rev. **D72** (2005) 052008, [arXiv:hep-ex/0507026](#).

- [67] BaBar collaboration, *Improved measurement of the CKM angle γ in $B^\mp \rightarrow D^{(*)} K^{(*)\mp}$ decays with a Dalitz plot analysis of D decays to $K_S^0 \pi^+ \pi^-$ and $K_S^0 K^+ K^-$* , Phys. Rev. **D78** (2008) 034023, arXiv:0804.2089.
- [68] G. J. Gounaris and J. J. Sakurai, *Finite width corrections to the Vector-Meson-Dominance prediction for $\rho \rightarrow \pi^+ \pi^-$* , Phys. Rev. Lett. **21** (1968) 244.
- [69] BaBar collaboration, *Dalitz plot analysis of the decay $B^0(\bar{B}^0) \rightarrow K^\pm \pi^\mp \pi^0$* , Phys. Rev. **D78** (2008) 052005, arXiv:0711.4417.
- [70] Belle collaboration, *Measurement of CP asymmetries and branching fractions in a time-dependent Dalitz analysis of $B^0 \rightarrow (\rho\pi)^0$ and a constraint on the quark mixing angle ϕ_2* , Phys. Rev. **D77** (2008) 072001, arXiv:0710.4974.
- [71] BaBar collaboration, *Measurement of CP-violating asymmetries in $B^0 \rightarrow (\rho\pi)^0$ using a time-dependent Dalitz plot analysis*, Phys. Rev. **D76** (2007) 012004, arXiv:hep-ex/0703008.
- [72] BaBar collaboration, *Amplitude analysis of $B^0 \rightarrow K^+ \pi^- \pi^0$ and evidence of direct CP violation in $B \rightarrow K^* \pi$ decays*, Phys. Rev. **D83** (2011) 112010, arXiv:1105.0125.
- [73] OBELIX collaboration, *Coupled channel analysis of $\pi^+ \pi^- \pi^0$, $K^+ K^- \pi^0$ and $K^\pm K_S^0 \pi^\mp$ from $\bar{p}p$ annihilation at rest in hydrogen targets at three densities*, Eur. Phys. J. **C26** (2003) 371.
- [74] I. I. Y. Bigi and H. Yamamoto, *Interference between Cabibbo allowed and doubly forbidden transitions in $D \rightarrow K_{S,L} \pi'$'s decays*, Phys. Lett. **B349** (1995) 363, arXiv:hep-ph/9502238.
- [75] LHCb collaboration, *Measurement of the difference of time-integrated CP asymmetries in $D^0 \rightarrow K^- K^+$ and $D^0 \rightarrow \pi^- \pi^+$ decays*, Phys. Rev. Lett. **116** (2016) 191601, LHCb-PAPER-2015-055, CERN-EP-2016-022, arXiv:1602.03160.
- [76] Winter 2016 update to Ref. [93] charm section.
- [77] E. Golowich, S. Pakvasa, and A. A. Petrov, *New Physics contributions to the lifetime difference in $D^0 - \bar{D}^0$ mixing*, Phys. Rev. Lett. **98** (2007) 181801, arXiv:hep-ph/0610039.
- [78] E. Golowich, J. Hewett, S. Pakvasa, and A. A. Petrov, *Implications of $D^0 - \bar{D}^0$ mixing for New Physics*, Phys. Rev. **D76** (2007) 095009, arXiv:0705.3650.
- [79] M. Bobrowski, A. Lenz, J. Riedl, and J. Rohrwild, *How large can the SM contribution to CP violation in $D^0 - \bar{D}^0$ mixing be?*, JHEP **03** (2010) 009, arXiv:1002.4794.
- [80] I. I. Bigi, M. Blanke, A. J. Buras, and S. Recksiegel, *CP violation in $D^0 - \bar{D}^0$ oscillations: general considerations and applications to the littlest Higgs model with T-parity*, JHEP **07** (2009) 097, arXiv:0904.1545.
- [81] L. Wolfenstein, *$D^0 - \bar{D}^0$ mixing*, Phys. Lett. **B164** (1985) 170.
- [82] J. F. Donoghue, E. Golowich, B. R. Holstein, and J. Trampetic, *Dispersive effects in $D^0 - \bar{D}^0$ mixing*, Phys. Rev. **D33** (1986) 179.

- [83] E. Golowich and A. A. Petrov, *Short distance analysis of D^0 - \bar{D}^0 mixing*, Phys. Lett. **B625** (2005) 53, [arXiv:hep-ph/0506185](#).
- [84] A. F. Falk, Y. Grossman, Z. Ligeti, and A. A. Petrov, *$SU(3)$ breaking and D^0 - \bar{D}^0 mixing*, Phys. Rev. **D65** (2002) 054034, [arXiv:hep-ph/0110317](#).
- [85] A. A. Petrov, *Dipenguin contribution to D^0 - \bar{D}^0 mixing*, Phys. Rev. **D56** (1997) 1685, [arXiv:hep-ph/9703335](#).
- [86] E. Golowich and A. A. Petrov, *Can nearby resonances enhance D^0 - \bar{D}^0 mixing?*, Phys. Lett. **B427** (1998) 172, [arXiv:hep-ph/9802291](#).
- [87] H. Georgi, *D^0 - \bar{D}^0 mixing in heavy quark effective field theory*, Phys. Lett. **B297** (1992) 353, [arXiv:hep-ph/9209291](#).
- [88] T. Ohl, G. Ricciardi, and E. H. Simmons, *D^0 - \bar{D}^0 mixing in heavy quark effective field theory: the sequel*, Nucl. Phys. **B403** (1993) 605, [arXiv:hep-ph/9301212](#).
- [89] I. I. Y. Bigi and N. G. Uraltsev, *D^0 - \bar{D}^0 oscillations as a probe of quark hadron duality*, Nucl. Phys. **B592** (2001) 92, [arXiv:hep-ph/0005089](#).
- [90] F. Buccella, M. Lusignoli, and A. Pugliese, *Charm nonleptonic decays and final state interactions*, Phys. Lett. **B379** (1996) 249, [arXiv:hep-ph/9601343](#).
- [91] H.-Y. Cheng and C.-W. Chiang, *Long-distance contributions to D^0 - \bar{D}^0 mixing parameters*, Phys. Rev. **D81** (2010) 114020, [arXiv:1005.1106](#).
- [92] T. Gershon, J. Libby, and G. Wilkinson, *Contributions to the width difference in the neutral D system from hadronic decays*, Phys. Lett. **B750** (2015) 338, [arXiv:1506.08594](#).
- [93] Heavy Flavor Averaging Group, *Averages of b -hadron, c -hadron, and τ -lepton properties as of summer 2014*, [arXiv:1412.7515](#), updated results and plots available at <http://www.slac.stanford.edu/xorg/hfag/>.
- [94] Note on “ D^0 - \bar{D}^0 mixing” in Ref. [54].
- [95] LHCb collaboration, *Measurement of the CKM angle γ using $B^\pm \rightarrow DK^\pm$ with $D \rightarrow K_S^0\pi^+\pi^-$, $K_S^0K^+K^-$ decays*, JHEP **10** (2014) 097, LHCb-PAPER-2014-041, CERN-PH-EP-2014-202, [arXiv:1408.2748](#).
- [96] A. Giri, Y. Grossman, A. Soffer, and J. Zupan, *Determining gamma using $B^\pm \rightarrow DK^\pm$ with multibody D decays*, Phys. Rev. **D68** (2003) 054018, [arXiv:hep-ph/0303187](#).
- [97] A. Bondar and A. Poluektov, *Feasibility study of model-independent approach to ϕ_3 measurement using Dalitz plot analysis*, Eur. Phys. J. **C47** (2006) 347, [arXiv:hep-ph/0510246](#).
- [98] A. Bondar and A. Poluektov, *The use of quantum-correlated D^0 decays for ϕ_3 measurement*, Eur. Phys. J. **C55** (2008) 51, [arXiv:0801.0840](#).
- [99] BaBar collaboration, *Evidence for direct CP violation in the measurement of the Cabibbo-Kobayashi-Maskawa angle γ with $B^\mp \rightarrow D^{(*)}K^{(*)\mp}$ decays*, Phys. Rev. Lett. **105** (2010) 121801, [arXiv:1005.1096](#).

- [100] Belle collaboration, *Evidence for direct CP violation in the decay $B^\pm \rightarrow D^{(*)}K^\pm$, $D \rightarrow K_S^0\pi^+\pi^-$ and measurement of the CKM phase ϕ_3* , Phys. Rev. **D81** (2010) 112002, [arXiv:1003.3360](https://arxiv.org/abs/1003.3360).
- [101] LHCb collaboration, *Model-independent measurement of mixing parameters in $D^0 \rightarrow K_S^0\pi^+\pi^-$ decays*, JHEP **04** (2016) 033, LHCb-PAPER-2015-042, CERN-PH-EP-2015-249, [arXiv:1510.01664](https://arxiv.org/abs/1510.01664).
- [102] C. De Melis, *The CERN accelerator complex*, OPEN-PHO-ACCEL-2016-001.
- [103] L. Evans and P. Bryant, *LHC machine*, JINST **3** (2008) S08001.
- [104] C. Elsasser, *$b\bar{b}$ production angle plots*, https://lhcb.web.cern.ch/lhcb/speakersbureau/html/bb_ProductionAngles.html.
- [105] LHC-B collaboration, *LHC-B Letter of Intent: A dedicated LHC collider beauty experiment for precision measurements of CP-violation*, CERN-LHCC-95-004.
- [106] CERN press release, *CERN Council gives go-ahead for Large Hadron Collider*, PRESSCUT-1994-072. CERN-PR-94-16-EN.
- [107] E. Aslanides *et al.*, *The Level-0 muon trigger for the LHCb experiment*, Nucl. Instrum. Meth. **A579** (2007) 989, [arXiv:0705.0310](https://arxiv.org/abs/0705.0310).
- [108] LHCb collaboration, *LHCb detector performance*, Int. J. Mod. Phys. **A30** (2015) 1530022, [arXiv:1412.6352](https://arxiv.org/abs/1412.6352).
- [109] J. Albrecht *et al.*, *Implications of post-LS1 running conditions on LHCb's data processing*, CERN-LHCb-PUB-2013-008.
- [110] LHCb collaboration, *The LHCb detector at the LHC*, JINST **3** (2008) S08005.
- [111] LHCb collaboration, *Precision measurement of the B_s^0 - \bar{B}_s^0 oscillation frequency in the decay $B_s^0 \rightarrow D_s^-\pi^+$* , New J. Phys. **15** (2013) 053021, LHCb-PAPER-2013-006, CERN-PH-EP-2013-054, [arXiv:1304.4741](https://arxiv.org/abs/1304.4741).
- [112] R. Aaij *et al.*, *Performance of the LHCb Vertex Locator*, JINST **9** (2014) P09007, [arXiv:1405.7808](https://arxiv.org/abs/1405.7808).
- [113] O. Steinkamp, *Silicon strip detectors for the LHCb experiment*, Nucl. Instrum. Meth. **A541** (2005) 83.
- [114] R. Arink *et al.*, *Performance of the LHCb Outer Tracker*, JINST **9** (2014) P01002, [arXiv:1311.3893](https://arxiv.org/abs/1311.3893).
- [115] S. Bachmann *et al.*, *Ageing in the LHCb outer tracker: Phenomenon, culprit and effect of oxygen*, Nucl. Instrum. Meth. **A617** (2010) 202.
- [116] M. Adinolfi *et al.*, *Performance of the LHCb RICH detector at the LHC*, Eur. Phys. J. **C73** (2013) 2431, [arXiv:1211.6759](https://arxiv.org/abs/1211.6759).
- [117] E. Nappi, *Aerogel and its applications to RICH detectors*, SLAC-J-ICFA-17-3.

- [118] A. A. Alves Jr. *et al.*, *Performance of the LHCb muon system*, JINST **8** (2013) P02022, arXiv:1211.1346.
- [119] R. Aaij and J. Albrecht, *Muon triggers in the High Level Trigger of LHCb*, CERN-LHCb-PUB-2011-017.
- [120] F. Archilli *et al.*, *Performance of the muon identification at LHCb*, JINST **8** (2013) P10020, arXiv:1306.0249.
- [121] LHCb collaboration, *Absolute luminosity measurements with the LHCb detector at the LHC*, JINST **7** (2012) P01010, LHCb-PAPER-2011-015, CERN-PH-EP-2011-157, arXiv:1110.2866.
- [122] M. Clemencic *et al.*, *Recent developments in the LHCb software framework gaudi*, J. Phys. : Conf. Ser. **219** (2010) 042006.
- [123] T. Sjöstrand, S. Mrenna, and P. Skands, *PYTHIA 6.4 physics and manual*, JHEP **05** (2006) 026, arXiv:hep-ph/0603175; T. Sjöstrand, S. Mrenna, and P. Skands, *A brief introduction to PYTHIA 8.1*, Comput. Phys. Commun. **178** (2008) 852, arXiv:0710.3820.
- [124] I. Belyaev *et al.*, *Handling of the generation of primary events in Gauss, the LHCb simulation framework*, J. Phys. Conf. Ser. **331** (2011) 032047.
- [125] I. Belyaev *et al.*, *Handling of the generation of primary events in Gauss, the LHCb simulation framework*, Nuclear Science Symposium and Medical Imaging Conference proceedings IEEE (2010) 1155.
- [126] D. J. Lange, *The EvtGen particle decay simulation package*, Nucl. Instrum. Meth. **A462** (2001) 152.
- [127] P. Golonka and Z. Was, *PHOTOS Monte Carlo: A precision tool for QED corrections in Z and W decays*, Eur. Phys. J. **C45** (2006) 97, arXiv:hep-ph/0506026.
- [128] Geant4 collaboration, *Geant4 developments and applications*, IEEE Trans. Nucl. Sci. **53** (2006) 270; Geant4 collaboration, *Geant4: A simulation toolkit*, Nucl. Instrum. Meth. **A506** (2003) 250.
- [129] M. Clemencic *et al.*, *The LHCb simulation application, Gauss: Design, evolution and experience*, J. Phys. Conf. Ser. **331** (2011) 032023.
- [130] I. Bird, *Computing for the LHC*, Ann. Rev. Nucl. Part. Sci. **61** (2011) 99.
- [131] F. Stagni *et al.*, *LHCbDirac: Distributed computing in LHCb*, J. Phys. Conf. Ser. **396** (2012) 032104.
- [132] LHCb HLT group, *Trigger schemes*, <https://twiki.cern.ch/twiki/bin/view/LHCb/LHCbTriggerConferenceDiagramsPlots>.
- [133] LHCb collaboration, *Measurement of the track reconstruction efficiency at LHCb*, JINST **10** (2015) P02007, arXiv:1408.1251.
- [134] A. J. Thor, *Prefixes for binary multiples*, Metrologia **37** (2000) 81.

- [135] R. Aaij *et al.*, *The LHCb trigger and its performance in 2011*, JINST **8** (2013) P04022, [arXiv:1211.3055](https://arxiv.org/abs/1211.3055).
- [136] O. Callot and S. Hansmann-Menzemer, *The forward tracking: algorithm and performance studies*, CERN-LHCb-2007-015.
- [137] V. V. Gligorov, *A single track HLT1 trigger*, CERN-LHCb-PUB-2011-003.
- [138] M. Needham and J. Van Tilburg, *Performance of the track matching*, CERN-LHCb-2007-020.
- [139] O. Callot and M. Schiller, *PatSeeding: a standalone track reconstruction algorithm*, CERN-LHCb-2008-042.
- [140] D. Campora, N. Neufeld, and R. Schwemmer, *Improvements in the LHCb DAQ*, in *Proceedings, 19th Real Time Conference (RT2014)*, 2014. doi: 10.1109/RTC.2014.7097512.
- [141] M. Frank *et al.*, *Deferred High Level Trigger in LHCb: a boost to CPU resource utilization*, J. Phys. Conf. Ser. **513** (2014) 012006.
- [142] O. Callot, *Downstream pattern recognition*, CERN-LHCb-2007-026.
- [143] G. Dujany and B. Storaci, *Real-time alignment and calibration of the LHCb Detector in Run II*, J. Phys. Conf. Ser. **664** (2015) 082010.
- [144] E. E. Bowen, B. Storaci, and M. Tresch, *VeloTT tracking for LHCb Run II*, CERN-LHCb-PUB-2015-024.
- [145] S. Benson and O. Lupton, *PID performance in the LHCb High Level Trigger*, CERN-LHCb-PUB-2014-038.
- [146] S. Malde. Private communication.
- [147] LHCb Tracking and Alignment group, *Conference plots*, <https://twiki.cern.ch/twiki/bin/view/LHCb/ConferencePlots>.
- [148] R. Aaij *et al.*, *Tesla : an application for real-time data analysis in High Energy Physics*, Comput. Phys. Commun. **208** (2016) 35, [arXiv:1604.05596](https://arxiv.org/abs/1604.05596).
- [149] M. W. Kenzie, *Lifetime unbiased beauty and charm triggers at LHCb*, CERN-LHCb-PUB-2015-026.
- [150] T. Likhomanenko *et al.*, *LHCb topological trigger reoptimization*, J. Phys. Conf. Ser. **664** (2015), no. 8 082025, [arXiv:1510.00572](https://arxiv.org/abs/1510.00572).
- [151] R. Bailey *et al.*, *Measurement of the lifetime of charged and neutral D mesons with high resolution silicon strip detectors*, Z. Phys. **C28** (1985) 357.
- [152] DELPHI collaboration, *Lifetimes of charged and neutral B hadrons using event topology*, Z. Phys. **C68** (1995) 363.
- [153] J. Rademacker, *Reduction of statistical power per event due to upper lifetime cuts in lifetime measurements*, Nucl. Instrum. Meth. **A570** (2007) 525, [arXiv:hep-ex/0502042](https://arxiv.org/abs/hep-ex/0502042).

- [154] CDF collaboration, *Measurement of the B^- lifetime using a simulation free approach for trigger bias correction*, Phys. Rev. **D83** (2011) 032008, [arXiv:1004.4855](https://arxiv.org/abs/1004.4855).
- [155] V. V. Gligorov, *Measurement of the CKM angle gamma and B meson lifetimes at the LHCb detector*, PhD thesis, University of Oxford, 2008.
- [156] M. Gersabeck, *Alignment of the LHCb Vertex Locator and lifetime measurements of two-body hadronic final states*, PhD thesis, University of Glasgow, 2009.
- [157] V. V. Gligorov *et al.*, *Swimming: a data driven acceptance correction algorithm*, J. Phys. Conf. Ser. **396** (2012) 022016.
- [158] LHCb collaboration, *Measurement of the effective $B_s^0 \rightarrow K^+K^-$ lifetime*, Phys. Lett. **B707** (2012) 349, LHCb-PAPER-2011-014, CERN-PH-EP-2011-167, [arXiv:1111.0521](https://arxiv.org/abs/1111.0521).
- [159] LHCb collaboration, *Measurement of mixing and CP violation parameters in two-body charm decays*, JHEP **04** (2012) 129, LHCb-PAPER-2011-032, CERN-PH-EP-2011-206, [arXiv:1112.4698](https://arxiv.org/abs/1112.4698).
- [160] LHCb collaboration, *Effective lifetime measurements in the $B_s^0 \rightarrow K^+K^-$, $B^0 \rightarrow K^+\pi^-$ and $B_s^0 \rightarrow \pi^+K^-$ decays*, Phys. Lett. **B736** (2014) 446, LHCb-PAPER-2014-011, CERN-PH-EP-2014-127, [arXiv:1406.7204](https://arxiv.org/abs/1406.7204).
- [161] O. Lupton, L. Anderlini, B. Sciascia, and V. V. Gligorov, *Calibration samples for particle identification at LHCb in Run 2*, CERN-LHCb-PUB-2016-005.
- [162] LHCb collaboration, *Studies of the resonance structure in $D^0 \rightarrow K_S^0 K^\pm \pi^\mp$ decays*, Phys. Rev. **D93** (2016) 052018, LHCb-PAPER-2015-026, CERN-PH-EP-2015-238, [arXiv:1509.06628](https://arxiv.org/abs/1509.06628).
- [163] A. Puig, *The LHCb trigger in 2011 and 2012*, CERN-LHCb-PUB-2014-046.
- [164] W. D. Hulsbergen, *Decay chain fitting with a Kalman filter*, Nucl. Instrum. Meth. **A552** (2005) 566, [arXiv:physics/0503191](https://arxiv.org/abs/physics/0503191).
- [165] M. Needham, *Momentum scale calibration using resonances*, CERN-LHCb-2008-037, LPHE-2008-08.
- [166] W. Verkerke and D. P. Kirkby, *The RooFit toolkit for data modeling*, eConf **C0303241** (2003) MOLT007, [arXiv:physics/0306116](https://arxiv.org/abs/physics/0306116).
- [167] N. L. Johnson, *Systems of frequency curves generated by methods of translation*, Biometrika **36** (1949) 149.
- [168] BaBar collaboration, *Study of $B \rightarrow X\gamma$ decays and determination of $|V_{td}/V_{ts}|$* , Phys. Rev. **D82** (2010) 051101, [arXiv:1005.4087](https://arxiv.org/abs/1005.4087).
- [169] K. S. Cranmer, *Kernel estimation in high-energy physics*, Comput. Phys. Commun. **136** (2001) 198, [arXiv:hep-ex/0011057](https://arxiv.org/abs/hep-ex/0011057).
- [170] T. Skwarnicki, *A study of the radiative cascade transitions between the Upsilon-prime and Upsilon resonances*, PhD thesis, Institute of Nuclear Physics, Krakow, 1986, DESY-F31-86-02.

- [171] R. Jacobsson, *Future wishes and constraints from the experiments at the LHC for the Proton-Proton programme*, ICFA Mini-Workshop on Beam-Beam Effects in Hadron Colliders (BB2013) proceedings **CERN** (2014) 167, [arXiv:1410.3663](https://arxiv.org/abs/1410.3663).
- [172] *LHCb Trigger and Online Upgrade Technical Design Report*, CERN-LHCC-2014-016.
- [173] S. Okubo, ϕ meson and unitary symmetry model, *Phys. Lett.* **5** (1963) 165.
- [174] G. Zweig, An $SU(3)$ model for strong interaction symmetry and its breaking, **CERN-TH-412**.
- [175] J. Iizuka, Systematics and phenomenology of meson family, *Prog. Theor. Phys. Suppl.* **37** (1966) 21.
- [176] B. Bhattacharya and J. L. Rosner, Relative phases in $D^0 \rightarrow K^0 K^- \pi^+$ and $D^0 \rightarrow \bar{K}^0 K^+ \pi^-$ Dalitz plots, [arXiv:1104.4962](https://arxiv.org/abs/1104.4962).
- [177] B. Bhattacharya and J. L. Rosner, Flavor $SU(3)$ tests from $D^0 \rightarrow K^0 K^- \pi^+$ and $D^0 \rightarrow \bar{K}^0 K^+ \pi^-$ Dalitz plots, *Phys. Lett.* **B714** (2012) 276, [arXiv:1203.6014](https://arxiv.org/abs/1203.6014).
- [178] Note on “Scalar mesons below $2 \text{ GeV}/c^2$ ” in Ref. [54].
- [179] D. Atwood, I. Dunietz, and A. Soni, Enhanced CP violation with $B \rightarrow K D^0(\overline{D^0})$ modes and extraction of the Cabibbo-Kobayashi-Maskawa angle γ , *Phys. Rev. Lett.* **78** (1997) 3257, [arXiv:hep-ph/9612433](https://arxiv.org/abs/hep-ph/9612433).
- [180] D. Atwood, I. Dunietz, and A. Soni, Improved methods for observing CP violation in $B^\pm \rightarrow K D$ and measuring the CKM phase γ , *Phys. Rev.* **D63** (2001) 036005, [arXiv:hep-ph/0008090](https://arxiv.org/abs/hep-ph/0008090).
- [181] Y. Grossman, Z. Ligeti, and A. Soffer, Measuring γ in $B^\pm \rightarrow K^\pm(KK^*)_D$ decays, *Phys. Rev.* **D67** (2003) 071301(R), [arXiv:hep-ph/0210433](https://arxiv.org/abs/hep-ph/0210433).
- [182] LHCb collaboration, A study of CP violation in $B^\pm \rightarrow DK^\pm$ and $B^\pm \rightarrow D\pi^\pm$ decays with $D \rightarrow K_S^0 K^\pm \pi^\mp$ final states, *Phys. Lett.* **B733** (2014) 36, LHCb-PAPER-2013-068, CERN-PH-EP-2014-017, [arXiv:1402.2982](https://arxiv.org/abs/1402.2982).
- [183] D. Atwood and A. Soni, Role of a charm factory in extracting CKM phase information via $B \rightarrow DK$, *Phys. Rev.* **D68** (2003) 033003, [arXiv:hep-ph/0304085](https://arxiv.org/abs/hep-ph/0304085).
- [184] W. Dunwoodie, Fits to $K\pi$ $I = 1/2$ S-wave amplitude and phase data, http://www.slac.stanford.edu/~wmd/kpi_swave/kpi_swave_fit.note.
- [185] D. Aston *et al.*, A study of $K^- \pi^+$ scattering in the reaction $K^- p \rightarrow K^- \pi^+ n$ at $11 \text{ GeV}/c$, *Nucl. Phys.* **B296** (1988) 493.
- [186] BaBar collaboration, Dalitz-plot analysis of the decays $B^\pm \rightarrow K^\pm \pi^\mp \pi^\pm$, *Phys. Rev.* **D72** (2005) 072003, [arXiv:hep-ex/0507004](https://arxiv.org/abs/hep-ex/0507004), erratum *Phys. Rev.* **D74** (2006) 099903.
- [187] BaBar collaboration, Amplitude analysis of the decay $D^0 \rightarrow K^- K^+ \pi^0$, *Phys. Rev.* **D76** (2007) 011102, [arXiv:0704.3593](https://arxiv.org/abs/0704.3593).
- [188] BaBar collaboration, Search for CP violation in neutral D meson Cabibbo-suppressed three-body decays, *Phys. Rev.* **D78** (2008) 051102, [arXiv:0802.4035](https://arxiv.org/abs/0802.4035).

- [189] K. M. Watson, *The effect of final state interactions on reaction cross-sections*, Phys. Rev. **88** (1952) 1163.
- [190] R. Andreassen *et al.*, *GooFit: A library for massively parallelising maximum-likelihood fits*, J. Phys. Conf. Ser. **513** (2014) 052003.
- [191] E791 collaboration, *Dalitz plot analysis of the decay $D^+ \rightarrow K^-\pi^+\pi^+$ and indication of a low-mass scalar $K\pi$ resonance*, Phys. Rev. Lett. **89** (2002) 121801, [arXiv:hep-ex/0204018](https://arxiv.org/abs/hep-ex/0204018).
- [192] Review of resonances in Ref. [54], p.514.
- [193] FOCUS collaboration, *Dalitz plot analysis of the $D^+ \rightarrow K^-\pi^+\pi^+$ decay in the FOCUS experiment*, Phys. Lett. **B653** (2007) 1, [arXiv:0705.2248](https://arxiv.org/abs/0705.2248).
- [194] E791 collaboration, *Model independent measurement of S-wave $K^-\pi^+$ systems using $D^+ \rightarrow K\pi\pi$ decays from Fermilab E791*, Phys. Rev. **D73** (2006) 032004, [arXiv:hep-ex/0507099](https://arxiv.org/abs/hep-ex/0507099).
- [195] Belle collaboration, *Study of $\tau^- \rightarrow K_S^0\pi^-\nu_\tau$ decay at Belle*, Phys. Lett. **B654** (2007) 65, [arXiv:0706.2231](https://arxiv.org/abs/0706.2231).
- [196] LHCb collaboration, *Observation of D^0 - \bar{D}^0 oscillations*, Phys. Rev. Lett. **110** (2013) 101802, LHCb-PAPER-2012-038, CERN-PH-EP-2012-333, [arXiv:1211.1230](https://arxiv.org/abs/1211.1230).
- [197] LHCb collaboration, *Measurement of D^0 - \bar{D}^0 mixing parameters and search for CP violation using $D^0 \rightarrow K^+\pi^-$ decays*, Phys. Rev. Lett. **111** (2013) 251801, LHCb-PAPER-2013-053, CERN-PH-EP-2013-176, [arXiv:1309.6534](https://arxiv.org/abs/1309.6534).
- [198] LHCb collaboration, *First observation of D^0 - \bar{D}^0 oscillations in $D^0 \rightarrow K^+\pi^+\pi^-\pi^-$ decays and a measurement of the associated coherence parameters*, Phys. Rev. Lett. **116** (2016) 241801, LHCb-PAPER-2015-057, CERN-EP-2016-021, [arXiv:1602.07224](https://arxiv.org/abs/1602.07224).
- [199] G. Punzi, *Comments on likelihood fits with variable resolution*, eConf **C030908** (2003) WELT002, [arXiv:physics/0401045](https://arxiv.org/abs/physics/0401045).
- [200] M. Vesterinen and V. V. Gligorov, *Charm analysis with HLT information*, CERN-LHCb-INT-2013-022.
- [201] SymPy Development Team, *SymPy: Python library for symbolic mathematics*, 2014.
- [202] S. Malde, C. Thomas, and G. Wilkinson, *Measuring CP violation and mixing in charm with inclusive self-conjugate multibody decay modes*, Phys. Rev. **D91** (2015) 094032, [arXiv:1502.04560](https://arxiv.org/abs/1502.04560).
- [203] S. Malde *et al.*, *First determination of the CP content of $D \rightarrow \pi^+\pi^-\pi^+\pi^-$ and updated determination of the CP contents of $D \rightarrow \pi^+\pi^-\pi^0$ and $D \rightarrow K^+K^-\pi^0$* , Phys. Lett. **B747** (2015) 9, [arXiv:1504.05878](https://arxiv.org/abs/1504.05878).